

Unclassified  
SECURITY CLASSIFICATION OF THIS PAGE

DTIC FILE COPY

REPORT DOCUMENTATION PAGE				
AD-A216 470		10. RESTRICTIVE MARKINGS		
11. DECLASSIFICATION/DOWNGRADING SCHEDULE		12. DISTRIBUTION/AVAILABILITY OF REPORT		
35 1990		Approved for public release; distribution unlimited.		
13. PERFORMING ORGANIZATION REPORT NUMBER		14. MONITORING ORGANIZATION REPORT NUMBER		
D-5		AFOSR-TR-89-1876		
15. NAME OF PERFORMING ORGANIZATION		16. NAME OF MONITORING ORGANIZATION		
Stevens Institute of Technology		Air Force Office of Scientific Research		
17. ADDRESS (City, State and ZIP Code)		18. ADDRESS (City, State and ZIP Code)		
Department of Physics Hoboken, NJ 07030		Bolling Air Force Base, DC 20332-6448		
19. NAME OF FUNDING/SPONSORING ORGANIZATION		20. OFFICE SYMBOL (if applicable)		
AFOSR		NP		
21. ADDRESS (City, State and ZIP Code)		22. PROCUREMENT INSTRUMENT IDENTIFICATION NUMBER		
Bolling Air Force Base, DC 20332-6448		AFOSR - 86 - 0299		
23. TITLE (Include Security Classification)		24. SOURCE OF FUNDING NOS.		
SURFACE PRODUCTION OF IONS		PROGRAM ELEMENT NO. PROJECT NO. TASK NO. WORK UNIT NO.		
61102F 2301 A7				
25. PERSONAL AUTHOR				
MILOS SEIDL				
26. TYPE OF REPORT		27. TIME COVERED		28. DATE OF REPORT (Yr., Mo., Day)
FINAL SCIENTIFIC		FROM 8-1-86 TO 9-30-89		1989 - 10 - 09
29. PAGE COUNT				
10 + 135				
30. SUPPLEMENTARY NOTATION				
31. COSATI CODES		32. SUBJECT TERMS (Continue on reverse if necessary and identify by block number)		
FIELD	GROUP	SUB. GR.		
		Ion Emission; Ion Sources; Atom, Molecule and Ion Impact.		
33. ABSTRACT (Continue on reverse if necessary and identify by block number)				
It has been shown that negative hydrogen ions can be produced with high efficiency by backscattering low energy (order of 1 eV) hydrogen atoms or ions from low work-function (less than 1.5 eV) surfaces. This has been demonstrated experimentally by backscattering the Maxwellian tail of thermally produced hydrogen atoms from a variety of low work function surfaces. The general nature of the electron transfer process has been described by a simple theoretical model. Low incident energy guarantees low energy spread of the negative hydrogen ions. It also makes it possible to consider a variety of adsorbates for reducing the work function of the converter surface. The work function of cesium-oxygen films on silicon can be as low as 0.9 eV but these films are too delicate for use on converter surfaces. Thick cesium oxide films with a work function ranging from 1.2 to 1.4 eV have been successfully used on converter surfaces. Surface production of cesium ions from solid electrolyte sources has been investigated. Three types of cesium ion guns were developed and used in the experiments.				
34. DISTRIBUTION/AVAILABILITY OF ABSTRACT		35. ABSTRACT SECURITY CLASSIFICATION		
UNCLASSIFIED/UNLIMITED <input checked="" type="checkbox"/> SAME AS RPT. <input type="checkbox"/> DTIC USERS <input type="checkbox"/>		Unclassified		
36. NAME OF RESPONSIBLE INDIVIDUAL		37. TELEPHONE NUMBER (Include Area Code)		38. OFFICE SYMBOL
Lt Col Bruce L. Smith		202/267-4908		NP

DD FORM 1473, 83 APR

EDITION OF 1 JAN 73 IS OBSOLETE.

UNCLASSIFIED

90 01 04 142



Grant AFOSR-86-0299

**SURFACE PRODUCTION OF IONS**

M. Seidl, Principal Investigator

Final Report Covering the Period

8-1-86 to 9-30-89

Accession For	
NTIS GRA&I	<input checked="" type="checkbox"/>
DTIC TAB	<input type="checkbox"/>
Unannounced	<input type="checkbox"/>
Justification	
By	
Distribution /	
Availability Codes	
Dist	Availability or Special
A-1	

**Table of Contents**

	<u>Page</u>
1. Introduction	2
2. Backscattering of hydrogen atoms from low work function surfaces	3
3. Electronic structure of converter surfaces	5
4. Production of cesium ions	7
5. List of papers published or submitted in the reporting period	8
6. List of professional personnel	10
7. Appendix: 15 papers	

Approved for release;  
information limited.

AIR FORCE OFFICE OF SCIENTIFIC RESEARCH (AFSC)  
REPORT NO. AFOSR-86-0299  
This report is approved and is  
available to the public under AFOSR-100-12.  
Distribution Division

## 1. Introduction

This final report covers a three year project entitled "Surface Production of Ions." The objectives of this research, as stated in the proposal, are as follows:

- a) Explore surface production of  $H^-$  on a variety of substrates, including metals, semiconductors and layered structures.
- b) Measure the surface electronic structure of these substrates and correlate it with the efficiency of  $H^-$  production.
- c) Acquire a better understanding of the role which surface electronic structure plays in the ion production process.

During the period under review we have published or submitted for publication 15 papers. The papers are listed in Section 5. They are also attached to the first five copies of this report

In the first year of the project we have completed our studies on cesium ion bombardment of metal surfaces. In a series of papers [1-4,6,7] we have presented a fairly comprehensive picture of work function changes due to cesium ion bombardment.

In the first year of the project we had made a discovery that fundamentally affected the thrust of our research for the remaining part of the project. While studying the production of negative hydrogen ions by simultaneous bombardment of metal targets with cesium and hydrogen [4] we had observed that a fraction of the  $H^-$  ion population had a low energy spread of 0.4 eV or less. Further studies had shown that the slow  $H^-$  ions were due to reflection of slow hydrogen atoms from the low work function target and that the slow atoms were produced by dissociation of hydrogen gas on hot tungsten filaments.

In a series of follow-up experiments [8,10,13] we have studied the production of  $H^-$  ions by backscattering the Maxwellian tail of thermally

produced hydrogen atoms from a variety of surfaces. The general nature of the electron transfer process has been described by a simple theoretical model [8,13]. It was shown that  $H^-$  ions can be produced with reasonable efficiency ( $> 10\%$ ) by backscattering low energy (order of 1 eV) H atoms from low work function (less than 1.5 eV) surfaces.

Low incident energy of the hydrogen atoms (or ions) guarantees low energy spread of the  $H^-$  ions, a very desirable feature in an ion source. An additional bonus of low incident energy is the elimination of physical damage to the surface by atom impact. This has opened up new avenues for the optimization of the surface electronic structure. We have studied electronic surface changes due to cesium, oxygen and hydrogen adsorption on silicon [11] and of cesium and hydrogen adsorption of beryllium [9]. Thick films of cesium oxide have been successfully used for converter surfaces [13].

In the course of this work we have developed and built several types of cesium ion guns providing cesium ions in the energy range from 20 eV to 5 keV [12,14,15]. All these guns are based on a novel solid source of  $Cs^+$  ions the development of which was originally supported by the State of New Jersey.

We have upgraded our instrumentation by adding photo-electron spectroscopy, ion guns, and data processing on our UHV system. The DoD Instrumentation grant recently received is used for constructing a UHV ion scattering chamber, acquisition of a Scanning Tunneling Microscope and of a Low-Energy Electron Diffraction System.

## 2. Backscattering of hydrogen atoms from low work function surfaces

Surface production of negative hydrogen ions by backscattering atomic

hydrogen from low work function surfaces has been studied theoretically and experimentally [8,10,13].

Theoretical analysis indicates that the dominant limitation in negative surface ionization at low incident energies is trapping of the  $H^-$  ions by the image force. An  $H^-$  ion created by electron transfer near the target surface can escape from the confine of the image force only if its kinetic energy is larger than the difference in potential energies of the  $H^-$  ion at infinity and at the point of creation. This difference has the smallest value  $W-A$  (where  $W$  is the work function of the target and  $A = 0.75$  eV is the electron affinity of the hydrogen atom) occurring when the  $H^-$  is created at the intersection of the Fermi level with the potential curve of the image force. Numerical estimates indicate that the negative ionization probability exceeds 50 percent when the incident kinetic energy exceeds  $W-A$  by about 50%. For example, the calculated ionization probability is between 50% to 70% for  $W = 1.5$  eV and an incident kinetic energy of the atom equal to 1.1 eV.

Based on the theoretical model we can describe the ideal surface for ionization of low energy H atoms. The work function should be low, less than 1.5 eV, so that it is possible to create ions that are weakly bound to the surface. The surface electron density (just below the Fermi level) should be smaller than typical metallic densities, so that the tunnelling does not occur close to the surface. Finally, the electron wave function tails should decay slowly to increase tunnelling probability far from the surface.

In the experiments, the atomic hydrogen was produced by thermal dissociation of hydrogen gas at a temperature of 2500°K (0.21 eV). This method produces an atomic flux of Maxwellian energy distribution in which about 1% of the atoms has a kinetic energy larger than 1 eV. This atomic

flux was backscattered from several low work function targets: cesiated molybdenum, cesiated n-type and p-type silicon (100) and thick film of cesium oxide. The negative hydrogen ions have an energy spread about equal to the temperature of the atomic hydrogen gas. The measured yield of the negative hydrogen ions depends exponentially on the inverse temperature of the atomic gas. The yield reaches about 1% of the total atomic flux, indicating that all atoms with an incident energy larger than 1 eV have been converted into negative hydrogen ions. The work function of the target surface ranged between 1.6 to 1.2 eV.

These experiments have clearly shown that it is indeed possible to efficiently produce  $H^-$  ions by backscattering hydrogen atoms of energy larger than 1 eV from converter surfaces that have a work function smaller than 1.5 eV. It should be noticed that both of these requirements are within practical reach. Hydrogen atoms produced in electron-molecule collisions originate with 2 eV kinetic energy (Franck-Condon process) and work functions lower than 1.5 eV can be obtained in many systems as discussed in the next section.

### 3. Electronic Structure of Converter Surfaces

In order to provide a high backscattering yield for  $H^-$  ions at low energies the converter surface must have the following properties: low work function, low image force, high electron tunneling rate near the intersection of the Fermi level with the image force potential, chemical stability for atomic hydrogen. These properties are largely determined by the electronic structure of the converter surface. We have studied the surface electronic structure of several substrate-absorbate combinations under ultra-high vacuum conditions using electron reflection measurements, photoelectron spectroscopy and Auger electron spectroscopy.

When the converter is bombarded with cesium ions of higher energy than 50 eV, sputtering and implantation become important. This restricts the converter material to a few refractory metals. We have completed our studies on work function of metal surfaces bombarded with cesium ions [1-4,6,7]. Due to the combined effect of implantation and sputtering a steady state coverage develops that primarily depends on the atomic mass of the converter atoms and on the bombarding energy. Minimum work function of 1.6 eV is obtained at 45 eV for W and at 100 eV for Mo.

When the bombarding energy is lower than 10 eV, sputtering and implantation are negligible, and the above mentioned restrictions on the converter material do not apply. Converter surfaces with lower work function and optimized electron density can be sought. We have undertaken a systematic search for such a converter. The large body of knowledge accumulated over decades of research on photoemitters and thermionic cathodes has provided a good starting point although, apart from the common requirements of a low work function, each field has its own specific problems: photoelectrons must have a high escape probability, thermionic cathodes must be stable at high temperatures, and hydrogen converters must survive in a hydrogen atmosphere.

We have studied work function changes due to adsorption of cesium, oxygen and hydrogen on silicon (100) surfaces [11]. Adsorption of cesium alone lowers the work function to 1.45 eV at a cesium coverage of 0.5 monolayers. Overcesiation followed by oxygen adsorption reduces the work function to 0.9 eV. However, this Cs-O system is so delicate that its use for converter surfaces is not practical. On the other hand, we have been successful in making thick "cesium oxide" films with a work function ranging from 1.2 to 1.4 eV. These films are easy to use as converter surfaces and are reproducible in day-to-day operation. Exposure to atomic hydrogen (up

to a flux of  $5 \times 10^{15}$  atoms/cm<sup>2</sup>s) does not erode the film and activates the surface [13]. More work is needed to reduce the work function to 1.1 eV reported in the literature for well activated thick Cs-O films. Exposure to larger fluxes of hydrogen atoms or ions should be investigated. Another thick film deserving more attention as a converter material is the Ba-O system.

#### 4. Surface production of cesium ions

In the course of our experiments on cesium ion bombardment of solid surfaces we have developed and built three types of cesium ion guns [14,15] providing Cs<sup>+</sup> ions in the energy range from 20 eV to 5 keV. All these guns are based on a novel solid source of Cs<sup>+</sup> ions. Cesium ions are chemically stored in a cylindrical pellet made of cesium mordenite which is a synthetic zeolite of the formula Cs<sub>2</sub>O·AlO<sub>3</sub>·10 SiO<sub>2</sub>. The pellet is operated at a temperature of 1000°C at which temperature the zeolite is a good ionic conductor. Cesium ions reaching the surface of the pellet are thermionically emitted into vacuum. About 80 coulombs of cesium is stored in the pellet of 0.2 cm<sup>3</sup> volume, 10% of which is extracted.

An improved version of this source provides a porous tungsten thin film on one circular face of the pellet and a thick platinum coating on the other. Cesium ions are driven to the porous electrode by an electric field generated in the solid electrolyte by a biasing voltage. The ions diffuse through the porous tungsten electrode to its surface where they are emitted by surface ionization.

We have studied theoretically and experimentally cesium ion transport across the solid electrolyte-porous tungsten interface [12,14]. A self-consistent theory of the solid electrolyte-metal interface was developed. Cs<sup>+</sup> ion emission current-voltage curves have been measured as



function of biasing current.  $\text{Cs}^+$  ion emission current density up to 10 mA/cm<sup>2</sup> has been extracted for 500 hours at 1100°C in steady state operation. The emission current can be controlled by the biasing current.

5. List of papers published or submitted in the reporting period.

1. Work Function Reduction of a Tungsten Surface Due to Cesium Ion Bombardment, by G. S. Tompa, W. E. Carr and M. Seidl, Appl. Phys. Lett. 49, 1511 (1986).
2. Composite Thin Film Production by Ion Bombardment, by W. Carr, M. Seidl, G. Tompa, and A. Souzis, J. Vacuum Sci. and Tech. A5, 1250 (1987).
3. Work Function of Cesium Covered Polycrystalline Beryllium, by G. S. Tompa, W. Ermler, W. Carr, M. Seidl, and A. E. Souzis, Surf. Sci. 185, L453 (1987).
4. Surface Production of Negative Hydrogen Ions by Hydrogen and Cesium Ion Bombardment of Metal Surfaces, M. Seidl, J. L. Lopes, S. T. Melnychuk, W. E. Carr, and G. S. Tompa, Production and Neutralization of Negative Ions and Beams, edited by J. Alessi (Brookhaven National Laboratory), American Institute of Physics Conference Proceedings No. 158, p. 432 (New York, NY, 1987).
5. G. S. Tompa, J. L. Lopes, and G. Wohlrab, Compact efficient modular cesium atomic beam oven. Rev. Sci. Instrum. 58, 1536 (1987).
6. G. S. Tompa, W. E. Carr and M. Seidl, Work function of metallic surfaces bombarded with cesium ions. Surface Science 198, 431 (1988).
7. G. S. Tompa, M. Seidl and W. E. Carr, Composite surface layer formation produced by low energy  $\text{Cs}^+$  bombardment on Be, Mo and W. In: Defect and Diffusion Forum, Trans Tech Publications, Aldermansford,

Switzerland, Vols. 57-58, p. 263 (1988).

8. M. Seidl, W. E. Carr, J. L. Lopes, S. T. Melnychuk, Backscattering of hydrogen atoms at low energies, Proc. 3rd European Workshop on Production and Application of Light Negative Ions, FOM Institute for Atomic and Molecular Physics, Amsterdam, February 1988, p. 157.
9. M. M. Marino and W. C. Ermler, G. S. Tompa and M. Seidl, Effects of hydrogen and cesium adsorption on a beryllium surface. Surface Science 208, 189 (1989).
10. S. T. Melnychuk, M. Seidl, W. Carr, J. Isenbergh and J. Lopes, Reflection of hydrogen atoms from metal and semiconductor targets. Journal of Vacuum Science and Technology A7, 2127 (1989).
11. A. E. Souzis, M. Seidl, W. E. Carr, H. Huang, Electronic surface changes induced in silicon by hydrogen, oxygen and cesium coverages. Journal of Vacuum Science and Technology A7, 720 (1989).
12. S. I. Kim, M. Seidl, Cesium ion transport across solid electrolyte-porous tungsten interface. J. of Vacuum Science and Technology A7, 1806 (1989).
13. M. Seidl, W. E. Carr, S. T. Melnychuk, A. E. Souzis, J. Isenberg and H. Huang, Surface production of negative hydrogen ions. Conference Proceedings, SPIE Vol. 1061, Microwave and Particle Beam Sources and Directed Energy Concepts (1989) p. 547.
14. S. I. Kim and M. Seidl, A new solid state cesium ion source. Submitted to Journal of Applied Physics.
15. A. E. Souzis, W. E. Carr, S. I. Kim and M. Seidl, Solid state cesium ion guns for surface studies. Submitted to Review of Scientific Instruments.

6. List of Professional Personnel

Faculty: Milos Seidl, Professor of Physics  
Wayne Carr, Professor of Physics

Consultant: Homer Hagstrum

Postdoctoral Research Associates:

Gary Tompa 8/86-5/87  
Seong In Kim 6/89-9/89

Graduate Doctoral Students:

Joseph Lopes 8/86-5/88  
Stephen Melnychuk 8/86-Present  
Andrew Souzis 6/87-Present  
Seong In Kim 6/87-5/89  
Enrique Samano Part-time  
Seung Whan Lee Part-time  
Handing Huang Part-time  
Joshua Isenberg Part-time

Master's Students:

Yonghwa Cha

Technician: George Wohlrab

Degrees Awarded:

Joseph Lopes, Ph.D. in Physics (May 89)  
Thesis: Surface Production of Negative Hydrogen Ions

Seong In Kim, Ph.D. in Physics (May 89)  
Thesis: Cesium-Mordenite Solid Electrolyte as a Cesium  
Ion Source

Yonghwa Cha, M.S. (May 89)  
Thesis: Sputter-Deposition of Porous Tungsten Thin Film  
for a Cesium Ion Emitter

# Work function reduction of a tungsten surface due to cesium ion bombardment

G. S. Tompa, W. E. Carr, and M. Seidl

Department of Physics and Engineering Physics, Stevens Institute of Technology, Hoboken, New Jersey 07030

(Received 24 July 1986; accepted for publication 6 October 1986)

The reduction of the work function of a polycrystalline W surface due to  $\text{Cs}^+$  bombardment has been investigated in the incident energy range below 500 eV. Upon exposure of the surface to a  $\text{Cs}^+$  beam, the work function decreases until a steady state is reached with a total  $\text{Cs}^+$  dose of less than  $1 \times 10^{16}$  ions/cm<sup>2</sup>. A minimum steady state work function surface is produced at an incident energy of  $\approx 40$  eV and the steady state work function rapidly increases with bombarding energy. Coverages are significantly lower than that produced on Mo for the same bombarding energies. Auger electron spectroscopy is used to confirm surface coverages. The cesium surface concentration is determined by reflection, sputtering, and implantation.

In past years the production of  $\text{H}^-$  beams has become important to the fusion program as well as for military applications. Surface converters are an important source of  $\text{H}^-$  ions.<sup>1</sup> A surface conversion source consists of a metallic converter surface immersed in a cesium-hydrogen plasma and biased at a few hundred volts negative with respect to the plasma potential. H atoms are converted to  $\text{H}^-$  ions at the surface by electron tunneling from the converter surface to the H atoms. Cs is used to reduce the work function, increasing the electron transfer probability. There exists an optimum coverage at which the work function is a minimum and hence the  $\text{H}^-$  yield is a maximum.<sup>2-7</sup> The mean free path of neutral Cs in the plasma is small,<sup>8</sup> hence the surface coverage is due to  $\text{Cs}^+$  bombardment, not vapor deposition. In working converters the Cs surface concentration is not well known<sup>8,9</sup> and doubt has been expressed whether the minimum work function surface can be achieved by cesium ion bombardment at typical converter energies.<sup>8,9</sup>

Previously we measured the steady state work function shifts on Mo due to  $\text{Cs}^+$  bombardment and found that a large coverage could be produced.<sup>10</sup> We have repeated these measurements on W and found that only at low incident energies (less than  $\approx 75$  eV) are coverages greater than  $\approx 25\%$  produced at steady state. For W, the optimum work function surface is produced at an incident energy of  $\approx 40$  eV. The experimental system is the same as that used in examining the Mo sample<sup>10</sup> and is described in detail elsewhere.<sup>11</sup>

The work function changes with dose, as is shown in Fig. 1. The work function starts with "zero" shift (clean W) and decreases with increasing dosage until it reaches a steady state value dependent upon the  $\text{Cs}^+$  energy. The total ion dose needed to reach steady state coverage is less than  $1 \times 10^{16}$  ions/cm<sup>2</sup>, and this takes a few minutes in our system. The dependence of the steady state work function on the Cs bombarding energy is shown in Fig. 2. Here the work function shift is plotted as a function of bombarding energy; the dosage is  $1 \times 10^{16}$  ions/cm<sup>2</sup>. At a bombarding energy of  $\approx 40$  eV, a distinct minimum in the work function is observed, the shift is  $\approx 2.9$  eV. Taking the clean polycrystalline W work function to be 4.5 eV,<sup>12</sup> the minimum work function

is  $\approx 1.6$  eV. This is in agreement with vapor deposition experiments.<sup>12</sup>

In order to determine the Cs coverage, the work function shifts are compared to those obtained by vapor deposition measurements.<sup>12</sup> Additionally, the relative Cs concentration is obtained from the amplitude of an Auger electron spectroscopy (AES) Cs line. Figure 2 shows the coverage derived from the work function shifts and the Cs Auger line intensity as a function of  $\text{Cs}^+$  energy. Since the AES amplitudes are not absolutely calibrated, the AES data were scaled to the 450 eV value, where the curves vary slowly with energy.

The surface in this experiment is composite, consisting of a mixture of Cs and W and a few monolayers deep. There is Cs both on and below the surface. The good agreement of the AES results with the coverage inferred from surface deposition work function values implies that the surface coverage is the dominant factor in determining the work function. Implanted Cs and surface roughening due to  $\text{Cs}^+$  ion bombardment do not strongly contribute at steady state for the energy range examined.

Above  $\approx 150$  eV in bombarding energy the work function shift is fairly constant at  $\approx -1.3$  eV and the coverage is below 15%. This is in agreement with predictions made by van Amersfoort *et al.*<sup>9</sup> The steady state coverage at bombarding energies less than  $\approx 40$  eV is larger than that giving an optimum work function surface. This can be seen in the 30 eV curve in Fig. 1. The work function decreases to a minimum, beyond which it increases with increasing dose; this shows that the coverage passes through optimum in reaching steady state. This is also shown clearly by the AES data in Fig. 2.

A delay of  $\approx 20$ –30 s is encountered between cleaning, dosing, and measuring due to the time taken to reposition the sample at each station. A possible source of error in the measurement of the work function is surface diffusion. For W, Taylor and Langmuir<sup>13</sup> give a jump frequency of  $1.5E-5$  s at 300 K and a diffusion coefficient ( $D$ ) on the order of  $10^{-11}$  cm<sup>2</sup>/s. We may estimate the distance traveled during the time required to make a measurement as  $d = (Dt)^{1/2}$ . For 100 s this gives  $3.2 \times 10^{-5}$  cm. On converters in a discharge,

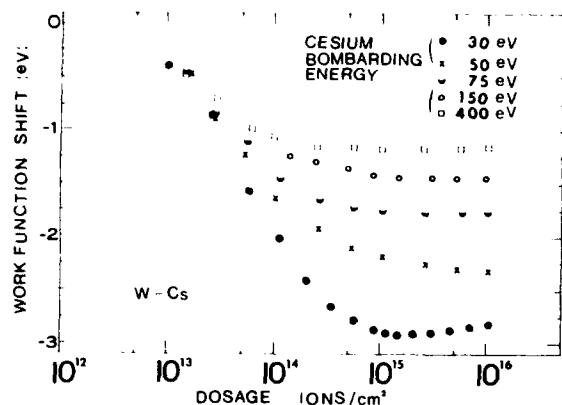


FIG. 1. Work function shift as a function of the positive cesium ion dosage, for five different bombarding energies.

Cs may be assumed to be spread uniformly on the converter surface due to the discharge, hence surface diffusion is not important for converters. At the temperature ( $\approx 300$  K) and fluxes we operated at, evaporation of Cs was not observed to be a significant loss mechanism at the surface, as confirmed by monitoring the work function and Cs AES signal in time after large dosings. At coverages greater than a monolayer, evaporation is a problem. A typical time for contamination to become observable is of the order of several hundred seconds, far longer than the time needed for taking a measurement.

A theoretical analysis of the steady state cesium surface concentration is pertinent to the understanding of these results. Over most of the energy range used in the experiment the implantation depth is greater than one layer so any description should include implantation. When Cs bombards a clean target some of the Cs is implanted. As the target material is sputtered away the previously implanted Cs is exposed, so that eventually a steady state surface is achieved that has a fractional Cs coverage. We will discuss this steady state situation. The present analysis is a generalization of the analysis of our previous letter.<sup>10</sup>

We define  $\phi_{in}$  as the incident flux,  $\phi_c$  as the sputtered Cs flux, and  $\phi_i$  as the sputtered target flux. A fraction  $\beta$  of the incident flux is backscattered, so that  $(1 - \beta)\phi_{in}$  is implanted. The probability that an ion is implanted in thickness  $dx$

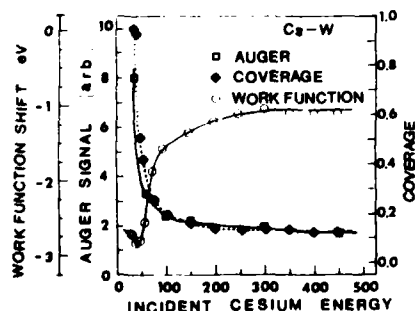


FIG. 2. Work function shift, Cs Auger signal, and coverage dependences on Cs<sup>+</sup> bombarding energy at steady state. Coverage is determined from the work function shift.

at  $x$  is given from Lindhard-Scharff-Schiott (LSS) theory by<sup>14-16</sup>

$$P(x)dx = \frac{0.57}{\Delta} \exp\left(-\frac{(x-R)^2}{\Delta^2}\right) dx,$$

where  $R$  is the average depth and  $\Delta$  is deviation. Note that this is normalized, i.e., the integral over  $x$  is unity. The rate of increase of Cs concentration,  $c_c$ , in  $dx$  at  $x$  due to implantation is thus given by

$$\frac{dc_c(x)}{dt} = \frac{(1-\beta)\phi_{in}}{\rho} P(x),$$

where  $\rho$  is the number density of the target (assumed constant). Note that  $x$  is the depth of a slab of the solid, which changes in time due to two effects. The depth decreases due to sputtering and it increases due to implantation. Our previous analysis<sup>10</sup> did not include this increase. The decrease in depth is given by

$$dx_s = -(\phi_i + \phi_c)dt/\rho.$$

The increase due to implantation is given by

$$\frac{dx_i}{dt} = \int_0^x dc_c dx = \frac{(1-\beta)}{\rho} \phi_{in} Q(x),$$

where  $Q(x) = \int_0^x P(x)dx$ . The total rate of change of depth is thus given by

$$dx = -[(\phi_i + \phi_c)/\rho + (1-\beta)\phi_{in}Q(x)/\rho]dt.$$

Since we are considering steady state there can be no net Cs buildup in the target, which means that the total Cs flux leaving the target must equal the incident flux. This gives the relation

$$\phi_{in} = \beta\phi_{in} + \phi_c \text{ or } \phi_c = (1-\beta)\phi_{in}.$$

All of the above relations may be combined to give a differential equation for the Cs concentration as a function of depth

$$\frac{dc_c}{dx} = \frac{dQ/dx}{Q(x) - 1 - \Gamma_i/(1-\beta)},$$

where  $\Gamma_i = \phi_i/\phi_{in}$  is the sputtering yield of the target species. Integrating, we have that

$$c_c(x) = \ln[1 - Q(x) + (1-\beta)/\Gamma_i].$$

The surface concentration is thus given by

$$c_c(0) = \ln[1 + (1-\beta)/\Gamma_i].$$

Note that in the limit of small concentration we have that  $c_c = (1-\beta)/\Gamma_i$ , which is the form we obtained in our previous paper.<sup>10</sup>

This model applies when the incident energy is large enough for implantation to take place. Below this energy range sputtering and implantation are not the important mechanisms and the vapor deposition model applies. The model assumes constant implantation range and spread, and constant backscattering. Both backscattering and implantation depend on the composition, and hence the model is not expected to be accurate at very large concentrations. In addition, the model becomes suspect when the range is comparable to a layer. It is interesting to note that the concentration is flux independent; this is a result of neglecting surface diffusion and evaporation which are negligible.

In general, the surface concentration is determined by reflection (backscattering), sputtering, and implantation. The target mass is an important factor since it determines the amount of backscattering and the depth scale for implantation. Implantation becomes of importance once the implantation depth is larger than about one layer of the target,  $\approx 2.7$  Å for Mo or W and  $\approx 2.2$  Å for Be. We can compare the implantation depth scale with the LSS<sup>15,16</sup> theory of implantation. LSS theory gives a relation between incident energy and range for low-energy ions (less than 10 keV). We calculated implantation depths ( $R$ ) using both LSS range statistics and the TRIM code<sup>17</sup> for Cs on Mo, W, and Be. The implantation depths (in Å) are presented in Table I for two incident energies. Also shown in the table are TRIM code derived backscatter coefficients. At a given energy the steady state surface concentration is determined by a balance between implantation and sputtering. Increasing the incident energy increases the implantation depth and the sputtering yield, decreasing the steady state surface concentration. For W, compared to Mo, the reflection coefficient is much larger and the implantation depth much less, resulting in a significantly lower surface concentration of Cs. Our results agree with the fact that Mo cathodes are better sources of  $H^-$  than are W cathodes in surface conversion sources.<sup>18</sup>

We have seen that  $Cs^+$  bombardment at a bombarding energy of  $\approx 100$  eV is capable of producing high Cs coverages on Mo<sup>10</sup> but not on W. The interpretation of coverage formation by van Amersfoort<sup>9</sup> holds for W where there is little implantation and large reflection, but not for Mo where the conditions are reversed. These results confirm our interpretation of the coverage formation process in these materials: that the coverage goes as  $(1 - \beta)/\gamma$ .

For an optimum work function surface to be produced at typical converter operating energies (greater than  $\approx 100$  V) the converter material should be lighter than Cs and have a low sputter yield. Recent work with alkali adsorbates on ruthenium<sup>19,20</sup> has produced very low work function surfaces. We have also observed a low work function surface to be produced by adsorbing Cs on Be. Near optimum coverages may be produced on Be or Ru at higher bombarding energies, which would also enhance  $H^-$  yields.<sup>3</sup> We plan to

TABLE I. Implantation depths (in Å) as determined by LSS theory and the TRIM computer code at incident energies of 30 and 300 eV. The TRIM derived backscatter coefficient  $\beta$  is also given.

	30 eV			300 eV		
	LSS	TRIM	$\beta$	LSS	TRIM	$\beta$
Be	2.0	3.0	0	9.7	13.0	0
Mo	0.97	2.8	0	4.5	9.1	0
W	0.95	2.0	0.14	4.4	5.0	0.20

examine the work function reduction on Be and Ru due to  $Cs^+$  bombardment as the next step in this series of experiments.

This work has been supported by the Air Force Office of Scientific Research and the Department of Energy.

<sup>1</sup>AIP Proceedings No. 111, *Production and Neutralization of Negative Ions and Beams*, edited by K. Prelec (AIP, New York, 1984), pp. 331-457.

<sup>2</sup>J. R. Hiskes, J. Phys. Paris C 7, 179 (1979).

<sup>3</sup>M. Seidl and A. N. Pargellis, Phys. Rev. B 26, 1 (1982).

<sup>4</sup>Ming L. Yu, Phys. Rev. Lett. 40, 574 (1978).

<sup>5</sup>J. N. M. van Wunnik, J. J. C. Geerlings, E. H. A. Granneman, and J. Los, Surf. Sci. 131, 17 (1983).

<sup>6</sup>K. W. Ehlers and K. N. Leung, Rev. Sci. Instrum. 51, 721 (1982).

<sup>7</sup>J. A. Greer and M. Seidl, J. Vac. Sci. Technol. A 2, 677 (1984).

<sup>8</sup>AIP Proceedings No. 111, *Production and Neutralization of Negative Ions and Beams*, edited by K. Prelec (AIP, New York, 1984), pp. 227-236.

<sup>9</sup>P. W. van Amersfoort, Ying Chun Tong, and E. H. A. Granneman, J. Appl. Phys. 58, 2317 (1985).

<sup>10</sup>G. S. Tompa, W. E. Carr, and M. Seidl, Appl. Phys. Lett. 48, 1048 (1986).

<sup>11</sup>G. S. Tompa, Doctoral dissertation, UMI, Ann Arbor, publication No. 86-24177 (1986).

<sup>12</sup>L. W. Swanson and R. W. Strayer, J. Chem. Phys. 48, 2421 (1968).

<sup>13</sup>J. B. Taylor and I. Langmuir, Phys. Rev. 44, No. 423 (1933).

<sup>14</sup>J. C. C. Tsai and J. M. Morbito, Surf. Sci. 44, 247 (1975).

<sup>15</sup>P. D. Townsend, J. C. Kelly, and N. E. W. Hartly, *Ion Implantation, Sputtering, and their Applications* (Academic, London, 1976), p. 32.

<sup>16</sup>J. W. Mayer, L. Eriksson, and J. D. Davies, *Ion Implantation in Semiconductors* (Academic, London, 1970), p. 36.

<sup>17</sup>J. P. Biersack and W. Eckstein, J. Appl. Phys. (German) A 34, 73 (1984).

<sup>18</sup>AIP Proceedings No. 111, *Production and Neutralization of Negative Ions and Beams*, edited by K. Prelec (AIP, New York, 1984), pp. 265-272.

<sup>19</sup>M. Kiskinova, G. Rangelov, and L. Surnev, Surf. Sci. 172, 57 (1986).

<sup>20</sup>M. Kiskinova, G. Rangelov, and L. Surnev, Surf. Sci. 150, 339 (1985).

# Composite thin-film production by ion bombardment

W. Carr, M. Seidl, G. S. Tompa, and A. Souzis

Physics Department, Stevens Institute of Technology, Hoboken, New Jersey 07030

(Received 19 September 1986; accepted 1 December 1986)

Composite thin-film production by low-energy cesium ion bombardment was investigated. An ion beam impinging on a target produces a steady-state film, with a total dose of less than  $10^{16}$  ions/cm<sup>2</sup>. The fractional concentration of the beam species depends on the incident energy. When the incident energy is sufficiently low, the surface binding energy is greater than the recoil energy and an overlayer forms. An analytical model describing the steady-state film, including sputtering, backscattering, implantation, and diffusion is given. In the absence of diffusion the surface concentration depends on the ratio of the implanted fraction to the target sputtering yield. When diffusion is important, the depth profile becomes exponential and the surface concentration is reduced.

## I. INTRODUCTION

Low-energy ion bombardment has been increasingly used to produce composite thin films. Cesium is convenient for experimental purposes because a small concentration reduces the work function of metal surfaces, permitting *in situ* measurements of surface modification. In addition, surface concentration may be determined by using results of vapor deposition measurements.<sup>1</sup>

The mechanism in the production of these composite thin films is the implantation of primary species proceeding simultaneously with the sputtering of target material. As the target is sputtered away, the surface concentration of primary species increases due to exposure of previously implanted atoms. This continues until a stationary state evolves.

The production of low work function surfaces has many potential applications, and the use of cesium bombardment is of interest in negative hydrogen ion sources,<sup>2</sup> where a low work function is needed for production efficiency. Cesium beams are also used in secondary ion mass spectrometry (SIMS) systems to increase the sensitivity to the electronegative elements

This paper describes measurements using several target materials. Results include work function shift and absolute surface concentration as a function of cesium beam energy. Depth profiling by sputtering indicates that profile broadening<sup>3</sup> during sputtering is important. An analytic model incorporating backscattering, sputtering, implantation, and diffusion of the implanted atoms is given.

## II. EXPERIMENTAL DETAILS

The apparatus used for the measurements consists of a UHV system, with a base pressure of  $5 \times 10^{-11}$  Torr, containing four experimental stations: a cesium ion gun; an electron gun for the work function shift measurement; a He-Ne laser of wavelength  $\lambda = 623.8$  nm, for absolute work function calibration; a PHI Auger electron spectrometer (AES) for detection of surface atoms; and an argon ion gun for sputter cleaning. A target, 3 mm in diameter, is mounted on a carousel, which allows rotation to the stations. The experi-

ment is connected to an Apple II + microcomputer, so that control and data acquisition are provided for the cesium gun, the work function station, and the AES. A second vacuum system is used for SIMS depth profiling measurements.

The target is cleaned by argon sputtering, using typically  $0.2 \mu\text{A}$  at 5 keV. The beam is rastered to clean the entire target uniformly. The Auger electron spectrum shows no observable contaminants for approximately 20 min after cleaning, and all of the measurements are obtained within this interval. In order to assure that the target remains clean, each measurement is preceded by sputter cleaning.

The cesium ion beam is produced by a gun designed and built in house. The source is a heated pellet of cesium mordenite which thermionically emits cesium ions. The ions are then extracted by mounting the pellet in a Pierce-type ion gun. In operation, the source is capable of providing incident current in excess of  $1 \mu\text{A}$  to the target. The beam is deflected before striking the target so that neutral cesium does not have a line of sight path to the target.

Work function shifts are measured using the retarding field diode method.<sup>4</sup> In this method an electron beam is directed toward a biased target and the bias voltage is adjusted to reflect part of the beam. The shift in bias voltage is equal to the work function shift of the surface. To find the absolute work function, the target is biased negatively, and we determine the calibration point at 1.96 eV by the onset of the photoelectron current generated by the He-Ne laser.

## A. Experimental results

As the cesium beam bombards the surface, there is a gradual evolution of the composite layer.<sup>5</sup> The work function decreases smoothly, and eventually reaches a steady-state value that does not change further with increased dosage. The total dose needed to reach steady state is less than  $1.0 \times 10^{16}$  ions/cm<sup>2</sup> for all of the measurements. The cesium concentration increases with decreasing energy, with the interesting cases occurring at and below 100 eV.

Two independent determinations of the cesium coverage are made. The first method is to measure the work function shift and determine the coverage from vapor deposition mea-

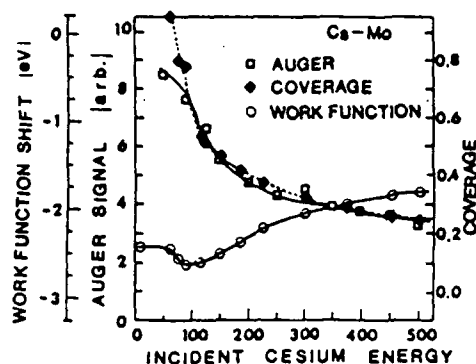


FIG. 1. Surface concentration, AES signal intensity, and work function shift on molybdenum as a function of incident cesium energy.  $\square$  Auger signal intensity;  $\circ$  work function shift;  $\blacklozenge$  coverage derived from work function shifts.

measurements.<sup>1</sup> The second method is to use cesium line intensities in the Auger spectrum. These intensities are not absolutely calibrated, but for less than monolayer coverages the line intensity is proportional to the cesium concentration.

Figures 1 and 2 show the work function shift and surface cesium concentration versus beam energy on molybdenum and tungsten, respectively. These two targets differ in an important way; tungsten is heavier than cesium, giving significant backscattering, while molybdenum is lighter, having essentially no backscattering. The open circles show the measured work function shifts and the open squares show the measured AES cesium line intensities. The filled diamonds are interpolated from the vapor deposition data. The Auger intensity curve is normalized to the concentration at 500 eV determined by the work function. The values of cesium coverage should be accurate, since the curves for the two methods essentially coincide. The molybdenum data show a minimum steady-state work function at a cesium beam energy of 90 eV, where the cesium coverage is 0.6 monolayers. The tungsten data show a similar minimum at a lower cesium beam energy of 45 eV. Thus we have shown that backscattering has a significant role in the formation of a large surface concentration. This has been further confirmed by our recent measurements on beryllium. Implantation depths in beryllium are greater than on either molybdenum or tungsten and we have produced large surface concentrations throughout the entire 0–500 eV energy range. Absolute calibrated minimum work functions were  $\approx 1.6$  eV for the three metals examined (W, Mo, Be).

In the energy range near the work function minimum, the data are ambiguous, i.e., the work function change could be due to a coverage which is either slightly higher or slightly lower than the optimum. The AES data resolve the ambiguity, and show that there is a monotonic increase in cesium coverage with decreasing energy.

In a separate system we have a Kratos SIMS apparatus, together with a high-energy version of the same cesium source. Using this, sputter profiles have been obtained for 4-keV cesium ions implanted into silicon. In Fig. 3, a SIMS profile of  $\text{Cs}^{133}$  counts per incident nA is plotted as a function of sputtering time. The surface erosion rate is calculated

using published values of the pure element sputter yield for Si,<sup>6</sup> multiplied by the ratio of the incident flux to the substrate atomic density. With this, we calculate a surface erosion rate of  $\approx 1.3 \times 10^{-2}$  Å/s. The  $\text{Cs}^{133}$  SIMS signal as measured by the pulse counting electronics is essentially an exponential. This dependence has been observed previously, and is attributed to radiation enhanced diffusion.<sup>3</sup> On log scale, a straight-line extrapolation of the exponential portion of the profile gives an implantation depth of approximately 90 Å. A computer calculation using the TRIM code,<sup>7</sup> gives a mean range of 75 Å plus straggling of 19 Å, adding to 94 Å. The nonexponential tail of the profile is primarily due to knock-on collisions of the primary argon beam with the implanted cesium.

### III. ANALYTICAL MODEL

Starting with a clean surface, the concentration evolves smoothly to a steady state. In the beginning there are few incident atoms on the surface because they are either backscattered or implanted. After target material is sputtered away, the surface concentration of beam species increases due to exposure of previously implanted atoms. These are also sputtered, and the surface film stabilizes when the net beam flux to the target is zero. Additional exposure to the beam does not change the film. The condition of zero net flux to the surface defines a threshold energy for composite film formation. At very low energy, sputtering is insufficient to achieve zero flux, and an overlayer results.

The model assumes that steady state has been reached. The differential implantation profile is represented by the probability of an implanted atom stopping in an interval  $dx$  at  $x$ , given by

$$P(x)dx = N \exp - [(x - R)/D]^2 dx, \quad (1)$$

where  $R$  is the range and  $D$  is the deviation. It should be pointed out that these values are for the composite material that is actually present. The normalization constant  $N$  is determined by the constraint that the total probability is unity; for  $R > D$ ,  $N = (1.75 D)^{-1}$ .

Defining  $\Phi_{in}$  as the incident flux,  $\Phi_b$  as the sputtered flux of the beam species, and  $\alpha$  as the implanted fraction (1 mi-

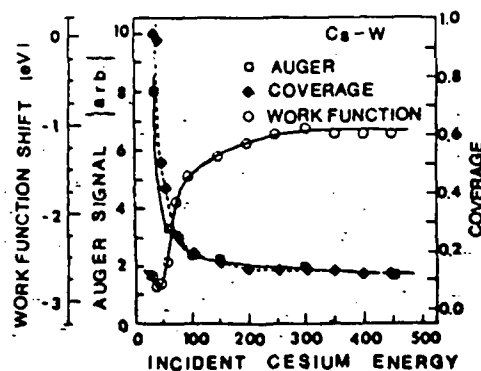


FIG. 2. Surface concentration, AES signal intensity, and work function shift on tungsten as a function of incident cesium energy.  $\square$  Auger signal intensity;  $\circ$  work function shift;  $\blacklozenge$  coverage derived from work function shifts.



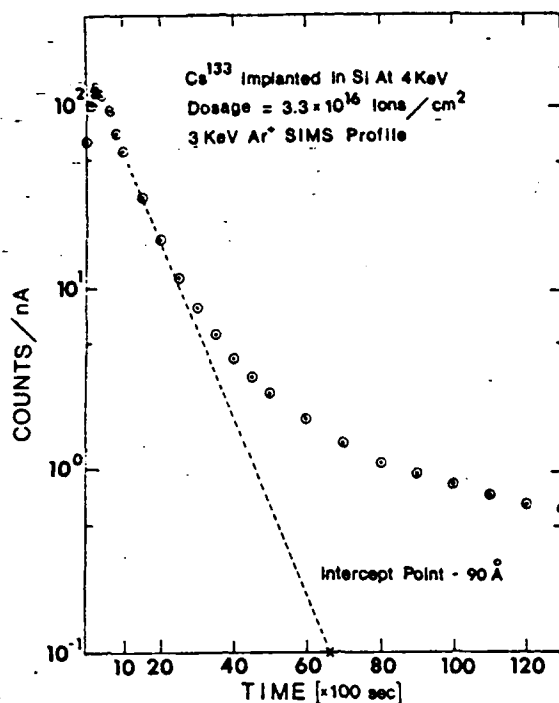


FIG. 3. Cesium SIMS profile in counts per incident nA plotted vs sputtering time for a composite cesium film on silicon. The surface erosion rate is  $\sim 1.3 \times 10^{-2}$  Å/s. The intercept point is extrapolated assuming a pure exponential decay.

nus the reflection coefficient), the steady-state condition of zero net beam flux is given by

$$\Phi_b = \alpha \Phi_{in}. \quad (2)$$

At steady state, the depth profile of the implanted atoms is constant in time when measured with respect to the surface, but a given slab of material moves toward the surface due to sputtering, and the concentration of beam species increases from zero, when it is far from the surface, to a finite value at the surface. Implantation tends to increase the concentration and diffusion decreases it. The expression for the implanted concentration is obtained using Eq. (1), given by

$$\frac{dc(x)}{dx} \frac{dx}{dt} = \alpha \Phi_{in} P(x)/\rho - \Delta \frac{d^2c}{dx^2}, \quad (3)$$

where  $c$  is the fractional concentration of beam atoms,  $\rho$  is the number density of the material (assumed constant), and  $\Delta$  is the effective diffusion coefficient.

At steady state the only time-dependent quantity is the depth of the slab, and there are two contributions to this change. It decreases due to sputtering, given by

$$\left. \frac{dx}{dt} \right|_{\text{sputt}} = -(\Phi_i + \Phi_b)/\rho = -(\Phi_i + \alpha \Phi_{in})/\rho, \quad (4)$$

where Eq. (2) has been used to obtain the final form. The target swells due to implantation of atoms above the slab, given by

$$\left. \frac{dx}{dt} \right|_{\text{impl}} = \left( \alpha \Phi_{in} \int_0^\infty P(x) dx \right) / \rho = \alpha \Phi_{in} G(x)/\rho, \quad (5)$$

where we have defined  $G(x) = \int_0^\infty P(x) dx$  for convenience.

The net speed of a slab is the sum of Eqs. (4) and (5). Upon substitution onto Eq. (3) we have that

$$\frac{\Delta}{\alpha \Phi_{in}} \frac{d^2c}{dx^2} + [G(x) - \Phi_i/\alpha \Phi_{in} - 1] \frac{dc}{dx} = \frac{dG(x)}{dx}. \quad (6)$$

Note that  $\Phi_i/\Phi_{in} = \Gamma$ , which is the sputtering yield of the target material from the composite surface.

If diffusion is neglected Eq. (7) has a simple integral, given by

$$c_b(x) = \ln([1 - G(x) + \Gamma/\alpha]/[\Gamma/\alpha]). \quad (7)$$

Here the surface concentration ( $x = 0$ ) depends only on the target sputtering yield and the fractional implantation coefficient, since  $G(0) = 0$ . In the limit of low concentrations we may write

$$c_b(0) = \ln(1 + \alpha/\Gamma) \approx \alpha/\Gamma, \quad (8)$$

which has been obtained previously.<sup>8,9</sup>

When diffusion is not negligible Eq. (6) may be integrated numerically, resulting in the curves shown in Fig. 4. In the uppermost curve diffusion is small and the profile has the same shape as that of a Monte Carlo calculation.<sup>10</sup> Strong diffusion changes the shape toward an exponential tail, which is a better fit to the observed SIMS depth profile. The thickness of the film is  $3 \times D$ , independent of the other parameters.

It should be pointed out that the implanted fraction  $\alpha$ , and the target atom sputtering yield  $\Gamma$ , must be the values for the steady-state composite surface. By way of illustration, a cesium beam has essentially no backscattering from a molybdenum target. In this case, a binary collision gives a small maximum scattering angle, so that several collisions are needed to turn a cesium atom around, resulting in a small escape probability. However, if a reasonable fraction of the surface is cesium, large-angle scattering can result from Cs-Cs collisions, and an incident atom can be reflected in one or two collisions. This means that although  $\alpha = 1$  for the pure target, it is less than unity for the composite surface.

At very low incident energy this description does not apply in two respects. First, it assumes steady state, which re-

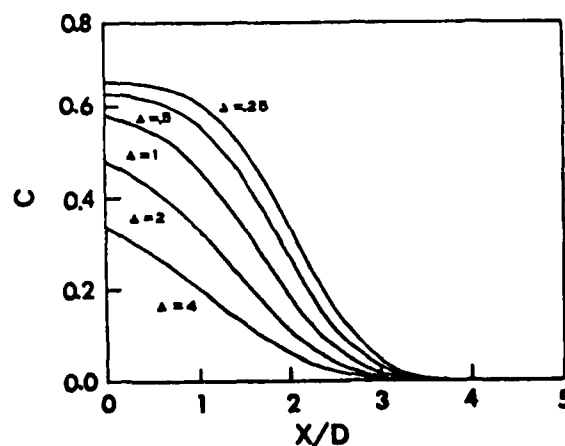


FIG. 4. Calculated concentration profile for  $\Gamma/\alpha = 1$ .  $\Delta$  is the effective diffusion coefficient normalized to the implanted flux,  $\Gamma$  is the sputtering yield of the target material, and  $\alpha$  is the implanted fraction.

quires that the net beam flux to the target is zero. For low enough incident energy, sputtering is not sufficient to satisfy this condition. (This actually occurs in the measurements. In Figs. 1 and 2 the lowest energy data points are for a cesium covered surface.) Second, when the implantation range is of the order of one layer the atoms are essentially merely sticking to the surface.

#### IV. SUMMARY

Work function reduction and surface concentration of a composite film produced by cesium ion bombardment have been measured for molybdenum and tungsten targets. The surface concentration decreases with increasing beam energy. A larger surface concentration can be formed on molybdenum because it is lighter than cesium and the implanted fraction is larger. Sputter profiling of the film shows evidence of strong diffusion effects, probably due to both the implantation and the profiling. A simple analytical model is described which exhibits the general features of the steady-state composite film.

#### ACKNOWLEDGMENTS

We would like to thank G. Wohlrab and G. Wirth for their help in building most of the experimental apparatus. This work was supported by the Air Force Office of Scientific Research, the Department of Energy, and the State of New Jersey.

<sup>1</sup>L. W. Swanson and R. W. Strayer, *J. Chem. Phys.* **48**, 2421 (1968).

<sup>2</sup>*Production and Neutralization of Negative Ions and Beams*, edited by K. Prelec (American Institute of Physics, New York, 1984), Proceedings No. 111.

<sup>3</sup>J. Remmerie, W. Vandervorst, and H. E. Maes, *Nucl. Instrum. Methods B* **13**, 416 (1986).

<sup>4</sup>A. G. Knapp, *Surf. Sci.* **34**, 289 (1973).

<sup>5</sup>G. S. Tompa, W. E. Carr, and M. Seidl, *Appl. Phys. Lett.* **48**, 1048 (1986).

<sup>6</sup>*Sputtering by Particle Bombardment I*, edited by R. Behrisch (Springer, Berlin, 1981), p. 169.

<sup>7</sup>J. P. Biersack and W. Eckstein, *Appl. Phys. (German) A* **34**, 73 (1984).

<sup>8</sup>V. R. Deline, C. A. Evans, Jr., and P. Williams, *Appl. Phys. Lett.* **33**, 578 (1978).

<sup>9</sup>M. Seidl, A. N. Pargellis, and J. Greer, in *Proceedings of the Joint Seminar on the Atomic Properties of Negative Ions*, edited by C. Cisneros and J. J. Morgan (Instituto de Fisica, UNAM Mexico, 1982), p. 393.

<sup>10</sup>E. A. Maydell-Ondrusz and I. H. Wilson, *Thin Solid Films* **114**, 357 (1984).

SURFACE SCIENCE LETTERS

WORK FUNCTION OF CESIUM-COVERED  
POLYCRYSTALLINE BERYLLIUM

G.S. TOMPA \*, M. SEIDL \*, W.C. ERMLER \*\* and W.E. CARR \*

*Stevens Institute of Technology, Hoboken, NJ 07030, USA*

Received 18 February 1987; accepted for publication 16 March 1987

The dependence of the work function on Cs coverage of clean polycrystalline Be has been measured. The maximum shift obtainable is 2.3 eV. Photoemission and thick Cs overlayer measurements indicate that the minimum work function surface is at 1.6 eV. This new measurement is one of many showing that cesium covered metals and semiconductors are observed to have a minimum work function close to 1.6 eV. In general the minimum work function value is observed to be weakly dependent on the substrate. The work function is determined by the polarization of the Cs overlayer with the increase of electronic charge in the Cs-substrate interface.

The work function reduction of many metal and semiconductor surfaces by coating with Cs is well known [1]. The change in work function of Be with Cs coverage has not been reported. This paper presents a summary of such an investigation. The work function as a function of dose shows the characteristic quadratic behavior, passing through a minimum before leveling off at high coverage. The minimum work function surface produced is 1.6 eV. This value is in agreement with the minimum value produced on other materials. The final work function value of 1.94 eV reported by Wilson for Cs on Be did not pass through a minimum before reaching this value [2]. The minimum work function produced is due to the outward-positive dipole layer formed by the polarization of Cs with the increase of electronic charge in the Cs-substrate interface. We have used Auger electron spectroscopy (AES) to verify surface purity.

Our experimental procedure and apparatus have been previously described and will only briefly be reviewed here [3]. The vacuum vessel has a base pressure  $\leq 5 \times 10^{-11}$  Torr. The experiment is performed at room temperature and at an operational pressure of  $(2-8) \times 10^{-10}$  Torr. Two analytic stations are employed: the retarding field electron diode work function shift measure-

\* Department of Physics and Engineering Physics.

\*\* Department of Chemistry and Chemical Engineering.

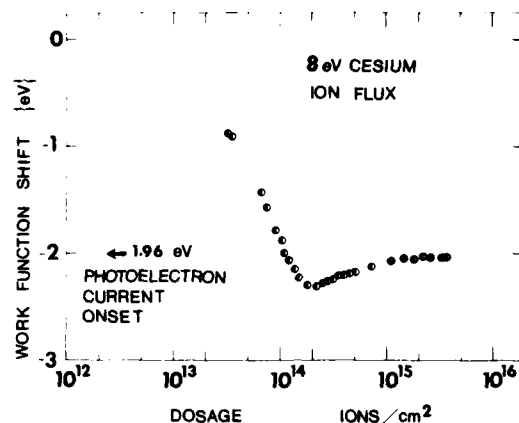


Fig. 1. Work function shift versus dose at 8 eV incident  $\text{Cs}^+$  energy.

ment [4,5] station and the cylindrical mirror analyzer station, used for AES. In addition, we have added a HeNe red laser ( $\lambda = 632.8$  nm, 1.96 eV) to our system. We use the onset of the laser induced photoelectric current to calibrate our work function shifts.

Measurements were taken as a function of Cs dose. A beam of low energy  $\text{Cs}^+$  ions (8 eV) provides our Cs flux. We have shown that on Mo all of the incident Cs will stick to the surface at low coverages [6]. Mo is much heavier than Be, but still lighter than Cs, so the same should be true for Be. The secondary electron yield is negligible at this energy [7,8]. Monitoring the ion current also gives us an accurate measurement of the dose. The target is 3 mm in diameter and the  $\text{Cs}^+$  flux is on the order of  $8 \times 10^{13}$  ions/cm<sup>2</sup> · s. Impurities and neutral Cs in the  $\text{Cs}^+$  beam are negligible. In situ cleaning of the sample is accomplished by  $\text{Ar}^+$  sputtering ( $\sim 0.2$   $\mu\text{A}$  at 3 keV), and cleaning precedes every dosing. After the sample is dosed, it is immediately rotated into position for work function shift measurements, photoelectron or AES measurements. Surface contaminants, including N and implanted Ar, as observed by AES, are less than 1%.

In fig. 1 the work function shift is plotted as a function of dose. Also indicated in fig. 1 is the value of the work function shift at which the photoelectron current begins. The maximum work function shift occurs at a dose of  $\sim 2 \times 10^{14}$  ions/cm<sup>2</sup>. This maximum shift corresponds to a 1.6 eV minimum work function surface. After going through a minimum, the work function shift decreases and levels off at a value of  $\sim 1.9$  eV. From the shifts we obtain a value of 3.92 eV for the clean work function of polycrystalline Be. This value is lower than the value of  $5.10 \pm 0.02$  eV for the Be(0001) surface

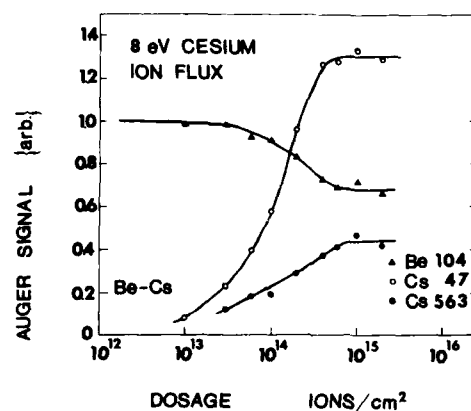


Fig. 2. Auger Cs and Be signal intensity versus dose at 8 eV incident  $\text{Cs}^+$  energy.

[9], but is higher than 3.67 eV reported by Wilson [2]. Such differences in work function with respect to different faces of crystal are known [10]. The surface roughness resulting from sputter cleaning is not known.

Shown in fig. 2 are the Be and Cs Auger signal intensities. The Be 104 eV and Cs 47 and 563 eV Auger transition peaks are monitored. The figure clearly shows the decrease in the Be Auger signal and the increase in Cs Auger signal with increasing Cs dose. The peaks are normalized to the clean Be signal. The Be Auger signal is seen to be attenuated by  $\sim 30\%$ . The Auger and work function curves both begin to saturate at a dose of  $\sim 6 \times 10^{14}$  atoms/cm<sup>2</sup>. In fig. 1 we see that the minimum work function occurs at a coverage of approximately one-half, as determined from the AES signal intensities. The true dose may be smaller if the surface is not perfectly flat.

Assuming that a complete Cs monolayer has a hexagonally close-packed surface structure (diameter 0.47 nm;  $5.2 \times 10^{14}$  atoms/cm<sup>2</sup>) [11], we may estimate the attenuation of the Be Auger signal. The Auger Be escape depth,  $\lambda_0$ , through a Cs overlayer is calculated to be 0.7 nm [12,13]. The average volumetric distance ( $\delta$ ) an electron travels in passing through this Cs layer is 0.28 nm. Using an exponential dependence on  $\delta$  for the attenuation of Be Auger electrons through the Cs layer ( $1 - e^{-\delta/\lambda_0}$ ), we obtain an attenuation of 33%. This is in excellent agreement with our observed value.

Although not shown here, at bombarding energies up to 900 eV, the work function passes through a minimum and then rises to the value associated with high Cs coverage as the dose is increased. The high Cs coverage is confirmed by AES. At the energies examined there is implantation, as evidenced by Auger depth profiling. The minimum that the work function reaches slowly increases with bombarding energy. The dose required to reach the minimum

Table 1

The work function ( $\phi_0$ ) of the clean surface, work function minimum ( $\phi_{\min}$ ) due to optimum cesium coverage, maximum change in work function ( $\Delta\phi_{\max}$ ), the cesium high coverage work function ( $\phi_{\text{HC}}$ ), and the work function minimum calculated with expression (1) ( $\phi_{\min}^{\text{calc}}$ ); the values listed are a small subset of those available in the literature [1,14]

Element/Z	Crystal face	$\phi_0$	$\phi_{\min}$	$\Delta\phi_{\max}$	$\phi_{\text{HC}}$	$\phi_{\min}^{\text{calc}}$	Ref.
Beryllium/4	Polycrystalline	3.67	1.94 <sup>a)</sup>	1.73	1.94 <sup>a)</sup>	1.83	[2]
Beryllium/4	Polycrystalline	3.92	1.6	2.32	1.9	1.77	<sup>b)</sup>
Aluminum/13	(111)	4.24	1.64	2.60	1.94	1.69	[19]
Silicon/14	(111)	4.70	1.53	3.17	—	1.58	[1]
Germanium/32	(111)	4.79	1.52	3.27	—	1.56	[1]
Niobium/41	Polycrystalline	4.19 (100)	1.44	2.75	1.63	1.70	[20]
Molybdenum/42	Polycrystalline	4.2	$1.54 \pm 0.05$	2.66	$1.82 \pm 0.05$	1.70	[1]
Ruthenium/44	(001)	5.52	1.42	4.10	2.2	1.38	[11]
Tungsten/74	Polycrystalline	4.52	$1.52 \pm 0.05$	3.0	$1.80 \pm 0.05$	1.62	[1]
Rhenium/75	Polycrystalline	4.85	$1.45 \pm 0.05$	3.40	$1.77 \pm 0.05$	1.54	[1]
SS304		4.21–4.3	1.52	—	1.60	1.70–1.68	[2]

<sup>a)</sup> Questionable result. <sup>b)</sup> This work.

also increases with energy. This increase in the minimum follows the increase in implantation depth. The important point is that even a subsurface concentration ( $\sim 10\%$  by dose) of Cs has only a small effect on the minimum work function produced by Cs surface coverage.

Minimum work functions of several elements associated with Cs adsorption are listed in table 1. The table lists a small set of the values available in the literature [1,14]. As can be seen in table 1, the minimum work function values are essentially constant at  $1.6 \pm 0.2$  eV. The work function value of the clean surfaces lie in a considerably larger range, 3.9 eV (Be) to 5.5 eV (Ru). The values for the work function shifts for the transition metals associated with Cs coverage are attributable to the shielding produced by the open d bands of these metals [15]. In Al, with no d band electrons, the shielding is provided by s and p electrons [16]. Be metal also possesses no d band electrons, but has partially filled s and p bands. This suggests that s and p band electrons may play a role analogous to the d band electrons in the Cs–W system.

We should distinguish the bulk (substrate) from the surface (extended adlayer of shielded Cs dipoles). Based on population analyses of ab initio self-consistent field wave functions for Be clusters containing up to 57 atoms, the surface atoms accumulate an excess of 0.2 electrons per atom over the inner atoms [17]. The excess electrons at the surface can spill-out into the vacuum. The distorted, but localized, nature of the Cs 6s valence electrons and their interaction with the spill-out electrons from the substrate is discussed in the analysis of Cs on W by Wimmer and co-workers [15]. For Cs on W, Wimmer and co-workers find that the charge redistribution is localized outside

the surface, the interior substrate charge density remaining unchanged [15]. We would expect the same to hold for Cs on Be. The surface structure is that formed by the Cs atoms and the shielding electrons, the latter forming an interface between the surface and the bulk. It apparently does not matter whether the interface layer is composed of s, p or d band electrons.

Broeder et al. [18] examined the initial work function lowering by the formation of adsorbate dipoles. Based on the work of Broeder et al. Alton employs an empirical relation for computing the maximum change in work function  $\Delta\phi_{\max}$ , at an optimum fractional coverage, associated with atomic adsorption [14]. A simple rearrangement of Alton's expression for  $\Delta\phi_{\max}$  yields the following expression for the minimum work function  $\phi_{\min}$  associated with atomic adsorption:

$$\phi_{\min} = 1.24 \left[ \frac{1}{2}(\text{IP} + \text{EA}) - 0.19\phi_0 \right], \quad (1)$$

where IP and EA are the ionization potential and electron affinity of the adsorbate atoms, respectively. This expression, in essence, equates the minimum work function to the difference between the Mulliken electronegativity of the isolated (gas phase) adsorbate atoms and the intrinsic work function  $\phi_0$  of the pure metal substrate.

The work function of Cs is 2.14 eV [10]. Using IP = 3.89 eV, EA = 0.47 eV and our value of 3.92 eV for the clean work function of Be in expression (1) gives a value of  $\phi_{\min} = 1.78$  eV compared to the photoelectron calibrated value of 1.6 eV. Some of the variations in  $\phi_{\min}$  from that calculated may be attributed to inaccuracies in the experimental values and to differences in coverage at which the minimum actually occurs. It is also interesting to note that a similar result is observed for K on metals [14]. When one evaluates the minimum work function produced by the adsorption of K, one again sees a minimum centered in a small range about a fixed value ( $2.0 \pm 0.2$  eV) which is lower than the work function of K (2.3 eV).

As long as a substrate possesses spill-out electrons, which can interact by the alignment and localization of the Cs 6s electrons with the surface, it would appear that the extended, shielded Cs dipole adlayer determines the minimum work function. This minimum lies in a small range for the materials examined.

We wish to thank Homer Hagstrum for helpful discussions, George Wohlrab and Gunther Wirth for machining most of the experimental apparatus. This work was supported in part by the Air Force Office of Scientific Research, the US Department of Energy, and the New Jersey Commission on Science and Technology.

## References

- [1] L.W. Swanson and R.W. Strayer, *J. Chem. Phys.* 48 (1968) 2421;  
R.E. Weber and W.T. Peria, *Surface Sci.* 14 (1969) 13.

- [2] R.G. Wilson, *J. Appl. Phys.* 37 (1966) 3161.
- [3] G.S. Tompa, PhD Thesis, Stevens Institute of Technology, 1986.
- [4] F.H. Haayes, M.P. Hill, S.M.A. Lecchini and B.A. Pethica, *J. Chem. Phys.* 42 (1965) 2919.
- [5] A.G. Knapp, *Surface Sci.* 34 (1973) 289.
- [6] G.S. Tompa, W.E. Carr and M. Seidl, *Appl. Phys. Letters* 48 (1986) 1048.
- [7] J.L. Lopes, J.A. Greer and M. Seidl, *J. Appl. Phys.* 60 (1986) 17.
- [8] C. Brunneé, *Z. Phys.* 147 (1957) 161.
- [9] A.K. Green and E. Bauer, *Surface Sci.* 74 (1978) 676.
- [10] H.B. Michaelson, *J. Appl. Phys.* 48 (1977) 4729.
- [11] J. Hrbek, *Surface Sci.* 164 (1985) 139.
- [12] D.R. Penn, *J. Electron Spectrosc. Related Phenomena* 9 (1976) 29.
- [13] M.P. Seah and W.A. Dench, *Surface Interface Anal.* 1 (1979) 2.
- [14] G.D. Alton, *Surface Sci.* 175 (1986) 226.
- [15] E. Wimmer, A.J. Freeman, J.R. Hiskes and A.M. Karo, *Phys. Rev. B* 28 (1983) 3074;  
S. Ohnishi, A.J. Freeman and E. Wimmer, *Phys. Rev. B* 29 (1984) 5267.
- [16] J. Paul, *Nature* 323 (1986) 701.
- [17] R.B. Ross, W.C. Ermler, R.M. Pitzer and C.W. Kern, *Chem. Phys. Letters* 134 (1987) 115.
- [18] J.J. Broeder, L.L. van Reijan, W.M.H. Satchler and G.C. Schuit, *Z. Elektrochem.* 60 (1956) 838.
- [19] S.D. Parker and P.J. Dobson, *Surface Sci.* 171 (1986) 267.
- [20] R.G. Wilson, *J. Appl. Phys.* 37 (1966) 4125.



AMERICAN INSTITUTE OF PHYSICS  
CONFERENCE PROCEEDINGS NO. 158  
NEW YORK 1987

# PARTICLES AND FIELDS SERIES 35

SERIES EDITOR: RITA G. LERNER

## PRODUCTION AND NEUTRALIZATION OF NEGATIVE IONS AND BEAMS

FOURTH INTERNATIONAL SYMPOSIUM  
BROOKHAVEN, NY 1986

EDITOR:  
JAMES G. ALESSI  
BROOKHAVEN NATIONAL LABORATORY

SURFACE PRODUCTION OF NEGATIVE HYDROGEN IONS BY HYDROGEN  
AND CESIUM ION BOMBARDMENT

M. Seidl, W. E. Carr, J. L. Lopes

S. T. Melnychuk, and G. S. Tompa

Department of Physics and Engineering Physics  
Stevens Institute of Technology, Hoboken, NJ 07030

## ABSTRACT

Metal targets have been bombarded with cesium and hydrogen ions in the energy range 100 to 1000 eV. Angular and energy distributions and the yield of the  $H^-$  ions have been measured as function of energy and ion mix. Synergistic effects due to simultaneous hydrogen and cesium ion bombardment produce a higher  $H^-$  yield than the sum of the individual processes. Cesium coverage on metal surfaces due to cesium ion bombardment has been studied. High coverages corresponding to a workfunction of 1.6 eV can be obtained at 100 eV energy when the target mass is smaller than the cesium mass.

## 1. INTRODUCTION

In surface conversion sources<sup>1</sup>, negative hydrogen ions are produced on the surface of a metal target placed into a hydrogen-cesium plasma and biased negatively with respect to the plasma. The surface of the target is bombarded by positive hydrogen and cesium ions typically in the 100 to 300 eV energy range. The target is also exposed to a flux of hydrogen molecules and atoms in ground and excited states. Surface production of negative hydrogen ions may be due to several processes, such as backscattering of hydrogen ions or atoms from the surface, or by sputtering of adsorbed or implanted hydrogen by cesium or hydrogen ion bombardment.

The first section of this paper is a short account of our studies<sup>3-5</sup> on sputtering adsorbed hydrogen from a molybdenum target bombarded with cesium ions. In the second section we discuss our experiments on  $H^-$  ion production by simultaneous bombardment of a ruthenium target with cesium and hydrogen ions. Preliminary results indicate that  $H^-$  ion production due to combined bombardment with hydrogen and cesium ions is considerably larger than the sum of the two individual processes. In order to investigate this "target chemistry" in more detail, we have started to study low energy ion bombardment of metal and semiconductor surfaces. The first part of this program, involving cesium ion bombardment of metal surfaces, is presented in Section 4 of this paper. This work explores the mechanism of cesium coverage due to  $Cs^+$  ion bombardment. In particular, it shows why molybdenum is a better target for surface conversion sources than tungsten.

## 2. PRODUCTION OF $H^-$ IONS BY CESIUM BOMBARDMENT

In these experiments a metal target (molybdenum or ruthenium) is bombarded with  $Cs^+$  ions. The target is also exposed to cesium vapor and hydrogen gas. Optimum cesium coverage for minimum work function is obtained by adjusting the ratio of the cesium ion to atom fluxes. Hydrogen coverage is provided by chemisorption of hydrogen on the target. Cesium ion bombardment is the only available process for desorption of the hydrogen from the surface of the target.

The latest experimental set-up<sup>5</sup> is shown in Fig. 1. The apparatus consists of a planar diode, rotating Faraday cup, and a rotating magnetic sector mass spectrometer.

The cathode of the diode is the molybdenum target. The anode is a fine tungsten mesh placed 2.0 mm from the cathode. During operation the mesh is heated to about 1000°C by passing current through it.

Cesium vapor is produced in a small oven and directed into a cesium manifold by means of a feeder tube. The cesium manifold is heated to 300°C and provides a uniform flux of cesium vapor to the diode region. Some of the cesium is surface ionized at the hot tungsten mesh which provides a source of  $Cs^+$  ions. These ions are accelerated onto the negatively biased cathode. The specific perveance of the geometry is large enough to provide a space-charge-limited  $Cs^+$  current of 100  $\mu A/cm^2$  at 100 V, almost two orders of magnitude larger than the residual water vapor flux. The lens effect of the mesh adds an intrinsic angular spread of 7.5 mrad to the negative ions accelerated by the mesh. This is about 10 X less than the typical spread due to sputtering. In order to monitor the uniformity of the  $Cs^+$  ion current density over the cathode area, the  $Cs^+$  ion current density is measured by two positive ion cups facing two 0.635-mm-diam holes drilled 1.19 cm apart in the molybdenum alignment plate. Typically, the two positive ion cup currents differ at most by 10%, which indicates that the neutral and ion fluxes to the Mo cathode are fairly uniform.

The basic operation of the experiment is as follows: Hydrogen and cesium are co-adsorbed on the molybdenum target surface which is continuously bombarded by  $Cs^+$  ions. The sputtered  $H^-$ ,  $Mo^-$  ions, and electrons are accelerated back across the diode gap, partially attenuated by the mesh and collected by the cesium manifold. A small sample of the sputtered beam passes through a 0.635-mm-diam aperture. All particles emitted in a cone of 14° half angle are accepted by the detection system.

The Faraday cup measures the total current due to all ( $H^-$ ,  $Mo^-$ , and  $e^-$ ) negative particles. When the Faraday cup is rotated out of the beam path, the mass spectrometer is used to measure the angular dependence of each species.

A typical set of angular distributions is shown in Fig. 2.

Measurements indicate that the  $H^-$  ion angular distribution is approximately Gaussian,  $f(\theta) = \exp - (\theta/\theta_0)^2$ , where  $\theta_0$  varies slightly with  $Cs^+$  bombarding energy. For  $U = 250$  eV,  $\theta_0 = 4.5^\circ$ , and for  $Cs^+$  energy of 1000 eV,  $\theta_0 = 3.2^\circ$ .

The exit angle  $\theta$  of a negative ion is related to its parallel energy  $E$  at the surface of the target by the equation  $\tan \theta = E/U$  where  $U$  is the accelerating voltage applied between the anode and cathode. Using this relationship, the angular distribution can be converted into parallel energy distribution. Fig. 3 shows that the  $H^-$  ion parallel energy distribution is approximately Maxwellian,  $f(E) = \exp(-E/T)$ . The ion temperature  $T$  depends on the bombarding  $Cs^+$  energy  $U$ , ranging from  $T/U = 0.37\%$  (for  $U = 750$  eV) to  $T/U = 0.60\%$  (for  $U = 250$  eV). The ion temperature increases when the hydrogen or cesium coverage is incomplete.

Measurements show that most  $H^-$  ions leave the target surface with an initial energy of 1.0 to 1.5% of the  $Cs^+$  energy. All  $H^-$  ions have an initial energy less than 3% of the  $Cs^+$  energy. This is consistent with the notion that a few binary elastic collisions are sufficient to describe the desorption process. The simplest model consists of only two collisions; an incoming  $Cs^+$  ion collides with a hydrogen atom that in turn is reflected from a molybdenum atom. The energy transferred from the  $Cs^+$  ion to the hydrogen atom is given by the equation

$$E_2/E_0 = 4M_1M_2 \cos^2 \theta / (M_1 + M_2)^2,$$

where  $E_0$  and  $M_1$  are the  $Cs^+$  ion energy and mass, respectively;  $E_2$  and  $M_2$  are the hydrogen energy and mass, respectively;  $\theta$  is the recoil angle (angle between the  $Cs^+$  ion velocity and the velocity of the hydrogen atom). The maximum energy transfer, occurring for head-on collisions, is  $E_2/E_0 = 0.03$ . The hydrogen-molybdenum collision does not change the hydrogen energy.

The negative ion yield is defined as the number of negative ions sputtered per incident cesium ion,  $Y_{ion} = J_{ion}/J_{Cs}$ , where  $J_{ion}$  is the current density of the sputtered ions leaving the target and  $J_{Cs}$  is the incident current density. The yield has a maximum value when the work function of the cathode reaches a minimum (about 1.6 eV for molybdenum covered with 2/3 monolayer of cesium). The yield also depends on hydrogen coverage of the target. Fig. 4 shows that the  $H^-$  yield reaches a saturation when the hydrogen pressure reaches about  $10^{-4}$  torr.

The optimum  $H^-$ ,  $Mo^-$ , and  $e^-$  yields are shown in Fig. 5 as function of  $Cs^+$  ion bombarding energy. The yield of  $H^-$  ions has a maximum value of 0.41 at a  $Cs^+$  energy of 750 eV. Under these conditions most of the  $H^-$  ions have an initial energy of about 10 eV. The same value of  $H^-$  energy has been obtained for maximum  $H^-$  production in backscattering experiments.<sup>10</sup> Fig. 5 shows that the  $H^-$  yield is smaller than  $10^{-3}$  for  $Cs^+$  energies less than 120 eV. The maximum energy a hydrogen atom can obtain in a collision with a 120 eV  $Cs^+$  ion is 3.6 eV. Since the binding energy of

hydrogen on molybdenum is about 2.7 eV the initial energy of the H<sup>+</sup> ion can be at most 0.9 eV. At this energy the survival probability of the H<sup>+</sup> ion is low.

Surface conversion sources are usually operated in the energy range of 100 to 200 eV. Fig. 5 shows that at these energies the H<sup>+</sup> yield is very small. It follows that sputtering of adsorbed hydrogen by cesium ion bombardment is not the dominant process in these sources. Hydrogen ion bombardment has to be an important process either on its own merit or in combination with cesium bombardment. Preliminary experiments along this line are described in the next section.

### 3. PRODUCTION OF H<sup>+</sup> IONS BY HYDROGEN AND CESIUM BOMBARDMENT

In these experiments the target is bombarded simultaneously with cesium and hydrogen ions. Cesium ions are again made by surface ionization while the hydrogen ions are produced in a planar magnetron discharge.

The apparatus, shown in Fig. 6, consists of the planar diode where the H<sup>+</sup> ions are produced and of a diagnostic section which analyzes a small sample of the H<sup>+</sup> beam. The cathode of the diode is a molybdenum plate with a center hole into which various targets can be inserted. The anode is again a heated tungsten mesh placed 0.5 cm from the cathode. Cesium vapor introduced into the diode region through slits in the cesium manifold is surface ionized at the hot mesh. The Cs<sup>+</sup> ions are accelerated to the cathode by a voltage of 100 to 500 V applied between cathode and anode.

Hydrogen ions are produced in a plasma slab filling the cathode-anode gap. The plasma is sustained by a magnetron discharge. A uniform magnetic field of 270 G, parallel to the cathode, is generated by two samarium-cobalt magnets (not shown). The ExB drift is from the hot filament (cathode of the discharge) to the discharge anode which is connected with the anode of the diode (hot mesh). The plasma potential is close to the anode potential so that the kinetic energy of the hydrogen ions hitting the target is close to eU where U is the anode-cathode voltage of the diode. The target is bombarded with an unknown mix of H<sup>+</sup>, H<sub>2</sub><sup>+</sup> and H<sub>3</sub><sup>+</sup> ions. The discharge typically operates at 60 V, 0.02 A and 1 torr pressure. This high pressure is only in the diode region, the rest of the chamber has a pressure much lower (10<sup>-6</sup>-10<sup>-7</sup>) due to differential pumping. The hydrogen ion current density at the target can be varied up to 0.5 mA/cm<sup>2</sup>.

The positive hydrogen and cesium ion current densities bombarding the target are monitored by two pairs of Faraday cups collecting ions passing through two holes drilled 1.19 cm apart in the cathode plate. A magnetic field of 3.3 kG deflects the hydrogen ions into the hydrogen cups. The cesium ions follow essentially straight trajectories and are collected in the cesium ion cups.

The diagnostics system is identical to that in the previous experiment (Section 2) except for a retarding grid analyzer which measures perpendicular energy distributions of the H<sup>-</sup> ions.

In this experiment the ion bombardment of the target can be varied from pure cesium ion bombardment to almost pure hydrogen ion bombardment. Optimum cesium coverage of the target is obtained by controlling the target temperature, cesium vapor pressure and the ion bombardment flux.

Several interesting phenomena can be observed when the target is exposed to mixed hydrogen and cesium ion bombardment. The bombardment energy threshold of 130 eV, typical for cesium ion bombardment, is no longer present. This can be attributed to hydrogen sputtering and backscattering. Indeed, the energy spectra of the H<sup>-</sup> ions indicate the existence of these processes. Fig. 7a shows that the distribution of H<sup>-</sup> ions in parallel energies can be represented by three exponential components. The part with the steepest slope corresponds to cesium sputtering, the intermediate slope is due to hydrogen sputtering and the smallest slope is due to hydrogen backscattering. The distribution of H<sup>-</sup> ions in perpendicular energies, Fig. 7b, shows a similar pattern.

However, yield measurements indicate that H<sup>-</sup> production is not a simple superposition of the three isolated processes of cesium sputtering, hydrogen sputtering and backscattering. Rather, the combined synergetic action of hydrogen and cesium gives higher yields than expected from the superposition of these processes taken individually. This point is illustrated in Table I which presents measured H<sup>-</sup> ion yields for several cesium and hydrogen current densities. In this table  $J_T = J_{Cs} + J_H$  is the sum of cesium and hydrogen current densities hitting the target, H<sup>-</sup> yield is defined as the ratio  $J_{H^-}/J_T$  where  $J_{H^-}$  is the H<sup>-</sup> current density integrated over all angles.

The brightness of an H<sup>-</sup> beamlet along the axis is defined by the quantity  $B = I/(S \times \Delta\Omega)$ , where  $I$  is the H<sup>-</sup> current emitted from a target area of  $3.2 \times 10^{-3} \text{ cm}^2$  in a solid angle of  $\Delta\Omega = 5.9 \times 10^{-5}$  steradians. If H<sup>-</sup> ion production was due to the superposition of cesium and hydrogen bombardment, the H<sup>-</sup> yield would have the form

$$J_{H^-}/J_T = Y_{Cs} J_{Cs}/J_T + Y_H J_H/J_T$$

where  $Y_{Cs}$  and  $Y_H$  would be constant for a given energy. Table I shows that this is not the case. At 200 eV bombarding energy the H<sup>-</sup> yields are small for pure cesium as well as for predominantly hydrogen bombardment. The yield increases to a high value of 0.31 for a 0.17/0.83 cesium/hydrogen mix. This yield is about 5 times higher than the yield at a surface conversion source operating at a similar voltage. The specific brightness  $B/J_T$  follows a similar trend.

U (Volts)	200				125
$J_{Cs}$ (mA/cm <sup>2</sup> )	0.03	0.04	0.06	0.13	0.35
$J_H$ (mA/cm <sup>2</sup> )	0.00	0.76	0.23	0.63	2.34
$J_T$ (mA/cm <sup>2</sup> )	0.03	0.80	0.29	0.76	2.69
$J_{Cs}/J_T$	1.00	0.05	0.20	0.17	0.13
$J_H/J_T$	0.00	0.95	0.80	0.83	0.87
H <sup>-</sup> Yield	0.02	0.03		0.31	0.18
B/ $J_T$ (ster <sup>-1</sup> )	0.95	0.57	2.8	4.9	1.32

Table I. H<sup>-</sup> ion yield and H<sup>-</sup> beam brightness for several cesium and hydrogen bombardment current densities.

These and similar observations of synergetic reactions in surface production of H<sup>-</sup> ions by combined cesium and hydrogen bombardment bring up new questions: What is the reaction mechanism? How can it be used for improving H<sup>-</sup> yield? In order to answer these questions we have initiated some fundamental studies in ion surface interactions. The first part of this program is described in the next section.

#### 4. WORKFUNCTION REDUCTION OF METAL SURFACES BY CESIUM ION BOMBARDMENT

In these experiments the formation of composite surfaces due to cesium ion bombardment of some metals has been studied. The results have direct relevance to surface conversion sources. The mean free path for cesium ionization by electron impact is smaller than the plasma dimensions in these sources. Consequently, cesium

coverage of the converter surface is due to  $\text{Cs}^+$  ion bombardment, not vapor deposition<sup>12</sup>. It has been suggested that the minimum workfunction surface may not be achieved by cesium ion bombardment at typical converter voltages.<sup>12,13</sup>

The apparatus used for measurements is shown in Fig. 8. It consists of a UHV system, with a base pressure of  $5 \times 10^{-11}$  Torr, containing 4 experimental stations; a cesium ion gun, an electron gun for the work function measurement, an Auger electron spectrometer (AES) for detection of surface atoms, and an argon ion gun for sputter cleaning and depth profiling. A target, 3 mm in diameter, is mounted on a carousel, which allows rotation to the stations. The experiment is connected to an Apple computer, so that control and data acquisition are provided for the cesium gun, the work function station, and the AES.

The target is cleaned by argon sputtering, using typically 0.1 microamps at 5 KeV. The beam is rastered to cover the entire target. The Auger electron spectrum shows no observable contaminants for approximately 20 minutes after cleaning, and all of the measurements are obtained within this interval. In order to assure that the target remains clean each measurement is preceded by sputter cleaning.

The cesium ion beam is produced by a gun constructed in house. The source is a heated cesium mordenite pellet which thermionically emits cesium ions, mounted in a Pierce gun. This source eliminates the contamination that is a problem with sources using cesium vapor. The maximum current is a few microamps, of which approximately one microamp strikes the target. The beam is deflected before striking the target so that neutral cesium does not have a line of sight to the target. Beam energy and total dose to the target are computer controlled.

Work function shifts are measured using the retarding field diode method<sup>14</sup>. In this method an electron beam is directed toward a biased target and the bias voltage is adjusted to reflect part of the beam. The shift in bias voltage is equal to the work function shift of the surface.

Figs. 9-11 show the dependence of the work function shift on cesium ion dosage for several bombarding energies. Fig. 9 refers to a polycrystalline tungsten target, Fig. 10 to polycrystalline molybdenum, and Fig. 11 to polycrystalline beryllium. In all cases the initial work function shift is zero (clean metal). The shift decreases smoothly with increasing dosage until it reaches a steady state value dependent upon the  $\text{Cs}^+$  ion energy. The total ion dose needed to reach steady state work function is less than  $10^{16}$  ions/cm<sup>2</sup> in all cases. The steady state work function shift is a function of incident ion energy and target mass. The steady state work function (absolutely calibrated by photo-emission) is plotted in Fig. 12 as function of incident cesium energy for all three targets.

For tungsten (atomic mass 183.8) the work function reaches a minimum of 1.6 eV at incident energy of 40 eV. Vapor deposition



experiments<sup>15</sup> give the same minimum work function for a cesium coverage of about 0.6. The steady state coverage at incident energies smaller than 40 eV is larger than the optimum coverage. This can be seen in the 30 eV curve in Fig. 9. The work function rises sharply with increasing bombarding energy reaching 2.9 eV at 100 eV and approaching a plateau of 3.4 eV. This is in general agreement with predictions of van Amersfoort, et al.<sup>15</sup>

In the case of molybdenum (atomic mass 95.6) the work function reaches the minimum of 1.6 eV at an incident energy of 100 eV. Comparison with vapor deposition experiments<sup>15</sup> again indicates optimum cesium coverage. At lower incident energies the coverage is larger than optimum and at higher energies the coverage decreases. This was confirmed by Auger electron spectroscopy. The increase of work function with energy is considerably slower than for tungsten.

For beryllium (atomic mass 9.0) there is a minimum work function for all energies. The minimum is almost energy independent (1.6 eV to 1.7 eV) only the required dose changes with energy as seen in Fig. 11. The steady state work function is 2 eV, constant in the entire energy range from 8 eV to 600 eV (Fig. 12). Auger electron spectroscopy confirms that cesium coverage in steady state is larger than optimum for all energies.

The fundamental processes responsible for cesium coverage by ion bombardment are cesium ion implantation and surface erosion due to sputtering by cesium ions. Starting with a clean surface the cesium concentration evolves smoothly to a steady state. In the beginning there are few cesium atoms on the surface because incident atoms are either backscattered or implanted. After target material is sputtered away the surface concentration of cesium increases due to exposure of previously implanted atoms. These are also sputtered, and the surface film stabilizes when the net cesium flux to the target is zero. Additional exposure to the cesium beam does not change the film. The threshold energy for composite film formation is a result of the zero net flux condition, since at low enough energy the sputtering is insufficient to achieve it and the beam forms an overlayer. A simple theoretical model<sup>8</sup> provides the following formula for the fractional steady state concentration  $c$  of cesium atoms on the surface:

$$c = \ln(1 + (1-\beta)/Y)$$

where  $\beta$  is the backscattering coefficient for cesium ions and  $Y$  is the sputter yield of the target material. This formula applies as long as  $c < 1$ . One can understand qualitatively Fig. 12 by noting that both  $\beta$  and  $Y$  increase with bombarding energy and target mass. When the target atomic mass is smaller than 133, which is the atomic mass of cesium, the reflection coefficient  $\beta$  is practically zero. If in addition the target material has also a large sublimation energy, the sputter yield  $Y$  is also small, resulting

in a large cesium concentration.

It has been known for some time that molybdenum is a better converter material than tungsten<sup>16</sup>. Our results indicate that the reason is the high work function of tungsten exposed to cesium bombardment in the energy range of 100 to 200 eV where most converter sources operate. On the other hand, the work function of molybdenum reaches the minimum value of 1.6 eV at the operating energy of most surface conversion sources. The mass of beryllium is so low that the steady state coverage of cesium exceeds the optimum value.

Production of layered composite surfaces by means of multi-ion bombardment of some semiconductor materials may lead to surfaces providing improved H<sup>-</sup> yield. This is the next step in our research.

#### ACKNOWLEDGMENTS

This work was supported by the Air Force Office of Scientific Research, Department of Energy, and State of New Jersey Commission on Science and Technology.

#### REFERENCES

1. Production and Neutralization of Negative Ions and Beams, edited by K. Prelec (Brookhaven National Laboratories, NY, American Institute of Physics Proceedings, No. 111, 1984), pp. 331-457.
2. Production and Neutralization of Negative Ions and Beams, edited by K. Prelec (Brookhaven National Laboratories, NY, American Institute of Physics Proceedings, No. 111, 1984), pp. 171-288.
3. M. Seidl and A. Pargellis, Phys. Rev. B 26, 1 (1982).
4. J. A. Greer and M. Seidl, Production and Neutralization of Negative Ions and Beams, edited by K. Prelec (Brookhaven National Laboratories, NY, American Institute of Physics Proceedings 111, 1984), p 220.
5. J. L. Lopes, J. A. Greer, and M. Seidl, J. Appl. Phys. 60, 17 (1986).
6. G. S. Tompa, W. E. Carr, and M. Seidl, Appl. Phys. Lett. 48, 1048 (1986).
7. G. S. Tompa, W. E. Carr, and M. Seidl. To be published in Appl. Phys. Lett.
8. W. Carr, M. Seidl, G. Tompa, and A. Souzis. To be

published in J. Vac. Sci. Technol.

9. P. J. M. van Bommel, J. J. C. Geerlings, J. N. M. van Wunnik, P. Messmann, E. H. A. Granneman, and J. Los, J. Appl. Phys. 54, 5676 (1983).
10. J. J. C. Geerlings, P. W. van Amersfoort, L. F. Iz. Kwakman, E. H. A. Granneman, and J. Los, Surf. Sci. 157, 151 (1985).
11. K. N. Leung and K. W. Ehlers, Rev. Sci. Instrum. 53, 803 (1982).
12. K. W. Ehlers and K. N. Leung, Production and Neutralization of Negative Ions and Beams, (K. Prelec, Editor), American Institute of Physics Proceedings, No. 111 (1984) pp.227-236.
13. P. W. van Amersfoort, Ying Chun Tong and E. H. A. Granneman, J. Appl. Phys. 58, 2317 (1985).
14. A. G. Knapp, Surf. Sci. 34, 289 (1973).
15. L. W. Swanson and R. W. Strayer, J. Chem. Phys. 48, 2421 (1968).
16. K. N. Leung and K. W. Ehlers, Production and Neutralization of Negative Ions and Beams, (K. Prelec, Editor), American Institute of Physics Proceedings, No. 111 (1984) p. 265.

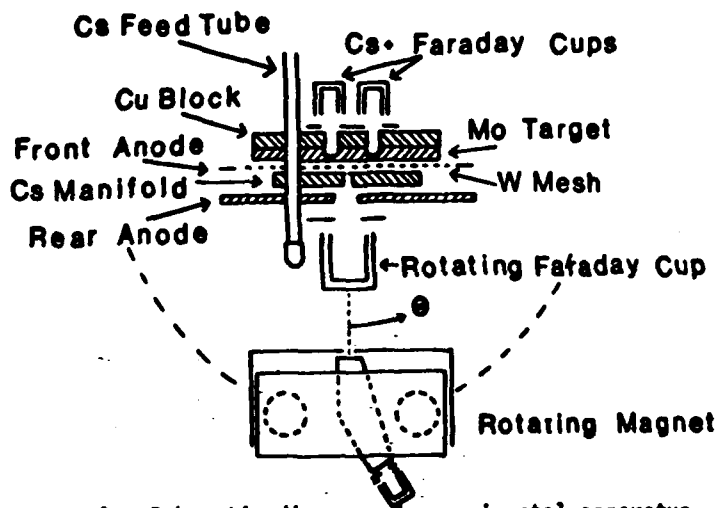


Fig. 1. Schematic diagram of experimental apparatus.

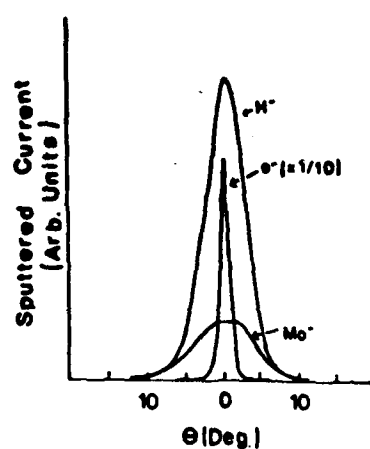


Fig. 2.  $H^-$ ,  $Mo^-$ , and  $e^-$  angular distribution for a  $Cs^+$  ion energy of 450 eV. Hydrogen pressure is  $2.4 \times 10^{-4}$  Torr.

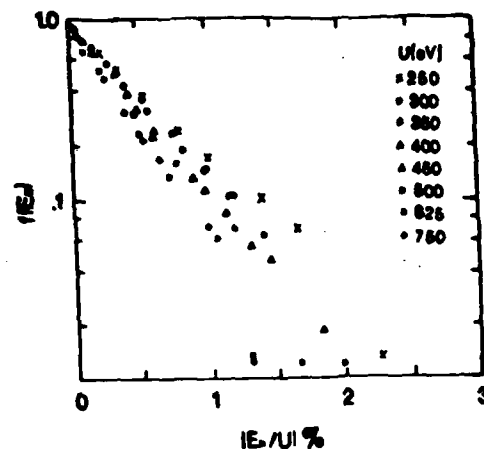


Fig. 3.  $H^-$  ion parallel energy distribution for various  $Cs^+$  ion energies for optimum work function.

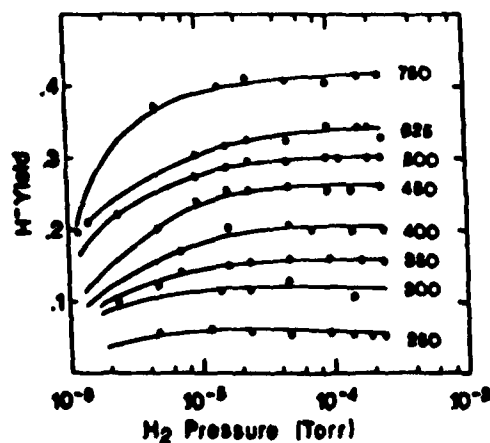


Fig. 4.  $H^-$  ion yield as a function of hydrogen pressure and  $Cs^+$  ion energy for optimum cathode work function.

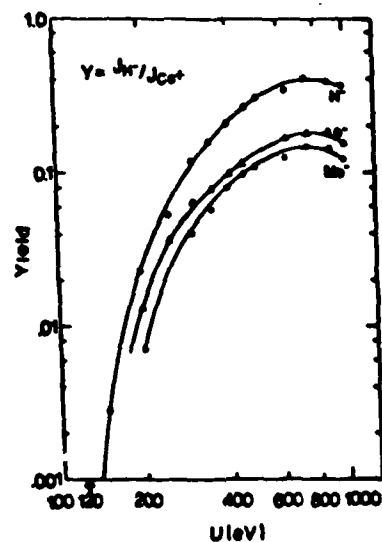


Fig. 5.  $H^-$ ,  $Mo^-$ , and  $e^-$  yield as a function of  $Cs^+$  ion energy for optimum work function.

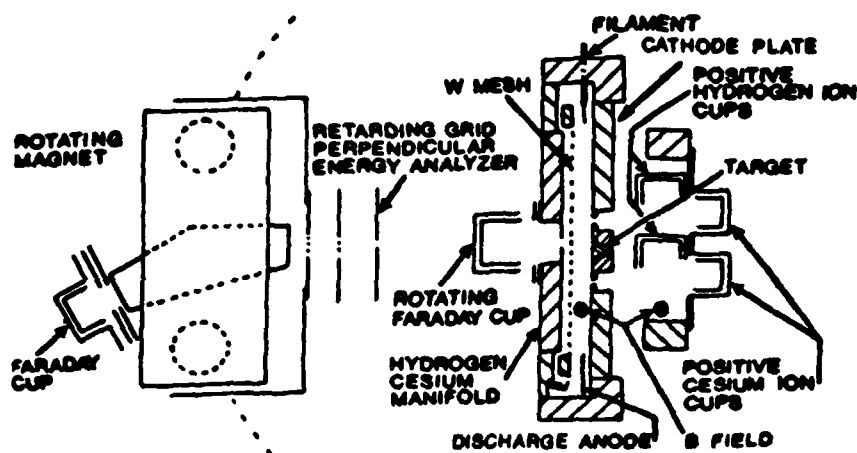


Fig. 6. Apparatus for  $H^-$  ion production by hydrogen and cesium bombardment.

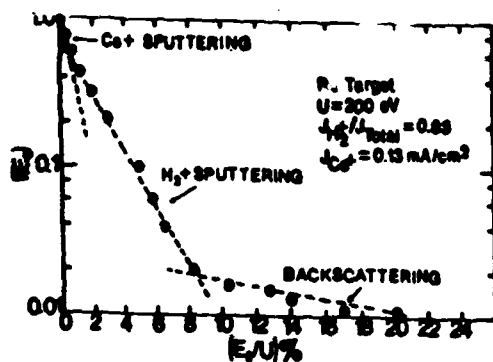


Fig. 7a. Distribution of  $H^-$  ions in parallel energies.

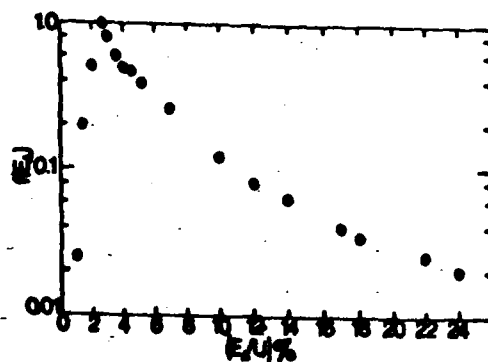


Fig. 7b. Distribution of  $H^-$  ions in perpendicular energies.

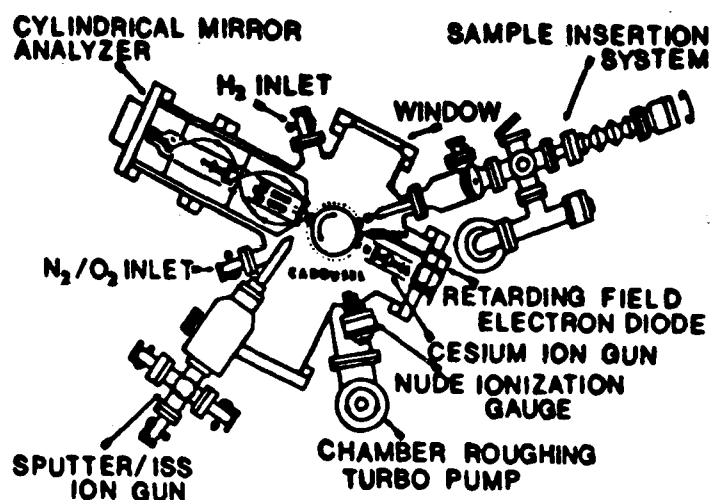


Fig. 8. UHV system for surface studies.

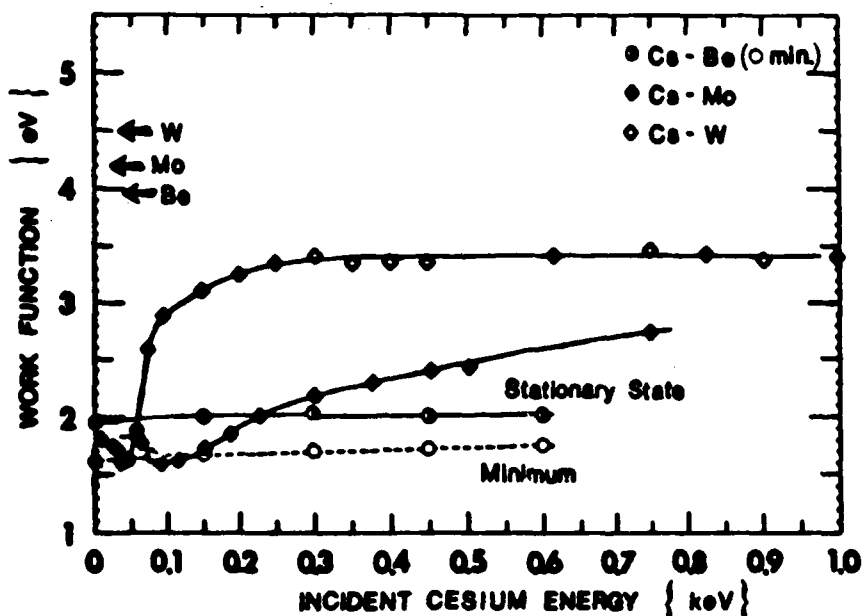


Fig. 12. Steady state work function of Be, Mo and W targets.

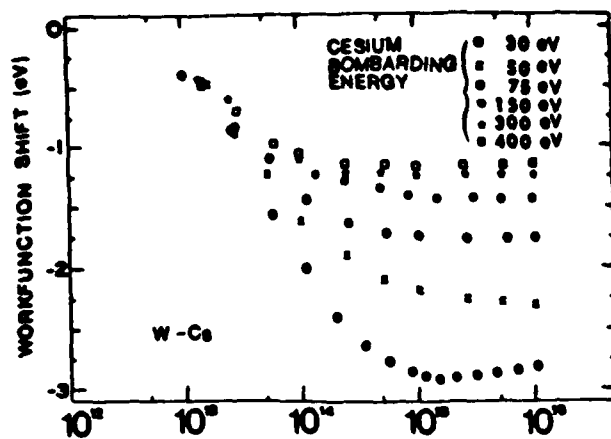


Fig. 9. Polycrystalline W target bombarded with Cs ions.

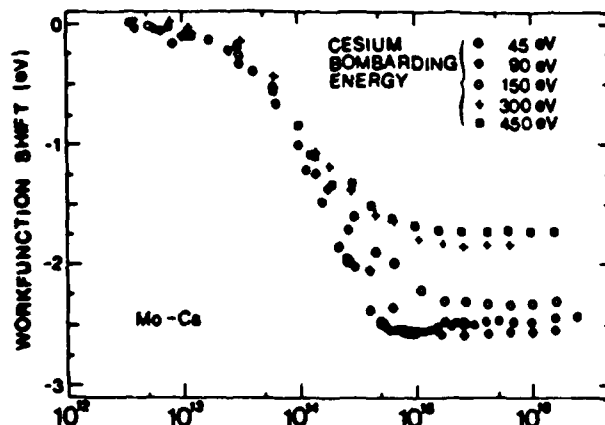


Fig. 10. Polycrystalline molybdenum target bombarded with cesium ions.

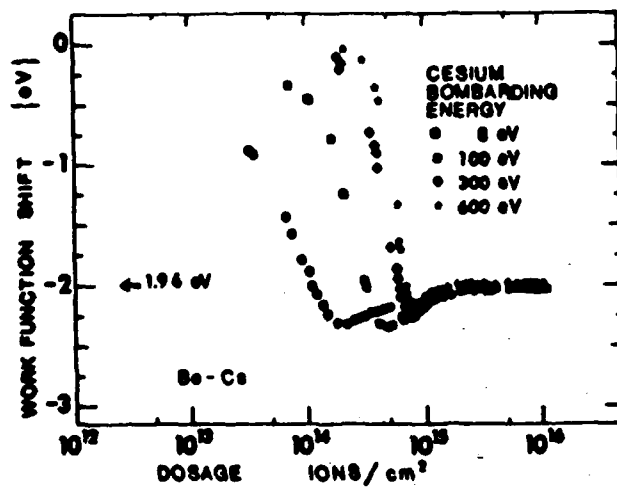


Fig. 11. Polycrystalline beryllium target bombarded with cesium ions.

# Compact efficient modular cesium atomic beam oven

G. S. Tompa, J. L. Lopes, and G. Wohlrab

*Stevens Institute of Technology, Plasma and Surface Physics Laboratory, Physics and Engineering Physics Department, Castle Point Station, Hoboken, New Jersey 07030*

(Received 16 March 1987; accepted for publication 13 April 1987)

A simple atomic beam oven is described. It uses a modified commercially available all metal sealed valve to break a glass cesium ampoule. Standard fittings are used to provide modularity and cost efficiency. Although designed for use with cesium ampoules, application to any volatile material is straightforward.

In past years several sources of alkali atomic beams have been developed for various uses.<sup>1-11</sup> In general they are limited in their ease of use and flexibility in switching from one system to another. We have designed a cesium oven to be extremely simple to use and made of standard components readily available. The use of standard components provides modularity and adaptability. In our lab, cesium is utilized in surface conversion experiments.<sup>12,13</sup> This oven is used to provide cesium for a Cs-H<sub>2</sub> discharge.<sup>13</sup>

The oven is shown in Fig. 1 along with its vacuum interface connections. The oven itself is a modified all metal sealed Nupro SS-8BG valve.<sup>14</sup> The valve itself comprises both ampoule holder and breaker. The valve is bored straight through. The bore hole diameter is 3/8 in., slightly larger than the diameter of the glass ampoule. The standard valve stem is used as a ram to break the glass ampoule. The only modifications to the ram are to reduce its total length and to add a vacuum pumping hole in its assembly. This is a simple process since the ram head is detachable. All connections for the system are Cajon VCR fittings,<sup>15</sup> using 316 stainless-steel gaskets. The through length of the valve is slightly larger than that of the ampoule such that the free riding ampoule lies beneath the ram. The oven is mountable in any orientation. An in-line spring has been used to keep the ampoule stationary.

The vacuum side of the oven is attached to a Nupro SS-4H all metal sealed high-temperature valve. The valve is

used to isolate the chamber from the oven when changing ampoules or to seal the unused portion of the cesium when letting the chamber up to atmosphere. The cesium would quickly react with the atmosphere and become contaminated. The oven, in our use, supplies cesium to a discharge through a biased manifold. To prevent shorting of the discharge the entire oven is floating. It is mounted on an electrically isolating vacuum feedthrough. The other end of the valve is presently sealed with a plug. The gasket between the oven and valve has a 145×145—0.001 in. tungsten mesh spot welded over its throughhole. The screen acts as a stop for any glass shards produced when breaking the ampoule.

Once assembled the oven is ready to use. Before breaking the ampoule the oven is baked under vacuum to remove any contaminants. The ampoule is then broken by simply turning the ram. Heating tapes are used to heat the oven and valve outside the vacuum chamber. Inside the chamber a molybdenum filament is used to heat the cesium feeder tube. Temperature controllers, employing "k"-type thermocouples, are used to maintain constant temperatures in the various regions of the assembly. Generally the feeder tube, feedthrough, and isolation valve are kept hotter than the oven. Keeping these portions hotter than the oven allows the flux to be controlled by the oven temperature. The beam itself is in equilibrium with the hotter portion of the ducting, since the mean-free path of the cesium is greater than that of the ducting dimensions. An additional bonus of the hot ducting

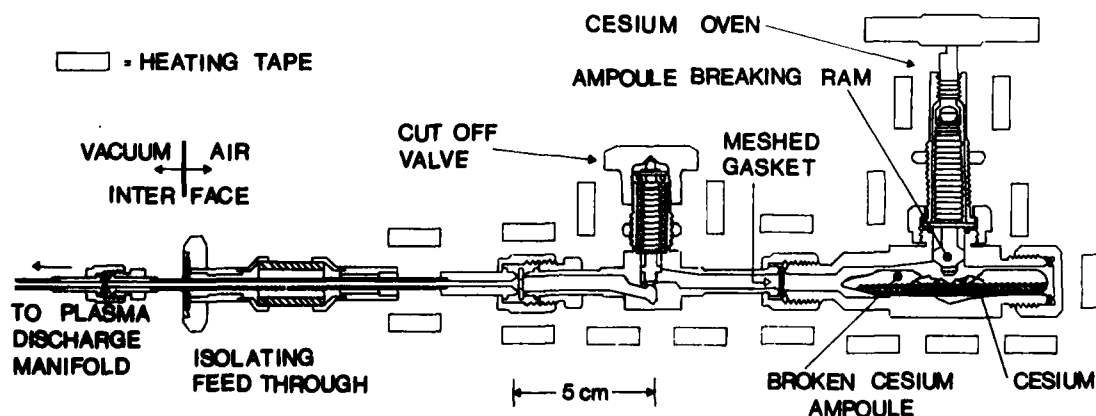


FIG. 1. The cesium oven, cutoff valve, and vacuum break as used to produce atomic cesium beam.



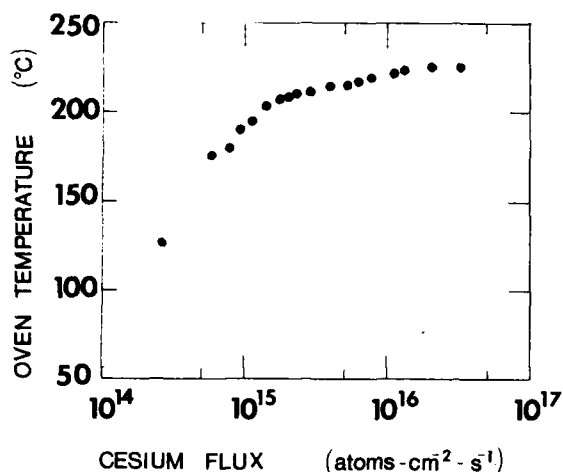


FIG. 2. The oven temperature vs cesium flux into the discharge region.

is that the dimer population of the atomic cesium beam is greatly reduced. The flux through the feeder tube is controlled by the oven temperature and the net conductance of the assembly. The entire assembly is bakable in excess of 315 °C, so a wide range of cesium vapor pressure (flux) may be produced. Presently, a copper water cooling block is attached to the oven. This is used to quickly terminate the flux and localize the cesium in general.

We have measured the cesium flux admitted into the discharge region as a function of oven temperature and the stability in time of the cesium flux at a given temperature. The experimental apparatus used for the measurements has been described previously<sup>12,13</sup> and will only be briefly discussed. The cesium flux is measured by ionizing a portion of the cesium flux with a hot tungsten mesh. The positive cesium ion current density ( $J_{Cs}$ ) is measured as a function of temperature. Thus the cesium flux can be obtained from

$$\text{cesium flux} = J_{Cs} / [e(1 - t)],$$

where  $t = 0.733$  is the mesh transmission and  $e$  is the charge of an electron. Figure 2 illustrates the cesium flux as a function of temperature. A change in oven temperature of 25 °C can vary the flux by more than an order in magnitude. The average deviation of the flux does not change more than a few percent at a given temperature over a period of several hours. Hence, this oven can provide a steady flux of cesium vapor.

The oven has been used many times with no degradation in performance. The isolation valve has allowed the chamber to be opened several times without changing the cesium ampoule. Routine maintenance is performed every time an ampoule is changed. Maintenance primarily includes removing the glass shards and boiling all components in deionized water. After boiling, several rinses are carried out to remove all residues. After drying, the components are given a final bath in acetone and methanol and then allowed to air dry before

reassembling. New gaskets are also used.

The merit of using standard components for this oven is apparent. Any Cajon VCR connections may be employed for ducting the cesium to any system, and of course adapter connections to any other type of connectors may be obtained. If alignment is difficult, standard flexible metal hoses are available. In its present use the chamber is opened more often than the ampoules are changed and there has been no need for differential pumping; but another valve for differential pumping may be connected where there is presently a plug. By installing a TEE and another valve, vials could be opened in various atmospheres as well as vacuum. The modularity of the system allows for a wide variety of applications. While this oven was designed to provide a convenient method for breaking a glass ampoule of cesium in vacuum, any volatile material may be used in this design; whether sealed in a glass ampoule or not. Note also that this design is capable of operation at cryogenic temperatures, so materials with high vapor pressures or low melting points could be cooled and opened with reduced vapor pressures or in the solid phase, respectively.

Finally, it should be noted that a ram type valve is not the only type that lends itself to simple modification into an ampoule breaking device. In particular, a ball valve may easily be adapted into an ampoule breaking device. If high vacuum and high temperatures are required the normal ball valve stem seal may be replaced by a bellows assembly that permits rotary action, such as that in a Nupro 24VFBG.<sup>14</sup>

We would like to thank the following for their support in constructing this system M. Seidl, Mark Yost, S. Melnychuk, and A. E. Souzis. Also we wish to thank Joseph Godino for his fine drafting.

<sup>1</sup>A. L. Eichenbaum and M. E. Moi, *Rev. Sci. Instrum.* **35**, 691 (1984).

<sup>2</sup>D. L. Schaefer, *Rev. Sci. Instrum.* **41**, 274 (1970).

<sup>3</sup>H. Yasunaga, *Rev. Sci. Instrum.* **47**, 726 (1976).

<sup>4</sup>T. Okutani, K. Shono, and R. Shimzu, *Secondary Ion Mass Spectrometry SIMS II, Proceedings of the Second International Conference on Secondary Ion Mass Spectroscopy (SIMS II)*, edited by A. Benninghoven, C. A. Evans, Jr., R. A. Powell, R. Shimzu, and H. A. Storms (Springer, Berlin, 1979), pp. 186-188.

<sup>5</sup>F. G. Allen and G. W. Gobeli, *Rev. Sci. Instrum.* **34**, 184 (1963).

<sup>6</sup>W. Klein, *Rev. Sci. Instrum.* **42**, 1082 (1971).

<sup>7</sup>K. H. Kaldenback, J. Kovals, and J. H. Pollard, U. S. Patent No. 3 759 282 (1973).

<sup>8</sup>G. M. Carter and D. E. Pritchard, *Rev. Sci. Instrum.* **49**, 120 (1978).

<sup>9</sup>T. Heindorff and B. Fischer, *Rev. Sci. Instrum.* **55**, 347 (1984).

<sup>10</sup>A. G. Zajonc, *Rev. Sci. Instrum.* **51**, 1682 (1980).

<sup>11</sup>M. Lambropoulos and S. E. Moody, *Rev. Sci. Instrum.* **48**, 131 (1977).

<sup>12</sup>J. L. Lopes, J. A. Greer, and M. Seidl, *J. Appl. Phys.* **60**, 17 (1986).

<sup>13</sup>M. Seidl, J. L. Lopes, S. T. Melnychuk, W. E. Carr, and G. S. Tompa, *Fourth International Symposium on the Production and Neutralization of Negative Ions and Beams*, Brookhaven National Laboratory, 27-31 October 1986 (to be published by American Institute of Physics).

<sup>14</sup>Nupro Company, 4800 East 48th Street, Willoughby, OH 44094.

<sup>15</sup>Cajon Company, 9780 Shepard Road, Macadonia, OH 44056.

## WORK FUNCTION OF METALLIC SURFACES BOMBARDED WITH CESIUM IONS

G.S. TOMPA \*, W.E. CARR and M. SEIDL

*Department of Physics and Engineering Physics, Stevens Institute of Technology, Hoboken, NJ 07030, USA*

Received 9 October 1987; accepted for publication 28 December 1987

Reduction of work function due to the build-up of cesium coverage on beryllium, molybdenum, and tungsten caused by cesium ion bombardment was investigated for incident energies between 5 eV and 1 keV. Surface characterization was performed as a function of incident ion energy and dose using Auger spectra and work function measurements. A steady state surface coverage is achieved in all cases for a dose of less than  $10^{16}$  ions/cm<sup>2</sup>. The coverage is strongly dependent on target mass. Beryllium has nearly monolayer coverage at all beam energies, while above 150 eV molybdenum has less than 50% coverage and tungsten has less than 20% coverage. The minimum steady state work function at 60% coverage can be achieved on molybdenum and tungsten at 100 and 45 eV, respectively. The effects of hydrogen coadsorption are also examined. The development of the surface coverage occurs due to the effects of implantation, reflection, and sputtering. A Monte Carlo calculation shows that a surface coverage of cesium on beryllium inhibits sputtering, which should be true for other light elements.

### 1. Introduction

It is well known that the work function of a metal is reduced by a partial coverage of cesium [1-9]. This can be achieved either by vapor deposition, or by cesium ion bombardment. In applications such as negative secondary ion mass spectroscopy and surface conversion negative hydrogen ion sources the ion bombardment method is necessary and/or desirable, and this work was done to study the build-up and maintenance of the cesium surface concentration.

In negative secondary ion mass spectroscopy the reduced work function greatly increases the negatively ionized fraction of sputtered particles, thus improving sensitivity. To achieve a reduced work function, a cesium surface concentration must be built up, and this concentration varies with ion dose and energy. A study of the mechanisms of composite surface formation will aid in understanding the enhanced yields.

\* Present address: EMCORE Corporation, 35 Elizabeth Avenue Somerset, NJ 08873, USA.

The typical surface conversion negative hydrogen ion source has a metal plate immersed in a cesium-hydrogen plasma and biased a few hundred volts negative with respect to the plasma. Positive hydrogen and cesium ions are extracted from the plasma and impinge upon the surface, producing a partial coverage of cesium. Negative hydrogen ions produced at the surface are extracted from the discharge region. It is desirable to have the minimum possible work function because this results in maximum negative hydrogen ion yield [10-14]. Vapor deposition does not contribute to the surface cesium coverage since the mean free path of neutral cesium in the plasma is too small (less than 1 cm) [15]. In working converters the surface work function is not known, and questions arose over whether the minimum work function surface can be produced by cesium ion bombardment [15,16].

Presented here are the results of an investigation of the build-up and maintenance of a cesium surface concentration on beryllium, molybdenum, and tungsten during cesium ion bombardment. Bombardment energies up to 1 keV were used. It requires a dose of nearly  $10^{16}$  ions/cm<sup>2</sup> to reach a steady state coverage, thus implantation, backscattering, and re-sputtering of cesium occur. In general, surface concentration is large for light target elements and becomes smaller with increasing target mass. The lowest possible steady state work function can be achieved on tungsten and molybdenum at low beam energy, (45 and 100 eV, respectively). Steady state for beryllium is near monolayer coverage at all beam energies, but the minimum work function can be obtained with a smaller dose. For all targets the minimum work functions occurs at a surface concentration between 1/2 and 2/3, and the values are  $1.6 \pm 0.1$  eV, independent of the target species.

## 2. Description of the experiment

### 2.1. General

The general surface analytical system set up is depicted in fig. 1. The view is from above and down the central axis. The experimental chamber is a UHV system with all metal seals, incorporating a Perkin-Elmer ion pump with titanium sublimators and cryopanel. The base pressure is  $5 \times 10^{-11}$  Torr, and with all components fully operating it is  $(2-3) \times 10^{-10}$  Torr. Shown in the figure are the cylindrical mirror analyzer (CMA) and the experimental station containing the work function diode and the cesium ion deposition gun. An argon ion gun, located at the CMA station, is used to provide ions for sputter cleaning of the surface and depth profiling with Auger electron spectroscopy (AES). A helium-neon laser is used to calibrate the work function shifts measured with the diode. Also shown is the sample handling system, consisting of a carousel and a sample insertion system, permitting sample changes at

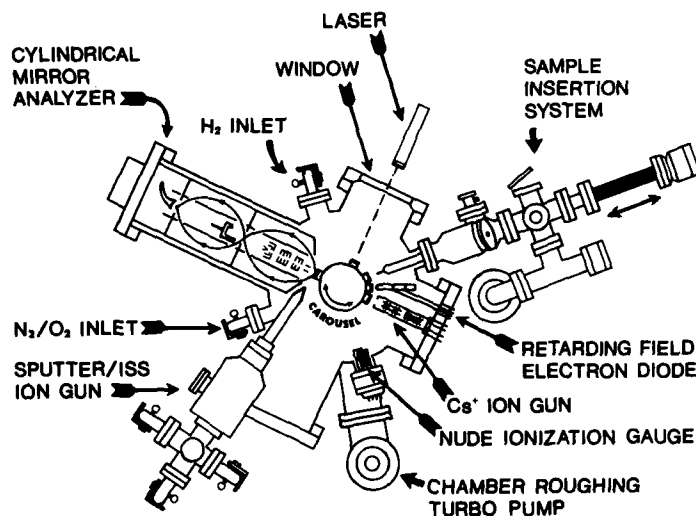


Fig. 1. Vacuum chamber and analytic apparatus.

a chamber pressure below  $10^{-7}$  Torr. Additional system elements are also shown in the figure. The experiment and data acquisition is primarily controlled by an Apple II + computer.

To study the evolution of a steady state cesium composite surface, the work function and AES signals are monitored as a function of cesium ion dosage at a given energy until a steady state is achieved. The dose is determined by integrating the cesium ion beam current to the target. For each measurement the surface is cleaned by argon sputtering, then exposed to the desired dose of cesium ions at fixed energy. Then the sample is rotated to the analytic stations and the work function and AES intensities are determined.

## 2.2. Sample preparation

The targets are 3 mm diameter discs attached to a threaded rod which threads into the sample holder, as shown in fig. 2. The threaded rod and sample holder have been described in detail elsewhere [17]. Polycrystalline beryllium, molybdenum and tungsten targets are made from material with 99.5%, 99.7%, 99.99% purity, respectively (Aesar Inc.). The molybdenum target is made by machining the entire piece from a 3 mm diameter rod. The tungsten target is a disc cut from a tungsten rod and copper brazed onto a molybdenum post. The beryllium target is sheared from foil and silver-soldered onto a molybdenum post. The samples are polished to a surface roughness of  $0.05 \mu\text{m}$ , verified by scanning electron microscopy. This was done to de-

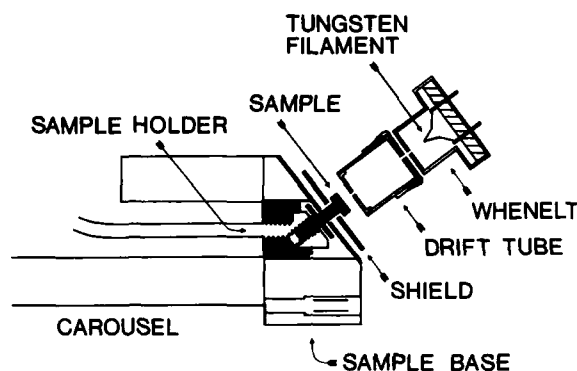


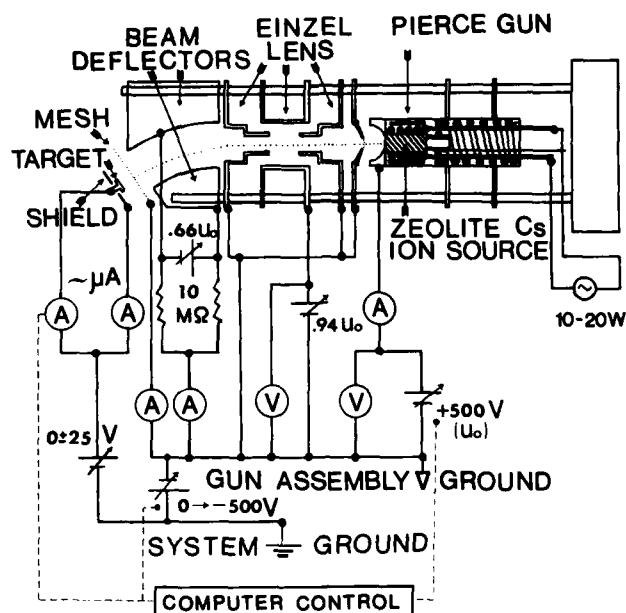
Fig. 2. Sample holder and electron diode. Key components are labelled.

termine the effects of surface roughness which develops due to sputter cleaning.

The target is cleaned initially, and between measurements by argon sputtering. Using published sensitivities [18,19], AES analysis of clean targets shows less than 0.07% carbon and 0.3% oxygen on tungsten, 1% argon and 2% nitrogen on beryllium, and no observable contaminants on molybdenum. Note that AES analysis showed no copper on the tungsten sample surface and no silver on beryllium.

### 2.3. Cesium dosing

The cesium ion source is an ion gun designed and built in house [17,20]. This gun combines the advantages of porous metal ionizers [21,22], with those of aluminosilicate emitters [23–29], to produce a clean, compact, and efficient ion gun. A drawing of the assembly is shown in fig. 3. Ions are produced by thermionic emission from a heated cesium mordenite pellet. The beam is formed by a Pierce gun [29,30], focused by an einzel lens, deflected by vertical deflecting plates, and passed through the exit mesh. The deflection is to prevent light from the filament and neutral cesium from reaching the target, thus the dose can be determined from the target current. The current to the target is larger than  $1 \mu\text{A}$ , corresponding to an ion flux of  $6 \times 10^{12}$  ions/cm<sup>2</sup> · s. The gun is easily outgassed, and there is no discernible gas load at  $10^{-10}$  Torr. After initial break-in the source is normally kept hot ( $\sim 800^\circ\text{C}$ ), eliminating start up outgassing, and preventing adsorption of contaminants on the gun assembly. It has been reported that zeolite sources are gassy and easily contaminated by active gases [7], but this has not proved to be a problem in this source.



CROSS SECTIONAL VIEW

Fig. 3. Positive cesium ion gun with electrical schematic.

Fig. 3 also shows the electric circuit schematic. For beam energies greater than 500 eV, gun assembly is grounded to system ground, and the final beam energy is the source voltage,  $U_0$  in the figure. For beam energies below 500 eV the source voltage is held at 500 V and the gun assembly is biased negatively with respect to system ground, so that the beam is decelerated between the mesh and the target. This method results in more than  $1 \mu\text{A}$  of beam current to the target for all beam energies greater than 5 eV.

#### 2.4. Work function diode

The retarding field electron diode method is used for monitoring the work function shifts [31,32]. An electron beam is directed toward a target which is biased to retard a fraction of the electrons. This bias voltage is proportional to the work function, thus the work function change after surface treatment is obtained from the difference between bias values for a fixed retarded fraction.

The entire  $V$ - $I$  curve was not determined for each measurement; instead the bias voltage was kept in the retarding region and the computer acquired the voltage and current and extrapolated to a reference current, using known values for the diode characteristic.

A modified Apex [33] electron gun, shown in fig. 2, was used in the diode. The lenses were replaced by a drift tube, and the barium oxide cathode was replaced by a custom fitted tungsten filament, since barium oxide is poisoned by exposure to atmosphere [34]. In addition, the hot filament is more immune to adsorbate induced shifts in the cathode work function. The cathode is normally kept at operating temperature. This prevents outgassing, keeps a stable work function, and prevents position changes of the filament.

The diode characteristic is governed by the Richardson equation, given by

$$j_{c \rightarrow a} = A_c T_c^2 \exp[-e(\phi_a + V_a)/kT_c], \quad (1)$$

where  $A_c$  is a constant dependent on the material. The subscripts c and a denote the cathode and anode respectively.  $V_a$  is the effective retarding potential on the anode and  $\phi_a$  is the anode work function. The quantum mechanical reflection coefficient is neglected, and the cathode work function is assumed constant. The beam temperature,  $T_c$ , is determined from two points on an experimental  $V$ - $I$  characteristic [31,32]. Using the subscripts i and f for the two measurements we have from eq. 1 that

$$kT_c = e(V_{ai} - V_{af})/\ln(I_i/I_f). \quad (2)$$

The measured value of  $T_c$  is 2300 K.

Using this value of  $T_c$  the extrapolation formula is obtained from eq. (2), given by

$$eV_{a0} = kT_c \ln(I_0/I) - eV_a, \quad (3)$$

where  $V_a$  and  $I$  are measured values,  $I_0$  is the reference current, and  $V_{a0}$  the extrapolated bias. The reference voltage for the work function shifts is taken to be the measured value for the clean substrate.

### 2.5. Auger electron spectrometer

The Auger electron spectrometer consists of a Perkin-Elmer double pass cylindrical mirror analyzer with a coaxial electron gun. The spectrometer is computer controlled, and software provides for energy spectra and simultaneous measurement of the time evolution of six Auger peaks. In addition to the usual lock-in detection the software does signal averaging.

## 3. Experimental results

### 3.1. Work function measurements

Figs. 4-6 show experimental work function versus dose on tungsten, molybdenum, and beryllium, respectively, for several beam energies. The

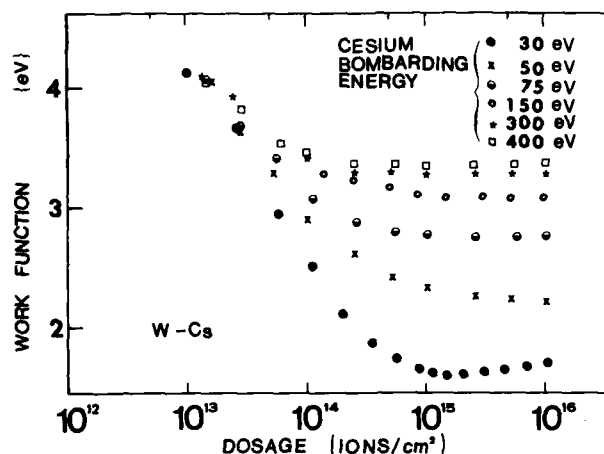


Fig. 4. Work function shift of tungsten versus cesium ion dose at several beam energies.

general behavior is that the work function decreases with increasing dose, and eventually reaches a steady state value. Note that for all curves this is accomplished with a dose of less than  $10^{16}$  ions/cm<sup>2</sup>. Tungsten and molybdenum show the same general tendencies. At low enough beam energy the work function passes through a minimum, then increases to reach steady state, while at higher beam energy this minimum does not occur and the final work function is higher. On beryllium the work function always passes

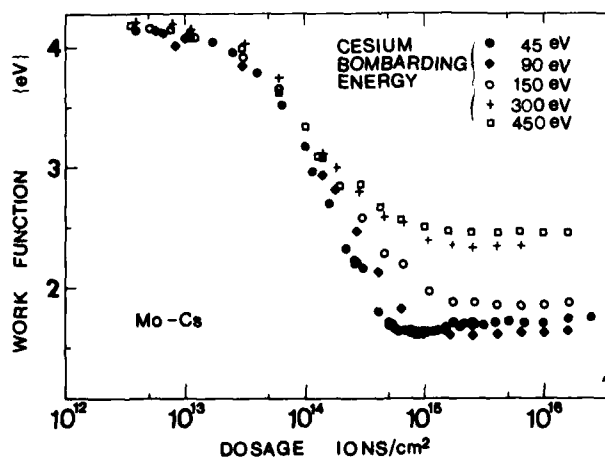


Fig. 5. Work function shift of molybdenum versus cesium ion dose at several beam energies.



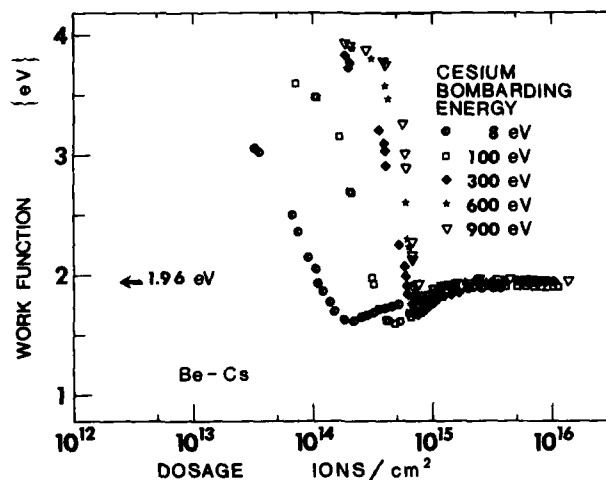


Fig. 6. Work function shift of beryllium versus cesium ion dose at several beam energies.

through a minimum and reaches a steady state value of approximately 2 eV. Note that the minimum increases slightly with increasing energy.

Fig. 7 shows the steady state work function versus beam energy for the three targets. The minima for tungsten and molybdenum occur at 45 and 100 eV, respectively. Since the beryllium curves always pass through a minimum, both the minimum and the steady state work function are shown in the figure.

Since the diode measurements give work function shifts with respect to the clean target value, additional measurements were used to calibrate the magnitude. When the minimum work function is low enough, the photoemission

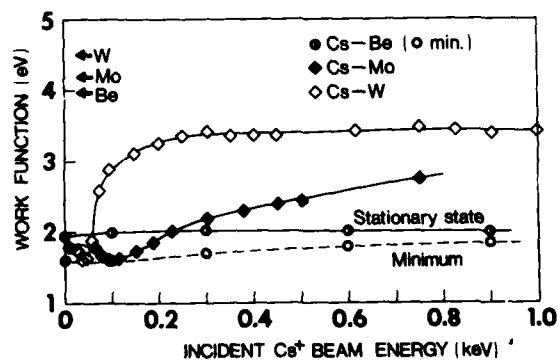


Fig. 7. Steady state work function of beryllium, molybdenum and tungsten versus incident cesium energy. The minimum work function on beryllium is also shown by the dashed curve.

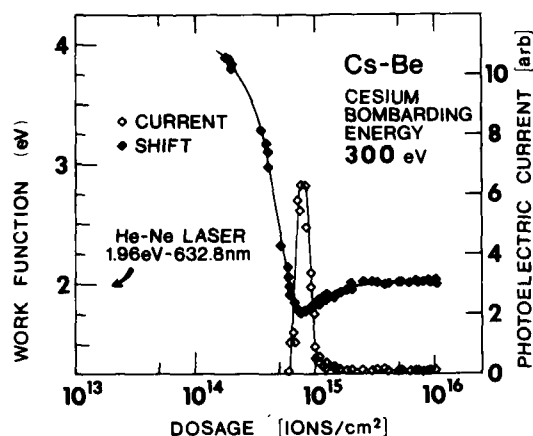


Fig. 8. Beryllium work function shift and photoelectric current versus  $\text{Cs}^+$  dose at 300 eV.

threshold for helium-neon laser light ( $\lambda = 632.8$  nm) may be used to determine a work function of 1.96 eV. Fig. 8 shows a photocurrent calibration superimposed on a work function shift curve for beryllium. For the case of molybdenum and tungsten, work function versus cesium coverage by vapor deposition has been determined [2], and these curves are reproduced in this experiment by using a beam energy of 5 eV. The magnitude of the minimum possible work function is approximately 1.6 eV for all three targets.

### 3.2. AES measurements

AES was used to obtain additional information about the cesium coverage. Fig. 9 shows typical AES versus dose curves for beryllium and tungsten. The tungsten data is for 150 eV beam energy: the 179 eV tungsten line and the 563 eV cesium line are shown in the figure. The beryllium data is for 8 and 450 eV beam energies: the 104 eV beryllium line and 47 and 563 eV cesium lines are shown. The beryllium and tungsten curves are normalized to signal intensities for a dose of  $10^{12}$  ions/cm<sup>2</sup>.

At steady state the beryllium line is attenuated by 30% for both beam energies. Using the model given by Seah and Dench [35] this is the expected attenuation for monolayer coverage [36]. Note that the cesium line intensity is larger at 450 eV than at 8 eV. With an 8 eV beam the ratio of the 47 to 563 eV cesium lines is 3.0, and with a 450 eV beam the ratio is 2.5. Since the electron escape depth is energy dependent, the change in this ratio shows that implanted cesium is detected after higher energy bombardment. This enhanced cesium signal is observed above 100 eV beam energy.

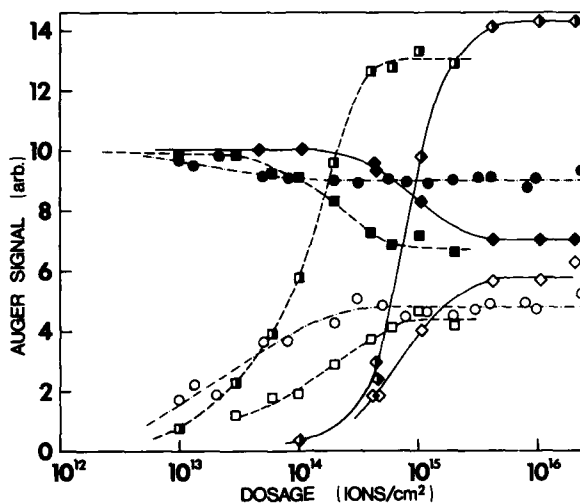


Fig. 9. Auger line intensity versus cesium dose. Circles: 150 eV cesium on tungsten, filled are tungsten line, open are 563 eV cesium line. Diamonds: 450 eV cesium on beryllium, squares: 8 eV cesium on beryllium. For diamonds and squares: filled are beryllium line, half-filled are 47 eV cesium line, and open are 563 eV cesium line.

A curve for tungsten is shown at an incident energy of 150 eV. At steady state the tungsten intensity is attenuated by 10%, corresponding to a coverage of 19%. This agrees well with the work function measurements as will be discussed later. For both molybdenum and tungsten the cesium signal decreases and the target signal increases with increasing bombarding energy. It is important to note that in all cases the line intensities become constant at the same dose as the work function curves. This is also true for molybdenum, not shown here.

A depth profile of cesium in beryllium was obtained by recording the Auger cesium line as a function of time during Ar ion sputtering at 3 keV with a flux of  $1 \times 10^{13}$  of ions/cm<sup>2</sup> · s. The results are shown in fig. 10. Two curves are shown, both for 450 eV implantation. The open symbols are for a dosage of  $2 \times 10^{16}$  ions/cm<sup>2</sup>, more than enough for steady state. In this case the cesium signal decreases monotonically with sputtering. The solid symbols are for  $4.4 \times 10^{14}$  ions/cm<sup>2</sup>, on the order of 10% of the dose needed for steady state. In this case the cesium signal begins at a small value, reaches a peak, then falls to zero. From fig. 6 it is clear that the work function is essentially the clean surface value at this dose and energy, so that the observed signal is due to implanted cesium. The curves shown in fig. 10 are original data, with no attempt to account for variations in sputter rate due to the change in surface composition. Similar curves were obtained at incident energies ranging from

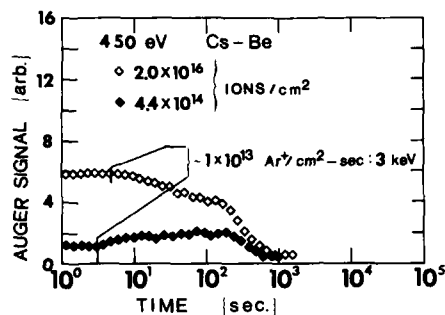


Fig. 10. AES Cs depth profiles in Be. Open symbols: steady state dose, filled symbols: 10% of steady state dose.

100 eV to 1 keV. Cesium depth profiles were not obtained in molybdenum and tungsten since the implantation depths are less than the resolution of the method in the beam energy range used.

### 3.3. Comparison of AES and work function data

Fig. 11 shows the steady state coverage derived from the work function measurements compared to the Auger cesium line intensities for the three

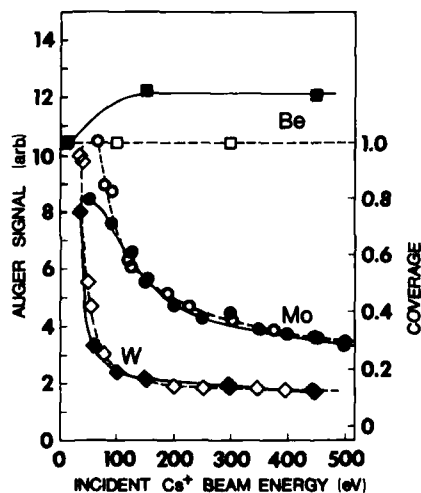


Fig. 11. Steady state coverage derived from work function measurements (open symbols), and cesium Auger line intensity (filled symbols) as a function of cesium energy. Beryllium coverage and AES curves (squares) are aligned to the low cesium energy values. Auger intensities are aligned with coverages at 450 eV for molybdenum (circles) and tungsten (diamonds).

substrates. The tungsten and molybdenum coverage curves are obtained from work function measurements by using vapor deposition measurements of work function versus coverage [2]. The Auger intensity is scaled to coincide with the coverage at a bombarding energy of 450 eV. The curves for tungsten overlap at all energies, while for molybdenum there is excellent agreement down to incident energies below  $\sim 90$  eV. The agreement of the Auger and work function results indicates that the derived coverage values are accurate. Since the work function is determined by surface cesium only, and the AES signal results from all of the cesium within an electron escape depth, the cesium must reside on the surface.

The steady state work function on the beryllium sample is always essentially that of cesium, so the coverage is taken to be unity. In this case the Auger line intensity is normalized to coverage at low energy, where implantation is small. The AES signal increases with increasing energy until it becomes nearly constant above 150 eV. The increase is attributed to implanted cesium, which levels off when the implantation depth becomes greater than the electron escape depth. These results indicate that there is substantial implantation in beryllium, resulting in a composite layer.

### 3.4. *Effects of hydrogen*

In order to study the effects of hydrogen, the work function changes due to hydrogen adsorption were measured, and the work function changes due to cesium bombardment with hydrogen present were determined. Fig. 12 shows work function changes of the clean substrates due to exposure to hydrogen at room temperature. As shown in fig. 12a, the beryllium work function does not change after exposure to several langmuirs (L) of hydrogen at  $2 \times 10^{-8}$  Torr, which implies that hydrogen does not adsorb on beryllium. On molybdenum and tungsten work function increases of 0.3 and 0.4 eV, respectively, are observed, figs. 12b and 12c, which agrees with other results [37–40]. In both cases an exposure of less than 1 L is required independent of the hydrogen pressure. Also shown are the typical work function shifts due to residual gas at base pressure, which gives an estimate of the contamination time.

Fig. 13 shows work function versus cesium dose on molybdenum and tungsten for three cases; ambient vacuum, hydrogen exposure after vacuum bombardment, and bombardment with hydrogen present. The bombardment in hydrogen was done at a pressure of  $7 \times 10^{-8}$  Torr, corresponding to a flux of  $1 \times 10^{14}$  atoms/cm<sup>2</sup> · s, or a current of 1  $\mu$ A to the target. This value was chosen to give a hydrogen dose comparable to the cesium ion beam. The hydrogen pressure for exposure after bombardment was  $2 \times 10^{-8}$  Torr ( $2.9 \times 10^{13}$  atoms/cm<sup>2</sup> · s). At very low cesium coverage the clean substrate behavior is reproduced. For work function shifts larger than 0.9 eV the two methods of adding hydrogen have opposite effects. Dosing in hydrogen results in a slightly

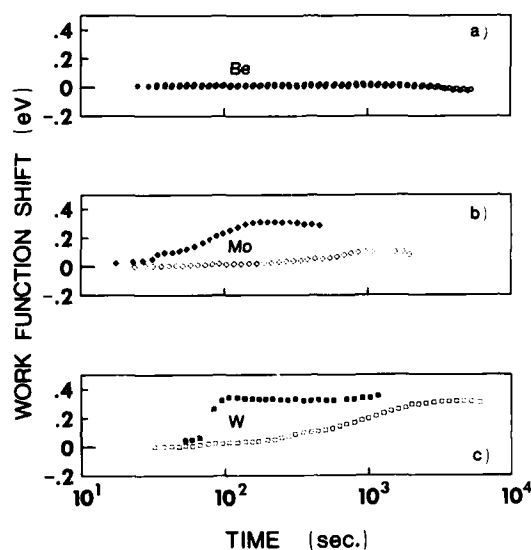


Fig. 12. Work function shift versus time. Open symbols: in ambient vacuum filled symbols: in  $2 \times 10^{-8}$  Torr hydrogen; (a) beryllium, (b) molybdenum, (c) tungsten.

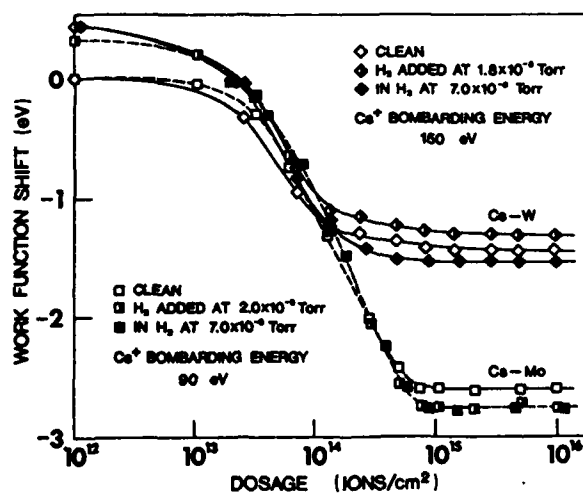


Fig. 13. Work function shift versus cesium dose on molybdenum (squares) and tungsten (diamonds). Open symbols: clean target, half-filled symbols: hydrogen added at  $2 \times 10^{-8}$  Torr after bombardment, filled symbols: bombardment in  $7 \times 10^{-8}$  Torr hydrogen.

lower work function, while hydrogen exposure after dosing results in a slightly higher work function, in both cases the magnitude is less than 0.2 eV. For coverage near the optimum (lowest) work function hydrogen decreases the steady state work function of the order of 0.1 eV, independent of how it is introduced.

These results agree with vapor deposition experiments by Papageorgopoulos [5]. He also found that the hydrogen sits beneath the cesium and that hydrogen does not adsorb on cesium. Hydrogen adsorption on tungsten or molybdenum results in a dipole layer with the negative pole toward the vacuum, increasing the work function. Cesium, on the other hand, produces a dipole layer with the positive pole toward the vacuum, which reduces the work function. When the hydrogen is beneath the cesium the positive dipole strength is increased because the cesium is farther from the substrate.

### 3.5. Effect of surface roughness

Surface structure in the 10  $\mu\text{m}$  range developed on the samples as a result of the sputtering. We found no difference between measurements on a freshly polished sample and those on the sample after enough sputter cleaning to produce the irregular surface. The full development of the structure required a dose of at least  $10^{18}$  ions/cm<sup>2</sup>.

## 4. Discussion

Since ion-target interactions are due to binary collisions [41], the target to beam mass ratio is an important parameter. It determines the amount of beam backscattering and the implantation depth scale. Table 1 shows some of the interaction parameters for the target materials for a 300 eV cesium energy. The table shows atomic mass (amu), density ( $\rho$ ), and maximum cesium atom (132.9 amu) deflection angle in a binary collision ( $\alpha_{\text{max}}$ ). Two estimates of the implantation depth ( $D$ ), are given, from LSS theory [41] and from a TRIM [42] Monte Carlo calculation. Also shown are the backscattering coefficients ( $\beta$ , the ratio of scattered to incident atoms), from TRIM, the clean surface

Table 1  
Cesium-substrate interaction parameters

Element	Mass (amu)	$\rho$ (g/cm <sup>3</sup> )	$\alpha_{\text{max}}^{\text{Cs}}$ (deg)	$D_{\text{LSS}}$ (Å)	$D_{\text{TRIM}}$ (Å)	$\beta$	$\gamma$	$\theta$
Be	9.0	1.85	3.9	9.7	13.0	6.0	0.5	~1.0
Mo	95.9	10.2	46.2	4.5	9.1	0.0	0.5	~0.32
W	183.0	19.3	180	4.4	5.0	0.2	0.5	~0.13

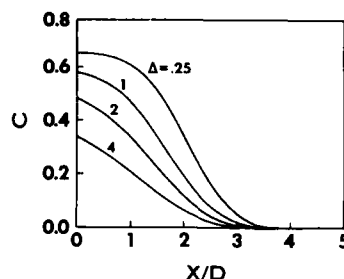


Fig. 14. Calculated concentration depth profiles, from ref. [44].

sputtering yields ( $\gamma$ , the ratio of sputtered to incident particles), and the experimental steady state cesium coverages ( $\theta$ ). For masses lighter than cesium there is no backscattering and the implantation depths are relatively large, while heavier targets have smaller implantation depths and produce backscattering. Implantation becomes of importance when the implantation depth is larger than one target layer, 2.0 to 2.5 Å. The sputtering yield is 0.5 and the surface density is approximately  $2 \times 10^{15}$  atoms/cm<sup>2</sup> for all targets, thus a dose of  $10^{16}$  ions sputters about 5 layers. Note also that this dose is equivalent to a fluence of approximately 20 layers of cesium.

There is a smooth evolution to steady state as follows. Starting with a clean surface, the incident atoms are either implanted or backscattered, and substrate atoms are sputtered. In the early stage there are very few cesium atoms on the surface, but eventually enough of the target is sputtered to expose previously implanted cesium atoms, and a fraction of these are also sputtered. The cesium surface concentration increases until a steady state is reached, where the net cesium flux to the surface becomes zero. (Backscattered flux plus sputtered flux equals incident flux.) We have previously developed an analytical model [43] that gives cesium concentration profiles shown in fig. 14. The fractional concentration is  $c$ ,  $x$  is the depth,  $D$  is the implantation depth, and  $\Delta$  is the radiation enhanced diffusion coefficient normalized to the implanted flux. For these curves the target sputter yields was taken to be unity. The model is a simplification of the approach given by Reynolds et al. [44].

The actual surface composition is determined by the sputter yields which are not included in the model. Thus, for example, if there is preferential sputtering, the model gives the concentration just under the surface, while the surface concentration is very different.

The evidence of implantation shown in fig. 10 agrees qualitatively with the model, although we have not attempted quantitative comparison of the results with theory. This would require sputtering coefficients, which are not known for composite materials. These depend not only on the composition, but also



on the degree of damage resulting from the cesium ion bombardment. Yields larger than pure substrate values are expected due to target damage.

The most important factor in determining the cesium coverage is the target mass. From fig. 11 we have that beryllium (target-to-beam mass ratio of 0.07) has essentially monolayer coverage, molybdenum (ratio = 0.7) has a much smaller coverage, and tungsten (ratio = 1.4) has about half the coverage of molybdenum. We attribute the mass dependence of cesium concentration ( $\theta$ ) to variation in backscattering ( $\beta$ ) and implantation depth ( $D$ ), as shown in table 1.

Beryllium shows a large surface cesium concentration throughout the energy range used, which indicates that cesium sputtering is suppressed in this case. We investigated this further using the TRIM program. The version used allows a layered target, so that 5 Å of cesium (approximately 1 layer) was placed on the surface of a beryllium target. The calculation showed no sputtering of either cesium or beryllium due to 5000 incident cesium ions. This has a straightforward explanation as follows. Assume the primary knock-on is cesium. All subsequent collisions are with beryllium, and from table 1 the maximum deflection of cesium is  $3.9^\circ$ , thus it cannot be deflected enough to sputter. In addition, all beryllium atoms in the cascade moving toward the surface collide with cesium atoms and are reflected, but the energy transfer to cesium is smaller than the binding energy. When implanted cesium is added, cesium sputtering does occur, because large angle collisions are possible. This effect greatly reduces cesium sputtering from beryllium, resulting in high cesium coverage at all energies.

## 5. Summary and conclusions

Cesium bombardment produces a steady state coverage which depends on the target mass. Beryllium is covered by a monolayer at all incident energies, because sputtering is inhibited. The minimum work function, obtained at lower dose, increases as the sub-surface cesium concentration increases. The coverage on molybdenum and tungsten is energy dependent, but the tungsten coverage is always smaller than that on molybdenum. It is possible to achieve the lowest possible work function on tungsten and molybdenum at 45 and 100 eV, respectively.

From these results we make some general conclusions. Ion bombardment of a target leads to a steady state coverage by the beam species which is strongly dependent upon the target mass. When the target mass is larger than, or the same order of magnitude as the beam mass, fractional coverage results, depending inversely on the target mass. When the target mass is much lighter than the beam, monolayer coverage will occur, because beam-target interactions inhibit re-sputtering of the beam species.

### Acknowledgements

We wish to acknowledge the many useful conversations with Homer D. Hagstrum, Walter C. Ermler and Bernard Gallois. Handing Huang, Joshua Isenberg, Kevin Carr, and Joeseeph Guardino should receive credit for general experimental assistance. Special thanks go to George Wohlrab whose machining capabilities and general assistance in keeping the experiment running are greatly appreciated, to Michael Dorota at Apex Electronics for useful discussions of electron guns, and to Gunter Wirth who also machined many of the system components. This work has been supported by the Air Force Office of Scientific Research, the Department of Energy and the New Jersey Commission on Science and Technology.

### References

- [1] D.L. Ferhs and R.E. Stickney, *Surface Sci.* 8 (1967) 267.
- [2] L.W. Swanson and R.W. Strayer, *J. Chem. Phys.* 48 (1968) 2421.
- [3] T.A. Karabaev, (USSR) *Nauchn. Tr. Tashkentsk. Gos. Univ.* 379 (1970) 79.
- [4] J.L. Desplat, *Surface Sci.* 34 (1973) 588.
- [5] C.A. Papageorgopoulos and J.M. Chen, *Surface Sci.* 39 (1973) 283, 313.
- [6] C.A. Papageorgopoulos and J.M. Chen, *Surface Sci.* 52 (1975) 40, 53.
- [7] H. Yasunaga, *Rev. Sci. Instr.* 47 (1976) 726.
- [8] D. Rodway, *Surface Sci.* 117 (1984) 103.
- [9] M. Kiskinova, G. Rangelov and L. Surnev, *Surface Sci.* 172 (1986) 57.
- [10] J.R. Hiskes, *J. Phys. (Paris)* C7 (1979) 179.
- [11] M. Seidl and A.N. Pargellis, *Phys. Rev.* B26 (1982) 1.
- [12] Ming L. Yu, *Phys. Rev. Letters* 40 (1978) 574.
- [13] J.N.M. van Wunnik, J.J.C. Geerlings, E.H.A. Granneman and J. Los, *Surface Sci.* 131 (1983) 17.
- [14] K.W. Ehlers and K.N. Leung, *Rev. Sci. Instr.* 51 (1982) 721.
- [15] K.N. Leung and K.W. Ehlers, in: *Production and Neutralization of Negative Ions and Beams*, Ed. K. Prelec, Brookhaven National Laboratories, N.Y., *Am. Inst. Phys. Proc.* 111 (1984) 265.
- [16] P.W. van Amersfoort, Ying Chun Tong and E.H.A. Granneman, *J. Appl. Phys.* 58 (1985) 2317.
- [17] G.S. Tompa, *Doctoral Dissertation*, Stevens Institute of Technology (May 1985).
- [18] L.E. Davis, N.C. McDonald, P.W. Palmberg, G.E. Riach and R.E. Weber, *Handbook of Auger Electron Spectroscopy* (Perkin-Elmer, Eden Prairie, 1976).
- [19] T. Sekino, Y. Nagasawa, M. Kudah, Y. Sakai, A.S. Parkes, J.D. Geller, A. Mogami and K. Hirata, *Handbook of Auger Electron Spectroscopy* (Jeol, Tokyo, 1982).
- [20] M. Seidl, A.E. Souza, W.E. Carr and G.S. Tompa, 37th Pittsburg Conference and Exposition, *Book of Abstracts*, No. 743 (March 1986).
- [21] G. Kuskevics and B. Thompson, *Rev. Sci. Instr.* 37 (1966) 710.
- [22] G.R. Brewer, *Ion Propulsion* (Gordon and Breach, New York, 1970) ch. 4.
- [23] O. Heinz and R.T. Reaves, *Rev. Sci. Instr.* 34 (1968) 1229.
- [24] R.K. Feeney, W.E. Sayle II and J.W. Hooper, *Rev. Sci. Instr.* 47 (1976) 964.
- [25] D.W. Hughes, R.K. Feeney and D.N. Hill, *Rev. Sci. Instr.* 51 (1980) 1471.

- [26] R.F. Weber and L.F. Cordes, *Rev. Sci. Instr.* 37 (1965) 112.
- [27] A.N. Pargellis and M. Seidl, *J. Appl. Phys.* 49 (1978) 4933.
- [28] J. Matossian and M. Seidl, *J. Appl. Phys.* 53 (1982) 6376.
- [29] O. Heinz and R.T. Reaves, *Rev. Sci. Instr.* 39 (1968) 1230.
- [30] J.R. Pierce, *Theory and Design of Electron Beams* (Van Nostrand, Princeton, NJ, 1954) pp. 173-193, ch. 10.
- [31] A.G. Knapp, *Surface Sci.* 34 (1973) 289.
- [32] F.H. Hayes, M.P. Hill, S.M.A. Lecchini and B.A. Pethica, *J. Chem. Phys.* 42 (1965) 6.
- [33] Apex Electronics, Inc., 100 Eight Street, Passaic, NJ 07055, USA.
- [34] G.A. Haas and J.T. Jensen, Jr., *Rev. Sci. Instr.* 28 (1957) 1007.
- [35] M.P. Seah and W.A. Dench, *Surface Interface Anal.* 1 (1979) 2.
- [36] G.S. Tompa, M. Seidl, W.C. Ermler and W.E. Carr, *Surface Sci.* 185 (1987) L453.
- [37] B.D. Barford and R.R. Rye, *J. Chem. Phys.* 60 (1974) 1046.
- [38] J.T. Yates and T.E. Madey, *J. Chem. Phys.* 54 (1971) 4969.
- [39] P.J. Estrup and J. Anderson, *J. Chem. Phys.* 45 (1966) 2254.
- [40] T.V. Vorburger, D.R. Sandstrom and J.B. Waclawski, *Surface Sci.* 60 (1976) 211.
- [41] J. Lindhard, M. Scharff and H.E. Schiott, *Kgl. Danske Selskab Mat.-Fys. Medd.* 33 (1963) 14.
- [42] J.P. Biersach and W. Eckstein, *Appl. Phys.* A34 (1984) 73.
- [43] W. Carr, M. Seidl, G.S. Tompa and A. Souzis, *J. Vacuum Sci. Technol.* A5 (1987) 1250.
- [44] G.W. Reynolds, *Nucl. Instr. Methods* B13 (1987) 467.

## COMPOSITE SURFACE LAYER FORMATION PRODUCED BY LOW ENERGY Cs<sup>+</sup> BOMBARDMENT ON: Be, Mo, & W

G.S. Tompa (a), M. Seidl and W.E. Carr

Plasma and Surface Physics Laboratory  
Physics and Engineering Physics Department  
Stevens Institute of Technology  
Castle Point Station, Hoboken, NJ 07030, U.S.A.

(a) EMCORE Corporation, 111 Corporate Blvd., South Plainfield, NJ 07080, U.S.A.

### ABSTRACT

Auger and work function shift measurements have been used to characterize the formation of a composite surface layer due to Cs bombardment in the energy range from 5 eV to 1 keV. Steady state surfaces are produced with dosages less than  $10^{16}$  ions/cm<sup>2</sup> and the steady state concentrations vary significantly between the three substrates at energies above 50 eV. The surface concentration is governed by dose, incident energy and substrate mass.

### INTRODUCTION

In general, composite surfaces are becoming increasingly important as more uses of these surfaces are found. In some cases there are presently no other ways to form such surfaces except by ion bombardment. Some surface enhancements include changes in the following properties: conductivity, catalysis, chemistry, porosity, topology, densification, diffusion barriers, hardness, structural, optical, wear, corrosion, abrasion, etc.. The production of new alloys is also possible. Reducing the  $\phi$  of a surface enhances negatively charged particle emission from the surface. The stability of the surface structures produced were also been examined.

The formation of a steady state composite surface produced by low energy ion bombardment of metal surfaces is examined. This experiment was performed to better understand and explain several practical problems associated with the controlled formation of a composite surface by ion beam deposition (IBD) and the production and use of low work function " $\phi$ " surfaces. In particular, Cs (132.9 amu) bombardment of polycrystalline Be (9.0 amu), Mo (95.6 amu) and W (183.8 amu) surfaces has been studied, providing a range of substrate to Cs mass ratios from 0.07 to 1.38. We have examined the energy range from 5 eV to 1 keV, covering the transition from essentially vapor deposition to true low energy ion beam deposition. The composite thin film consists of the upper layers of the substrate interacting with the ion beam deposited Cs,

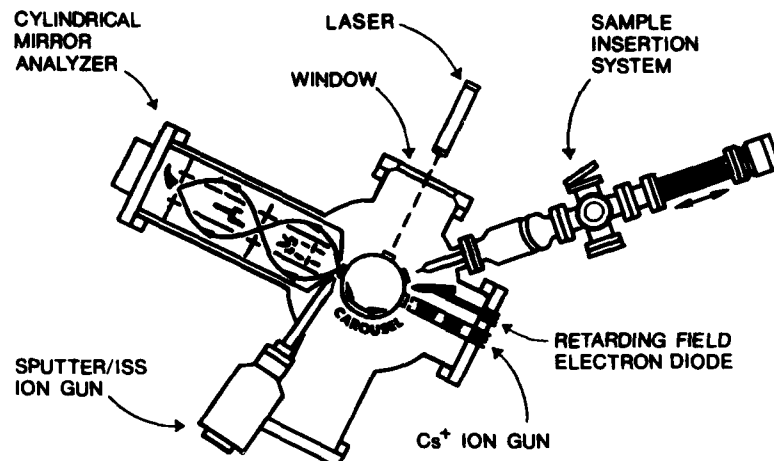


**FIGURE 1.** Experimental chamber depicting major analytic tools.

both on and within the surface. For the energy range examined, this amounts to the first 10 to 20 atomic layers. Surface characterization is performed as a function of incident ion energy and Cs dosage.

In general, a simple sticking and sputtering relationship, not including implantation, cannot account for the steady state coverage. We have seen that the incident energy, the sputter yields, the amount of implantation and backscattering of the incident beam along with radiation enhanced diffusion must all be considered in understanding the surface formed. Depending on the Cs-substrate mass ratio, implantation and backscattering play the key roles in determining the concentration of Cs. On Be the formation of a Cs overlayer acts as a buffer, limiting further sputtering of the substrate. We have previously presented an analytic model of composite surface formation[1-3] and the model is qualitatively reviewed here.

A steady state surface is produced with a dose less than  $10^{16}$  ions/cm<sup>2</sup> on each substrate as determined by Auger electron spectroscopy "AES" and  $\phi$  measurements. The nature of the steady state surface varies significantly for the substrates examined. The general functional dependence of the  $\phi$  change with Cs surface coverage is well known[1,2,4]. In the past we have seen for the energy range examined that the  $\phi$  change is a good indication of the surface concentration[1-3]. The minimum  $\phi$  for Cs-substrate systems is in general seen to be  $\sim 1.6$  eV. A steady state minimum  $\phi$  surface is obtained on Mo and W at incident ion energies of  $\sim 100$  eV[1] and  $\sim 45$  eV[2] respectively. At all incident energies, a large steady state Cs surface concentration is produced on Be, resulting in a  $\phi$  that is roughly that of Cs,  $\sim 2$  eV[5]. AES confirms the Cs concentrations producing the  $\phi$  values on the substrate.

#### EXPERIMENTAL APPARATUS

The general experimental apparatus is depicted in figure 1. The view is from above and down the central axis. The vacuum chamber is an all metal seal system, incorporating a Perkin-Elmer TNBX 3001/s ion pump with Ti sublimators and cryopanel. Post bakeout pressure is  $5 \times 10^{-11}$  Torr. With all components operating an operational pressure of  $\sim 2-8 \times 10^{-10}$  is standard. The cylindrical mirror analyzer "CMA" is a Perkin-Elmer 15-255GAR double pass, angle resolved and aperture limited. The CMA has an electron gun coaxial with the cylinder, which is used for AES. The Perkin-Elmer 04-303

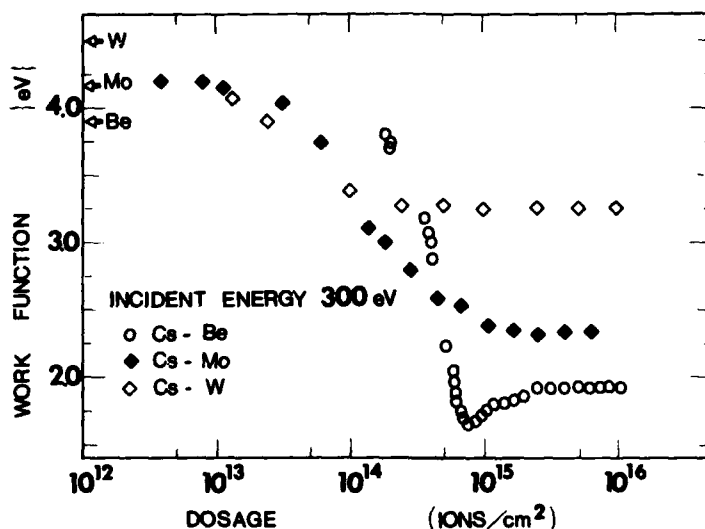


FIGURE 2. The work function vs. the Cs ion dose at an incident energy of 300 eV for the three elements.

differential ion gun, located at the CMA station, is used to provide ions for sputter cleaning of the surface and depth profiling with AES. Ar<sub>+</sub> ions are typically used. The Cs source, consisting of a zeolite thermionic emitter and focusing electrodes, is capable of providing a Cs flux of  $\sim 1 \times 10^{14}$  ions/cm<sup>2</sup>-s to the substrate [6,7]. The energy spread of the beam is essentially thermal, with a small additional contribution due to aberrations in the lenses. Adjacent to the Cs gun is the retarding field diode used for measuring  $\phi$  shifts [8,9]. The electron source is a hot W filament. The retarding potential needed to stop the electrons is proportional to the  $\phi$ . The  $\phi$  shifts of the Mo and W substrates were calibrated to vapor deposition measurements [4], the shifts agreed with the clean, minimum and high coverage  $\phi$  values. The HeNe laser (632.8nm, 1.96eV) was added to calibrate the  $\phi$  shifts measured with the diode on Be. The carousel on which the samples are placed is also shown along with the sample insertion system. The experiment and data acquisition is primarily controlled by an Apple II+ computer.

#### EXPERIMENTAL PROCEDURE

The  $\phi$  and AES signals are monitored as a function of Cs<sup>+</sup> dosage at a given energy until steady state is achieved. The dosage is determined by monitoring the Cs beam current to the target. Before any series of measurements were taken both methods of AES and  $\phi$  shift were used to determine the amount of time available to perform a measurement without contamination. For this system typical times available in which a measurement might be taken were in excess of  $\sim 600$  s, far more than the 100 to 200 s needed to dose a sample and take measurements of it. The measurements are obtained as follows. The surface is cleaned by Ar sputtering, then exposed to the desired dose of Cs ions at fixed energy. The surface conditions are then determined by rotating the sample to the analytic stations, allowing measurement of surface properties versus dose, with Cs beam energy as a variable parameter.

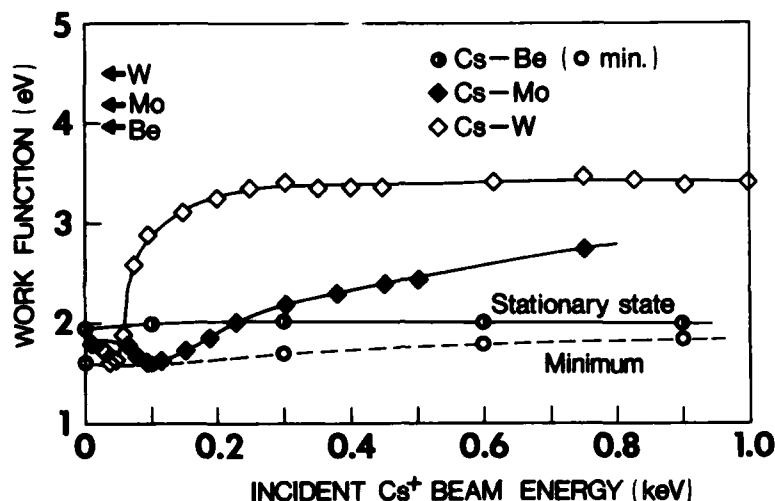


FIGURE 3. The work function versus incident Cs energy at steady state ( $10^{16}$  cesium ions/cm<sup>2</sup>) for the substrates examined. The minimum which the work function passes through before reaching steady state is depicted for Be and Si by the dashed line curves.

#### EXPERIMENTAL RESULTS

In this section we present results measured experimentally. The change in the three substrates  $\phi$  with increasing Cs ion dosage at an incident ion energy of 300 eV is presented first, as it most clearly demonstrates the differences in the  $\phi$  vs. dose curves (hence coverage [1-3]) for the energy range examined. The steady state work function " $\phi_s$ " (Cs dosage  $10^{16}$  ions/cm<sup>2</sup>) is plotted in figure 3 as a function of incident Cs ion energy for all three substrates. The differences in  $\phi_s$  are clearly seen in the figure. Implantation curves are also shown for Be.

The Be curve, in figure 2, demonstrates the general aspect of vapor deposition curves, the exception being that the doses are larger than vapor deposition doses at a given shift. On Be, at an incident Cs energy of 8.0 eV the  $\phi$  decreases, passing through a minimum at 1.6 eV, rises and finally levels off at about 2.0 eV. The value of 2.0 eV is approximately that of elemental Cs [10]. The minimum  $\phi$  is produced at a dosage of  $\sim 2.0 \times 10^{14}$  ions/cm<sup>2</sup> for the 8.0 eV case, corresponding to a coverage of  $\sim 1/2$  [5]. At 300 eV a similar curve is produced, but a dosage greater than  $\sim 2.0 \times 10^{14}$  ions/cm<sup>2</sup> is needed before significant decreases in the  $\phi$  occur. The Be 300 eV curve reaches a minimum at a dose of  $\sim 8.0 \times 10^{14}$  ions/cm<sup>2</sup>, 4x the dose needed at 8 eV. The minimum  $\phi$  produced at this energy is 1.7 eV. Beryllium has a  $\phi_s$  that is essentially constant with incident bombarding energy. The  $\phi_s$  has the value of  $\sim 2.0$  eV. In figure 3 the minimum  $\phi$  passed through before a steady state is achieved on Be is indicated by the dashed curve. The minimum produceable  $\phi$  is increasing with increasing bombarding energy, this is shown clearly in figure 3. The dose needed to produce both the minimum and steady state was observed to increase with increasing bombarding energy. At incident energies where Cs is implanted in Be, subsurface Cs ( $\sim 10\%$  by dose) had little to no effect on  $\phi$ .

The change in the  $\phi$  of Mo under Cs<sup>+</sup> bombardment as a function of dose at 300 eV shows a striking difference from the Be curve. The curve does not

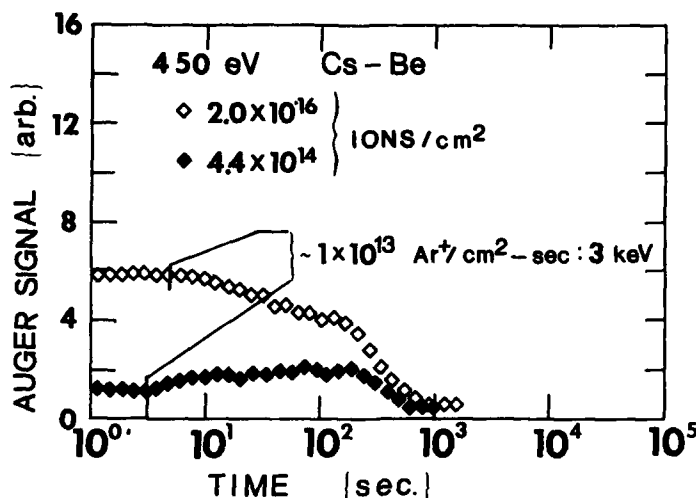


FIGURE 4. AES Cs depth profiles into Be for doses giving steady state (open symbol curves) and less than steady state (solid symbol curve).

pass through a minimum before reaching a  $\phi_s$ . Figure 3 shows that only for incident energies below 100 eV does the  $\phi_s$  pass through a minimum before reaching steady state. At 300 eV the steady state corresponds to a coverage of ~30%. At increasing incident  $\text{Cs}^+$  energies the  $\phi_s$  increases but at a rate noticeably slower than that for W.

The  $\phi_s$  shift due to Cs bombardment of W at 300 eV is different from the Be and Mo curves. In figure 2 we see that on W a  $\phi_s$  is produced at a lower dose than on Mo or Be. The  $\phi_s$  shift is also much less than on the other substrates. At low energy ( $\leq 45$  eV), as shown in figure 3, the  $\phi_s$  rises to a value approaching that of Cs with decreasing bombarding energy. The magnitude of the  $\phi_s$  shift decreases rapidly with increasing Cs bombarding energy until reaching a shift of ~1.3 eV at a bombarding energy of 150 eV, corresponding to a coverage of about 13%. Thereafter the change in  $\phi_s$  increases little with increasing energy.

In figure 3 we see for Mo and W that  $\phi_s$  decreases with decreasing energy, reaching a minimum at 1.6 eV and then rising. That this rise is due to large Cs coverage is confirmed by AES. At all energies, for the three substrates examined a  $\phi_s$  is produced with a Cs ion dosage less than  $10^{14}$  ions/cm<sup>2</sup>.

AES curves (not shown) track the  $\phi_s$  curves in dose and concentration (at all bombarding energies examined) to steady state. Not only do the Cs and substrate signals track the  $\phi_s$  curves, but the substrate signal attenuation follows the surface concentration. At doses producing a steady state on Be, the Be AES signal is attenuated by 30%, the amount one would expect for monolayer coverages. In general for Mo and W increasing the bombarding energy resulted in decreasing the Auger signal for Cs and increasing that of Mo or W. We note that for Be, Mo and W the AES signals level off at the same dosage as do the  $\phi_s$  curves.

We have adjusted the AES steady state curves to line up with the coverage (determined from vapor deposition curves) for Mo and W at a bombarding energy of 450 eV[3]. The W coverage and AES curves overlap at all energies. For Mo there again is excellent agreement until energies below ~90 eV. At the low energies the AES signal levels out before the coverage. This is most likely due to the fact that monolayer coverage is being produced.



The agreement between the derived coverage and AES for Mo and W strongly implies that the Cs resides on the surface for these substrates. On the other hand for Be, we had no coverage calibration curve except that of our low energy measurements. It was seen that at increasing energies the curves did not overlap, the Cs steady state AES signal rose with energy until leveling off above an incident energy of 100 eV. The increase is attributed to detection of subsurface Cs, the leveling off is attributable to no further implanted Cs being detectable due to the escape depth. The high and low energy Cs AES signals leveled out at different incident energies for Be. The increase in Cs steady state AES signal and the implantation curves shown in figure 4 show that the Cs-Be system forms a true composite at all but the lowest incident energies.

That Cs is implanted in Be for the energy range examined is shown in figure 4 where Cs AES depth profiles are shown for two different doses at an incident energy of 450 eV.  $\text{Ar}^+$  sputtering at 3 keV with a flux of  $1 \times 10^{13}$  of  $\text{Ar}^+$ /cm<sup>2</sup>-sec was used to depth profile into the Be. The open symbol curve is for a dosage of  $2 \times 10^{16}$  ions/cm<sup>2</sup>, well exceeding that producing a steady state. In this case the Cs signal is seen only to decrease with sputtering. The solid symbol curve is a depth profile of a dosage of  $4.4 \times 10^{14}$  ions/cm<sup>2</sup>, much less than that giving steady state. It clearly shows an increase in Cs signal before going to zero. At this dose and bombarding energy there is little change in the  $\phi$  indicating a coverage less than a few percent, much less than that if the dose were spread uniformly over the surface. Similar curves could be produced on Be down through incident energies of 100 eV. The curve is original data, no attempt has been made to adjust the results to account for changes in sputter rate associated with the change in composition as the Cs is sputtered away. We were unable to produce curves showing implanted Cs for Mo or W over the energy range examined.

#### DISCUSSION

The effects of surface diffusion and evaporation of Cs from the substrates has been considered and found not to measurably contribute to the type of measurements made here[2]. We have monitored both the AES and  $\phi$  signals in time and have not observed changes associated with surface diffusion or evaporation for our measurements at room temperature for periods in excess of 1 hr. AES and  $\phi$  monitoring of Cs doses equal to and less than that giving steady state for Be showed no bulk diffusion to the surface for periods >1 hr.

The target mass is an important factor since it determines the amount of backscattering and the depth scale for implantation. For target masses lighter than Cs there is no backscattering and implantation depths are relatively large, while heavier targets give smaller implantation depths and significant backscattering. Implantation becomes of importance once the implantation depth is larger than about one layer of the target,  $\sim 2.7$  Å for Mo or W and  $\sim 2.2$  Å for Be. LSS[11] theory gives a relation between incident energy and range for low energy ions (less than 10 KeV). We calculated implantation depths (R) using both LSS range statistics and the TRIM code[12] for Cs on Mo, W and Be. The implantation depths in angstroms are presented in table I for an incident energy of 300 eV. Also shown in the table are TRIM code derived backscatter coefficients ( $\beta$ ), the density ( $\rho$ ), sputter yield (Y)[13], the coverage ( $\theta$ ), and the maximum forward scattering angle ( $\alpha$ ) of the normally incident Cs with the substrate as determined by binary collision theory.

The formation of the composite surface is governed by the simultaneous deposition of Cs on and within the surface and by the sputtering of the

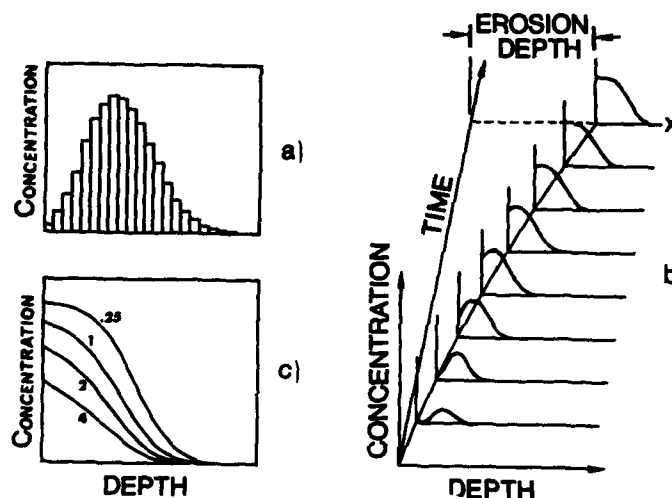


**FIGURE 5.** The evolution of a composite surface is shown graphically. a) instantaneous implantation profile. b) evolution and growth of a composite steady state layer. c) structural dependence of a steady state on the magnitude of radiation enhanced diffusion.

substrate (including implanted Cs). Reflected Cs does not contribute. With the sputtering of substrate material, previously implanted Cs is exposed, this process continues until a steady state is achieved.

The general process is shown graphically in figure 5 a, b and c. In 5.a an instantaneous gaussian implantation profile is shown. This profile is what one would see if the surface is exposed to a dose less than that giving appreciable surface erosion (due to sputtering) and the energy is large enough for a significant implantation depth. The normalized probability of an ion being implanted in an interval  $dx$  at  $x$  expressed in the terms of LSS theory is[11]:

$$P(x)dx = \{0.57/D\} \exp[-([x-R]/D)^2] dx \quad (1)$$

where  $R$  is the range and  $D$  is the deviation. In 5.b we show the evolution of a composite surface due to implantation and sputtering. As time increases the implanted concentration increases, but at the same time the surface is eroded due to sputtering. The erosion rate will in general change with time (implant concentration) since the implanted species changes the nature of the substrate. Instead of eroding it is possible for the surface to grow if sputtering is low and deposition large. Another factor effecting the implanted concentration distribution is radiation enhanced diffusion "RED". RED will allow implanted species to penetrate deeper into the substrate than allowed for by LSS theory. Taking into account RED and the time dependance of the substrates surface we have written the following expression for the implanted concentration[3]:

$$[d(c(x))/dx][dx/dt] = \alpha \phi_{in} P(x)/\rho - \Delta[d^2(c(x))/dx^2] \quad (2)$$

where  $c(x)$  is the fractional concentration of implanted species,  $\alpha$  is the reflection coefficient (percent of incident ions not remaining at the substrate) and  $\phi_{in}$  is the incident flux,  $\rho$  is the substrate density, and  $\Delta$  is the RED coefficient. We have evaluated the  $dx/dt$  term with regard to

ELEMENT	a.m.u.	$\rho(\text{g/cm}^3)$	$\alpha_{\text{max}}^{\text{Cs}}(\text{deg})$	LSS( $\text{\AA}$ )	TRIM( $\text{\AA}$ )	$\beta$	$\gamma$	$\theta$
Be	9.0	1.85	3.9	9.7	13.0	0	.5	~1
Si	28.1	2.42	12.2	9.4	16.6	0	.5	—
Mo	95.9	10.2	46.2	4.5	9.1	0	.5	~.32
Ru	101.1	12.4	49.5	3.9	5.8	.008	—	—
W	183.9	19.3	—	4.4	5.0	.20	.5	~.13

**TABLE I.** Listing of substrate characteristics relative to IBD. The substrate density  $\rho$ , the maximum forward scattering angle ( $\alpha$ ) of the normally incident Cs<sup>+</sup> with the substrate, LSS implantation depth for Cs at 300 eV, TRIM code implantation for Cs at 300 eV, TRIM code derived backscatter coefficients ( $\beta$ ), sputter yield ( $\gamma$ )[13], and the coverage ( $\theta$ ).

surface sputter erosion and surface growth due to implantation, whence, for the case of steady state equation 2 may be written[3]:

$$[\Delta/\alpha\phi_{\text{in}}][d^2\{c(x)\}/dx^2] = [G(x) - \phi_s/\alpha\phi_{\text{in}} - 1]d\{c(x)\}/dx = d\{G(x)\}/dx \quad (3)$$

where  $\phi_s/\phi_{\text{in}}$  is the total sputter flux divided by the incident flux defining the total sputter yield  $\gamma$ , and  $G(x) = \int_0^x P(x)dx$ . The values used for  $\alpha$ ,  $\gamma$  and  $\Delta$  must be the steady state values. Equation 3 may be solved numerically. Figure 5.c demonstrates the effect of increasing the RED coefficient. The larger the coefficient, the lower the concentration near the surface and the tail of the profile becomes more drawn out.

Neglecting diffusion and evaluating for the surface concentration ( $x=0$ ) one obtains  $\ln(1 + \alpha/\gamma)$ , which reduces to  $\alpha/\gamma$  in the limit of low surface concentration[3].

We investigated Cs sputtering of Cs covered Be using the TRIM code. The version used allows layered targets, so that 5 Å of Cs was placed on a thick layer of Be. The calculation showed no sputtering of either Cs or Be due to 5000 incident Cs ions. This can be understood in terms of binary collision processes. A Cs primary knock-on is produced, which subsequently collides only with Be atoms. From table 1, the maximum deflection is 3.9°, thus the Cs cannot be deflected enough to sputter. Be atoms in the cascade that move toward the surface collide with Cs atoms and are reflected, transferring insufficient energy to the Cs atoms for sputtering to occur. It requires the addition of implanted Cs in order for sputtering to occur.

When ion implantation exists, we find that a composite surface coverage is formed. Coverages, derived from our  $\phi$  shift measurements by comparison to  $\phi$  shifts obtained by vapor deposition [4], are in good agreement with AES measurements. Through depth profiling with AES, we are able to determine when implantation becomes important. The results have shown the importance of the incident ion mass to target mass ratio in determining the energy range at which large coverages of the incident ion species may be produced on a target material.

The three elements examined all have similar pure element sputter yields over the range of energies examined[13]. High concentrations are produced on Be due to implantation and little to no backscattering. For W the high backscattering and limited implantation result in low Cs concentrations. Mo behaves in a fashion between the low mass Be substrate and the higher mass

W substrate. Si with a mass between Mo and Be is presently being examined. Ru with a mass comparable to Mo and a crystalline structure the same as Be would also be useful to examine.

This work has been supported by the Air Force Office of Scientific Research, the Department of Energy and the New Jersey Commission on Science and Technology.

#### REFERENCES

- 1) G. S. Tompa, W. E. Carr and M. Seidl, Appl. Phys. Lett. **48** 16 (1986) 1048
- 2) G. S. Tompa, W. E. Carr and M. Seidl, Appl. Phys. Lett. **49** 22 (1986) 1511
- 3) W. Carr, M. Seidl, G. S. Tompa and A. Souzis, J. Vac. Sci. Technol., **A5** 4 (1987) 1250
- 4) L. W. Swanson and R. W. Strayer, J. of Chem. Phys. **48** 6 (1968) 2421
- 5) G. S. Tompa, M. Seidl, W. C. Ermler and W. E. Carr, Surf. Sci. Lett. **185** (1987) L453
- 6) G. S. Tompa, Ph.D. Thesis, Stevens Institute of Technology (1986)
- 7) M. Seidl, A. E. Souzis, W. E. Carr, and G. S. Tompa, 37<sup>th</sup> Pittsburg Conference and Exposition, Book of Abstracts, No. 743 (March 1986)
- 8) A. G. Knapp, Surf. Sci. **34** (1973) 289
- 9) F. H. Haayes, M. P. Hill, S. M. A. Lecchini, and B. A. Pethica, J. Chem. Phys. **42** 8 (1965) 2919
- 10) Herbert B Wilson, J. Appl. Phys. **48** 11 (1977) 4729
- 11) J. Lindhard, M. Schariff and H. E. Schiott, Kgl. Danske Selsk. Mat-Fys. Medd. **33** 14 (1963)
- 12) J. P. Biersack and W. Ecstein, Appl. Phys. (German) **A34** (1984) 73
- 13) Sputtering by Particle Bombardment I, (R. Behrisch, editor) Springer-Verlag Topics in Applied Physics V47, Berlin, Heidelberg, NY (1981)

**PROCEEDINGS OF THE III-rd EUROPEAN  
WORKSHOP ON**

**PRODUCTION AND  
APPLICATION OF LIGHT  
NEGATIVE IONS**

**Edited by:**

**Henk Hopman and Wim van Amersfoort**

**FOM-Institute for Atomic and Molecular Physics**

**Kruislaan 407, 1098 SJ AMSTERDAM - The Netherlands**

**EUROASE CONGRESS CENTER AMERSFOORT  
THE NETHERLANDS**

**February 17 - 19, 1988**

## BACKSCATTERING OF HYDROGEN ATOMS AT LOW ENERGIES

M. Seidl, W. E. Carr, J. L. Lopes, and S. T. Melnychuk  
Department of Physics and Engineering Physics  
Stevens Institute of Technology, Hoboken, NJ 07030

### ABSTRACT

Partially cesiated metallic and semiconductor targets have been exposed to a flux of atomic hydrogen produced by thermal dissociation of hydrogen gas. Surface production of negative hydrogen ions and of electrons has been studied. The energy distribution of the  $H^-$  ions is maxwellian with a temperature equal to the atomic gas temperature. The  $H^-$  yield increases exponentially with inverse temperature and reaches a few percent of the incident atomic flux for a cesiated (100) n-type silicon target, 0.2 eV temperature and 1.5 kV/cm extraction field. Theoretical analysis indicates that the dominant limitation is trapping of the  $H^-$  ions by the image force. This effect can be reduced by a large extraction field.

### 1. INTRODUCTION

Surface production of negative hydrogen ions at escape energies below 1 eV has not yet been studied in any detail. This is in contrast to many excellent studies in the energy range above a few electron volts.

Theoretical models [1-5] have been developed to evaluate the ionization probability as function of the work function of the metal, the electron affinity and perpendicular velocity of the atom. Recently the effect of hydrogen coverage has been studied [6].

The ionization probability at cesiated metal surfaces was measured by backscattering protons with incident energy in the 1000 to 50 eV energy range [7-15]. By using glancing angle detection the measurements could be extended to a few electron volts of  $H^-$  escape energy [9-11,15]. This seems to be the lowest energy practically obtainable in positive ion backscattering. The technical difficulty of making high permeance ion beams limits the energy of the incident beam. The fundamental problem related to the effect of parallel velocity on the ionization probability [9,16] poses a limit on the glancing angle.

Low escape energies of  $H^-$  ions can be obtained by cesium ion bombardment of metal surfaces partially covered with cesium and hydrogen [17-19]. However, in these experiments the measured quantity is the  $H^-$  sputter yield and the ionization probability can be obtained only if the total sputter yield is known.

Backscattering of thermally produced hydrogen atoms from low work function surfaces offers a technique suitable for studies of  $H^-$  formation at low energies.

The observation of  $H^-$  ions produced by scattering thermal hydrogen atoms from a cesiated surface was first reported by Graham [20]. Pargellis and Seidl [21] measured the yield of  $H^-$  ions and electrons when thermal hydrogen atoms were incident on a thick cesium target.

In this work we have studied backscattering of hydrogen atoms from cesiated polycrystalline molybdenum and n-type (100) silicon targets. We have measured the energy distribution of the  $H^-$  ions and the average ionization probability. The theory of Rasser et al [3] has been modified to include time

dependence of velocity and compared with the experiments. The dominant effect is trapping of the  $H^-$  ions by the image force. However, because of the absence of positive ions, a large extraction electric field can be applied to partially compensate the image force and thus increase the  $H^-$  yield.

## 2. EXPERIMENTAL APPARATUS

The experimental apparatus is schematically shown in Fig. 1. It consists of a planar diode and a rotating magnetic sector mass spectrometer.

The cathode of the diode is a cooled molybdenum plate into which various targets can be mounted with good thermal contact. The anode is a fine tungsten mesh (180 wires per 2.54 cm with 20  $\mu m$  wire diameter) placed 2-4 mm from the cathode. The mesh is heated up to 2000°C by passing current through it. Hydrogen gas admitted into the chamber is dissociated on the hot tungsten mesh, which provides a source of atomic hydrogen of flux density up to  $10^{17}$  atoms/cm<sup>2</sup> sec and in a temperature range of 1400°C to 2000°C. Cesium vapor is produced in a small oven and is directed into the diode through a manifold. Some of the cesium vapor condenses on the cathode surface and some cesium is surface ionized on the hot tungsten mesh. The  $Cs^+$  ions are accelerated onto the negatively biased cathode. The  $Cs^+$  current density is monitored by two  $Cs^+$  Faraday cups facing two 0.631 mm-diam holes drilled in the Mo cathode. Cesium coverage is controlled by the oven, cathode and mesh temperatures. The work function is monitored by the photoelectron current produced by a HeNe laser beam.

A small sample of the negative hydrogen ions and electrons produced on the target passes through a 0.631 mm-diam aperture and enters the diagnostics region. When the Faraday cup is rotated out of the beam path, the rotating magnet is used to measure the angular dependence of the particles. The angular resolution of the measurement is about 0.5°. The detection system accepts all particles emitted in a cone of 14° half angle.

In this work we have investigated the following two target materials:

- a) Cesiumated polycrystalline molybdenum (minimum work function 1.6 eV [22]) and
- b) Cesiumated single crystal (100) silicon n-type doped (minimum work function 1.45 eV [23]).

## 3. EXPERIMENTAL RESULTS

The basic operation of the experiment is as follows: First the mesh temperature, hydrogen pressure, and cathode-anode voltage are selected. Then the optimum cesium coverage of the target is obtained by varying the target temperature and the cesium oven temperature. The work function is monitored by the photo-electron current produced by the He-Ne laser beam (photon energy 1.96 eV). Fig. 2 shows that the maxima for the photo-electron current and  $H^-$  ion current occur at the same target temperature. This confirms the fact that maximum  $H^-$  production occurs at minimum work function.

The flux density of atomic hydrogen produced by the hot tungsten mesh is calculated from the theory of Hickmott [24]. The rate of evaporation of atomic hydrogen from a hot tungsten surface ( $T > 1100^\circ K$ ) immersed in hydrogen gas of room temperature is given by the equation

$$k_A n = \{-k_A + (k_A^2 + 4 \phi(H_2) S k_2)^{1/2}\} / 2 k_2 \quad (1)$$

where

$$k_A = 2.2 \times 10^{13} \exp - (67,000/RT) \quad (2)$$

$$k_2 = 5 \times 10^{-3} \exp -(31,000/RT) \quad (3)$$

$S = 0.05$  is the sticking coefficient of molecular hydrogen onto tungsten, and  $\phi(H_2)$  is the impingement flux density of molecular hydrogen. The impingement flux density of atomic hydrogen on the target is calculated by the formula

$$\phi(H) = k_A n (1-t) \quad (4)$$

where  $t = 0.733$  is the transmission coefficient of the mesh.  $\phi(H)$  is plotted in Fig. 3 as function of  $H_2$  pressure for several mesh temperatures. It may be noted that  $\phi(H)$  is almost proportional to the hydrogen pressure indicating that atomic hydrogen desorption is supply limited for the low pressures and high temperatures used in this experiment. Also plotted in Fig. 3 are curves of measured  $H^-$  current densities. It can be seen that they are parallel to the corresponding  $\phi(H)$  curves, a fact that strengthens our confidence in Hickmott's formulas.

Angular dependence of  $H^-$  current density has been measured with the rotating magnet. Fig. 4 shows three distributions corresponding to three different mesh temperatures. The exit angle  $\theta$  of the  $H^-$  ion is related to the parallel energy  $E_{||}$  at the surface of the target by the equation

$$\tan^2 \theta = E_{||} / U \quad (5)$$

where  $U$  is the accelerating voltage applied between the anode and cathode. Using this equation the angular distribution can be converted into parallel energy distribution. Fig. 5 shows two such energy distributions corresponding to two different mesh temperatures. The  $H^-$  ions have clearly a Maxwellian energy distribution with a temperature equal to the mesh temperature. Since the target is approximately at room temperature, this result shows that the fast hydrogen atoms are reflected from the target in elastic collisions.

Figure 6 illustrates the effect of  $Cs^+$  ion bombardment on the energy distribution of  $H^-$  ions. In this experiment all the parameters (including the work function) were kept constant except for the  $Cs^+$  ion bombardment current density. The  $H^-$  ion distribution consists of two Maxwellian distributions produced by hydrogen backscattering ( $T = 0.16$  eV) and sputtering by  $Cs^+$  ion bombardment ( $T = 3$  eV).

We define the negative hydrogen yield as

$$\beta = \phi(H^-) / \phi(H) \quad (6)$$

where  $\phi(H^-)$  is the measured flux density of  $H^-$  ions and  $\phi(H)$  is the flux density of the incident hydrogen atoms calculated from eqn. (4). The yield  $\beta$  is also the ionization probability averaged over the Maxwellian distribution of the incident atoms. Fig. 7 shows the yield as function of inverse temperature for the molybdenum and silicon targets. The yield depends exponentially on the inverse temperature,  $\beta \sim \exp (-\text{const}/kT)$ . This expression can be justified theoretically, as shown in the next section. The yield from the silicon target is about 3 times larger than the yield from the molybdenum target. This is attributed to the lower work function of the cesiated silicon. Only a small fraction (one percent) of the incident atoms is reflected as  $H^-$  ions. The remaining atoms are either reflected as neutrals or are trapped as negative ions near the surface of the target as discussed in the next section. The trapped ions eventually recombine into hydrogen molecules or chemically react



with the target. These reactions are accompanied by electron emission. Pargellis and Seidl [21] observed about 100 times more electrons than  $H^-$  ion in backscattering hydrogen atoms from a thick cesium target (work function 2.1 eV). In the present experiments the electron current is of the same order of magnitude as the  $H^-$  current.

The  $H^-$  yields in Fig. 7 were obtained with a small anode-cathode voltage. Fig. 8 shows that the logarithm of the yield increases with the square root of the electric field  $E$ . This is a typical Schottky effect dependence [25]. It may be noted, however, that the slope of both curves is about 8 times larger than expected from the standard Schottky formula

$$I(E)/I(E=0) = \exp(3.79 \times 10^{-4} \sqrt{E/kT}) \quad (7)$$

where  $E$  is in V/cm and  $kT = 0.16$  eV is the temperature of the  $H^-$  ions.

#### 4. THEORY

In this section we describe a Monte Carlo calculation of negative ion formation and survival at large distance for incident thermal atoms. This was analyzed previously [2,3] for atoms with constant perpendicular velocities, corresponding to hydrogen beam reflection experiments [7-15]. In our experiment the incident atoms are thermal at a few tenths of an eV, and it is important to include the change in velocity as an ion moves away from the surface.

The potential energy of the negative ion is essentially determined by the image charge and is given by;

$$U(z) = -A - \frac{e^2}{4\pi\epsilon_0} \frac{1}{4(z+b)} \quad (8)$$

where the screening distance,  $b$ , is taken to be 3.2 Bohr radii [15], and the binding energy of the second electron for an isolated ion,  $A$  is 0.75 eV. This holds for  $z$  not too close to the surface. Figure 9 shows the potential given by (8) as a function of distance from the surface. Note that this potential is used for two purposes. It determines the crossing distance,  $z_c$ , where the potential energy is equal to the work function,  $W$ , which is used in determining the charge state of a fixed ion. In addition, eqn (8) is used via energy conservation to determine the change in perpendicular velocity of an ion as it moves away from the surface.

Also shown in Fig 9 is the Schottky effect, obtained by adding a term  $-Ez$ , where  $E$  is the extraction field. The Schottky field increases the crossing distance and decreases the potential barrier for ions.

Since the atom thermal energies used in the experiment are smaller than the depth of the potential well, most of the atoms that are ionized near the surface will not have enough kinetic energy to escape. Thus, slow ions produced near the surface are trapped.

Next, we extract the essential features from the probability model [3]. The motion of the atom is treated classically, so that the quantum electron dynamics are calculated at fixed position. There are two quantities that are needed. First, the charge state of an atom at a fixed distance,  $z$ , has been determined [15]. For cesiated metal with a 0.5 monolayer hydrogen adsorption the probability that the atom is a negative ion is very near unity inside the crossing distance, and very near zero outside. This is not unreasonable, since for  $z < z_c$  electron transfer is only from filled states below the Fermi level

to the atom, and for  $z > z_c$  electron transfer is from negative ions to vacant states above the Fermi level.

Second, the electron transition rate,  $\omega(z)$ , between the atom and the solid is given, for distances not too close to the surface, by [6];

$$\omega(z) = \omega_0 \exp(-az) \quad (9)$$

where  $z$  is the distance from the surface, and  $\omega_0$  and  $a$  are constants. For a cesiated surface with 0.5 monolayer adsorbed hydrogen the values are  $\omega_0 = 10^{15} \text{ sec}^{-1}$ , and  $a = 0.6$  Bohr radii [6].

Using these ideas the ionized fraction may be estimated by the rate equation given by;

$$\frac{dP}{dt} = \omega(z) (\theta(z - z_c) - P) \quad (10)$$

where  $P$  is the probability that the atom is a negative ion.  $\theta(z)$  is the charge state of a fixed atom, approximated in this case by the Heavyside step function. In previous work [3] (10) was integrated using a constant velocity, which is reasonable if atom kinetic energy is larger than the height of the potential barrier.

We have integrated the rate equation, (10) using the potential given by (8) to determine the kinetic energy at each point, with the results shown in fig 10. This shows the probability of ionization as a function of distance for several initial energies. Those with the smallest energies have a very high likelihood of being ionized because they spend a long time near the surface, but they do not have enough kinetic energy to get over the potential barrier. The atoms with just enough energy to escape are slow and are likely to be ionized, but they are also likely to be neutralized outside  $z_c$ . The faster ions have lower probability for ionization. Note that these curves are only approximate, since the kinetic energy changes with distance only for an ion, and the point of ionization is a random process.

The Monte Carlo calculation determines the ionized fraction of a thermal distribution of atoms as follows. An atom is placed near the surface and assigned an initial speed,  $u$ , from a Gaussian random number generator with the appropriate spread. This atom is moved in constant steps,  $dz$ . At each step  $R$  is assigned from a uniform random number generator in the interval  $(0,1)$ , and if  $R < \omega(z) dz/u$  then ionization took place. Once ionized, it is assumed that the atom cannot be neutralized inside  $z_c$  since there are no vacant states in the solid. The ion is then moved to  $z_c$  and the kinetic energy is reduced by the change in potential energy. If the resulting kinetic energy is negative the ion is counted as trapped. Atoms that reach  $z_c$  without being ionized are counted as escaping atoms.

Ions that reach  $z_c$  untrapped are moved in steps of  $dz$ , but the expression  $R < \omega(z) dz/u$  is used to determine whether the ion is neutralized. Those that are neutralized are counted as escaping atoms. Slow enough ions can be trapped outside  $z_c$ , and these are added to the trapped count. Finally, ions that survive at a large distance are counted as collected ions.

Figure 11 show the ionized fraction and the neutral fraction as a function of inverse temperature for several values of the work function. Since the sum of ionized, neutral, and trapped fractions is unity, it is clear that the trapped fraction is large. The dependence of the ion fraction on temperature and work function is in good qualitative agreement with the experimental results.

This simple model works reasonably well because it is in effect an integration of a stochastic process, so that the important quantities are: the scale length for electron transitions, the crossing point, and the ratio of the temperature to the image potential well depth. The Schottky effect can also be incorporated into the model, and this is currently being carried out.

## 5. CONCLUSIONS

a) An atom produced on the surface of a solid by atomic collisions (reflection or sputtering) has in the average the same parallel and perpendicular initial velocity in all but a few exceptional cases. In consequence, the parallel temperature of surface produced ions is approximately equal to their average perpendicular energy,  $T \sim E_{\parallel} \sim E_{\perp}$ .

b) The yield of negative hydrogen ions produced by reflection of thermal hydrogen atoms from cesiated surfaces depends exponentially on the inverse ion temperature according to  $\exp(-\text{const}/T)$ . The highest measured yield is  $2.5 \times 10^{-2}$  at  $T = 0.19$  eV and for low extraction fields. Theory indicates yields in excess of 0.1 for  $T = 0.5$  eV, work function 1.2 eV and low extraction field.

c) Analysis indicates that the basic limitation of  $H^{-}$  production at low temperature is trapping of the  $H^{-}$  ions by the image force. Large extraction field can partially compensate the image force and thus increase the yield.

## ACKNOWLEDGEMENT

This research has been supported by the U. S. Air Force Office of Scientific Research.

## REFERENCES

1. J. R. Hiskes, J. Phys. (Paris) 40, 179 (1979).
2. E. G. Overbosch, B. Rasser, A. D. Tenner, and J. Los, Surf. Sci. 92, 310 (1980).
3. B. Rasser, J.N.M. van Wunnik, and J. Los, Surf. Sci. 118, 697 (1982).
4. R. Brako and D. M. Newns, Surf. Sci. 108, 253 (1981).
5. N. D. Lang, Phys. Rev. B27, 2019 (1983).
6. J. P. Gauyacq, J.J.C. Geerlings, Surf. Sci. 182, 245 (1987).
7. W. Eckstein, H. Verbeek, and R.S. Bhattacharya, Surf. Sci. 99, 356 (1980).
8. J. R. Hiskes, P. J. Schneider, Phys. Rev. B23, 949 (1981).
9. J.N.M. van Wunnik, J.J.C. Geerlings, and J. Los, Surf. Sci. 131, 1 (1983).
10. J.N.M. van Wunnik, J.J.C. Geerlings, E.H.A. Granneman, and J. Los, Surf. Sci. 131, 17 (1983).
11. P.J.M. van Bommel, J.J.C. Geerlings, J.N.M. van Wunnik, P. Massmann, E.H.A. Granneman, and J. Los, J. Appl. Phys. 54, 5676 (1983).
12. P. J. Schneider, K. H. Berkner, W. G. Graham, R. V. Pyle, and J. W. Stearns, Phys. Rev. B23, 941 (1981).
13. P. W. van Amersfoort, J.J.C. Geerlings, L. F. Tz. Kwakman, A. Hershcovitch, E.H.A. Granneman, and J. Los, J. Appl. Phys. 58, 3566 (1985).
14. P. W. van Amersfoort, J.J.C. Geerlings, R. Rodink, E.H.A. Granneman, and J. Los, J. Appl. Phys. 59, 241 (1986).

15. P. W. van Amersfoort, Formation of Negative Ions on a Metal Surface. FOM Amsterdam (1987).
16. J.N.M. van Wunnik, R Brako, K. Makoshi, and D. M. News, Surf. Sci. 126, 618 (1983).
17. M. Seidl and A. Pargellis, Phys. Rev. B26, 1 (1982).
18. J. L. Lopes, J. A. Greer, M. Seidl, J. Appl. Phys. 60, 17 (1986).
19. M. Seidl, W. E. Carr, J. L. Lopes, S. T. Melnychuk, and G. S. Tompa, Production and Neutralization of Negative Ions and Beams, edited by J. Alessi (Brookhaven National Laboratory), American Institute of Physics Conference Proceedings No. 158, p. 432 (New York, NY) 1987.
20. W. G. Graham, Phys. Lett. 73A, 186 (1979).
21. A. Pargellis and M. Seidl, Phys. Rev. B25, 4356 (1982).
22. G. S. Tompa, W. E. Carr, and M. Seidl, Appl. Phys. Lett. 48, 1048 (1986).
23. R. E. Weber and W. T. Peria, Surf. Sci. 14, 13 (1969).
24. T. W. Hickmott, J. Chem. Phys. 32, 810 (1960).
25. L. N. Dobretsov and M. V. Gomoyunova, Emission Electronics (IPST Jerusalem 1971).

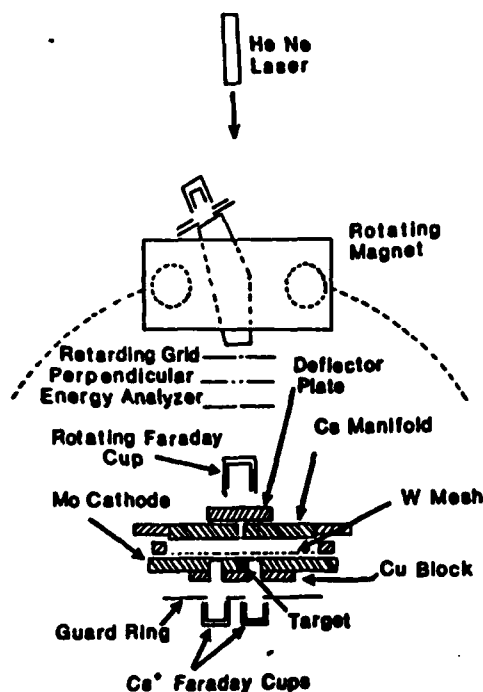


Fig. 1. Experimental arrangement.

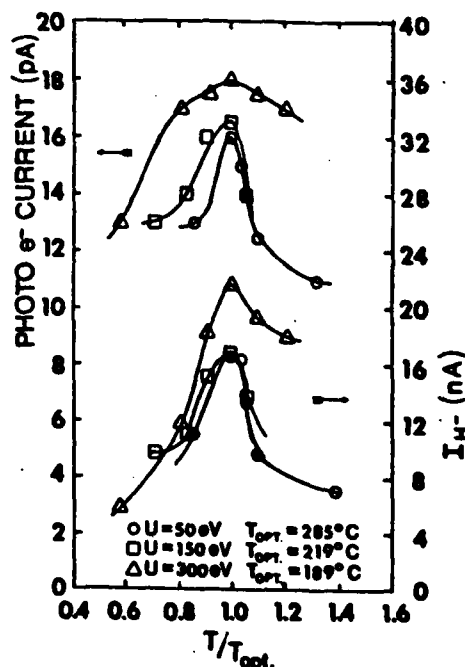


Fig. 2. Photo emission current and H<sup>-</sup> ion current as function of target temperature.

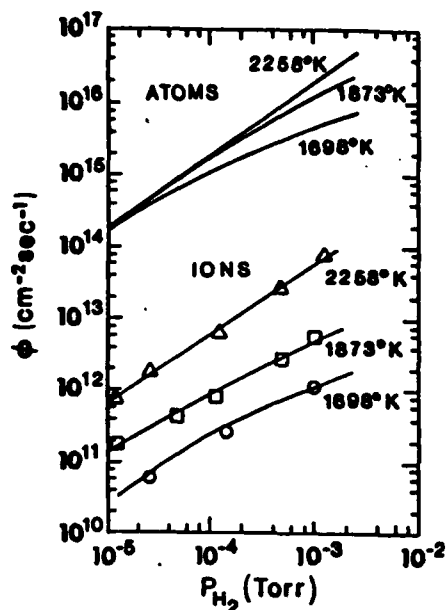


Fig. 3. Atomic and  $H^-$  ion flux densities as function of  $H_2$  pressure and mesh temperature.  $M_0$  target.

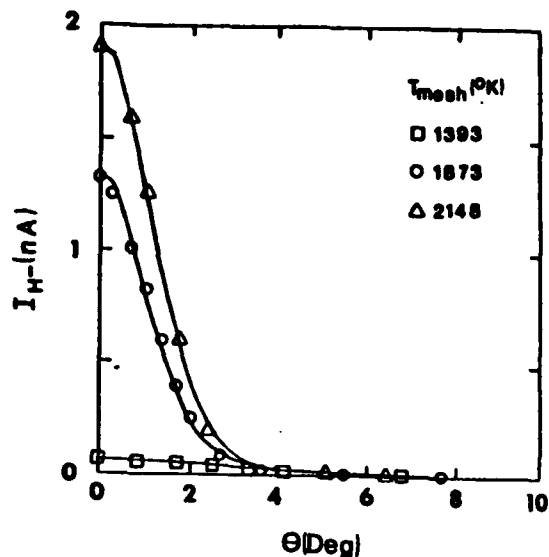


Fig. 4. Angular dependence of  $H^-$  ion current. Mo target,  $P_{H_2} = 1.6 \times 10^{-3}$  Torr, and  $U = 300$  eV.

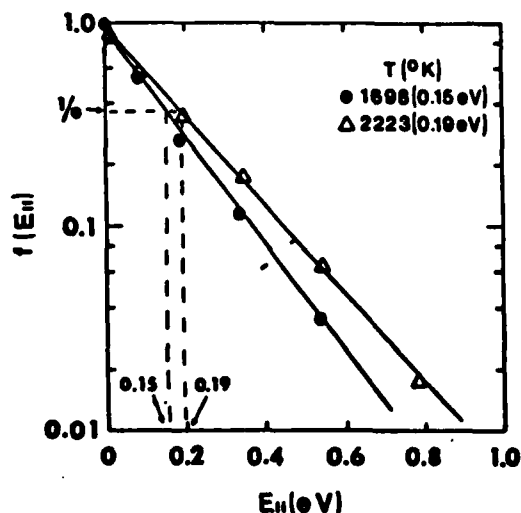


Fig. 5. Energy distribution of  $H^-$  ions for two mesh temperatures. Mo target,  $P_{H_2} = 1.6 \times 10^{-3}$  Torr,  $U = 100$  eV, and a diode gap of 4.5 mm.

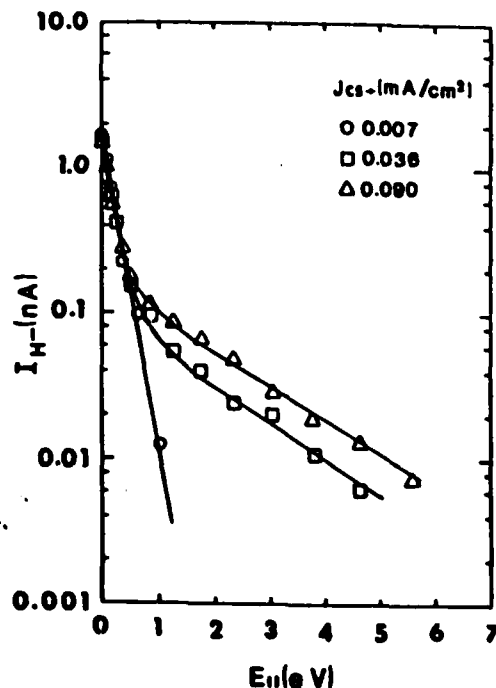


Fig. 6. Energy distribution of  $H^-$  ions as a function of  $Cs^+$  ion current density.  $M_0$  target,  $P_{H_2} = 1.4 \times 10^{-3}$  Torr, and  $T_{mesh} = .17$  eV.

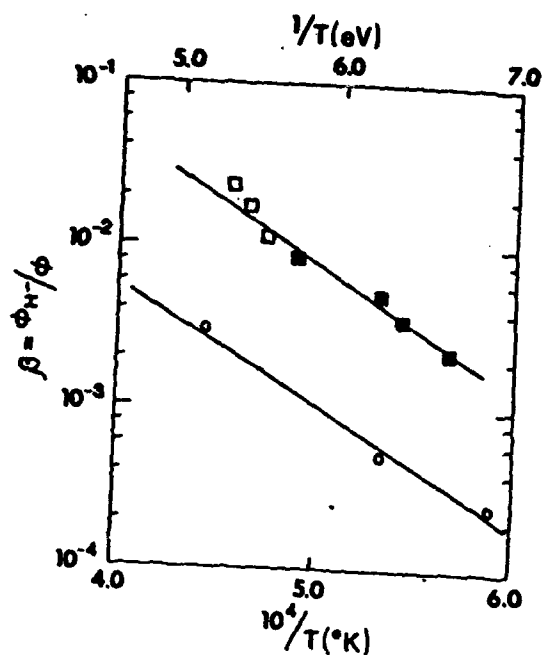


Fig. 7.  $H^-$  ion yield for  $U = 100$  eV as function of mesh temperature. Circles: Mo target, Squares: Si(100) target.

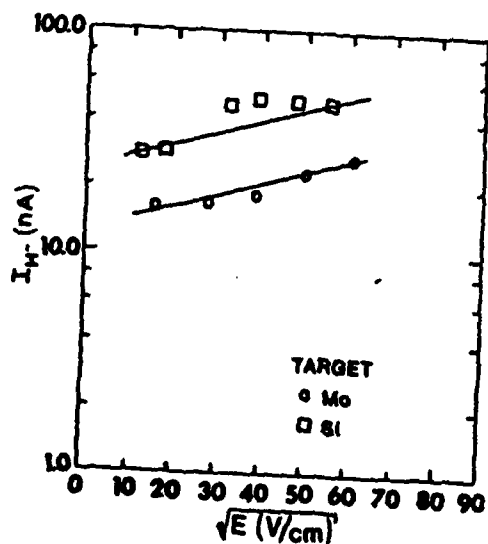


Fig. 8. Dependence of  $H^-$  ion current on extraction field  $E$ .  $PH_2 = 10^{-3}$  Torr,  $T_{\text{mesh}} = .16$  eV.

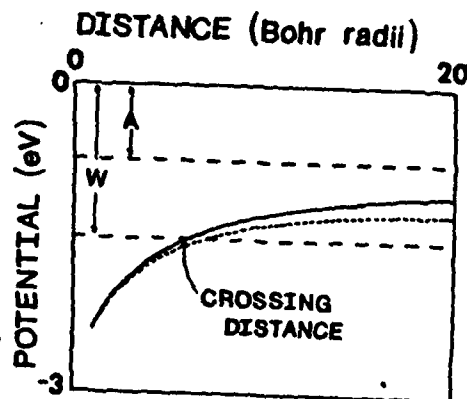


Fig. 9. Image potential as function of distance.

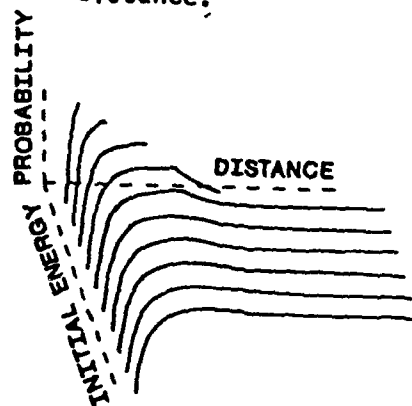


Fig. 10. Ionization probability as function of distance. Largest initial energy corresponds to 1.6 times the potential energy depth.

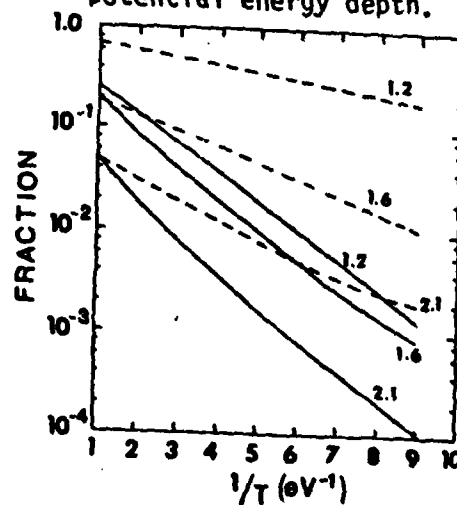


Fig. 11. Ionized (solid) and neutral (dashed) functions. Work functions (in eV) are indicated.

**EFFECTS OF HYDROGEN AND OF CESIUM ADSORPTION  
ON A BERYLLIUM SURFACE:  
A THEORETICAL AND EXPERIMENTAL STUDY**

**M.M. MARINO, W.C. ERMLER**

*Department of Chemistry and Chemical Engineering, Stevens Institute of Technology, Hoboken,  
NJ 07030, USA*

**G.S. TOMPA \* and M. SEIDL**

*Department of Physics and Engineering Physics, Stevens Institute of Technology, Hoboken,  
NJ 07030, USA*

Received 29 February 1988; accepted for publication 19 September 1988

Cesium and hydrogen adsorption on beryllium clusters containing 19, 33 and 45 atoms are studied using restricted Hartree–Fock (RHF) calculations and ab initio relativistic effective core potentials. The Be clusters are taken as cylindrical plugs from a Be metal wafer. Be–Cs and Be–H internuclear distances are optimized, while Be–Be internuclear distances are frozen at the bulk metal values. For each system, numerous low-lying electronic states are investigated. The calculations are carried out in the context of an experimental study to determine the effects of Cs and of H adsorption on the work function of Be metal. Auger electron spectroscopy and experimental work function measurements indicate that H<sub>2</sub> does not adsorb on polycrystalline Be, while photoemission and thick Cs overlayer measurements show a 2.3 eV lowering in the work function of Be metal upon Cs adsorption. RHF calculations indicate that Be<sub>19</sub>, with three layers of atoms, is too small to adequately model the Be surface. Calculations on Be<sub>33</sub>, a five-layered system, and Be<sub>45</sub>, a seven-layered system, show that H does not chemisorb on the surfaces of these clusters, whereas Cs does and lowers the ionization potential of Be<sub>33</sub> by 1.5 eV. The emitted electron from the Be<sub>33</sub>Cs<sub>2</sub> cluster vacates a molecular orbital which is localized in the surface layer.

**1. Introduction**

It is well known that adsorption of cesium on a metal surface lowers the work function of that metal [1,2]. In particular, the reduction in the work function of beryllium arising from cesium adsorption has been the focus of a very recent study [3]. In the present work, cesium and hydrogen adsorption on a beryllium surface are studied using ab initio quantum mechanical calculations. H<sub>2</sub> adsorption on polycrystalline Be is also studied by monitoring the work function and the Be (104 eV) differentiated Auger electron signal intensity.

\* Current address: EMCORE Corporation, 35 Elizabeth Avenue, Somerset, NJ 08873, USA.

Theoretical studies of the adsorption process yield detailed information about the metal surface which is not easily obtained experimentally. For example, results related to charge distributions and orbital structure are calculated. Many such studies have used clusters as models of the surface [4–7]. A good model of the adsorption process, however, requires the use of clusters large enough to accurately describe the metal surface and its interaction with the substrate, while remaining small enough for application of accurate theoretical methods. In this study, the clusters are taken as cylindrical plugs from a Be wafer having Be–Be internuclear distances equal to those in the bulk hcp metal. Larger spherical clusters were the focus of recent studies [8]. The use of effective core potentials to describe the core electrons in cesium and beryllium allow the calculations to remain tractable while maintaining a well-defined level of theory. The complexity of the calculations is simplified further by preserving full  $D_{3h}$  point-group symmetry in each cylindrical cluster.

## 2. Methodology

### 2.1. Theoretical model and calculations

The model systems are taken as cylindrical “plugs” from Be wafers having surfaces corresponding to the (0001) hcp metal faces. A view of this wafer along the  $c$  direction is illustrated in fig. 1. Table 1 defines all the cylinders of a given radius which may be formed from a wafer of a given thickness. In this study, three such cylinders are treated. The first has a thickness of three layers and is comprised of 19 Be atoms; the second is five layers thick and contains 33 Be atoms, while the third contains 45 atoms and seven layers. All three cylinders have a radius  $R_3$  which includes a one-unit cell step along the  $a$  direction. Be–Be internuclear distances are equal to those in the bulk hcp metal ( $a = 2.29 \text{ \AA}$ ,  $c = 3.58 \text{ \AA}$ ) [9]. The resulting cylinders have  $D_{3h}$  point-group symmetry, and the adsorption of atomic hydrogen, one on the top surface and one on the bottom surface of all three cylinders, is modeled such that the three-fold symmetry is preserved. The same applies to the adsorption of atomic cesium. In all cases, the Be–adsorbate internuclear distances have been optimized in self-consistent field (SCF) calculations. The 19- and 33-atom cesiated and hydrogenated cylinders are shown in figs. 2 and 3. The 45-atom cylinder is not shown, but it is similar to the one picture in fig. 3, except that it contains seven layers instead of five, and the two surface layers are identical to the surface layers of  $\text{Be}_{19}$  (fig. 2). Results obtained using these systems are compared to those calculated by treating identical bare Be cylinders.

Calculations were accomplished on a Cray X-MP supercomputer using programs based on the “equal contribution theorem” for two-electron in-



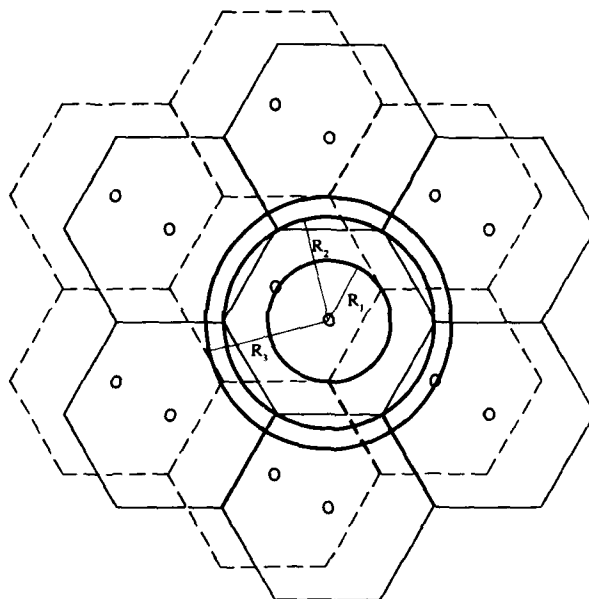
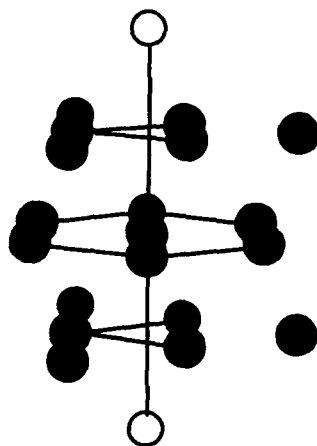
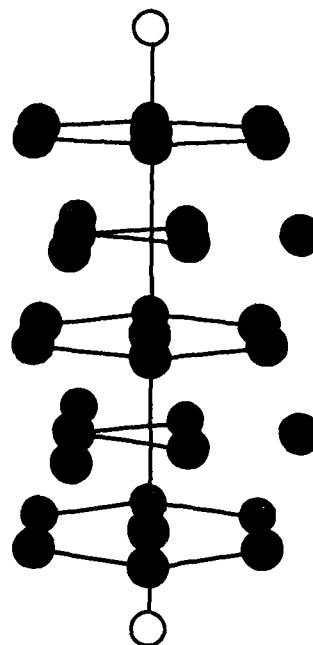


Fig. 1. A view of bulk Be metal along the  $c$  direction. Nuclei are situated at the apices of the hexagons, as well as at their centers. Layers represented by dashes lie at  $c/2$  on the  $c$  axis (see table 1.)

tegrals [10]. Ab initio restricted closed-shell and restricted open-shell Hartree-Fock calculations, each corresponding to an average energy of configuration, were carried out on numerous low-lying states of each cluster. (The

Table 1  
Be clusters by coordination cylinder and hcp layer

Cylinder height ( $z$ -coordinate)	$R_0$	$R_1$	$R_2 = a$	$R_3$
$+\infty c/2$				
$3c/2$	0	3	3	6
$c$	11	1 1	7 7	7 7
$c/2$	000	3 3 3	3 3 3	6 6 6
0	1111	111 1	7 7 7 7	7 7 7 7
$-c/2$	000	3 3 3	3 3 3	6 6 6
$-c$	11	1 1	7 7	7 7
$-3c/2$	0	3	3	6
$-\infty c/2$				
No. atoms	1133	17915	7132731	7193345

Fig. 2.  $\text{Be}_{19}\text{X}_2$ ,  $\text{X} = \text{Cs}, \text{H}$ .Fig. 3.  $\text{Be}_{33}\text{X}_2$ ,  $\text{X} = \text{Cs}, \text{H}$ .

average energy of configuration is defined as the weighted mean of the energies of all the multiplets for the configuration.) The largest clusters required about one hour of Cray X-MP time for each geometric orientation. The following basis sets of contracted Gaussian-type functions were used for beryllium, cesium and hydrogen, respectively: (3s2p)/[2s1p] [11], (5s5p)/[3s2p] [12], and (4s1p)/[2s1p] [13]. Ab initio effective potentials (EP) [14] were used to represent the 1s core electrons on Be [11] and the 1s–4s, 2p–4p, and 3d–4d core electrons in Cs [12]. In the case of Cs, relativistic effects were incorporated into the EP [14]. Binding energies calculated relative to the completely dissociated clusters are given in table 2. (Valence SCF energies for atomic Be,  $\text{Be}^+$ , Cs,  $\text{Cs}^+$ , H and  $\text{H}^-$  are  $-0.95083$ ,  $-0.65457$ ,  $-19.84225$ ,  $-19.72876$ ,  $-0.49928$  and  $-0.44815$  hartrees, respectively, for the basis sets used in this study.) The total adsorption energies given in table 2 for the cesiated and hydrogenated clusters were calculated relative to the SCF energies of the naked clusters plus that of two adsorbate atoms.

Theoretical work functions are given in table 3. The first values in each row were calculated as the difference between the total valence SCF energy of a neutral cluster and that of the ion generated by removing one electron from

Table 2  
Restricted Hartree-Fock energies of states of  $\text{Be}_m$  and  $\text{Be}_m\text{X}_2$  clusters

Cluster	Occupied MO's <sup>a)</sup>						Cluster BE (kcal/mol)	Total adsorption energy (kcal/mol·atom)
	$a_1'$	$a_2'$	$a_2''$	$e'$	$e''$	$a_1''$		
$\text{Be}_{10}^{b,c1}$	4	1	3	4	2	0	325.25	
$[\text{Be}_{10}]^+$	4	<b>0</b>	3	4	2	0	294.70	
$\text{Be}_{10}\text{Cs}_2$	6	1	5	5	3	0	402.99	38.87
$[\text{Be}_{10}\text{Cs}_2]^+$	6	<b>1</b>	5	5	3	0	405.37	
$\text{Be}_{10}\text{H}_2^{b,d1}$	4	1	3	4	2	1	393.76	34.25
$[\text{Be}_{10}\text{H}_2]^+$	4	1	3	4	2	<b>0</b>	579.66	
$\text{Be}_{13}$	6	1	5	6	4	1	724.94	
$[\text{Be}_{13}]^+$	6	1	6	<b>6</b>	4	1	815.76	
$\text{Be}_{13}\text{Cs}_2^{b,e1}$	8	1	7	7	6	1	768.46	21.76
$[\text{Be}_{13}\text{Cs}_2]^+$	8	1	7	7	<b>6</b>	1	779.74	
$\text{Be}_{13}\text{H}_2^{b,f1}$	7	1	5	6	4	1	727.32	1.19
$[\text{Be}_{13}\text{H}_2]^+^{b1}$	7	1	5	<b>6</b>	4	1	818.70	
$\text{Be}_{45}^{b,g1}$	8	2	7	8	6	2	1078.74	
$[\text{Be}_{45}]^+$	8	2	7	<b>7</b>	5	2	1196.77	
$\text{Be}_{45}\text{H}_2^{b,h1}$	8	2	7	8	6	2	1115.07	18.16
$[\text{Be}_{45}\text{H}_2]^+$	8	2	7	<b>8</b>	6	2	1228.41	

<sup>a)</sup> Entries correspond to total number of occupied MO's of each entry. Bold numbers denotes orbital from which the electron was removed.

<sup>b)</sup> State corresponds to the weighted average of configuration.

<sup>c)</sup> Open-shell state:  $(a_2')^1(a_2'')^1$ .

<sup>d)</sup> Open-shell state:  $(a_2')^1(a_1'')^1$ .

<sup>e)</sup> Open-shell state:  $(e'')^2$ .

<sup>f)</sup> Open-shell state:  $(a_1')^1(a_2'')^1$ .

<sup>g)</sup> Open-shell state:  $(a_2')^1(e')^1$ .

<sup>h)</sup> Open-shell state:  $(a_2')^1(e')^1$ .

the highest occupied orbital of that cluster. The values immediately following are due to Koopmans' theorem and correspond to the negative of the energy of the molecular orbital (MO) from which the electron was ionized. Experimental values obtained as discussed below are also shown.

Atomic net electron charge values are given in tables 4–6, as calculated using a Mulliken population analysis [15]. Values of  $R$  appearing in these tables correspond to optimum atom-to-surface distances. These distances were calculated from the minimum of a curve fit to SCF energies for three or more distances.

## 2.2. Experimental procedure

Experimental measurements were performed in an ultrahigh vacuum system with a base pressure of  $5 \times 10^{-11}$  Torr. Pressures were monitored with a nude ionization gauge whose controller allowed calibration for  $\text{H}_2$ . The general

Table 3  
Work functions of  $\text{Be}_m$  and  $\text{Be}_m\text{X}_2$  clusters

Cluster	$\phi$ (eV) <sup>a)</sup>
$\text{Be}_{19}$	5.35, 5.04
$\text{Be}_{19}\text{Cs}_2$	3.41, 2.99
$\text{Be}_{19}\text{H}_2$	4.30, 3.96
$\text{Be}_{33}$	4.41, 4.11
$\text{Be}_{33}\text{Cs}_2$	2.92, 2.60
$\text{Be}_{33}\text{H}_2$	4.37, 4.09
$\text{Be}_{45}$	3.16, 2.94
$\text{Be}_{45}\text{H}_2$	3.40, 3.15
Be (expt)	3.92
BeCs (expt) <sup>b)</sup>	1.6
BeH (expt)	3.92
$\Delta\phi[\text{Be}_{19}-\text{Be}_{19}\text{Cs}_2]$ <sup>c)</sup>	1.94, 2.05
$\Delta\phi[\text{Be}_{19}-\text{Be}_{19}\text{H}_2]$ <sup>c)</sup>	1.05, 1.08
$\Delta\phi[\text{Be}_{33}-\text{Be}_{33}\text{Cs}_2]$ <sup>c)</sup>	1.49, 1.51
$\Delta\phi[\text{Be}_{33}-\text{Be}_{33}\text{H}_2]$ <sup>c)</sup>	0.05, 0.01
$\Delta\phi[\text{Be}_{45}-\text{Be}_{45}\text{H}_2]$ <sup>d)</sup>	-0.24, -0.21
$\Delta\phi[\text{Be}-\text{BeCs}]_{\text{expt}}$ <sup>c)</sup>	2.3
$\Delta\phi[\text{Be}-\text{BeH}]_{\text{expt}}$	0

<sup>a)</sup> Where two values appear, these are Koopmans' theorem and  $^{\Lambda}E_{\text{SCF}}$  values, respectively.

<sup>b)</sup> At optimum Cs coverage.

<sup>c)</sup> Values correspond to a work function lowering.

<sup>d)</sup> Values correspond to a work function increase.

experimental apparatus was described previously [3,16]. The sample was mounted on a carousel that allowed rotation to either a retarding field electron diode station [17,18], where work function shifts were measured, or to a cylindrical mirror analyzer station having a center-mounted electron gun with which Auger electron spectroscopy (AES) measurements were made. A sputter ion gun was co-focused onto the sample with the AES system and was used to sputter clean the surface.

AES showed that no O or C contaminants were present after sputter cleaning. The only contaminants present were Ar (< 1.1%) and N (< 2.4%), and these were due to the sputter cleaning. After cleaning, AES and work function shifts indicated the Be surface to be free of contaminants for a period in excess of one hour.

The experimental procedure was as follows. The sample was first sputter cleaned.  $\text{H}_2$  could be introduced into the system at any time before, during or after sputter cleaning. Cs was deposited onto the surface from a low-energy Cs (5 eV) source [3] before or after sputter cleaning at a separate deposition station adjacent to the work function station. The Auger signal was generally monitored during cleaning. After cleaning, the Auger signal either continued to be monitored or the sample was rotated from its position facing the

AES/sputter cleaning station to a new position facing the work function diode, thus allowing the work function shift to be monitored. The repositioning was accomplished in approximately twenty seconds.

### 3. Results and discussion

Total adsorption energies for the cesiated and the hydrogenated clusters appear in table 2. As was previously mentioned, the energies were calculated relative to the total SCF energies of the naked clusters plus that of the two adsorbate atoms in their ground states. These energies are 38.9, 21.8, 34.3, 1.2 and 18.2 kcal/mol · atom for  $\text{Be}_{19}\text{Cs}_2$ ,  $\text{Be}_{33}\text{Cs}_2$ ,  $\text{Be}_{19}\text{H}_2$ ,  $\text{Be}_{33}\text{H}_2$  and  $\text{Be}_{45}\text{H}_2$ , respectively. For  $\text{Be}_{19}\text{Cs}_2$  dissociation to  $\text{Be}_{19}^+ + \text{Cs}^+ + \text{Cs}$  requires 58.9 kcal/mol · atom. Dissociation of  $\text{Be}_{19}\text{H}_2$  to yield  $\text{Be}_{19}^+ + \text{H} + \text{H}^-$  and  $\text{Be}_{19}^- + \text{H} + \text{H}^+$  requires 108.6 and 175.3 kcal/mol · atom, respectively. Dissociation of  $\text{Be}_{33}\text{Cs}_2$  to  $\text{Be}_{33}^+ + \text{Cs} + \text{Cs}^+$  needs 49.4 kcal/mol · atom. Energies of 149.8, and 64.6 kcal/mol · atom are needed to dissociate  $\text{Be}_{33}\text{H}_2$  to  $\text{Be}_{33}^+ + \text{H} + \text{H}^-$  and  $\text{Be}_{33}^- + \text{H} + \text{H}^+$ , respectively. Finally, the dissociation of  $\text{Be}_{45}\text{H}_2$  to yield  $\text{Be}_{45}^+ + \text{H} + \text{H}^-$  and  $\text{Be}_{45}^- + \text{H} + \text{H}^+$  requires 68.1 and 150.12 kcal/mol · atom, respectively. Therefore, the lowest-energy dissociation limit is of the form  $\text{Be}_n + 2\text{X}$ , where X is an adatom in the ground state. This procedure will be named method 1. There are two alternative ways of calculating the adsorption energy, methods 2 and 3. Method 2 involves calculation of the adsorption energy relative to the total energy of the lowest electronic state and MO configuration for the equilibrium geometry of the cluster-adsorbate system and the same electronic state for a cluster-adsorbate separation of approximately 10 Å, which is taken as infinite separation. This method assumes no crossings among electronic states.

For  $\text{Be}_{19}\text{Cs}_2$ ,  $\text{Be}_{33}\text{Cs}_2$ ,  $\text{Be}_{19}\text{H}_2$  and  $\text{Be}_{45}\text{H}_2$ , this assumption leads to sizeable errors. In these cases, the lowest energy electronic state corresponding to the calculated equilibrium geometry is not the lowest energy state calculated at infinite cluster-adsorbate separation. This method yields adsorption energies of 53.7, 56.3, 136.4 and 177.0 kcal/mol · atom for  $\text{Be}_{19}\text{Cs}_2$ ,  $\text{Be}_{33}\text{Cs}_2$ ,  $\text{Be}_{19}\text{H}_2$  and  $\text{Be}_{45}\text{H}_2$ , respectively. Clearly, method 2 overestimates the adsorption energies of  $\text{Be}_{19}\text{Cs}_2$ ,  $\text{Be}_{33}\text{Cs}_2$ ,  $\text{Be}_{19}\text{H}_2$  and  $\text{Be}_{45}\text{H}_2$  (by 14.8, 23.8, 102.1 and 158.8 kcal/mol · atom, respectively, relative to method 1). No electronic state crossings were found for  $\text{Be}_{33}\text{H}_2$ . However, the ground state of  $\text{Be}_{33}\text{H}_2$  is open-shell and nearly degenerate (0.01 eV lower in energy) with a closed-shell state that is 3.65 eV higher in energy at dissociation than the ground state.

Method 3, the second alternative method for calculation of the adsorption energy, involves taking the energy difference between the lowest electronic state of the cluster-adsorbate system at equilibrium and the lowest electronic

state of the same system at a cluster-adsorbate separation of approximately 10 Å. This method yielded adsorption energies of 43.8, 36.8, 99.0, 47.1 and 64.2 kcal/mol·atom for  $\text{Be}_{19}\text{Cs}_2$ ,  $\text{Be}_{33}\text{Cs}_2$ ,  $\text{Be}_{19}\text{H}_2$ ,  $\text{Be}_{33}\text{H}_2$  and  $\text{Be}_{45}\text{H}_2$ , respectively. Relative to method 1, this method overestimates the adsorption energy of  $\text{Be}_{19}\text{Cs}_2$ ,  $\text{Be}_{33}\text{Cs}_2$ ,  $\text{Be}_{19}\text{H}_2$ ,  $\text{Be}_{33}\text{H}_2$  and  $\text{Be}_{45}\text{H}_2$  by 4.9, 15.0, 64.7, 45.9 and 46.0 kcal/mol·atom, respectively. No electronic state crossings were found for  $\text{Be}_{33}\text{H}_2$ . Consequently, methods 2 and 3 yield the same value of the adsorption energy for this cluster. Ideally, methods 1 and 3 should agree, provided that the lowest energy electronic state at both the equilibrium geometry and at infinite cluster-adsorbate separation has been found.

There are several problems inherent in using method 3. First of all, the calculations presented here all involve restricted Hartree-Fock theory, which is not generally accurate for the description of systems having geometries far from equilibrium. As was previously stated, method 3 requires calculation of the total energy for the system at a cluster-adsorbate separation of approximately 10 Å. Inspection of the gross atomic populations (GAP) for  $\text{Be}_{19}\text{Cs}_2$  at this distance reveals improper dissociation to neutral atoms. The GAP of cesium for this system should be 18, 9 electrons per Cs atom. In this case, the GAP is 17, with approximately 1/2 electron from each cesium 6s orbital being donated to the cluster. There should be no such ionization at this cluster-adsorbate separation, unless an electron is transferred from Cs to Be upon dissociation, yielding  $\text{Be}_{19}$  and  $\text{Cs} + \text{Cs}^+$ . However, dissociation to these species requires 40.1 kcal/mole more energy than dissociation to  $\text{Be}_{19} + 2 \text{Cs}$ .

RHF calculations predict a net energy gain of 18.2 and 1.2 kcal/mol upon hydrogen approach to the  $\text{Be}_{45}$  and  $\text{Be}_{33}$  surfaces, respectively. The approach of hydrogen on the  $\text{Be}_{19}$  surface, on the other hand, results in an energy gain of 34.3 kcal/mol. Cesium adsorption on both the  $\text{Be}_{19}$  and  $\text{Be}_{33}$  surfaces yields energy gains of 38.9 kcal/mol·atom and 21.8 kcal/mol·atom, respectively. Therefore, while cesium is predicted to adsorb on both  $\text{Be}_{19}$  and  $\text{Be}_{33}$  (i.e. at a hole and at a head-on site) at the SCF level of theory, hydrogen adsorbs strongly on  $\text{Be}_{19}$  and appears to adsorb moderately on  $\text{Be}_{45}$  (i.e., at a hole site) but only negligibly on  $\text{Be}_{33}$  (i.e., at a head-on site).

Table 3 contains calculated values for the ionization potentials of all the clusters studied, as well as values for the shift in ionization potential ( $\Delta\phi$ ) resulting from Cs or H adsorption. Experimentally determined values of the work functions due to Cs or  $\text{H}_2$  adsorption on Be metal are also included. Results for the  $\text{Be}_{45}$  system indicate a slight rise by 0.2 eV in the ionization potential of the cluster due to H adsorption, while results for the  $\text{Be}_{33}$  system indicate a lowering by 1.5 eV in the ionization potential of the cluster due to Cs adsorption, and no lowering due to H adsorption. The experimental findings are 2.3 and 0.0 eV lowering in the work function of Be metal due to adsorption of Cs and of  $\text{H}_2$ , respectively. Adsorption of Cs and of H on  $\text{Be}_{19}$ , however, results in ionization potential lowerings of approximately 2.0 and 1.0

Table 4  
Electron populations of  $\text{Be}_{19}$ ,  $\text{Be}_{19}\text{Cs}_2$  and  $\text{Be}_{19}\text{H}_2$

Cluster	z-coordinate <sup>a)</sup>	Atom label	No. atoms <sup>b)</sup>	Net charge per atom		Total net charge difference ([Cluster] <sup>+</sup> - Cluster)
				Cluster	[Cluster] <sup>+</sup>	
$\text{Be}_{19}$	0	BeO	1	1.43	1.41	-0.02
	$c/2$	BeA	6	-0.08	-0.07	0.06
	$c/2$	BeC	6	-0.09	0.00	0.54
	0	BeB	6	-0.07	0.00	0.42
$\text{Be}_{19}\text{Cs}_2$	0	BeO	1	1.36	1.35	-0.01
	$c/2$	BeA	6	-0.05	-0.07	-0.12
	$c/2$	BeC	6	-0.17	-0.11	0.37
	0	BeB	6	-0.14	-0.07	0.43
	$R^c)$	Cs	2	0.39	0.55	0.33
$\text{Be}_{19}\text{H}_2$	0	BeO	1	1.38	1.33	-0.05
	$c/2$	BeA	6	-0.16	-0.15	0.06
	$c/2$	BeC	6	-0.06	0.07	0.78
	0	BeB	6	-0.02	0.01	0.18
	$R^d)$	H	2	0.04	0.05	0.02

<sup>a)</sup>  $c = 3.58 \text{ \AA}$ .

<sup>b)</sup> Number of symmetry equivalent atoms.

<sup>c)</sup>  $R = 3.70 \text{ \AA}$  for Be plane to Cs distance. (Be to Cs distance is  $3.93 \text{ \AA}$ .)

<sup>d)</sup>  $R = 0.85 \text{ \AA}$  for Be plane to H distance. (Be to H distance is  $1.57 \text{ \AA}$ .)

eV, respectively. Although the first value is in close agreement with experiment, the second is not.

These discrepancies are explained using the electron populations listed in tables 4 and 5. In the case of  $\text{Be}_{19}$ , total net charge differences indicate participation in charge redistribution by both the surface (BeC, z-coordinate =  $c/2$ ) and middle (BeB, z-coordinate = 0) layers upon ionization of the cluster. In  $\text{Be}_{19}$ , ionization of the cluster results in a contribution of 0.4 electron from Be atoms (BeB) in the middle layer compared to 0.5 electron for Be atoms on the surface. Thus, the middle and surface layers of the cluster are involved almost equally in the electron ionization process. For  $\text{Be}_{19}\text{Cs}_2$ , both the surface (BeC) and middle (BeB) layers contribute 0.4 electron, while Cs donates 0.3 electron. Since electron emission is from the surface of the bulk metal, it is concluded that  $\text{Be}_{19}$  is too small a cluster to model the Be metal surface involved in Cs adsorption.

On the other hand, the middle layer of  $\text{Be}_{19}\text{H}_2$  contributes 0.2 electron, with the surface layers (BeC) being predominantly involved in ionization. H donates only a minimal amount (0.02) of charge. Part of the charge contributed by the middle (BeB) layer is shifted toward the BeC group of atoms in  $\text{Be}_{19}\text{H}_2$ . Since the greatest charge perturbation occurs on the surface, this

Table 5  
Electron populations of Be<sub>33</sub>, Be<sub>33</sub>Cs<sub>2</sub> and Be<sub>33</sub>H<sub>2</sub>

Cluster	z-coordinate <sup>a)</sup>	Atom label	No. atoms <sup>b)</sup>	Net charge per atom		Total net charge difference ([Cluster] <sup>+</sup> - Cluster)
				Cluster	[Cluster] <sup>+</sup>	
Be <sub>33</sub>	0	BeO	1	0.96	0.97	0.01
	c/2	BeA	6	0.55	0.53	-0.14
	c/2	BeC	6	-0.10	-0.07	0.14
	0	BeB	6	-0.32	-0.29	0.21
	c	BeH	12	-0.18	-0.10	0.89
	c	BeD	2	0.20	0.14	-0.11
Be <sub>33</sub> Cs <sub>2</sub>	0	BeO	1	0.94	0.93	-0.01
	c/2	BeA	6	0.57	0.52	-0.25
	c/2	BeC	6	-0.12	-0.07	0.27
	0	BeB	6	-0.34	-0.33	0.09
	c	BeH	12	-0.28	-0.22	0.67
	c	BeD	2	0.44	0.40	-0.08
	R <sup>c)</sup>	Cs	2	0.46	0.60	0.29
Be <sub>33</sub> H <sub>2</sub>	0	BeO	1	1.00	1.00	0.00
	c/2	BeA	6	0.45	0.44	-0.12
	c/2	BeC	6	-0.06	-0.04	0.12
	0	BeB	6	-0.30	-0.26	0.24
	c	BeH	12	-0.23	-0.16	0.84
	c	BeD	2	0.87	0.82	-0.10
	R <sup>d)</sup>	H	2	-0.24	-0.23	-0.02

<sup>a)</sup> c = 3.58 Å.

<sup>b)</sup> Number of symmetry equivalent atoms.

<sup>c)</sup> R = 3.77 Å for Be to Cs distance.

<sup>d)</sup> R = 1.58 Å for Be to H distance at local minimum (see text).

model appears to be adequate for the description of H adsorption. However, further analysis reveals that this is not the case. As was stated previously, the middle layer (BeB) of Be<sub>33</sub> participates appreciably (donating 0.4 electron) in the ionization process, indicating that this cluster does not reasonably model the bulk surface. Adsorption of Cs or H onto this surface, therefore, yields information about the interaction of these two species with a Be cluster, but this information cannot be interpreted as also applying to the process whereby a Cs or H atom adsorbs onto the bulk surface. Such an extension may be made only in cases where the bare cluster is a good model of the bulk metal.

Be<sub>33</sub>, a five-layer cluster, and Be<sub>45</sub>, a seven-layer cluster, appear to model the Be metal surface more appropriately. Ionization of these clusters indicates that the surface layers (BeH for Be<sub>33</sub> and BeG for Be<sub>45</sub>) donate most of the emitted electron. Although the middle layers also contribute charge, the involvement of the surface layers is three to four times as great. The adsorp-



Table 6  
Electron populations of Be<sub>45</sub> and Be<sub>45</sub>H<sub>2</sub>

Cluster	z-coordinate <sup>a)</sup>	Atom label	No. atoms <sup>b)</sup>	Net charge per atom		Total net charge difference ([Cluster] <sup>+</sup> - Cluster)
				Cluster	[Cluster] <sup>+</sup>	
Be <sub>45</sub>	0	BeO	1	1.00	1.00	0.00
	c/2	BeA	6	0.42	0.41	-0.06
	c/2	BeC	6	-0.18	-0.16	0.12
	0	BeB	6	-0.34	-0.30	0.24
	c	BeH	12	-0.18	-0.17	0.12
	c	BeD	2	1.36	1.34	-0.04
	3c/2	BeF	6	-0.14	-0.14	0.00
	3c/2	BeG	6	-0.02	0.08	0.60
Be <sub>45</sub> H <sub>2</sub>	0	BeO	1	0.99	0.98	-0.01
	c/2	BeA	6	0.43	0.41	-0.12
	c/2	BeC	6	-0.14	-0.12	0.12
	0	BeB	6	-0.36	-0.32	0.24
	c	BeH	12	-0.14	-0.13	0.12
	c	BeD	2	1.32	1.30	-0.04
	3c/2	BeF	6	-0.18	-0.18	0.00
	3c/2	BeG	6	-0.06	0.04	0.60
	R <sup>c)</sup>	H	2	0.01	0.01	0.00

<sup>a)</sup>  $c = 3.58 \text{ \AA}$ .

<sup>b)</sup> Number of symmetry equivalent atoms.

<sup>c)</sup>  $R = 0.86 \text{ \AA}$  for Be plane to H distance at local minimum (see text). Be to H distance is  $1.58 \text{ \AA}$ .

tion process, then, is represented more reasonably by using Be<sub>33</sub> or Be<sub>45</sub> rather than Be<sub>19</sub> to model the metal surface.

Table 6 shows that the surface (BeG,  $z$ -coordinate =  $3c/2$ ) layers of Be<sub>45</sub> and Be<sub>45</sub>H<sub>2</sub> are most affected during the ionization process, although the inner layers of Be<sub>45</sub>H<sub>2</sub> are also involved in ionization, their contribution is minimal compared to the charge donated by the surface (BeG) layers (0.2 versus 0.6). As with the Be<sub>19</sub> systems, some of the contributed charge is shifted toward several groups of atoms in the Be<sub>45</sub> clusters, for example, BeA ( $z$ -coordinate =  $c/2$ ). However, the largest percentage of the charge involved in ionization is donated by the BeG atoms in the surface layer. It is also interesting to note that the net charge differences for Be<sub>45</sub>H<sub>2</sub> are nearly identical to those for Be<sub>45</sub>, the only difference being 0.06 for the BeA layer. The approach of H on the Be<sub>45</sub> surface does not affect the ionization process. The same conclusion is reached from an analysis of the electron populations of Be<sub>33</sub> and Be<sub>33</sub>H<sub>2</sub>, which appear in table 5. The values of  $\Delta\phi$  appearing in table 3 are another indication that H has no effect on the Be<sub>33</sub> and Be<sub>45</sub> surfaces. The greatest shift in ionization potential occurs for the latter surface and is 0.2.  $\Delta\phi$  for Be<sub>33</sub> is practically 0. Therefore, H is not predicted to chemisorb on

the Be surface and, in fact, does not in the case of  $\text{Be}_{33}$  (the adsorption energy is 1 kcal/mol · atom). The adsorption energy of H on  $\text{Be}_{45}$ , although greater (18 kcal/mol · atom), is attributed to a local minimum since both the population analysis and  $\Delta\phi$  values indicate no effect on the  $\text{Be}_{45}$  surface due to H adsorption.

H approaches the  $\text{Be}_{33}$  surface directly above a Be atom (directly overhead site) in the present calculations. There are three other possible sites for adsorption. These are the Be-Be midpoint, eclipsed and open sites. The first has the adsorbate approaching the Be surface directly between two Be atoms located on the surface. The second involves adsorption on the center of a triangle of Be atoms located on the surface, the center of which is directly above a Be atom situated in a layer next to the surface (which is the case for  $\text{Be}_{45}$ ). The open site has the adsorbate approaching the Be surface directly above the center of a triangle of Be atoms located on the surface, directly below which there is no Be atom. According to a study by Bagus et al., the directly overhead site is the least stable for the adsorption of H onto a Be surface [19]. These adsorption energies were obtained in SCF calculations using clusters containing two to three layers.  $\text{Be}_{33}$  is a five-layer cluster and thus should yield a reasonable value for the adsorption energy associated with the directly overhead approach of an atom to the surface, while adsorption on an eclipsed site is adequately modeled by the seven-layer  $\text{Be}_{45}$  cylinder. Method 3 yields 47.1 kcal/mol · atom, while method 1 predicts only negligible adsorption for H on  $\text{Be}_{33}$ . For reasons already stated, method 1 is expected to be more accurate. Therefore, H is predicted to adsorb very weakly, if at all on  $\text{Be}_{33}$ . The lowest energy  $\text{Be}_{33}$ -H distance is 1.58 Å, which represents a local minimum since, as discussed above, H does not bind to  $\text{Be}_{33}$ . Bagus et al. reported an SCF adsorption energy of 32 kcal/mol for H on  $\text{Be}_{36}$  (a three-layer cluster with 14 atoms on the top and bottom layers and 8 atoms in the middle) and a  $\text{Be}_{36}$ -H distance of 1.38 Å [19]. These values also correspond to adsorption on a directly overhead site.

Adsorption of H on  $\text{Be}_{45}$  amounts to 18.2 kcal/mol · atom. The optimum H-to-Be-plane distance is 0.86 Å, which is also a local minimum since the electron populations of  $\text{Be}_{45}$  and  $\text{Be}_{45}\text{H}_2$  are nearly identical, indicating that H has no effect on – i.e., does not chemisorb to – the  $\text{Be}_{45}$  surface. The corresponding values for adsorption onto a  $\text{Be}_{36}$  cluster reported by Bagus et al. are 42.3 kcal/mol for the adsorption energy and 0.95 Å for the distance from H to the surface.

It is also the surface layers ( $\text{BeH}$ ) of  $\text{Be}_{33}\text{Cs}_2$  that are predominantly involved in electron removal. These layers contribute 0.7 electron, whereas the greatest charge contributed by the inner layers is 0.3. The total net charge differences of  $\text{Be}_{33}\text{Cs}_2$  differ from those of  $\text{Be}_{33}$ , indicating that Cs, unlike H, is affecting electron removal. In fact, Cs donates 0.3 electron to this process. The effects of charge redistribution resulting from ionization are greater for

the inner layers (relative to the surface layers) of  $\text{Be}_{33}\text{Cs}_2$  than for those of  $\text{Be}_{33}\text{H}_2$ . The BeC group of atoms contribute 0.3 electron, while the BeA atoms accept 0.3 electron in  $\text{Be}_{33}\text{Cs}_2$ . These amounts correspond to less than half of the charge contributed by the surface layers. In  $\text{Be}_{33}\text{H}_2$ , the greatest contribution by the inner layers is approximately one fourth of the charge contributed by the surface. The small but non-negligible involvement of the inner layers of  $\text{Be}_{33}\text{Cs}_2$  in the ionization process indicates that the discrepancy between the calculated and measured work function lowering (table 3) may be improved by treating a cluster corresponding to a larger cylinder height; for example, the 45 atom cylinder of table 1. Another possibility is the treatment of cylinders having the same height as  $\text{Be}_{33}$  or  $\text{Be}_{45}$  but a greater radius (see table 1 and fig. 1). In addition to improvements in  $\Delta\phi$ , adsorption of Cs on an eclipsed site (for example, Be45) is predicted to be more stable. Unlike the head-on site, this position allows the Cs to interact more closely with the surface triangles of Be since there is no center atom present.

It is noted that the present study contains certain constraints and assumptions. First, no geometry relaxation was attempted for the Be clusters. Although the Be-adatom distances were optimized, the full  $D_{3h}$  symmetry of the cluster was maintained, and the Be-Be distances were held fixed at the experimental lattice constants of Be metal. For clusters of this size, it is probable that the optimum geometry may not match precisely that of the bulk metal. Surface geometries do not generally match the corresponding bulk lattice constants. Most materials are known to experience some degree of reconstruction at the surface due to the bending of outward-directed (from the surface) unpaired orbitals. Second, adsorption of Cs and of H was modeled using only one atom above the top and bottom layers of the cluster. Since the shift in the work function of Be metal depends on the degree of surface coverage [3], the results may be altered by adsorption of more than one atom of Cs or H on each cluster.

Third, the calculations do not include electron correlation effects. As previously mentioned, all low-lying electronic states of each cluster were studied. Several of these states were nearly degenerate (within 0.1 eV), making a reordering of states possible upon inclusion of electron correlation. Such effects may be accounted for, at least in part, through the use of local-density-functional approaches. These methods replace the exchange terms in the Hartree-Fock equations by spherical potentials, otherwise known as muffin-tin potentials, through which some electron correlation corrections are introduced into the system. Metal surfaces such as that of tungsten have been studied using these approaches [20]. However, the results presented here are *ab initio*, unlike those obtained using density-functional theory. Furthermore, correlation energy cancellation is expected between the neutral and cationic cluster systems. Although this cancellation is not complete because the neutral system contains a greater number of electrons, the clusters treated here are large enough (e.g.,  $\text{Be}_{33}\text{Cs}_2$  contains 84 electrons) so as to minimize this error.

Fourth, the valence basis sets used in this study were not complete. Additional p-type functions, as well as d-type GTF's may alter the computed adsorption energies to some degree. Finally, no periodic boundary conditions were imposed on the clusters, making the results dependent on cluster size.

Despite these conditions, the work presented here provides useful information about the adsorption process, including a detailed analysis of the nature of the interactions at the surface, the latter of which cannot be obtained via experiment alone. All of the theoretical results are calculated using fully ab initio procedures; that is, no experimental parameters were used, no integrals were approximated and all terms in the Hamiltonian were retained. Relativistic effects for cesium were incorporated into the calculations through the ab initio effective core potential. Despite the neglect of periodic boundary conditions, the clusters used to model the Be surface were large, containing three layers, five layers and seven layers in the case of  $\text{Be}_{19}$ ,  $\text{Be}_{33}$  and  $\text{Be}_{45}$ , respectively. Energies for numerous low-lying electronic states were studied.

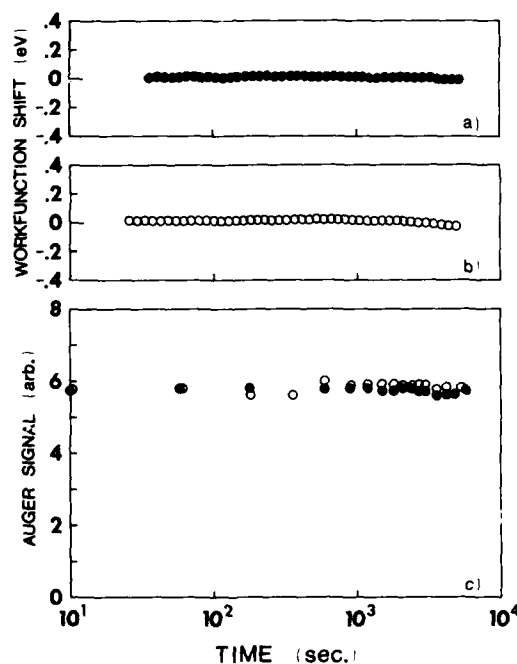


Fig. 4. (a) The work function shift of sputter cleaned Be in time exposed to the residual gas in the chamber ( $7.6 \times 10^{-11}$  Torr). (b) The work function shift of sputter cleaned Be exposed to  $\text{H}_2$  ( $2.0 \times 10^{-8}$  Torr) at  $t = 50$  s. (c) The change in sputter cleaned Be AES signal in time upon exposure to the residual gas ( $7.6 \times 10^{-11}$  Torr) in the chamber (dark curve) and upon exposure to  $\text{H}_2$  ( $3.0 \times 10^{-8}$  Torr).

The states were chosen by analyzing the highest occupied and lowest unoccupied molecular orbitals. Finally, independent SCF calculations were used to determine the ionization potentials of the clusters in addition to the use of Koopmans' theorem.

The experimental findings of Cs adsorption on Be have been presented and discussed elsewhere [3]. Exposure of the surface to  $H_2$  yielded no observable change. That is, the Be substrate Auger signal was not attenuated and there was no discernable work function shift. Typical results are shown in fig. 4. In curve a, the change in the work function with time is shown for sputter cleaned polycrystalline Be exposed to the residual gases in the chamber at  $7.6 \times 10^{-11}$  Torr. Curve b corresponds to the same sample with the exception that at time  $t = 50$  s,  $H_2$  was let into the chamber at  $2.0 \times 10^{-8}$  Torr. This corresponds to a flux of  $3 \times 10^{13}$  molecules/cm<sup>2</sup> · s at room temperature. No change in the work function was seen for a period in excess of  $10^3$  s, corresponding to a fluence greater than  $3 \times 10^{16}$  molecules/cm<sup>2</sup>. Curve c shows the Be (104 eV) Auger electron signal for a sample first sputter cleaned and exposed to the residual gases in the vacuum (solid symbol curve) and for the same sample sputter cleaned in and maintained in  $H_2$  at  $3 \times 10^{-8}$  Torr.

#### 4. Conclusions

Analysis of the Mulliken populations for  $Be_{19}$  indicates that this cluster is too small to model the bulk surface. However, the population analyses for  $Be_{33}$  and  $Be_{45}$  indicate that these clusters are adequate models of the Be metal surface. The adsorption energy of Cs on  $Be_{33}$  is calculated as 21.8 kcal/mol · atom. The decrease in the ionization potential of  $Be_{33}Cs_2$  relative to  $Be_{33}$  is calculated to be 1.5 eV. The experimental work function lowering resulting from Cs adsorption is measured as 2.3 eV [3]. The adsorption energies of H on  $Be_{33}$  and  $Be_{45}$  are 1 and 18 kcal/mol · atom, respectively. The first value is negligible, while the latter is attributed to a local minimum since Mulliken population analysis and  $\Delta\phi$  values for both  $Be_{33}$  and  $Be_{45}$  indicate no effect on these clusters due to H adsorption. Experiment reveals no adsorption of  $H_2$  on Be metal, thus ruling out dissociative chemisorption.

#### Acknowledgments

This research was supported in part by the National Science Foundation under grant No. CHE-8712315, which included supercomputer time at the Pittsburgh Supercomputing Center, and by the Air Force Office of Scientific Research. The Newark Remote Access Center and the New Jersey Commission on Science and Technology are acknowledged for providing computing

equipment and network access to Pittsburgh. We thank N.W. Winter and J.M. Powers for their assistance and advice regarding the construction of the figures.

## References

- [1] L.W. Swanson and R.W. Strayer, *J. Chem. Phys.* 48 (1968) 2421.
- [2] R.E. Weber and W.T. Peria, *Surface Sci.* 14 (1969) 13.
- [3] G.S. Tompa, M. Seidl, W.C. Ermler and W.E. Carr, *Surface Sci.* 185 (1987) L453.
- [4] J. Rubio, F. Illas and J.M. Ricart, *J. Chem. Phys.* 84 (1986) 3311.
- [5] G. Pacchioni, W. Pewesdorf and J. Kouter'y, *Chem. Phys.* 83 (1984) 201.
- [6] C.W. Bauschlicher, D.H. Liskow, C.F. Bender and H.F. Schaefer III, *J. Chem. Phys.* 62 (1975) 4815.
- [7] C.W. Bauschlicher, *Chem. Phys. Letters* 117 (1985) 33.
- [8] R.B. Ross, W.C. Ermler, C.W. Kern and R.M. Pitzer, *Chem. Phys. Letters* 134 (1987) 115; W.C. Ermler, R.B. Ross, C.W. Kern, R.M. Pitzer and N.W. Winter, *J. Phys. Chem.* 92 (1988) 3042.
- [9] R.G. Wyckoff, *Crystal Structures*, 2nd ed. (Interscience, New York, 1974).
- [10] R.M. Pitzer, *J. Chem. Phys.* 58 (1973) 3111; private communication.
- [11] W.C. Ermler, C.W. Kern, R.M. Pitzer and N.W. Winter, *J. Chem. Phys.* 84 (1986) 3937.
- [12] R.B. Ross, T. Atashroo, J.M. Powers, W.C. Ermler, L.A. LaJohn and P.A. Christiansen, to be published.
- [13] T.H. Dunning, Jr., *J. Chem. Phys.* 53 (1970) 2823; 55 (1971) 3958.
- [14] P.A. Christiansen, W.C. Ermler and K.S. Pitzer, *Ann. Rev. Phys. Chem.* 36 (1985) 407; W.C. Ermler, R.B. Ross and P.A. Christiansen, *Advan. Quantum Chem.* 19 (1988) 139.
- [15] R.S. Mulliken, *J. Chem. Phys.* 23 (1955) 1833.
- [16] G.S. Tompa, W.E. Carr and M. Seidl, *Surface Sci.* 198 (1988) 431.
- [17] A.G. Knapp, *Surface Sci.* 34 (1983) 289.
- [18] F.H. Haayes, M.F. Hill, S.M.A. Lecchini and B.A. Pethica, *J. Chem. Phys.* 42 (1965) 2919.
- [19] P.S. Bagus, H.F. Schaefer and C.W. Bauschlicher, *J. Chem. Phys.* 78 (1983) 1390.
- [20] S. Ohnishi, A.J. Freeman and E. Wimmer, *Phys. Rev. B* 29 (1984) 5267.

# Reflection of hydrogen atoms from metal and semiconductor targets

S. T. Melnychuk, M. Seidl, W. Carr, J. Isenberg, and J. Lopes

Department of Physics/Engineering Physics, Stevens Institute of Technology, Hoboken, New Jersey 07030

(Received 8 September 1988; accepted 12 December 1988)

Partially cesiated Si and Mo targets have been exposed to a flux of atomic hydrogen produced by thermal dissociation of hydrogen gas on a heated tungsten mesh. Hydrogen atoms in the tail of the distribution are elastically reflected from the surface, and some fraction are negatively ionized by electron transfer from the surface. The  $H^-$  energy distributions and the ion yields have been measured. The backscattered  $H^-$  ions have a Maxwellian energy distribution with a temperature equal to the atomic gas temperature. The ion yield depends exponentially on the inverse temperature of the gas. The highest measured yield is  $\sim 0.01$  for  $T = 0.21$  eV on Si. Monte Carlo calculations of the ionized and neutral fractions using the probability model of Rasser *et al.* are in good qualitative agreement with experimental results. Calculations show that most  $H^-$  ions formed near the surface do not have enough kinetic energy to overcome the potential barrier due to the image charge interaction.

## I. INTRODUCTION

Surface production of negative hydrogen ions at escape energies below 1 eV has not been studied in any detail. This is in contrast to numerous experiments carried out in the energy range above a few eV where production of  $H^-$  ions was studied by backscattering of energetic protons from alkali and metal targets,<sup>1-9</sup> and in surface conversion-type sources where  $H^-$  production is due to both ion impact desorption and backscattering of primary ions.<sup>10-14</sup> Backscattering of thermally produced hydrogen atoms from low work function surfaces offers a technique suitable for studies of  $H^-$  formation at low energies.

The production of  $H^-$  ions by backscattering of thermal hydrogen atoms from cesiated surfaces was first observed by Graham.<sup>15</sup> Pargellis and Seidl<sup>16</sup> measured the yield of  $H^-$  ions and electrons for backscattering of thermal hydrogen atoms from thick cesium targets.

Theoretical models for the ionization probability of atoms scattered from metal targets have been developed.<sup>17-23</sup> These theories relate the ionization probability of the incident atom to the target work function, the atomic velocity, and the position and width of the affinity level. Good agreement between calculated and measured ionization probabilities have been obtained for incident atomic energies above 10 eV. We have adapted the probability model of Rasser *et al.*<sup>20</sup> to the case where trapping of low-energy incident atoms is significant.

Understanding the mechanism for the formation of  $H^-$  ions at low energies is of practical significance in explaining the observed  $H^-$  yields from surface conversion- and volume-type sources. Analysis of the atomic and molecular hydrogen densities present in volume sources indicates that a significant fraction of the neutral particle density is atomic hydrogen.<sup>24</sup> Recently experiments carried out at Lawrence Berkeley Laboratory have shown that the addition of cesium vapor to their multicusp  $H^-$  ion source resulted in a 16-fold increase in the extracted  $H^-$  ion current.<sup>25</sup> They conclude that a possible production mechanism may be backscattering from the cesiated chamber walls.

In this experiment we have studied backscattering of thermal hydrogen atoms from partially cesiated polycrystalline Mo and *n*- and *p*-type (100) Si targets. We have measured parallel energy distributions and the average ionization probability as a function of average atomic energy. The dominant effect in the low-energy reflections is trapping of  $H^-$  ions by the image force.

## II. EXPERIMENTAL APPARATUS

The experimental apparatus is shown in Fig. 1. It consists of a vacuum system, a planar diode, a rotating magnetic sector mass spectrometer, a tungsten mesh atomic hydrogen source, an atomic beam hydrogen oven, a neutral Cs oven,<sup>26</sup> and a HeNe laser. This apparatus has been described in detail elsewhere.<sup>27,28</sup> The only major change in the apparatus is

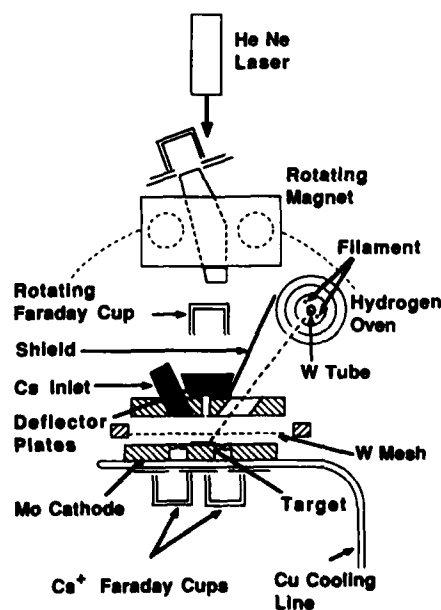


FIG. 1. Experimental apparatus.

the addition of the atomic beam hydrogen oven to be used in future experiments.

The production rate of atomic hydrogen by thermal dissociation of molecular hydrogen on a hot tungsten filament is calculated from the theory of Hickmott.<sup>29</sup>

The surface concentration,  $n$  (#/cm<sup>2</sup>), of hydrogen molecules on the hot filament is determined by the balance between the rate of adsorption of molecular hydrogen from the gas phase, and the rates of desorption of molecular and atomic hydrogen from the filament.

The isothermal evaporation rates of molecular and atomic hydrogen are given by the expression:  $dn/dt = -k_i n^i$  ( $i = 1, 2$  corresponds to atomic and molecular hydrogen, respectively). The constants  $k_i$  are given by the expression  $k_i = \nu_i \exp(\Delta H_i / RT)$  where  $\Delta H_i$  is the activation energy for the desorption process, and  $T$  is the mesh temperature. We have used values of  $\nu_1 = 2.2 \times 10^{13} \text{ s}^{-1}$ ,  $\Delta H_1 = 67 \text{ kcal}$ , and  $\nu_2 = 5 \times 10^{-3} \text{ s}^{-1}$ ,  $\Delta H_2 = 31 \text{ kcal}$ .<sup>29</sup> The rate of adsorption of molecular hydrogen from the gas phase is given by:  $dn/dt = \Phi(H_2)s$ , where  $\Phi(H_2) = p(2\pi m_2 k T_0)^{-1/2}$  is the impingement flux density,  $s = 0.07$  is the sticking coefficient of molecular hydrogen on tungsten,<sup>30</sup> and the temperature  $T_0$  is taken as the chamber wall temperature. Combining the expressions for the evaporation and adsorption rates of atomic and molecular hydrogen and using the condition  $dn/dt = 0$  at steady state, the rate of evaporation of atomic hydrogen from the hot tungsten surface is given by the equation:

$$k_1 n = k_1 / 2k_2 \{ -k_1 + [k_1^2 + 4\Phi(H_2)sk_2]^{1/2} \}. \quad (1)$$

The impingement flux density of atomic hydrogen on the target is calculated from the formula

$$\Phi(H) = k_1 n (1 - t), \quad (2)$$

where  $t = 0.745$  is the transmission coefficient of the tungsten mesh.

### III. EXPERIMENTAL PROCEDURE

For each of the targets tested we measured the dependence of the  $H^-$  yield and energy distributions on mesh temperature, hydrogen pressure, cesium flux, and target voltage.

The basic operation of the experiment is as follows: We select the target voltage, mesh temperature, and hydrogen pressure. Under these conditions we obtain an optimum coverage of Cs on the target surface by varying the Cs oven temperature and the target temperature. The target work function is monitored by the photoelectric current produced by the HeNe laser beam (photon energy 1.96 eV). The optimum coverage is reached when the photoelectric current reaches a maximum. Since the target is continuously bombarded with a flux of  $Cs^+$  ions we operate the experiment at target voltages below 150 V, or at very low  $Cs^+$  ion current densities where the  $H^-$  sputter yield is negligible.<sup>27,28</sup>

The Si samples tested were sputter cleaned at 750 V with  $Cs^+$  ion doses on the order of  $10^{17}$  ions/cm<sup>2</sup> in order to optimize the photo signal and the  $H^-$  yield. The optimum photoelectric signal increases by two orders of magnitude after sputter cleaning. The growth in the photoelectric signal

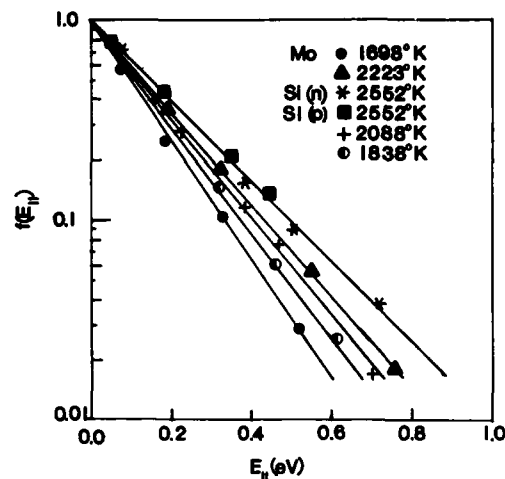


FIG. 2. Parallel energy distributions of  $H^-$  ions obtained from Mo,  $n$ - and  $p$ -type Si targets for several mesh temperatures. The parallel energies at  $f(E) = 1/e$  show that the ion temperatures are equal to the atomic hydrogen/mesh temperatures.

after cleaning is most likely due to the removal of an  $SiO_2$  overlayer not removed by the chemical etching. Large increases in the photoelectric yield after sputter cleaning of  $SiO_2$  covered Si have been observed by Allen and G'belli.<sup>31</sup> They conclude that thin oxide films (from 10 to 30 Å) on Si can trap up to 94% of the incident photoelectrons.

The maxima for the photoelectric current and the  $H^-$  current occur at the same target temperature for each of the targets tested. This confirms that the maximum negative ion yield occurs at the minimum work function.

### IV. ENERGY DISTRIBUTIONS AND $H^-$ YIELDS

The angular dependence of the  $H^-$  current density is measured with the rotating magnet. The angular distribution  $I(\theta)$  is a plot of the current measured by the magnetic mass spectrometer as a function of the exit angle  $\theta$ . For a planar diode geometry we can relate the angular distribution to the parallel energy distribution by the relation<sup>27</sup>:  $\tan^2 \theta = E_p / U$ , where  $E_p$  is the ion energy parallel to the target surface and  $U$  is the accelerating voltage. Figure 2 shows normalized distributions for several different mesh temperatures with the Mo and Si targets. The  $H^-$  ions clearly have a Maxwellian energy distribution,  $f(E_p) = \exp(-E_p/kT)$  with a temperature equal to the mesh temperature. Since the targets are approximately at room temperature these results show that the fast hydrogen atoms are reflected from the target in elastic collisions.

We define the negative ion yield as  $\beta = \Phi(H^-) / \Phi(H)$  where  $\Phi(H^-)$  is the measured flux density of the  $H^-$  ions and  $\Phi(H)$  is the flux density of the incident hydrogen atoms calculated from Eq. (2). The yield  $\beta$  is also the ionization probability averaged over the Maxwellian distribution of the incident atoms.

We calculate  $\Phi(H^-)$  by integrating the  $H^-$  angular distribution  $I(\theta)$  to obtain the total  $H^-$  ion current leaving the



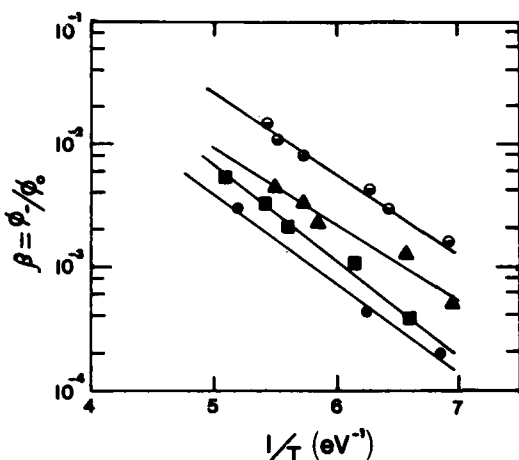


FIG. 3.  $H^-$  yields as a function of the mesh temperature: (●) polycrystalline Mo target; (■)  $n$ -type (100) Si; (▲)  $p$ -type (100) Si targets sputter cleaned at 750 V and  $Cs^+$  ion current densities  $\sim 50$ – $90 \mu A/cm^2$ ; and (◊)  $n$ -type (100) Si target (Ref. 21) sputter cleaned at 100 V and low  $Cs^+$  ion current densities  $\sim 7 \mu A/cm^2$ .

exit aperture and dividing this current by the area ( $A_e$ ) of the exit aperture.

Figure 3 shows the yield as a function of inverse temperature for the Mo and Si targets. The yield depends exponentially on the inverse temperature,  $\beta \sim \exp(-A/kT)$  where  $A$  is a constant. The measured yields from the  $p$  and  $n$  doped targets differ by  $\sim 22\%$  at 0.2 eV. Also shown in Fig. 3 are yields measured by Seidl *et al.*<sup>28</sup> for  $n$ -type Si not subject to large ion bombarding doses. In all cases the yields from the Si targets are larger than from the Mo target. We attribute the difference between the yield measurements of Seidl *et al.* and our results to differences in the cleaning procedure. Our samples were cleaned at 750 V and  $50$ – $90 \mu A/cm^2$  while those of Seidl *et al.* were bombarded at 100 V and  $\sim 7 \mu A/cm^2$ . The role of surface structure in the charge exchange process is not clearly understood yet. Van Bommel *et al.*<sup>5</sup> obtained a  $H^-$  conversion efficiency from cesiated polycrystalline  $W$  a factor of 3 lower than from cesiated monocrystalline (110)  $W$  targets. They concluded that the differences between the two targets could not be explained theoretically on the basis of differing work functions only. The effect of ion bombardment on the yields is currently under investigation.

Figure 3 shows that only a small fraction ( $\sim 1\%$ ) of the incident atoms are reflected as  $H^-$  ions. The remaining atoms are either reflected as neutrals or are trapped as negative ions near the surface of the target. The trapped ions eventually recombine into hydrogen molecules or chemically react with the target. These reactions are accompanied by electron emission. Pargellis and Seidl<sup>16</sup> observed about 100 times more electrons than  $H^-$  ions in backscattering of hydrogen atoms from a thick Cs target (work function 2.1 eV). In the present experiments the electron current is of the same order of magnitude as the  $H^-$  ion current. Theoretical calculations of  $H^-$  yields including the effects of trapping are discussed in the following section.

## V. THEORY

There have been earlier calculations of  $H^-$  ion formation due to atomic hydrogen reflection.<sup>17–20</sup> The calculations assume that ions leave the surface at constant velocity, which is valid for a kinetic energy large compared to the potential, or surface binding energy. They agree reasonably well with proton beam reflection experiments<sup>1–9</sup> where kinetic energies are at least a few eV, but some modification is needed to apply these ideas to thermal atomic hydrogen at a few tenths of an eV.

Here we use a Monte Carlo calculation to integrate over the thermal distribution. We take the main features of the probability model,<sup>19,20</sup> with simplifying approximations since the Monte Carlo integration is insensitive to the details.

The potential energy of a negative charge near a conducting surface can be approximated by the image potential. The classical formula is a good approximation for distances not too near the surface. Estimates of the critical distance vary but it is always a few Bohr radii. Because we have a negative charge on the hydrogen ion we must include the binding energy (electron affinity)  $A = 0.75$  eV. The potential energy of the  $H^-$  ion as a function of the distance  $z$  from the surface is given by

$$U(z) = -A - (e^2/4\pi\epsilon_0)\{1/[4(z+b)]\}, \quad (4)$$

where  $b$  is a screening distance which we have taken to be 3.2 Bohr radii from van Amersfoort *et al.*<sup>9</sup> Deviations from this potential very close to the surface ( $< 3$  Bohr radii),<sup>32</sup> and the effect of the composite Cs/substrate potential<sup>17</sup> have been ignored in this approximation. This potential is used in calculating the crossing distance  $Z_c$  where the hydrogen affinity level crosses the Fermi level. Equation (4) is also used to conserve energy so that the change in the perpendicular ion velocity may be determined as it moves away from the surface.

The probability model<sup>19,20</sup> determines the electronic activity. The motion of the atom is treated classically so that the quantum electron dynamics are calculated at a fixed position of the H atom. Two quantities are needed for the calculation. First, the charge state of an atom at a fixed distance  $z$  has been determined.<sup>9</sup> For a cesiated metal with 0.5 monolayers of hydrogen adsorbed, the probability that the atom is negative is very near unity inside the crossing distance, and near zero outside. This is only true if the atom is held fixed for a long time. This result is not unreasonable since for  $z < Z_c$  the atom is ionized by electron transfer from filled states below the Fermi level, and for  $z > Z_c$  a negative ion is neutralized by electron transfer to vacant states above the Fermi level.

The rate  $\omega(z)$  at which electron transfer between the atom and the solid occurs has been calculated. This may be approximated by

$$\omega(z) = \omega_0 \exp(-\alpha z), \quad (5)$$

where  $z$  is the distance from the surface, and  $\omega_0$  and  $\alpha$  are constants. This approximation is valid for distances greater than a few Bohr radii from the surface.

Using these ideas the ionized fraction may be estimated by the rate equation:

$$dP/dt = \omega(z) [\theta(z - Z_c) - P], \quad (6)$$

where  $P$  is the probability that the atom is a negative ion.  $\theta(z)$  is the Heaviside step function which approximates the equilibrium charge state of a fixed atom.

In previous work<sup>19,20</sup> Eq. (6) was integrated using a constant velocity. This is reasonable if the atom's kinetic energy is larger than the height of the potential barrier. In our case hydrogen atoms produced by thermal dissociation have a temperature of a few tenths of an eV. Typical kinetic energies are smaller than the depth of the potential well and the velocity cannot be considered constant.

We have integrated the rate Eq. (6) using the potential given by Eq. (4) to determine the kinetic energy at each point. The results are shown in Fig. 4. This figure shows the probability for ionization as a function of the distance for several initial energies. Atoms with the smallest energies have a very high likelihood of being ionized because they spend a long time near the surface, but they do not have enough kinetic energy to get over the potential barrier. The atoms with just enough energy to escape are slow and are likely to be ionized, but they are also likely to be neutralized outside  $Z_c$ . The faster ions have a lower probability for ionization. The curves in Fig. 4 are only approximate since the kinetic energy changes with distance only for an ion, and because the point of ionization is a random process; they do, however, show an important feature. Most ions formed near the surface do not have enough kinetic energy to escape, and hence are trapped. This shows in an approximate way the dynamics of ionic chemisorption.

The Monte Carlo calculation determines the ionized fraction of a thermal distribution as follows. An atom is placed near the surface and assigned an initial speed  $u$  from a Gaussian random number generator with the appropriate spread. This atom is moved in constant steps  $dz$ . At each step a number  $R$  is assigned from a uniform random number generator in the interval (0,1). If  $R < \omega(z)dz/u$  then ionization took place. Once ionized it is assumed that the atom cannot be neutralized inside  $Z_c$  since there are no vacant states in the solid at that energy. The ion is then moved to  $Z_c$  and the kinetic energy is reduced by the change in potential energy. If the resulting kinetic energy is negative the ion is counted as trapped. Atoms that reach  $Z_c$  without being ionized are

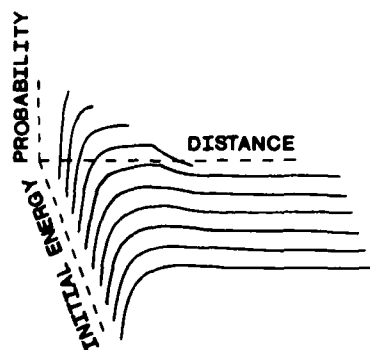


FIG. 4.  $H^-$  ionization probability as a function of distance. The largest initial energy corresponds to 1.6 times the potential energy depth.

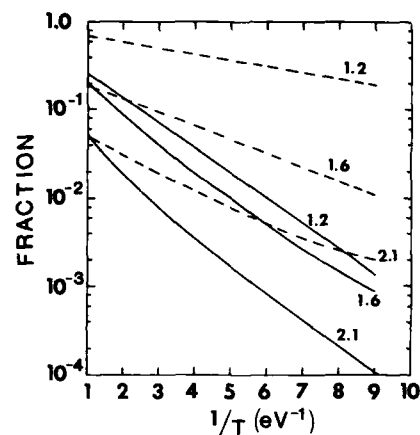


FIG. 5. Theoretical calculation of neutral (dashed line) and ionized (solid line) fractions as a function of energy for several different work functions (eV).

counted as escaping atoms.

Ions that reach  $Z_c$  untrapped are moved in steps of  $dz$ , but the expression  $R < \omega(z)dz/u$  is used to determine whether the ion is neutralized. Those that are neutralized are counted as escaping atoms. Slow enough ions can be trapped outside of  $Z_c$ , and these are added to the trapped count. Finally ions that survive at a large distance are counted as collected ions.

The results of this calculation are shown in Fig. 5. This figure shows the ionized fraction and the neutral fraction as a function of inverse temperature for several values of the work function. Since the sum of the ionized, neutral, and trapped fractions is unity, it is clear that the trapped fraction is large. The dependence of the ion fraction on temperature and work function is in good qualitative agreement with the experimental results.

This simple model works reasonably well because it is in effect an integration of a stochastic process. The important quantities are the scale length for electron transitions, the crossing point, and the ratio of the temperature to the image potential well depth.

## VI. CONCLUSION

$H^-$  ions produced by backscattering of thermal hydrogen atoms from surfaces have an average parallel energy equal to the incident atomic temperature. This implies that the atoms are elastically scattered from the surface.

The  $H^-$  yields depends exponentially on the reciprocal atomic temperature. On average yields from cesiated Si targets are several times larger than for cesiated Mo targets. Backscattering yields from heavily ion bombarded  $n$ - and  $p$ -type Si targets are approximately equal. Theory indicates that yields in excess of 0.1 can be achieved for atomic temperatures  $\sim 0.5$  eV and work functions of  $\sim 1.2$  eV.

The basic limitation of  $H^-$  production at low incident energies is trapping of  $H^-$  ions by the image force.

## ACKNOWLEDGMENTS

We wish to thank George Wohlrab for many helpful technical suggestions in designing the experimental apparatus

and for machining most of the apparatus. This work is supported by the U.S. AFOSR.

- <sup>1</sup>W. Eckstein, H. Verbeek, and R. S. Bhattacharya, *Surf. Sci.* **99**, 356 (1980).
- <sup>2</sup>J. R. Hiskes and P. J. Schneider, *Phys. Rev. B* **23**, 949 (1981).
- <sup>3</sup>J. N. M. van Wunnick, J. J. C. Geerlings, and J. Los, *Surf. Sci.* **131**, 1 (1983).
- <sup>4</sup>J. N. M. van Wunnick, J. J. C. Geerlings, E. H. A. Granneman, and J. Los, *Surf. Sci.* **131**, 17 (1983).
- <sup>5</sup>P. J. M. van Bommel, J. J. C. Geerlings, J. N. M. van Wunnick, P. Massmann, E. H. A. Granneman, and J. Los, *J. Appl. Phys.* **54**, 5676 (1983).
- <sup>6</sup>P. J. Schneider, K. H. Berkner, W. G. Graham, R. V. Pyle, and J. W. Stearns, *Phys. Rev. B* **23**, 941 (1981).
- <sup>7</sup>P. W. van Amersfoort, J. J. C. Geerlings, L. F. Tz. Kwakman, A. Hershco-vitch, E. H. A. Granneman, and J. Los, *J. Appl. Phys.* **58**, 3566 (1985).
- <sup>8</sup>P. W. van Amersfoort, J. J. C. Geerlings, R. Rodnik, E. H. A. Granneman, and J. Los, *J. Appl. Phys.* **59**, 241 (1986).
- <sup>9</sup>P. W. van Amersfoort, *Formation of Negative Ions on a Metal Surface* (FOM, Amsterdam, The Netherlands, 1987).
- <sup>10</sup>K. Wieseman, K. Prelec, and Th. Sluyters, *J. Appl. Phys.* **48**, 2668 (1977).
- <sup>11</sup>K. N. Leung and K. W. Ehlers, *J. Appl. Phys.* **52**, 3905 (1981).
- <sup>12</sup>K. N. Leung and K. W. Ehlers, *Rev. Sci. Instrum.* **53**, 803 (1982).
- <sup>13</sup>M. Wada, R. V. Pyle, and J. W. Stearns, *AIP Conf. Proc.* **111**, 247 (1984).
- <sup>14</sup>P. J. M. van Bommel, K. N. Leung, and K. W. Ehlers, *J. Appl. Phys.* **56**, 751 (1984).
- <sup>15</sup>W. G. Graham, *Phys. Lett.* **73A**, 186 (1979).
- <sup>16</sup>A. Pargellis and M. Seidl, *Phys. Rev. B* **25**, 4356 (1982).
- <sup>17</sup>J. R. Hiskes and A. M. Karo, in *Proceedings of the Symposium on Production and Neutralization of Negative Hydrogen Ions and Beams*, (Brookhaven National Laboratory, Upton, NY, 1977), p. 42.
- <sup>18</sup>J. R. Hiskes, *J. Phys. (Paris)* **40**, 179 (1979).
- <sup>19</sup>E. G. Overbosch, B. Rasser, A. O. Tenner, and J. Los, *Surf. Sci.* **92**, 310 (1980).
- <sup>20</sup>B. Rasser, J. N. M. van Wunnick, and J. Los, *Surf. Sci.* **118**, 697 (1982).
- <sup>21</sup>R. Bracko and D. M. News, *Surf. Sci.* **108**, 253 (1981).
- <sup>22</sup>N. D. Lang, *Phys. Rev. B* **27**, 2019 (1983).
- <sup>23</sup>J. P. Gauyacq and J. J. C. Geerlings, *Surf. Sci.* **182**, 245 (1987).
- <sup>24</sup>M. Bacal, M. Capitelli, C. Gorse, and O. A. Skinner, in *Proceedings of the Third European Workshop on Production and Application of Light Negative Ions*, edited by H. Hopman and W. van Amersfoort (FOM, Institute for Atomic and Molecular Physics, Amsterdam, The Netherlands, 1988), p. 112.
- <sup>25</sup>S. R. Walther, K. N. Leung, and W. B. Kunkel, *J. Appl. Phys.* (submitted).
- <sup>26</sup>G. S. Tompa, J. L. Lopes, and G. S. Wohlrab, *Rev. Sci. Instrum.* **58**, 1536 (1987).
- <sup>27</sup>J. L. Lopes, J. A. Greer, and M. Seidl, *J. Appl. Phys.* **60**, 17 (1986).
- <sup>28</sup>M. Seidl, W. E. Carr, J. L. Lopes, and S. T. Melnychuk, in Ref. 24, p. 157.
- <sup>29</sup>T. W. Hickmott, *J. Chem. Phys.* **32**, 810 (1960).
- <sup>30</sup>P. W. Tamm and L. O. Schmidt, *J. Chem. Phys.* **55**, 4253 (1971).
- <sup>31</sup>F. G. Allen and G. W. Gobelli, *J. Appl. Phys.* **35**, 597 (1964).
- <sup>32</sup>N. O. Lang and A. R. Williams, *Phys. Rev. Lett.* **34**, 531 (1975).

# Electronic surface changes induced in silicon by hydrogen, oxygen, and cesium coverages

A. E. Souzis, M. Seidl, W. E. Carr, and H. Huang

*Physics/Engineering Physics Department, Stevens Institute of Technology, Hoboken, New Jersey 07030*

(Received 8 September 1988; accepted 28 November 1988)

The electronic surface state changes for low-energy cesium ion deposition, oxygen, and hydrogen adsorption on Si(100) are investigated. The change in surface potential (work function) is probed by electron reflection. This shift is then calibrated using photoemission onset measurements. The surface states are examined using ultraviolet photoemission spectroscopy (UPS). Results indicate that low work function surfaces attained previously by cesium and oxygen vapor deposition techniques are also attainable by ion bombardment. Results of work function and UPS measurements of atomic hydrogen adsorption are consistent with an asymmetric dimer model for the clean Si(100) surface. Atomic hydrogen adsorption on a cesiated and oxygenated surface has little effect on the work function, indicating that these surfaces may be viable in an actual dynamic negative hydrogen ion source.

## I. INTRODUCTION

The electronic and structural properties of semiconductor surfaces are governed to a great extent by surface adsorbates and implanted species. Cesium coatings, whether formed by adsorption or by implantation, lower the surface work function,<sup>1,2</sup> and are thus of great interest for use as high-efficiency electron emitters or negative ion sources. Particularly interesting are effects due to hydrogen and oxygen exposure. Oxygen adsorption on cesiated silicon can lead to a surface with a very low work function.<sup>3,4</sup> The effects of hydrogen adsorption on these surfaces is of great interest in the field of negative hydrogen ion converter surfaces. While it is clearly possible to produce very low work function surfaces, the ability to maintain them in a dynamic situation remains unclear. This paper addresses the preparation of these surfaces and the electronic surface changes associated with them.

## II. EXPERIMENTAL DETAILS

All experiments were performed in an ultrahigh vacuum system, with a base pressure of  $4 \times 10^{-11}$  Torr. The target wafer is *n*-type Si(100), with a resistivity of 5 to 9  $\Omega$  cm. It is mounted on an *xyz* manipulator with both azimuthal rotation and sample tilt. The manipulator is also equipped for electron beam (e-beam) heating and liquid-nitrogen (LN<sub>2</sub>) cooling of the target. A thermocouple is available for monitoring the sample temperature while performing various experiments. The sample can be rotated to any of seven different experimental stations. These are (i) A low-energy electron gun for determining the work function shift, (ii) dual (Cs<sup>+</sup> and H<sup>+</sup>) ion guns for sample bombardment, (iii) a hot filament for coating the sample with atomic hydrogen, (iv) a low-energy (5–50 eV) Cs<sup>+</sup> ion source, also used for coating, (v) a window, used for admittance of a tunable light source for calibration of the work function shifts, (vi) an ultraviolet photoelectron spectrometer (UPS) for investigation of surface energy states, and (vii) a PHI Auger electron spectrometer (AES) for detection of surface atoms. Both the UPS and the AES use a double-pass, angular resolved cylindrical mirror analyzer (CMA) for electron energy analysis. Experimental control and data acquisition are ac-

complished with an Apple II + microcomputer. A schematic of the experimental arrangement is shown in Fig. 1.

The target is cut from a commercial wafer and cleaned before placing it into vacuum. First, it is rinsed in a hot solvent such as xylene. Then the top few layers are chemically removed by etching the target in a solution of HF:H<sub>2</sub>O = 1:50 by volume. After placing the sample in vacuum, an Auger scan shows that the target is covered with a thick oxide layer. This layer is then removed by sputtering with the Cs<sup>+</sup> source, typically at 500 eV and 0.5  $\mu$ A/cm<sup>2</sup>, followed by heating of the sample to 850 °C to remove the cesium and anneal the wafer. Auger scans afterwards show the surface to be oxide and contaminant free. The sample is monitored for contamination with the AES, and no observable increase is seen within the amount of time necessary (~1 h) to complete a given experimental run. A clean silicon wafer is seen with AES to remain in the background

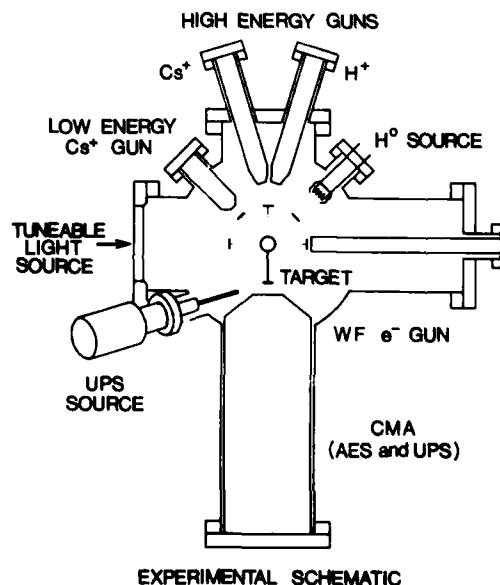


FIG. 1. Experimental setup, showing the arrangement of the various experimental stations.

vacuum for several days adsorbing only small amounts of oxygen and nitrogen, with peak intensity ratios compared to silicon of  $1.3 \times 10^{-2}$  and  $7.8 \times 10^{-3}$ , respectively. This observation is consistent with results seen by other authors,<sup>5</sup> where it is shown that oxygen adsorption on a clean silicon surface is smaller by a factor of  $\approx 10^5$  than adsorption on a cesiated surface.

The work function shifts are determined by the retarding field diode method.<sup>6,7</sup> In this method, the shift in target bias necessary to reflect a fixed portion of the electron beam is equal to the work function change of the target surface. The electron beam is modulated, and the target current is monitored with a lock-in amplifier to remove any dc leakage or pickup effects. In order to convert this shift to an absolute work function the target is biased negatively, and the onset of photoelectron emission is measured using the tunable light source. This method gives work function values repeatable to within  $\pm 0.05$  eV. This error is due primarily to uncertainty in the onset of the photoemission current. The shift measurements themselves are accurate to within  $\pm 0.01$  eV.

Both Cs<sup>+</sup> guns were designed and built in house<sup>8</sup> and use the same source. The source is a pellet of sintered cesium mordenite powder which becomes an ionic conductor when heated to  $\approx 1000^\circ\text{C}$ , and thermionically emits cesium ions. The difference between the two guns lies in the extraction optics. The high-energy version uses a Pierce-type extraction followed by a standard Kratos Minibeam I optical column for acceleration to high energy (100–5000 eV). This gun is available commercially from Kratos as an ion gun for negative secondary ion mass spectrometry (SIMS). The low-energy gun uses a simple planar diode geometry to produce a beam with an energy range of 5 to 50 eV. The H<sup>+</sup> gun is also a Minibeam I gun modified to use hydrogen. The two high-energy beams impinge on the target at  $18^\circ$  from the normal.

### III. EXPERIMENTAL RESULTS AND DISCUSSION

#### A. Low-energy cesium ion deposition

We examine the work function of an *n*-type (100) silicon target bombarded by a low-energy (20 eV) cesium ion beam. At this energy the source provides in excess of  $1 \mu\text{A}/\text{cm}^2$  to the target. Placing the target in front of the ion source results in radiative heating of the wafer to 325 K. At this temperature, we are unable to reach the coverage of cesium necessary for a minimum work function. When cooled to  $\sim 200$  K, monolayer coatings of cesium are obtained. It should be noted that the coverage also depends on ion flux, and higher temperatures may be used if accompanied by an increase in the cesium flux.

In Fig. 2, the solid squares show the work function shift as a function of cesium dose. The total dose is determined by integrating the ion flux incident on the target. The coverage is calibrated using published data<sup>9</sup> on the ratio of cesium to silicon Auger peaks as a function of coverage, where a coverage of 1.0 monolayer (ML) corresponds to  $6.78 \times 10^{14}$  atoms/cm<sup>2</sup>. The curve in Fig. 2 passes through a minimum at a dosage of  $3 \times 10^{15}$  ions/cm<sup>2</sup>. This corresponds to a coverage of 0.5 ML. The curve then rises to a constant value at a dosage of  $1.6 \times 10^{16}$  ions/cm<sup>2</sup>. Here, the coverage is equal to 1.0 ML. Note that it takes much longer to go from 0.5 to 1

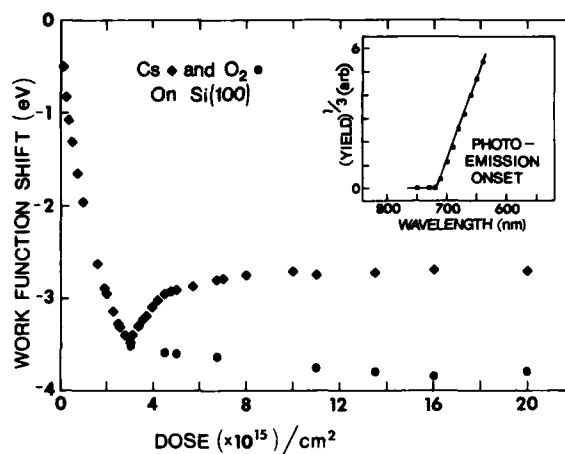


FIG. 2. Work function shift vs dose for 20-eV Cs<sup>+</sup> on Si(100) (■). Maximum work function shift after oxygen is added (●). Inset shows sample photoemission onset curve used to calibrate the shift measurements.

ML than from 0 to 0.5 ML. This is attributed to a reduced sticking coefficient at coverages  $> 0.5$  ML. In each of these regions, the coverage increases linearly with dose.<sup>9</sup> The shift measurements in Fig. 2 are calibrated with the tunable light source. It should be noted that in general, the photoemission onset is not numerically equal to the work function. However, in the case of sputtered and annealed silicon, it has been shown that the two values are equal.<sup>10</sup> Therefore, graphing (yield)<sup>1/3</sup> versus photon wavelength,<sup>11</sup> we extrapolate photoemission currents to the thresholds giving absolute values for the work function. These values are  $2.00 \pm 0.05$  eV at 1.0-ML cesium coverage, and  $1.47 \pm 0.05$  eV at the minimum. The inset in Fig. 2 shows an example of a photoemission onset measurement used to calibrate the shifts. The photoelectrons are measured with the lock-in amplifier, and this signal is then taken to the  $\frac{1}{3}$  power. In the figure, it is plotted in arbitrary units.

#### B. Adsorption of oxygen

It is well known that the adsorption of cesium followed by the adsorption of oxygen on silicon can lead to a surface with a work function smaller than 1.0 eV. These studies have been done with cesium vapor deposition, and claim to be very sensitive to the surface condition. In this experiment, we use low-energy ions to see if bombardment induced damage to the surface prevents this effect. Theoretical values calculated with the TRIM computer code<sup>12</sup> indicate that at 20-V incident Cs<sup>+</sup> energy, the average implantation depth is 3.89 Å ( $\approx 1$  layer), and that for every two incident ions, one vacancy/interstitial is created. Postdislocation recombination is not considered in this calculation.

Looking again at Fig. 2, the solid circles represent the work function shift after first dosing the surface with cesium, and then admitting oxygen into the chamber while monitoring the work function. Below 0.5-ML cesium coverage, oxygen adsorption causes the work function to rise (not shown). Only for cesium coverages  $> 0.5$  ML does adsorption of oxygen cause the work function to drop to a minimum value and then to rise again. The points on the curve

represent the minimum value reached. Once the oxygen is shut off, the work function is seen to remain stable for extended periods of time. The largest change, and lowest absolute work function is seen when oxygen is admitted after 1.0 ML of cesium is deposited. The minimum absolute work function reached upon adsorption of oxygen is  $0.90 \pm 0.05$  eV. The oxygen exposure needed to achieve this minimum is  $\approx 2.5$  L ( $10^{-6}$  Torr s). We find this surface to be easily reproduced using the above procedure. Our work function value corresponds precisely to values seen by other authors using vapor deposition.<sup>3,4,9</sup> Thus, at least for 20-V incident ion energy, we see that these low work function surfaces are still attainable. Higher energies are presently being investigated.

Progressive oxidation of thick ( $\approx 10$  at. layers) cesium films has been shown to give a minimum work function of  $\approx 1.0$  eV by Woratschek *et al.*<sup>13</sup> It was also determined that the minimum work function corresponded to completion of a subsurface layer of oxygen. While this work function is slightly larger than our result, it indicates that the substrate may not be crucial in obtaining a work function on the order of 1.0 eV. Thick layers, on the order of several hundred angstroms, of cesium suboxide may produce the same result. We intend to investigate this possibility, especially with regard to its use in negative hydrogen ion sources.

## C. Adsorption of atomic hydrogen

### 1. On clean silicon

In this setup, the target is placed  $\sim 3$  cm in front of a hot ( $\approx 2100$  K) tungsten filament. Molecular hydrogen is then admitted to the chamber at a  $H_2$  pressure of  $1 \times 10^{-6}$  Torr. Since the amount of actual atomic flux from the filament is not known, the data are referenced to the number of L of  $H_2$  exposure. However, as we shall see later, an approximate value for the rate of coverage accumulation can be calculated. In Fig. 3, the work function change versus  $H_2$  exposure is shown. The work function change is  $-0.34 \pm 0.05$  eV for a  $H_2$  exposure of  $\approx 480$  L. This decrease in the work function is consistent with the asymmetric dimer model for the clean Si(100) surface.<sup>14,15</sup> In this model, the work function of a clean surface is increased from that of an ideal surface by a dipole moment due to the displacement of surface and subsurface atoms. This displacement is due to the bonding of adjacent surface atoms via dangling bonds. The adsorption of atomic hydrogen then saturates these dangling bonds, and removes the surface reconstruction, causing the work function to decrease. Within experimental error, our value matches that seen by other authors.<sup>16,17</sup> More recent support for this asymmetric dimer model has been seen with scanning tunneling microscope (STM) data,<sup>18</sup> where it is seen that in regions of high surface defect structure, such as might be expected in a sputter cleaned and annealed target, the primary surface structure is that of buckled (asymmetric) dimers.

Looking again at Fig. 3, we see essentially two regions, one where the work function is changing rapidly, and a second where it changes much more slowly. From the work of Law,<sup>19</sup> it is known that the sticking coefficient of atomic hydrogen on silicon decreases by two orders of magnitude between coverages of  $1 \times 10^{14}/\text{cm}^2$  and  $3 \times 10^{14}/\text{cm}^2$ . If the

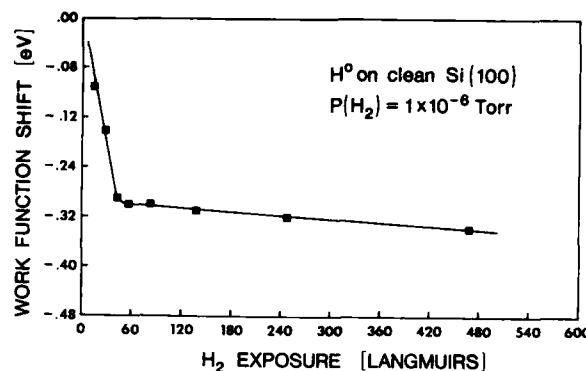


FIG. 3. Work function shift vs  $H_2$  exposure for Si(100) placed in front of atomic hydrogen source.

breakpoint of the work function curve is assumed to be at a coverage of  $2 \times 10^{14}/\text{cm}^2$ , a rate of coverage accumulation can be calculated. Knowing that the time to reach the breakpoint is 45 s, it follows that the accumulation rate is equal to  $4.4 \times 10^{12}$  atoms/ $\text{cm}^2$  s.

In order to verify that the work function reduction is due to atomic, and not molecular hydrogen adsorption, the work function is monitored while the target sits in a background  $H_2$  pressure of  $1 \times 10^{-6}$  Torr. During this measurement, all other filaments in the chamber except for the work function gun are shut off. The data show essentially the same behavior except for an increase by a factor of 50 in the exposure of molecular hydrogen needed to reach the breakpoint in the curve. This slow work function decrease is attributed to a combination of atomic hydrogen production by the electron gun and adsorption of molecular hydrogen. Molecular hydrogen has been seen to only adsorb on silicon in very small ( $< 3\%$ ) amounts.<sup>19-21</sup> Thus the majority of the work function change is presumed to be due to the atomic as opposed to the molecular flux. The possibility of contamination is also checked. After an exposure of  $\approx 1800$  L of  $H_2$  the Auger spectra show only the growth of an oxygen peak with an intensity of  $8 \times 10^{-3}$  times that of the silicon peak. Thus, the work function shift is due to atomic hydrogen adsorption only.

UPS spectra using He I (21.2 eV) photons have been taken for clean and hydrogenated silicon. The results are shown in Fig. 4. On the clean surface, features are seen at  $-5.7$ ,  $-7.7$ ,  $-12.2$ , and  $-15.7$  eV, where these values are referred to the vacuum level. These results agree with other authors,<sup>20</sup> where they have been interpreted<sup>17,22</sup> as indicating the asymmetric dimer bonds discussed earlier. Changes in these features are seen after exposure to 300 L of  $H_2$ , while placed in front of the atomic hydrogen filament. The bump at  $-5.7$  eV has disappeared, consistent with its interpretation as due to dangling bond surface states,<sup>22</sup> which are saturated upon adsorption of atomic hydrogen. The features at  $-7.7$ ,  $-12.2$ , and  $-15.7$  eV remain, to a greater or lesser degree, and are thus attributed to the silicon bulk. In addition to changes in the spectra due to the surface states, there was also a shift in the low-energy cutoff of secondary electrons due to a shift in the work function. This shift is equal to 0.32 eV, which is the same value that was arrived at using the retarding field technique (see Fig. 3).

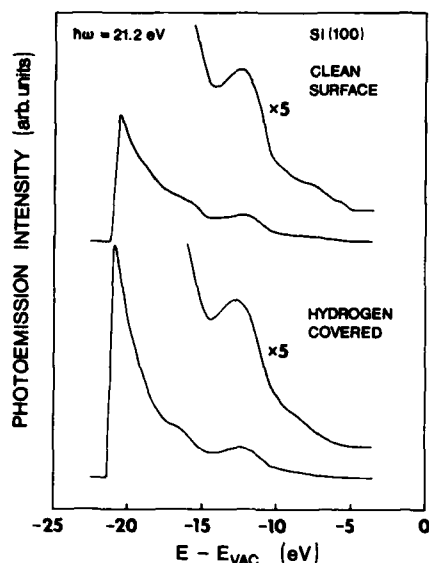


FIG. 4. UPS spectra for a clean Si(100) target (top curve), and for the same target after a 300 L exposure to  $H_2$  while placed in front of the atomic hydrogen source (bottom curve).

## 2. On cesiated silicon

Atomic hydrogen is deposited on cesiated silicon, both at full-monolayer coverage and on the oxygenated surface. For the case of full-monolayer coverage, the work function decreases by  $\approx 0.12$  eV after an exposure of 200 L of  $H_2$ . In the case of oxygenated silicon, the target is first cesiated and oxygenated until the optimum work function surface is reached. The target is then placed in front of the hot filament and hydrogen is admitted to the chamber. The effect of this adsorption on the surface work function is an immediate increase of  $< 0.15$  eV, followed by a very slow rise. Taking runs with and without the atomic hydrogen filament operating serves to put an upper limit on the effect of the atomic hydrogen adsorption. Our data thus far indicate that atomic hydrogen has only a small effect on the work function of the cesiated targets and thus it may be possible to maintain a surface with a work function of  $\approx 1$  eV in a dynamic system. We are presently examining this effect in greater detail.

## IV. SUMMARY

We have seen that it is possible to attain work functions on silicon of sub-eV values, by coating the surface with cesium and oxygen. Although these values have been obtained before by vapor deposition, we have shown that at least for low ion energies, they are also attainable by ion bombardment. The effect of atomic hydrogen exposure on clean and on these low work function surfaces has also been investigated.

On clean silicon, the results of atomic hydrogen adsorption, namely, the passivation of surface states and the work function changes, support the asymmetric dimer model for the Si(100) surface. We have seen that the hydrogen on a low work function surface has only a small effect. This is of great practical importance in the field of negative hydrogen ion sources where the yield of negative ions depends strongly on the work function of the surface. Theory indicates that negative ion yields in excess of 0.1 for reflection of thermal atomic hydrogen with a temperature of 0.5 eV from a surface with a 1.2-eV work function can be obtained.<sup>23</sup>

## ACKNOWLEDGMENTS

We gratefully thank George Wohlrab, for his invaluable machining expertise and overall general assistance in keeping the system running. This work was supported by the Air Force Office of Scientific Research.

- <sup>1</sup>W. Carr, M. Seidl, G. S. Tompa, and A. E. Souzis, *J. Vac. Sci. Technol. A* **5**, 1250 (1987).
- <sup>2</sup>R. E. Weber and W. T. Peria, *Surf. Sci.* **14**, 13 (1969).
- <sup>3</sup>B. Goldstein, *Surf. Sci.* **35**, 227 (1973).
- <sup>4</sup>J. D. Levine, *Surf. Sci.* **34**, 90 (1973).
- <sup>5</sup>P. Soukiasian, M. H. Bakshi, Z. Hurych, and T. M. Gentle, *Phys. Rev. B* **35**, 4176 (1987).
- <sup>6</sup>P. A. Anderson, *Phys. Rev.* **47**, 958 (1935).
- <sup>7</sup>A. G. Knapp, *Surf. Sci.* **34**, 289 (1973).
- <sup>8</sup>M. Seidl, A. E. Souzis, W. E. Carr, and G. S. Tompa, in the 37th Pittsburgh Conference and Exposition, Book of Abstracts, No. 743, 1986.
- <sup>9</sup>J. E. Ortega, E. M. Oellig, J. Ferron, and R. Miranda, *Phys. Rev. B* **36**, 6213 (1987).
- <sup>10</sup>F. G. Allen and G. W. Gobeli, *J. Appl. Phys.* **35**, 597 (1964).
- <sup>11</sup>G. W. Gobeli and F. G. Allen, *Phys. Rev. A* **137**, 245 (1965).
- <sup>12</sup>W. Eckstein, H. Verbeek, and J. P. Biersack, *J. Appl. Phys.* **51**, 1194 (1980).
- <sup>13</sup>B. Woratschek, W. Sesselman, J. Kuppers, G. Ertl, and H. Haberland, *J. Chem. Phys.* **86**, 2411 (1987).
- <sup>14</sup>W. S. Verwoerd, *Surf. Sci.* **99**, 581 (1980).
- <sup>15</sup>D. J. Chadi, *J. Vac. Sci. Technol.* **16**, 1290 (1979).
- <sup>16</sup>P. Koke and W. Monch, *Solid State Commun.* **36**, 1007 (1980).
- <sup>17</sup>K. Fujiwara, *Phys. Rev. B* **26**, 2036 (1982).
- <sup>18</sup>R. J. Hamers, R. M. Tromp, and J. E. Demuth, *Phys. Rev. B* **34**, 5343 (1986).
- <sup>19</sup>J. T. Law, *J. Chem. Phys.* **30**, 1568 (1959).
- <sup>20</sup>H. Ibach and J. E. Rowe, *Surf. Sci.* **43**, 481 (1974).
- <sup>21</sup>T. Sakurai, M. J. Cardillo, and H. D. Hagstrum, *J. Vac. Sci. Technol.* **14**, 397 (1977).
- <sup>22</sup>F. J. Himpsel and D. E. Eastman, *J. Vac. Sci. Technol.* **16**, 1297 (1979).
- <sup>23</sup>M. Seidl, W. E. Carr, J. L. Lopes, and S. T. Melnychuk, in *Proceedings of the 3rd European Workshop on Production and Application of Light Negative Ions* (FOM Institute for Atomic and Molecular Physics, Amsterdam, The Netherlands, 1988), p. 157.

# Cesium ion transport across a solid electrolyte-porous tungsten interface

S. I. Kim and M. Seidl

Stevens Institute of Technology, Hoboken, New Jersey 07030

(Received 19 August 1988; accepted 6 September 1988)

The electrified interface between a cesium-mordenite solid electrolyte and a porous tungsten electrode has been studied theoretically and experimentally. This interface double layer plays a major role in a novel cesium ion source of high current density. A self-sustained theory of the solid electrolyte-metal interface is presented. The coverage of cesium on the surface of the porous tungsten electrode (i.e., inner layer) is calculated to be 0.3–0.35 in the temperature range 800–1100 °C. The concentration profile in the diffusion layer is obtained numerically in equilibrium and steady state. The  $\text{Cs}^+$  ion emission current-voltage curves have been measured experimentally as a function of temperature and the biasing current.  $\text{Cs}^+$  ion emission current of up to 10 mA/cm<sup>2</sup> has been extracted for 500 h at 1100 °C in steady-state operation. The emission current can be controlled by the biasing current.

## I. INTRODUCTION

Recently, a novel solid source of  $\text{Cs}^+$  ions has been developed in this laboratory.<sup>1</sup> It combines the advantages of porous metal ionizers<sup>2,3</sup> with those of aluminosilicate emitters.<sup>4</sup>

A schematic diagram of the cesium ion source is shown in Fig. 1. Cesium ions are chemically stored in a cylindrical pellet made of cesium mordenite (Cs-M) which is a synthetic zeolite of formula  $\text{Cs}_2\text{O} \cdot \text{Al}_2\text{O}_3 \cdot 10\text{SiO}_2$ .<sup>5</sup> The pellet is operated at a temperature of ~1000 °C. At this temperature, the Cs-M is a good ionic conductor for  $\text{Cs}^+$  ions. A porous tungsten thin film is sputter deposited on one circular face of the pellet while the other side is provided with a thick platinum coating. Cesium ions are driven to the porous electrode by an electric field generated in the solid electrolyte (SE) by the biasing voltage  $U_b$ . The ions diffuse through the porous tungsten electrode to its surface where they are emitted by surface ionization. The emitted ions are accelerated by the voltage  $U_a$  applied between the emission surface and the accelerator electrode.

In this paper, we summarize our experimental and theoretical studies on  $\text{Cs}^+$  ion transport from the SE through the porous tungsten electrode to vacuum. We present a self-consistent theory of the SE-cathode interface. The SE-anode interface will be treated in another paper.

## II. CESIUM-MORDENITE SOLID ELECTROLYTE (Cs-M SE)

Cs-M has an aluminosilicate matrix with an interchangeable cation. The structure of Cs-M consists of a single-layer framework containing five-membered rings of the Al and Si tetrahedral. It has a two-dimensional channel system with a pore size of ~6–7 Å in diameter which is known as large-port mordenite.<sup>5,6</sup> The high ionic conductivity of Cs-M SE is due to its channel structure.<sup>7</sup>

### A. Pellet preparation

The Cs-M powder is formed from Na-M powder [ $\text{Na}_2 \cdot \text{Al}_2\text{O}_3 \cdot 10\text{SiO}_2$ ] (large port Na-M, Union Carbide Inc.) by the ion exchange method.<sup>8</sup> The ion-exchanged Cs-

M powder is fired in order to recrystallize to a Cs-M structure at 1050 °C. The recrystallized Cs-M is crushed and ground in a high-purity zirconia ball mill to obtain uniform particle size. The powder is pressed into a cylindrical pellet which is sintered at 1370 °C for 3 h. To obtain a thermally stable emitter (i.e., minimize outgassing at an operating temperature of 1100 °C), it is sintered at just below its melting temperature (1400 °C). The final dimensions of the pellet are 0.5 cm in diameter and 1.0 cm in length. The density of the pellet is 2.60 g/cm<sup>3</sup>. The theoretical density of Cs-M is 2.83 g/cm<sup>3</sup>.<sup>5</sup> About 80 C of cesium are stored in the Cs-M pellet.

### B. Ionic conductivity

The current interruption method<sup>9</sup> is employed to measure the ionic conductivity and the double layer capacitances. In the Cs-M SE, the  $\text{Cs}^+$  ion is the only mobile charge moving through the negatively charged matrix skeleton by the hopping mechanism.<sup>10</sup> The ionic conductivity  $g$  has an Arrhenius-type dependence on the temperature;  $g = g_0 \exp - [\Delta G^0/kT]$ . The conductivity is the order of  $10^{-5}$  [ $\Omega \text{ cm}$ ]<sup>-1</sup> at 1000 °C and the activation energy  $\Delta G^0$  is found

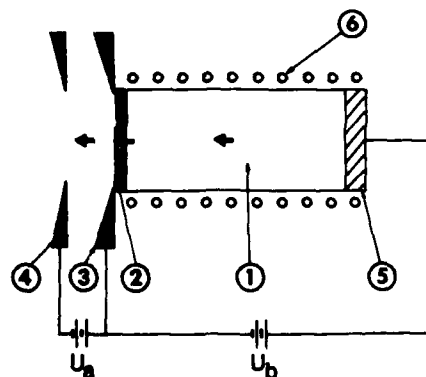


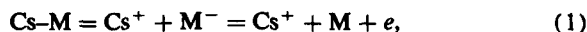
FIG. 1. Schematic diagram of the cesium ion source: (1) Cs-M solid electrolyte, (2) porous tungsten emitting electrode, (3) beam forming electrode, (4) accelerator electrode, (5) nonporous platinum anode, and (6) beater.



to be 0.7 eV/ion. The electronic conductivity of Cs-M SE is so small that it could not be observed.

### C. Electrode reaction

There are charge transfer reactions on both the electrodes. The anode reaction is



and the cathode reaction is



The time dependence of the cathode-SE interface potential after current interruption has been studied. Two different time constants in the decay of the interface potential are observed. They are a manifestation of a double layer at the interface (i.e., inner layer and diffusion layer).<sup>11</sup> The time constant of the inner layer is of the order of seconds while the time constant of the diffusion layer is of the order of hundred seconds. The corresponding capacitances are of the order of few tens  $\mu\text{F}$  for the inner layer and of few mF for the diffusion layer at a temperature of 1000 °C.

### III. ION EMISSION

A thin film of porous tungsten, a few  $\mu\text{m}$  thick, is sputter-deposited on the emitting surface of a Cs-M pellet. Pore size is of the order of 0.1  $\mu\text{m}$  in diameter and pore density is  $2.7 \times 10^8/\text{cm}^2$ . The anode electrode is coated with platinum paste.

The planar diode arrangement has been used for the studies of the emission current-voltage characteristics. The emitter surface is 0.5 cm in diameter and the spacing between emitter and extracting mesh (145  $\times$  145 tungsten mesh) is 0.2 cm.

The characteristics of the  $\text{Cs}^+$  ion emission current vs extraction voltage are shown in Fig. 2. In the low-voltage range, the emission current follows the Child-Langmuir law, indicating space-charge-limited flow. In the high-voltage range where temperature-limited operation should be effective, saturation occurs, and the emitted current is observed to be of the Schottky type. In this range, the current can be raised to the space-charge limit by additional cesium supply obtained by pellet biasing (Fig. 2).

The maximum current density of 0.3  $\text{mA}/\text{cm}^2$  shown in Fig. 2 does not represent a fundamental limit but rather a practical experimental limitation due to large total current. In order to increase the current density while keeping the total current below 30  $\mu\text{A}$  we have reduced the emitting area by covering the porous tungsten electrode with a diaphragm provided with an aperture of 0.06 cm in diameter. All cesium supplied to the porous tungsten electrode is delivered to this emitting area by surface diffusion. The ratio of the tungsten electrode area to the emitting area is  $\sim 100$ . Thus, the emission current density is 100 times larger than the biasing current density. Cesium ions are extracted by an immersion lens system, commonly used for electron guns.<sup>12</sup> The maximum current density measured as a function of temperature in this system is shown by circles in Fig. 3. With the tungsten emitter at 1100 °C, a steady-state current density of 10  $\text{mA}/\text{cm}^2$  was extracted for a period of 500 h.

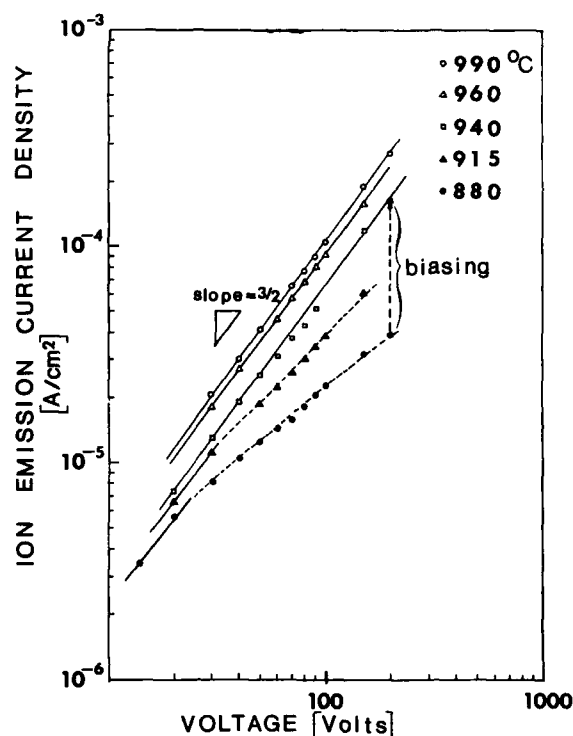


FIG. 2.  $\text{Cs}^+$  ion emission current density vs extraction voltage as function of temperature and the biasing current.

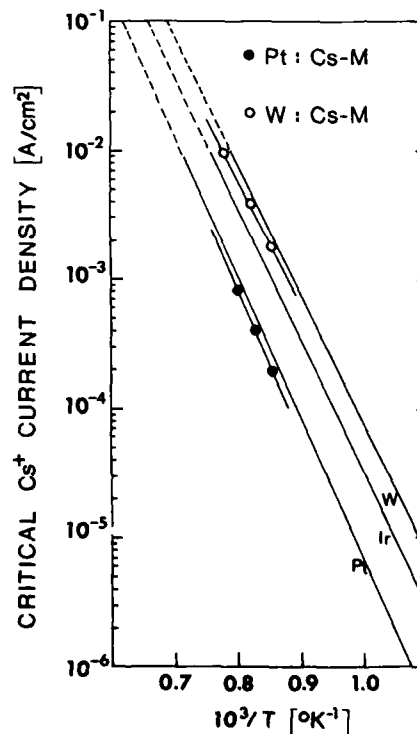


FIG. 3. The dependence of critical  $\text{Cs}^+$  ion emission current density on temperature: solid lines are from Wilson (Ref. 14), and data points are measured values from the porous platinum and tungsten electrode-Cs-M SE system.

In this case, we have reached the fundamental limit of surface ionization. All cesium supplied to the emitter surface is emitted as  $\text{Cs}^+$  ions as long as the current density is smaller than a critical current density which is given by the condition that the work function of the emitter surface is larger than the ionization potential of cesium. Wilson<sup>13</sup> measured the critical  $\text{Cs}^+$  ion current densities for several solid metal surfaces. His results are shown in Fig. 3, as solid lines. It can be seen that our measurements closely follow Wilson's curves. The slightly smaller values compared to Wilson's data can be attributed to the porous surface of the emitters.

### III. THEORY AND DISCUSSION

The theory of ion transport across the metal-SE interface is based on a Gouy-Chapman-Stern model<sup>14</sup> which we have modified to include the specific features of the SE. Figure 4 schematically shows the metal-SE interface. It can be divided into the diffusion layer and the inner layer. The current density  $J$  in the diffusion layer is given by the equation:

$$J = -qD \frac{dC}{dx} + q\mu EC, \quad (3)$$

where  $q$  is the electron charge,  $C$  is a concentration,  $\mu$  is the mobility,  $D$  is the diffusion constant of cesium ions, and  $E$  is the electric field. In contrast to LE, the conduction term ( $q\mu EC$ ) is not negligible with respect to the diffusion term for SE. This is due to the fact that only the positive ion is mobile. In consequence, space-charge neutralization is less effective on the local scale. We shall restrict the theory to steady state (no time dependence). Hence,  $J$  is a constant, independent of distance  $x$ , and is equal to the current density in the bulk.

The electric field satisfies Poisson's equation:

$$\frac{dE}{dx} = q(C - C_0)/\epsilon, \quad (4)$$

where  $\epsilon$  is a dielectric constant and  $C_0$  is the cesium concentration in the bulk. Assuming Einstein's relationship between  $D$  and  $\mu$ , the two equation can be normalized as follows:

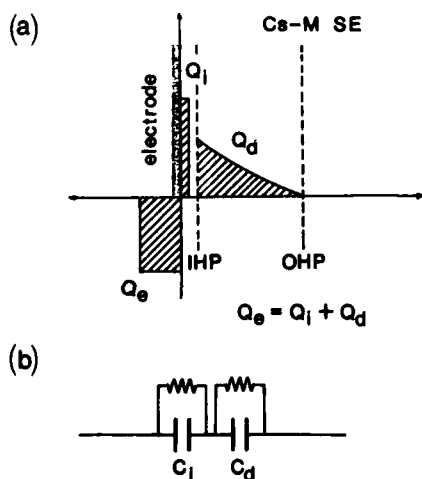


FIG. 4. Schematic diagram of the double layer: (a) charge distribution and (b) equivalent electric circuit.

$$j = -\frac{dn}{d\tau} + \tilde{E} \cdot n, \quad (5)$$

$$\frac{d\tilde{E}}{d\tau} = n - 1, \quad (6)$$

where  $j = J/J_d$ ,  $n = C/C_0$ ,  $\tau = x/L_d$ , and  $\tilde{E} = d\phi/d\tau$ . The normalized potential is  $\phi = eU/kT$ . The normalization constants are the cesium ion density in the bulk  $C_0$ , the Debye length  $L_d = [kT\epsilon/Cq^2]^{1/2}$ , and  $J_d = qDC_0/L_d$  which is equal to the limiting diffusion flux.<sup>15</sup>

Equations (5) and (6) have two boundary conditions:

$$\begin{aligned} n &= n_{\max} \exp - [(\mu_b - \mu_s)/kT] & (\tau = 0) \\ &= 1 & (\tau \gg 1). \end{aligned} \quad (7)$$

The other boundary condition will be introduced later. In Eq. (7),  $\mu_b$  and  $\mu_s$  are the chemical potentials for bulk and surface of the Cs-M SE. The difference between  $\mu_b$  and  $\mu_s$  will be taken equal to 0.05 eV.<sup>16</sup> The maximum ion concentration  $n_{\max}$  is given by the number of available sites on the surface of the Cs-M SE. There are three available sites per unit cell, which are 6 Å and 3–2 Å in diameter.<sup>17,18</sup> The 6-Å site is due to the channel which contributes to the ionic conduction. Since all these three sites are possible adsorption sites, we take  $n_{\max} = 3$ .

The surface concentration  $n(\tau = 0)$  is related to the coverage  $\theta$  of the tungsten electrode by means of the Langmuir isotherm:

$$\theta/(1 - \theta) = (K/\alpha)n(\tau = 0), \quad (8)$$

where  $K = \exp[(E_M - E_Z)/kT]$ , and  $E_M$  and  $E_Z$  are the binding energies of cesium on tungsten and Cs-M SE, respectively. They are  $E_M = 3.37 - 2.78 \cdot \theta_{\text{Cs}}$  (Ref. 19) and  $E_Z = 2.49$  eV.<sup>20</sup> The normalization factor  $\alpha = \sigma_M/\sigma_Z$  depends on the surface concentrations of cesium in a monolayer on tungsten ( $\sigma_M = 4.5 \times 10^{14} \text{ cm}^{-2}$ ) and on Cs-M SE ( $\sigma_Z = 0.3 \times 10^{14} \text{ cm}^{-2}$ ).

The specifically adsorbed cesium ions on the tungsten electrode represent a positive surface charge density ( $Q_i = q\theta\sigma_M$ ) which is stored in the inner layer. This charge and the positive charge accumulated in the diffusion layer  $Q_d$  are compensated by the negative charge  $Q_s$  induced in the metal electrode [Fig. 4(a)]. The equivalent electrical circuit of the interface is series connection of two capacitors with leakage resistances [Fig. 4(b)].

The diffusion layer is balanced by the field  $E_0$  due to the electron charge on the metal electrode. By using Gauss's law:

$$E_0 = Q_s/\epsilon. \quad (9)$$

Equation (9) is another boundary condition for Eqs. (5) and (6). The electron surface charge density on the metal electrode is  $Q_s = Q_e - Q_i$ .

The solutions of Eqs. (5), (6), and (8) depend on only two free parameters: the temperature  $T$  and the normalized current density  $j$ .

The important result of these calculation is that the coverage  $\theta$  is practically independent of the current density  $j$ , and a weak function of temperature, changing from 0.35 (at  $T = 1100^\circ\text{C}$ ) to 0.3 (at  $T = 800^\circ\text{C}$ ). On the other hand, the potential difference across the sheath (i.e., electrochemical

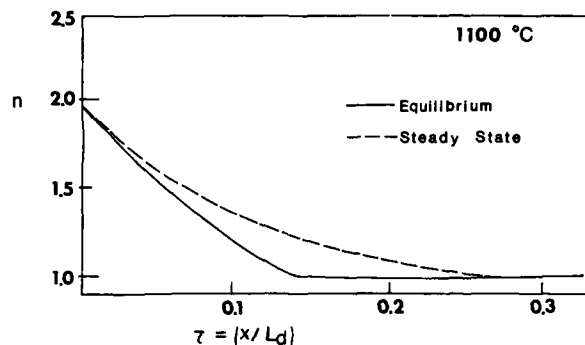


FIG. 5. Cesium concentration profiles in the diffusion layer, numerically calculated for 1100 °C (solid line  $J = 0$ ; dashed line  $J = 50 \mu\text{A}/\text{cm}^2$ ).

overpotential for the electrode reaction) increases with the current. The exponential dependence of current on the overpotential (i.e., Butler-Volmer equation<sup>21</sup>) is not obtained here, due to the effect of the double layer (Frumkin effect<sup>22</sup>). The theoretical current-overpotential characteristics will be shown in another paper.

Figure 5 shows the concentration profile in the diffusion layer for  $J = 0$  and  $50 \mu\text{A}/\text{cm}^2$ . The thickness of the diffusion layer is of the order of one-tenth of the Debye length, which corresponds to the high potential regime of the Gouy-Chapman model for LE.<sup>22</sup> The typical thickness of the diffusion layer is of the order of a few tens Å at 1100 °C.

All the cesium delivered to the porous tungsten electrode (biasing current) must diffuse to its surface exposed to vacuum. The biasing current can be controlled by the external biasing voltage between cathode and anode while the diffusion current depends only on the gradient of cesium concentration and the temperature. The diffusion of cesium through the porous tungsten has been theoretically treated by Forrester.<sup>23</sup> According to Forrester's Eq. (1), maximum current density of the order of few  $\text{mA}/\text{cm}^2$  is obtained at 1100 °C by using the values of our system (i.e., the coverage on the back surface of the tungsten electrode is 0.35, the pore size is  $0.1 \mu\text{m}$  in diameter, pore density is  $2.7 \times 10^8 \text{ cm}^{-2}$ , and the thickness of the tungsten electrode is  $5 \mu\text{m}$ ). For the high current density ion source,  $100 \mu\text{A}/\text{cm}^2$  of supplying current density is needed to have a  $\text{Cs}^+$  ion emission current

density of  $10 \text{ mA}/\text{cm}^2$ . This means that diffusion through the porous tungsten electrode does not limit the ion transport. Experimentally, the  $\text{Cs}^+$  ion emission current can be completely controlled by the biasing current in any range of the emission limited current region.

Full details of both experiments and theory will be published in forthcoming papers.

## ACKNOWLEDGMENTS

We gratefully thank George Wohlrab for his invaluable machining expertise and overall general assistance in keeping the system running. This work was supported by the AFOSR and the State of New Jersey.

- <sup>1</sup>M. Seidl, A. E. Souzis, W. E. Carr, and G. Tompa, Pittsburgh Conference on Analytical Chemistry and Applied Spectroscopy, Atlantic City, 1986, Abstract. No. 743.
- <sup>2</sup>G. R. Brewer, *Ion Propulsion* (Gordon and Breach, New York, 1970).
- <sup>3</sup>D. G. Welkie, *Secondary Ion Mass Spectroscopy SIMS V*, edited by A. Benninghoven, R. J. Colton, D. S. Simons, and H. W. Werner (Springer, Berlin, 1986), p. 146.
- <sup>4</sup>O. Heinz and R. T. Reaves, *Rev. Sci. Instrum.* **39**, 1230 (1968).
- <sup>5</sup>J. Ito, *Am. Mineral.* **61**, 170 (1976).
- <sup>6</sup>D. W. Breck, *Zeolite Molecular Sieves* (Wiley, New York, 1973).
- <sup>7</sup>D. C. Freeman and D. N. Stetters, *J. Chem. Phys.* **35**, 799 (1961).
- <sup>8</sup>A. P. Bolton, *Molecular Sieve Zeolites* (Academic Press, 1976), p. 13.
- <sup>9</sup>D. Y. Wang and A. S. Nowick, *J. Electrochem. Soc.* **126**, 1155 (1979).
- <sup>10</sup>Y. Haven and P. Hagenmuller, *Solid Electrolytes*, edited by W. Van Gool (Academic, New York, 1978), Chap. 5.
- <sup>11</sup>J. O'M. Bockris and A. F. Reddy, *Modern Electrochemistry* (Plenum, New York, 1970), Vol. 2, Chap. 7.
- <sup>12</sup>B. Paszkowski, *Electron Optics* (Academic, New York, 1978), p. 196.
- <sup>13</sup>R. G. Wilson, *J. Appl. Phys.* **37**, 4125 (1966).
- <sup>14</sup>P. Delahay, *Double Layer and Electrode Kinetics* (Wiley, New York, 1965), Chaps. 2 and 3.
- <sup>15</sup>J. O'M. Bockris, in Ref. 11, p. 1075.
- <sup>16</sup>D. E. Parry, *Surf. Sci.* **49**, 433 (1975).
- <sup>17</sup>K. Ogawa, M. Nitta, and K. Aomura, *J. Phys. Chem.* **82**, 1655 (1978).
- <sup>18</sup>H. Knozinger and P. Ratnasamy, *Catal. Rev. Sci. Eng.* **17**, 31 (1978).
- <sup>19</sup>P. W. van Amersfoort, J. J. C. Geerlings, R. Rodlink, E. H. A. Granne-man, and J. Los, *J. Appl. Phys.* **58**, 3566 (1985).
- <sup>20</sup>J. N. Matossian and M. Seidl, *J. Appl. Phys.* **53**, 6376 (1982).
- <sup>21</sup>A. J. Bard and L. R. Faulkner, *Electrochemical Methods* (Wiley, New York, 1980), p. 103.
- <sup>22</sup>B. E. Conway, *Theory and Principles of Electrode Process* (Ronald, New York, 1965), Chaps. 4 and 5.
- <sup>23</sup>A. T. Forrester, *J. Chem. Phys.* **42**, 972 (1965).

 **PROCEEDINGS**  
SPE—The International Society for Optical Engineering

# Microwave and Particle Beam Sources and Directed Energy Concepts

Howard E. Brandt  
*Chair/Editor*

16–20 January 1989  
Los Angeles, California

Sponsored by  
SPE—The International Society for Optical Engineering

*Cooperating Organizations*

Applied Optics Laboratory/New Mexico State University  
Center for Applied Optics Studies/Rose-Hulman Institute of Technology  
Center for Applied Optics/University of Alabama in Huntsville  
Center for Electro-Optics/University of Dayton  
Center for Excellence in Optical Data Processing/Carnegie Mellon University  
Center for Microwave-Lightwave Engineering/Drexel University  
Center for Research in Electro-Optics and Lasers/University of Central Florida  
Jet Propulsion Laboratory/California Institute of Technology  
Optical Sciences Center/University of Arizona  
Optoelectronic Computing Systems Center/University of Colorado,  
Colorado State University

*Published by*

SPE—The International Society for Optical Engineering  
P.O. Box 10, Bellingham, Washington 98227-0010 USA  
Telephone 206/676-3290 (Pacific Time) • Telex 46-7053



**Volume 1061**

SPE (The Society of Photo-Optical Instrumentation Engineers) is a nonprofit society dedicated to advancing engineering and scientific applications of optical, electro-optical, and optoelectronic instrumentation, systems, and technology.

## SURFACE PRODUCTION OF NEGATIVE HYDROGEN IONS

M.Seidl, W.E.Carr, S.T.Melnychuk, A.E.Souzis, J.Isenberg and H.Huang

Department of Physics and Engineering Physics  
Stevens Institute of Technology, Hoboken, NJ 07030

### ABSTRACT

Negative hydrogen ions are produced by electron tunnelling from a solid surface (converter) to hydrogen atoms moving away from the surface. A simple theoretical model of this process indicates reasonable ionization probability ( $>0.1$ ) for low initial energy of the H atoms (order of 1 eV) when the work function of the converter is smaller than 1.5 eV. Low initial energy guarantees low  $H^-$  ion energy spread. It also makes it possible to use a variety of compounds for reducing the converter work function. Experimental studies of Cs oxide films (work function 0.9 to 1.2 eV) are presented. Production of  $H^-$  ions by backscattering thermally produced H atoms from a thick film of Cs oxide is demonstrated.

### 1. INTRODUCTION

Surface production of  $H^-$  ions is based on electron tunnelling from a solid surface to an H atom moving away from the surface. The theory of this process has been studied over the past decade by several authors using various approximations<sup>1-6</sup>. A generic model of the process which also takes into account particle trapping is presented in Chapter 2. The model indicates, that in order to obtain a high surface ionization rate, the work function of the surface must be as low as possible and the initial velocity of the H atom must have an optimum value which depends primarily on the surface electron density near the Fermi level.

The motion of the H atom away from the surface is caused by atom-atom collisions. Because of the statistical nature of the collisions, the average initial kinetic energy parallel,  $\langle E_{||} \rangle$ , and perpendicular,  $\langle E_{\perp} \rangle$ , to the surface are equal. For high brightness beams,  $\langle E_{||} \rangle$  must be small, say 1 eV, which implies that  $\langle E_{\perp} \rangle$  will also be 1 eV. Since  $\langle E_{\perp} \rangle$  affects the ionization probability, there is in general a trade-off between beam intensity and beam temperature.

Experimentally the motion of the H atom is due to either sputtering or scattering. In the case of sputtering, H atoms adsorbed on the converter surface (or implanted close to the surface) are desorbed by Cs ion bombardment<sup>7,8</sup> or H ion bombardment<sup>9</sup> or a combination of both<sup>10,11</sup>. In order to obtain acceptable yield the bombarding energy must exceed 100 eV, which is sufficient for sputter erosion and structural damage to the converter surface. This fact restricts the choice of the converter material, as discussed in Chapter 3.

Backscattering of H atoms or ions from low work function surfaces is another method for surface production of  $H^-$  ions. For high ionization probability the perpendicular energy of the incident H atoms must be in a certain range that depends on the properties of the surface but roughly extends from 0.5 eV to 30 eV. At lower energies the  $H^-$  ions are trapped by the image force (chemisorbed) on the surface and undergo chemical reactions. At higher energies most of the atoms are implanted in the converter or are inelastically reflected. The upper part of the allowed energy

range was studied in proton backscattering experiments<sup>12-20</sup>.  $H^-$  ion yields higher than 50% have been measured<sup>19</sup>. The lower part of the allowed energy range was studied by backscattering of thermally produced H atoms<sup>21-23</sup>. Low energy (1eV) backscattering eliminates surface damage to the converter by momentum transfer. New avenues for surface optimization opened up by this approach are discussed in Chapter 3. The other advantage of low energy backscattering is the low energy spread of the  $H^-$  ions. Both points are demonstrated in Chapter 4 which presents experimental results on backscattering of thermally produced H atoms from Cs oxide surfaces.

## 2. THEORETICAL MODEL

It is generally agreed that electron transfer between the H atom and the surface can be described by electron tunnelling, with the motion of the atom treated classically. According to the probability model<sup>4</sup> the frequency of electron transition between the H atom affinity level and the surface is given by;

$$\omega(z) = \Omega \exp(-\gamma z) \quad (1)$$

where  $z$  is the distance between the atom and the surface, and  $\Omega$  and  $\gamma$  are constants. This holds for separations greater than a few atomic radii, which is the important region for negative ion production. The transitions are energy conserving, so that they occur between the state in the atom and states on the surface at the same energy. The constants are given by Gauyac<sup>6</sup>. For a cesiated metal surface with 50% adsorbed H the values are  $\Omega=10^{15}$  /sec, and  $1/\gamma=0.62$  Bohr radii.

Eq. (1) suggests a simple physical picture, in which  $\Omega$  is determined by surface electron density and  $\gamma$  is determined by the exponential decay of the wave functions with distance from the surface. The analogy for metals is straightforward, for example, electron in a square well gives a reasonable result. The case for semiconductors is not as simple, but, since surface electrons dominate, the filled surface states near the Fermi level are probably important.

The potential energy of the negative ion (or the electron affinity level) is determined by the image charge and is given by;

$$U(z) = -A - \frac{e^2}{4\pi\epsilon_0} \frac{1}{4(z+b)} \quad (2)$$

where the screening distance,  $b=3.2$  Bohr radii, and the isolated H atom affinity level,  $A$  is 0.75 eV. This is valid for  $z$  not too close to the surface. Figure 1 shows the potential given by (2) as a function of distance from the surface, as well as the work function,  $W$ .

Note that there is a crossing distance,  $Z_c$ , where the potential energy is equal to the work function,  $W$ . When the atom is inside  $Z_c$  the affinity level is below the Fermi level, allowing electron transfer from filled surface states to the atom, and when the atom is outside  $Z_c$ , transfer takes place from the occupied affinity level to empty surface states.

The energy diagram given in Fig 1 also shows the binding energy of an  $H^-$  ion to the surface. The potential energy for an ion depends on where it is ionized; ions formed close to the surface are deeper in the potential well than those formed farther away. Low energy atoms have kinetic energy comparable to the potential energy well depth, thus atoms that are ionized too near the surface do not have enough energy to escape and are trapped.

A rate equation determines the ionized fraction, given by;

$$\frac{dP}{dt} = \omega(z) \tau ( \theta(z - Z_c) - P ) \quad (3)$$

where  $P$  is the probability that the atom is a negative ion,  $\omega(z)$  is the transition rate given by (1),  $\theta(z)$  is the charge state of a fixed atom at position  $z$ , and  $\tau = 10^{-15}$  sec is the time normalization. Here the Heavyside step function is a good approximation to  $\theta$ . In order to solve (3), a relation between  $z$  and  $t$  is needed. In previous work<sup>4</sup> eq. (3) was solved using  $z = vt$ , where  $v$  is a constant, which is a reasonable assumption when the atom kinetic energy is much larger than the potential well depth.

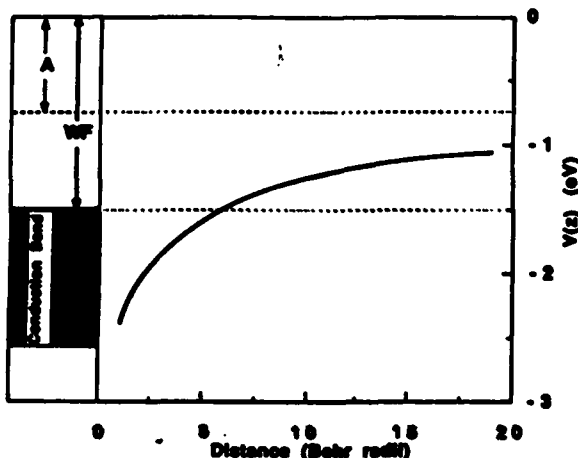


Figure 1. Potential Energy Diagram for a Negative Ion

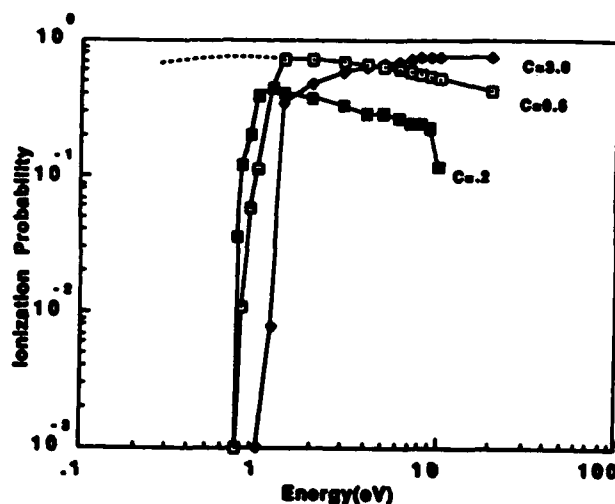


Figure 2. Ion Fraction vs Incident Energy for  $W = 1.5$  eV

In order to obtain results applicable to low energy atoms, energy conservation must be applied to the ion motion. The position of ionization is the result of a statistical process, so that the following Monte Carlo technique was used. An atom of speed  $u$  is placed near the surface, and is moved away in constant steps,  $dz$ . At each step  $R$  is assigned from a uniform random number generator in the interval  $(0,1)$ , and if  $R < \omega(z) dz/u$  then ionization took place. Once ionized, it is assumed that the atom cannot be neutralized inside  $Z_c$  since there are no vacant states in the solid. The ion is then moved to  $Z_c$  and the kinetic energy is reduced by the change in potential energy. If the resulting kinetic energy is negative the ion is counted as trapped. Atoms that reach  $Z_c$  without being ionized are counted as escaping atoms.

Ions that reach  $Z_c$  untrapped are moved in steps of  $dz$ , but in this region neutralization occurs if  $R < \omega(z) dz/u$ . Those that are neutralized are counted as escaping atoms. Slow enough ions can be trapped outside  $Z_c$ , and these are added to the trapped count. Finally, ions that survive at a large distance are counted as collected ions.

Figure 2 shows the ion fraction vs. initial atom energy for several values of  $C=0.2$  when  $W = 1.5$  eV. In addition, the dotted curve shows the ion fraction with  $C = 0.6$  when the atom velocity is held constant. This clearly shows that constant velocity approximation is good above a few eV. The velocity variation dominates below about one eV, where the ion fraction falls to zero. There are no escaping ions

when the initial kinetic energy is less than 0.75 eV, since for this work function the minimum potential energy at the crossing point is 0.75 eV.

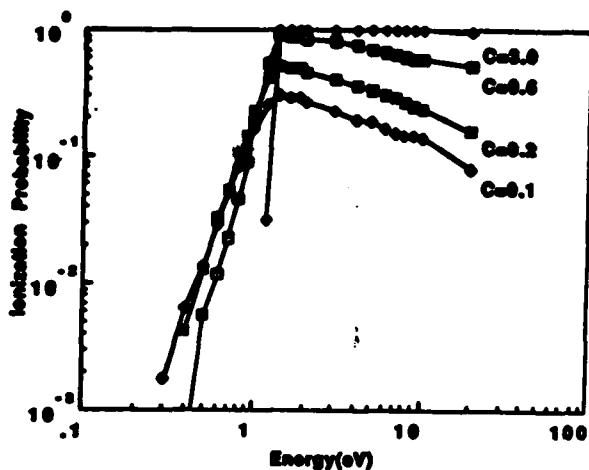


Figure 3. Ion Fraction vs. Incident Energy for  $W = 1.0$  eV

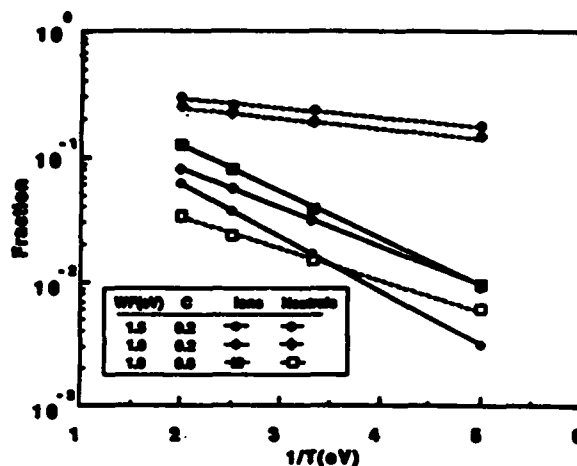


Figure 4. Ion and Neutral Fractions for a Thermal distribution of incident atoms.

Figure 3 shows the ion fraction vs. initial atom energy for several values of  $C$  when  $W = 1.0$  eV. In this case all ions are trapped for energies below 0.25 eV. The ion fraction at several tenths of an eV has significantly increased. The value of  $C$  also influences the ion fraction; below 1 eV ions increase with decreasing  $C$ , and above 1 eV the reverse is true. This is because ions can escape most readily when formed near  $Z_c$ , and reducing the transition rate allows ionization to take place at larger  $z$ . However, lower transition rates decrease the probability of ionization, thus the ion fraction is smaller at higher energy.

Figure 4 shows the ion fraction and neutral fraction of a thermal distribution of ions vs. inverse temperature for work functions of 1.0 eV and 1.5 eV. These were obtained by repeating the Monte Carlo calculations, using a Gaussian random number generator to select initial velocities. Since the sum of ionized, neutral, and trapped fractions is unity, it is clear that the trapped fraction is large. The dependence of the ion fraction on temperature and work function is in good qualitative agreement with the experimental results.

Based on this model we can describe the ideal surface for ionization of low energy H atoms. The work function should be low, less than 1.5 eV, so that it is possible to create ions that are weakly bound to the surface. The surface electron density (just below the Fermi level) should be smaller than typical metallic densities, so that the tunnelling does not occur close to the surface, but near  $Z_c$ . Finally, the electron wave function tails should decay slowly to increase tunnelling probability far from the surface.

### 3. CONVERTER MATERIALS

The desired properties of the converter surface as derived from the tunneling model must be supplemented by additional requirements which depend mainly on the energy of the H and Cs ions (or atoms) bombarding the converter. When the bombarding energy is higher than 100 eV, sputtering, backscattering and implantation become important. This restricts the converter material to a few refractory metals such as Mo and W. However, only Mo is acceptable when the additional requirement of a low work function at 100 eV bombarding energy is included.



The work function of many polycrystalline metal surfaces can be reduced to a minimum value of 1.6 eV by an adsorbed layer of Cs atoms with a submonolayer coverage. In a typical surface conversion source Cs coverage is provided entirely by ion bombardment. Due to the combined effect of implantation and sputtering a steady state coverage develops that primarily depends on the atomic mass of the converter atoms and on the bombarding energy. Minimum work function of 1.6 eV is obtained at 45 eV for V and at 100 eV for Mo<sup>24</sup>.

When the bombarding energy is lower than 10 eV, sputtering and implantation are negligible, and the above mentioned restrictions on the converter material do not apply. Converter surfaces with lower work function and optimized electron density can be sought. We have undertaken a systematic search for such a converter. The large body of knowledge accumulated over decades of research on photoemitters<sup>25,26</sup> and thermionic cathodes<sup>27</sup> has provided a good starting point although, apart from the common requirement of a low work function, each field has its own specific problems: photoelectrons must have a high escape probability, thermionic cathodes must be stable at high temperatures, and hydrogen converters must survive in a hydrogen atmosphere.

Work functions considerably lower than 1.6 eV can be obtained with several adsorbates on a variety of substrates. Submonolayer coverage of Cs on single crystal V(110) and Si(100) results in a work function of 1.45 eV and on GaP in 1.3 eV. Deposition of a Cs/O dipole layer on many metallic and semiconductor single crystal surfaces produces a work function of 0.9 eV. Possible substitutes for Cs are: Rb, K, Ba, Sr, and substitutes for O are: F, Cl, S. Thicker films (500 Angstroms) of Cs oxide have a work function of 1.1 eV independent of the substrate<sup>28,29</sup>. They are n-type semiconductors consisting of a mixture of Cs suboxides, that has not been characterized. Another example of an n-type semiconductor of great engineering importance is the Ba/Sr/O cathode coating which has a work function of 1.3 eV at 700°K. More work is needed for finding the material combination that would give a converter with high H<sup>-</sup> ion yield and stable operation. We have decided to explore the Cs-O system first.

Recently we have studied electronic surface changes due to adsorption of Cs, O and H on Si(100) surfaces<sup>30</sup>. In Fig. 5, the solid squares show the work function (measured by electron reflection) as function of Cs dose. The minimum occurs at 1.45 eV for a coverage of 0.5 monolayer (determined from the ratio of Cs/Si Auger peaks). In this case the sample was n-type doped, however, the same minimum is obtained for a p-type sample because of Fermi level pinning by surface states<sup>31</sup>. The solid circles in fig.5 show work functions obtained after first dosing the surface with Cs, then with O<sub>2</sub> until the minimum was reached. The lowest work function of 0.9 eV is reached for 1 monolayer of Cs and 2.5 Langmuir of O<sub>2</sub> in excellent agreement with literature<sup>20-22</sup>. It is worth noting that the optimized Cs/O/Si surface can be heated to 250°C without significant increase in the minimum work function<sup>32</sup>. This surface has not yet been tested in H atom backscattering experiments. We have, however, tested thick Cs-O films as described in the next chapter.

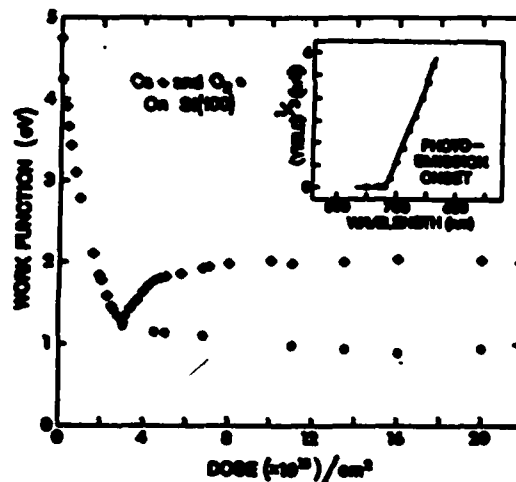


Figure 5. Work Function of Si(100) as a Function of Cesium dose (squares) and with Oxygen added (circles)

#### 4. BACKSCATTERING OF HYDROGEN ATOMS

The experimental set-up is shown in Fig. 6. H atoms are produced by thermal dissociation of  $H_2$  gas in a W tube oven heated to  $2500^\circ K$ . The H and residual  $H_2$  effuse from a 0.7 mm diameter hole in the oven onto the converter. The atoms have a Maxwellian energy distribution with a temperature equal to the oven temperature. Assuming thermal equilibrium, the atomic flux incident on the converter can be calculated as function of oven temperature and pressure<sup>21</sup>. Typically the flux is  $10^{16}$  atoms/cm<sup>2</sup> s (for  $2500^\circ K$  and  $10^{-6}$  torr chamber pressure).

The converter is a Ni or W ribbon 6 x 0.05 mm in cross section which can be ohmically heated. Its surface is coated with a thick film presumed to be a mixture of Cs suboxides which is produced by decomposition of  $Cs_2CO_3$ . Originally the film was deposited by evaporation using the method described by Briere and Sommer<sup>20</sup>. By controlling the evaporation rate and the ribbon temperature a steady state work function of 1.2 eV (measured from the photoemission threshold) could be obtained. A simpler method, analogous to the conventional way of making BaO thermionic cathodes, was used in the backscattering experiments.  $Cs_2CO_3$  powder suspended in a solution of organic binder was brush-painted on the Ni ribbon. The coating was about 0.05 mm thick. After evacuation of the chamber to less than  $5 \times 10^{-6}$  torr, the ribbon was heated to  $400^\circ C$  to remove the binder and to  $600^\circ C$  to decompose the cesium carbonate into oxides. At this stage the work function was about 2.1 eV.

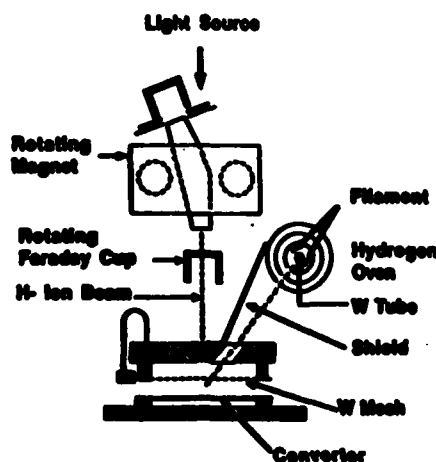


Figure 6. Experimental Set-up

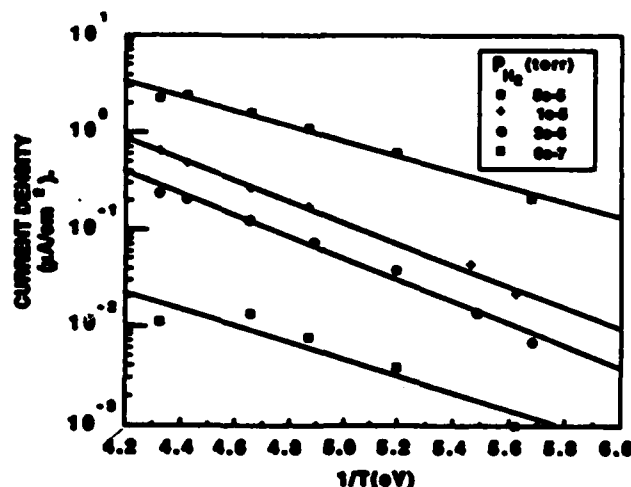


Figure 7.  $H^+$  current density vs  $1/T$  for different  $H_2$  pressures

Further reduction of the work function was achieved by exposing the surface to a flux of atomic hydrogen keeping the ribbon temperature below  $400^\circ C$ . The activation was monitored by backscattered  $H^+$  ions and by photoelectron and thermionic electron emission. After about 30 minutes of activation with a flux of  $10^{16}$  H atoms/cm<sup>2</sup> s the white light photocurrent increased 100 times and the work function dropped to 1.45 eV, the lowest value achieved so far.

Negatively charged particles produced on the converter surface are accelerated to 100 eV by a voltage applied between the converter and the tungsten mesh placed about 2.5 mm from the converter. A small sample of the particles passes through an aperture into the diagnostic region. When the Faraday cup is rotated out of the beam path, the rotating magnet is used to measure the mass and angular distribution of the particles.

Fig. 7 shows the current density of backscattered  $H^-$  ions at the exit aperture as a function of inverse oven temperature and  $H_2$  gas pressure in the chamber. The dependence of the current density on inverse temperature should be compared with the theoretical curves shown in Fig. 4. The extracted current consists of electrons and  $H^-$  ions (in 2:1 ratio) and of a small impurity (less than 1%) of  $O^-$  and  $OH^-$  ions. The  $H^-$  yield is about the same (2% for 0.2 eV oven temperature) as for cesiated Si(100) as reported previously<sup>23</sup>. The backscattered  $H^-$  ions have a Maxwellian energy distribution with a temperature equal to the oven temperature, indicating elastic collisions of the fast hydrogen atoms with the converter surface.

The thick "cesium oxide" film is easy to make. Exposure to atomic hydrogen (up to a flux of  $5 \times 10^{15}$  atoms/cm<sup>2</sup> s) not only does not erode the film, but it activates it. Remarkable reproducibility of the results in day-to-day operation has been observed. The film has not shown any deterioration after more than 50 hours of operation. The activation process is not understood; more work is needed to reduce the work function to 1.1 eV, typical for a well activated thick Cs-O film<sup>28,29</sup>. Exposure to larger fluxes of hydrogen atoms or ions should be investigated.

### 5. CONCLUSIONS

$H^-$  ions can be produced with reasonable efficiency by backscattering low energy (order of 1 eV) H atoms or ions from low work function (less than 1.5 eV) surfaces. This has been demonstrated experimentally by backscattering the Maxwellian tail of thermally produced H atoms from a thick film of Cs oxide. The general nature of the electron transfer process has been described by a simple theoretical model.

Low incident energy guarantees low energy spread of the  $H^-$  ions. It also makes it possible to consider a variety of compounds for reducing the work function of the converter surface. Oxides of alkali and alkali earth metals appear to be most promising for this purpose. They have a low work function and a considerably lower vapor pressure than the corresponding metals. More work is needed to assess the erosion rate of the oxides by atomic hydrogen.

Apparently, surface production of  $H^-$  ions by the process described above was recently observed in LBL experiments<sup>34</sup>. Considerable increase in  $H^-$  ion current density extracted from a bucket volume source was observed when the source was operated with Cs vapor. This increase has been attributed to surface production on the cesiated walls of the source<sup>35</sup>. It is likely that this mechanism is effective in other  $H^-$  ion sources operating with Cs vapor, such as the Dudnikov type Penning source<sup>36</sup>, in which surface production near the extraction aperture may contribute to the extracted  $H^-$  ion current.

### 6. ACKNOWLEDGEMENT

This work has been supported by the Air Force Office of Scientific Research.

### 6. REFERENCES

1. J.R. Hiskes, J. Phys. (Paris) 40, 179 (1979).
2. E.G. Overbosch, B. Rasser, A.D. Tenner and J. Los, Surf. Sci. 92, 310 (1980).
3. R. Brako and D.M. Nevns, Surf. Sci. 108, 253 (1981).
4. B. Rasser, J.N.M. van Vunnik and J. Los, Surf. Sci. 118, 697 (1982).
5. N.D. Lang, Phys. Rev. B27, 2019, (1983).
6. J.P. Gauthier, J.J.C. Geerlings, Surf. Sci. 182, 245 (1987).
7. M. Seidl and A. Fargellis, Phys. Rev. B 26, 1 (1982).
8. J.L. Lopes, J.A. Greer and M. Seidl, J. Appl. Phys. 60, 17 (1986).

9. C.F.A. van Os, P.W. van Amersfoort and J. Los, *J. Appl. Phys.* 64, 3863 (1988).
10. K.N. Leung, K.W. Ehlers, *J. Appl. Phys.* 52, 3905 (1982).
11. K.N. Leung, K.W. Ehlers, *Rev. Sci. Instrum.* 53, 803 (1982).
12. V. Eckstein, H. Verbeek, R.S. Bhattacharya, *Surf. Sci.* 99, 356 (1980).
13. J.R. Hiskes, P.J. Schneider, *Phys. Rev.* B23, 949, (1981).
14. J.N.M. van Vunnik, J.J.C. Geerlings and J. Los, *Surf. Sci.* 131, 1 (1983).
15. J.N.M. van Vunnik, J.J.C. Geerlings, E.H.A. Granneman and J. Los, *Surf. Sci.* 131, 17 (1983).
16. P.J.M. van Bommel, J.J.C. Geerlings, J.N.M. van Vunnik, P. Massmann, E.H.A. Granneman and J. Los, *J. Appl. Phys.* 54, 5676 (1983).
17. P.J. Schneider, K.H. Berkner, W.G. Graham, R.V. Pyle, and J.V. Stearns, *Phys. Rev.* B23, 941 (1981).
18. P.W. van Amersfoort, J.J.C. Geerlings, L.F. Tz. Kvakman, A. Hershcovitch, E.H.A. Granneman, and J. Los, *J. Appl. Phys.* 58, 3566 (1985).
19. P.W. van Amersfoort, J.J.C. Geerlings, R. Rodink, E.H.A. Granneman, and J. Los, *J. Appl. Phys.* 59, 241 (1986).
20. J.J.C. Geerlings, P.W. van Amersfoort, L.F. Tz. Kvakman, E.H.A. Granneman, J. Los and J.P. Gauyacq, *Surf. Sci.* 157, 151 (1985).
21. V.G. Graham, *Phys. Lett.* 73A, 186 (1979).
22. A. Pargellis and M. Seidl, *Phys. Rev.* B25, 4356 (1982).
23. M. Seidl, W.E. Carr, J.L. Lopes, and S.T. Melnychuk, *Proceedings of the Third European Workshop on: Production and Application of Light Negative Ions*, edited by H. Hopman and W. van Amersfoort (FOM-Institute for Atomic and Molecular Physics, Amsterdam-The Netherlands) p. 157 (1988).
24. G.S. Tompa, W.E. Carr and M. Seidl, *Surf. Sci.* 198, 432 (1988).
25. A.H. Sommer, *Photoemissive Materials*, John Wiley, New York, 1968.
26. R.U. Martinelli and D.G. Fisher, *Proc. of IEEE*, 62, 1339 (1974).
27. G. Herrmann and S. Vagener, *The Oxide-Coated Cathode*. Chapman & Hall, London, 1951.
28. T.R. Briere and A.H. Sommer, *J. Appl. Phys.* 48, 3547 (1977).
29. B. Woratschek, W. Sesselmann, J. Küppers, G. Ertl and H. Haberland, *J. Chem. Phys.* 86, 2411 (1987).
30. A.E. Souzis, M. Seidl, W.E. Carr, H. Huang, *J. Vac. Sci. and Technol.*, to be published.
31. F. J. Allen and G. W. Gobeli, *Phys. Rev.* 127, 152 (1962).
32. J.E. Ortega, E.M. Oellig, J. Ferron, R. Miranda, *Phys. Rev.* B36, p. 6213 (1987).
33. D. Edwards and V. T. Peria, *Appl. Surf. Sci.* 1, 419 (1978).
34. S.R. Valther, K.N. Leung and V.B. Kunkel, *J. Appl. Phys.* 64, 3424 (1988).
35. K.N. Leung, L3L, Private Communication.
36. H.V. Smith, Jr., P. Allison, and J.D. Sherman, *IEEE Trans. Nucl. Sci.* 32, 1797 (1985).

submitted to The Journal of Applied Physics

A NEW SOLID STATE CESIUM ION SOURCE

S.I. Kim and M. Seidl, Physics/Engineering Physics Department,  
Stevens Institute of Technology, Hoboken, NJ 07030

ABSTRACT

A novel  $\text{Cs}^+$  ion source combining the advantages of porous metal ionizers with those of zeolite emitters has been developed. Cesium ions are chemically stored in a cesium-mordenite solid electrolyte (Cs-M SE) pellet whose emitting surface is coated with a porous tungsten thin film. Cesium supply to the emitting surface is controlled by a voltage applied across the solid electrolyte pellet.  $\text{Cs}^+$  ion emission takes place on the surface of the porous tungsten electrode by surface ionization. The ionic conductivity of  $\text{Cs}^+$  ion in the Cs-M SE is of the order of  $10^{-5} [\Omega \cdot \text{cm}]^{-1}$  at  $1000^\circ\text{C}$ . The interface properties between electrolyte and electrodes play a major role in the cesium ion source. The cathode electrode interface (emitting electrode) determines the stability of the supply current density to the emitting surface. The life time of the source is found to depend on the anode interface. In a steady state operation, ion emission current density of the order of  $20 \text{ mA/cm}^2$  has been extracted for 30 hours at a total ion emission current of  $100 \mu\text{A}$  at  $1100^\circ\text{C}$ . The life time of the source corresponds to 10 coulombs of cesium charge.

## I. INTRODUCTION

Cesium ions are widely used in Secondary Ion Mass Spectroscopy (SIMS) [1], in the production of negative hydrogen ions by surface conversion [2], and in sources of cold electrons [3], etc. There are two basic types of  $\text{Cs}^+$  ion sources presently available: porous metal ionizer [4,5], shown in Fig.1,(a) and zeolite emitter [6], Fig.1,(b).

Recently a novel solid source of  $\text{Cs}^+$  ions has been developed in this laboratory.[7,8] It combines the advantages of porous metal ionizers with those of zeolite emitters. A schematic diagram of the cesium ion source is shown on Fig.1,(c). Cesium ions are chemically stored in a cylindrical pellet of cesium mordenite solid electrolyte (Cs-M SE). The pellet is operated at a temperature of about  $1000^\circ\text{C}$ . At this temperature, Cs-M is a good ionic conductor for  $\text{Cs}^+$  ions. A porous tungsten thin film (about  $1\mu\text{m}$  in thickness) is sputter deposited on one circular face of the pellet while the anode is provided with a thick platinum coating. Cesium ions are driven to the porous electrode by the biasing current across the electrolyte which is controlled by the biasing voltage,  $U_b$ . The cesium atoms diffuse through the porous tungsten electrode to its surface where they are emitted as ions or neutrals depending on the work function of the surface. The emitted ions are accelerated by the voltage,  $U_a$ , applied between the emission surface and the accelerator electrode. In this way, we could achieve a high performance

solid state cesium ion source which has the current density of a porous metal ionizer and the simplicity of a zeolite emitter. In this paper we present experimental studies of the Cs-M SE and porous tungsten electrode system. Theory has been published elsewhere [9].

In the first part of this paper, material aspects of the Cs-M SE such as: structural and chemical properties and preparation of the pellet and of the electrodes will be discussed. In the second part, the effects of the interface properties on the ion transport from the electrolyte to the emitter surface will be presented. Finally, measurements of cesium ion and neutral emission will be discussed.

## II. CESIUM-MORDENITE SOLID ELECTROLYTE (Cs-M SE)

### 2.1 Cesium-Mordenite (Cs-M)

Cs-M is a synthetic zeolite of formula  $\text{Cs}_2\text{O} \cdot \text{Al}_2\text{O}_3 \cdot 10\text{SiO}_2$  (unit cell formula in  $4 \cdot \text{Cs} \cdot [(\text{AlO}_2) \cdot (\text{SiO}_2)_3]$ ) which has an aluminosilicate matrix with an interchangeable cation. The structure of Cs-M consists of a single layer frame work containing 5-membered rings of the Al and Si tetrahedra. It has a two dimensional channel system with pore size about 6 Å in diameter. This is known as the large-port mordenite [10].

**Ion Exchange:** The Cs-M powder is formed from Na-M powder  $[8 \cdot \text{Na} \cdot \{(\text{AlO}_2) \cdot (\text{SiO}_2)_3\}]$  (large-port Na-M, Union Carbide Inc.) by the ion exchange method [11]. The sodium cation is exchanged for cesium in a CsCl acid solution. Ion exchange is done by the following method: 31 gram of Na-M powder in a 2 M CsCl solution is heated at about 80°C with magnetic stirring for several days. The solution is filtered through a vacuum frit (5 µm) and the residual powder is dried in a hot vacuum oven.

**Phase Transformation:** The ion exchanged Cs-M is in an unstable phase both chemically and structurally. Chemical analysis [Table 1] shows that the ion exchanged Cs-M contains more cesium than the stoichiometrical value as well as residual sodium. X-ray powder diffraction of the ion exchanged powder shows that it still has a Na-M structure. It has been found that the structural change to Cs-M occurs after firing the powder



above 1050°C. After transformation, Cs-M has become also stable in chemical composition.[Table 1]

By the DTA (Differential Thermal Analysis), two exothermic reactions are observed at 1050°C and 1420°C. The former one is due to the phase transformation (Na-M structure to Cs-M structure) and the latter is due to glass transformation (melting). A volume shrinkage of 59% is observed at 1050°C. 17% is due to the structure change and the rest of the volume shrinkage is due to the sintering effect. A good DTA thermogram could not be obtained since bad thermal insulation resulted from such a big volume shrinkage.

**Pellet Preparation:** The ion-exchanged Cs-M powder is fired at 1050°C. The recrystallized Cs-M is crushed and ground in a high purity zirconia ball mill. The particle size of the Cs-M powder is controlled by the grinding time in the ball mill. After grinding, the powder is dried in a hot vacuum oven and it is press formed in a hardened steel cylindrical plunger (0.95 cm in diameter) at a pressure of about 200 atm. The cylindrical pellet is sintered at 1350°C for 3 hours. The final density of the pellet depends on the particle size and also on the sintering time and temperature. At a sintering temperature and time given above, the densities of the sintered pellets vary in the range of 2.00 to 2.6 g/cm<sup>3</sup> for pre-sintered particle sizes from 3μm to 1μm. Theoretical density of the Cs-M is 2.83 g/cm<sup>3</sup>.

## 2.2 Electrode Preparation

The emitting cathode is made by sputter deposition of tungsten. A triode magnetron sputter source (L.M. Simard Inc.,) has been used. To obtain a porous thin film, high pressure (about 30 mtorr.) of argon gas has been used. The deposition rate of the thin film is about  $2 \text{ \AA}/\text{sec.}$  at a target current density of  $0.5 \text{ Amps}/\text{cm}^2$ , and a target voltage of  $500 \text{ V}_{\text{dc}}$ . The thin film has a submicron size of pores and pore density of the order of  $3 \cdot 10^8 / \text{cm}^2$ . SEM pictures of the porous tungsten thin film electrode are shown in Fig.2.

The anode electrode is prepared by applying platinum paste (Engelhard Co.). Thick platinum paste is painted and it is cured at  $800^\circ\text{C}$  for 2 hours.

## 2.3 Ionic Conductivity

In Cs-M SE,  $\text{Cs}^+$  is the only mobile charge moving through the negatively charged matrix skeleton by the hopping mechanism [12]. Fig.3 shows the temperature dependence of the cesium ion conduction. The ionic conductivity,  $g$ , has an Arrhenius type dependence on the temperature;  $g = g_0 \cdot \exp[-(\Delta G^0/kT)]$ . The activation energy of the ionic conduction,  $\Delta G^0$ , is found to be  $0.71 \text{ eV/ion}$ . The effect of the current on the conductivity is negligible in the current density range up to  $1 \text{ mA}/\text{cm}^2$ . A slight decrease of conductivity has been seen in the high current range ( $>1 \text{ mA}/\text{cm}^2$ ).

### III. ION TRANSPORT ACROSS THE INTERFACE

#### 3.1 Interface Process

A comprehensive theory of the metal-SE interface has been presented in the previous paper[13]. Distribution of the space charge and the potential across the interface are shown in Fig.4, (a) and (b). The electrified interface (i.e. double layer) consists of the inner layer and the diffusion layer. Those layers are equivalent to a series connection of two capacitors.

**Current Interruption Method:** In order to explore the interface properties, the current interruption method[14] is employed, using the circuit diagram given in Fig.5. The cathode and the reference electrode are electrically separated by a groove in the porous tungsten thin film. The pellet is heated with the tungsten filament, placed inside the cylindrical cavity in the pellet. A constant current source has been used. The interruption of the current is controlled by a mercury relay with a response time of less than  $10^{-7}$  sec. The potential of the cathode with respect to the reference electrode is measured by an electrometer and the output signal from the electrometer is plotted with a high speed strip chart recorder.

The current interruption method is a technique of constant current interruption chronopotentiometry. A constant current is applied between the anode and the cathode.[Fig.6,(a)] Since the

reference electrode is not affected by the biasing current, the dependence of the electrochemical properties such as; current-overpotential characteristics and the capacitances of the double layer, could be obtained by measuring the potential difference between the reference electrode and the cathode electrode. The schematic diagram of potential transient by current interruption is shown in Fig.6 (b). The abrupt drop of the potential is the potential drop across the bulk of the electrolyte (i.e. ohmic). The transient of the potential is the interface potential (i.e. electrochemical overpotential). Two different time constants of the interface potential decay have been observed. It is believed that this is the effect of the double layer (i.e. inner layer and diffusion layer) at the interface.

**Electrode Reaction:** There are charge transfer reactions on both of the electrodes:



where M is matrix anion,  $[(\text{AlO}_2) \cdot (\text{SiO}_2)_2]$ . Electric field is applied between the anode and cathode electrodes. Cathode electrode is the emitting electrode in cesium source arrangement as shown in Fig.1,(c). On the anode, the matrix anions ( $\text{M}^-$ ) are deionized and the electrons are transferred to the anode metal electrode as indicated in eq.(1,a).  $\text{Cs}^+$  ions are driven to the

cathode and neutralized on the cathode as in eq.(1,b). The neutralized cesium atoms diffuse through the porous tungsten cathode to its surface where they evaporate as either ions or atoms.

### 3.2 Cathode Interface

At the cathode interface, cesium ions are accumulated and a double layer is formed. The measured current-overpotential characteristics for the cathode are presented in Fig.7. In order to compare the results with the theoretical curve, obtained in the previous paper[15], the measured current density is normalized to the exchange current, obtained numerically in the previous paper. The exchange current is only a function of temperature. A good agreement between theoretical curves and experimental results has been found. The limiting current density across the interface is about the same as the exchange current. A typical limiting current density of the order of 1 mA/cm<sup>2</sup> has been observed at 1000°C.

The capacitances of the double layer depend on temperature and current density. The absolute value of the capacitances of the double layer could not be measured by the current interruption method, however, the difference of the capacitances between the steady state ( $J \neq 0$ ) and the equilibrium state ( $J=0$ ), could be obtained. The typical capacitances and time constants (at 1000°C,  $J=50\mu\text{A}/\text{cm}^2$ ) are found to be of the order of milli

farad and minutes for the diffusion layer and of the order of a few tens of micro farad, and seconds for the inner layer.

### 3.3 Cesium Diffusion through the Porous Tungsten electrode

The dc steady emission current depends on the steady supply of cesium onto the surface of the emitting electrode. As seen on the schematic diagram of the ion source[Fig.1,(c)], the supply of cesium is provided by the biasing current in the electrolyte and cesium diffusion through the porous tungsten electrode. The biasing current can be controlled externally by the biasing voltage, however, the cesium diffusion through the porous tungsten electrode depends only on the concentration gradient which can not be controlled externally. According to the theoretical results of the previous paper, high coverage(about 0.4 at 1000°C) is found on the tungsten surface at the interface which is the inner layer in Fig.3,(a). The high coverage of cesium on the interface automatically enhance the cesium diffusion through porous tungsten electrode. Theoretical study of cesium diffusion through porous tungsten was done by A.T. Forrester[16]. By substituting the variables of our system such as porosity, pore size, and the thickness of the tungsten electrode and also the boundary value of the cesium concentration to his equation, a cesium flux density corresponding to 50 mA/cm<sup>2</sup> is obtained at 1000°C. Thus cesium diffusion through the porous tungsten electrode is not the limiting factor for the supply of cesium on to the emitting surface.

### 3.4 Anode Interface

On the anode, the matrix anions ( $M^-$ ) are deionized and the electrons are transferred to the anode metal electrode as seen in eq.(1,b). Since the matrix anions are fixed and no electron conduction occurs in Cs-M SE, there is a large electric field needed to pull the electrons to the anode after one interface layer of anions is depleted. Fig.8 shows the voltage needed to draw a constant current measured as function of the amount of charge passed per unit area of anode surface. The sharp increase of the voltage after a critical amount of charge,  $Q_0$ , could be explained by the depletion of electrons at the interface layer of matrix anions. The critical amount of charge,  $Q_0$ , depends on the effective area of the interface, according to equation;

$$Q_0 = \sigma \cdot l \cdot A_{eff}. \quad (2)$$

where  $\sigma$  is the charge density,  $l$  the average interatomic distance between anions which is about  $7 \text{ \AA}$ , and the effective area is  $A_{eff.} = k \cdot A_0$  (where  $k$  is a constant and  $A_0$  is a geometrical area). The constant  $k$  depends on the porosity, which in turn depends on the particle size,  $d_0$ . The pore volume is proportional to  $d_0^{3/5}$ , thus the incremental factor of the effective area,  $k$ , is linearly proportional to  $d_0^{4/5}$  (i.e.  $k = \alpha \cdot d_0^{4/5}$ ). The value of  $\alpha (=5.0 \cdot 10^7 [\text{cm}]^{5/4})$  has been empirically obtained for the  $1 \mu\text{m}$  particle size pellet. The values of  $Q_0$  for 2 and 3  $\mu\text{m}$  particle size calculated by using eq.(2), are shown on Table.2. The calculated values

1

reasonably agree with the experimental results in Fig.8.

After depletion, the current depends exponentially on the applied potential which could be explained by the electron tunneling current through the depleted layer[17]. Thus the life time of the cesium source is limited by the anode depletion. Life time of the order of 10 coulombs of cesium charge can be easily obtained by using about 5 cm<sup>2</sup> anode coating area.



#### IV. ION AND NEUTRAL EMISSION

##### 4.1 Experimental Arrangement

The schematic diagram of the measurement of ion and neutral emission is shown in Fig.9. The Cs-M pellet is heated to its operating temperature (800 to 1200°C) by an alumina coated tungsten filament. The planar diode type arrangement has been used for ion extraction and the spacing between emitter and extracting mesh (145x145 tungsten mesh) is 0.2 cm. A Faraday cup is used to measure the ion current. In order to suppress secondary electrons due to Cs<sup>+</sup> ion bombardment of the cup, retarding field is applied in front of the cup. Thus the current to the Faraday cup is solely due to the ion emission current. Cesium neutrals are measured by a hot tungsten filament which is heated to 1700°C. At this temperature, all the neutrals are ionized so that the neutral flux is equal to the ion current produced on the hot filament.

##### 4.2 Surface Ionization

On the emitter surface, Cs<sup>+</sup> ion emission takes place by surface ionization. The surface ionization process depends on temperature and work function of the emitter surface according to the Saha-Langmuir surface ionization equation;

$$J_n/J_i = w \cdot \exp[e(V_i - \phi)/kT] \quad (3)$$

where  $J_n$  and  $J_i$  are neutral and ion emission current densities respectively,  $w$  is the statistical weight ratio of atoms to ions,  $V_i$  (=3.9 eV) is the ionization potential of cesium, and  $\phi$  is the work function of the metal electrode. From the slope of  $\ln(J_n/J_i)$  as function of  $1/kT$  in Fig.10, the effective work function of the emitting tungsten surface is calculated and its value is 4.2 eV.

#### 4.3 Dependence of Cs<sup>+</sup> Ion Emission on Cesium Supply

In steady state operation, the ion emission current density must be equal to the supply current density. Thus the Cs<sup>+</sup> ion emission characteristics have to be studied in conjunction with the supply of cesium on the emitter surface. In our Cs<sup>+</sup> ion source arrangement the supply has two limitations which are the limiting current density across the interface and the self-consistent thermal leakage flux across the interface. In order to see the dependence of ion emission on cesium supply, ion emission current was measured as function of extraction voltage with and without cesium supply by biasing current across the electrolyte. The I-V characteristics of ion emission is shown in Fig.11. In the low voltage range where space charge limited operation should be in effect, emission current density follows the Child-Langmuir law

$$J = k \cdot V^{3/2} / d^2 \quad (4)$$

where  $k=4.7 \times 10^{-9}$  [Volt, A, cm] for cesium, and  $d$  ( $=0.2$  cm) is the spacing between the extraction mesh and the emitter surface. In the high voltage range, the emission current is limited by supply of cesium to the emitter surface. The emission currents have been extracted without biasing (i.e. open circuit between anode and cathode of the Cs-M SE pellet). The cesium supply without biasing could be explained by the thermal leakage flux across the interface which is due to the self-consistent potential across the interface. With additional supply of cesium by biasing current, one can extend the space charge limited region in the low temperature range.

The thermal leakage flux is also observed in neutral emission. When there is no extraction field on the emitter surface, cesium is vaporized from the surface as neutral atoms. The flux is equal to the supply of cesium to the emitter surface in steady state. Since there is no supply by external biasing current across the electrolyte, the neutral flux is just due to the thermal leakage flux. The dependence of the thermal leakage flux on temperature is shown in Fig.12. The maximum space charge limited ion emission flux without supply by biasing current, shown in Fig.11., is drawn as dashed line in Fig.12. It is seen that both fluxes are approximately the same. According to the potential diagram of the interface, shown in Fig.4,(b), a positive electric field directed toward the emitting electrode is induced due to the interfacial potential difference,  $U_i$ , between

the tungsten electrode surface and Cs-M SE surface. The electric field is extracting electrons from the Cs-M SE surface. The electrons are then combined with the adsorbed cesium ions on the inner layer. The neutralized cesium atoms diffuse out to the vacuum interface of the emitting electrode. The flux of cesium is the thermal leakage flux across the interface. Thus one can interpret the results in Fig.12 as the electron emission characteristics on the Cs-M SE surface. The linear slope in Fig.12 indicates that the extracting field (i.e. potential difference across the interface,  $\Delta U^1$ ) is independent of temperature. The potential difference across the interface, numerically obtained in the previous paper[19], is almost constant in the temperature range of 800-1000°C.

There is one more evidence that the thermal leakage flux is due to the electron emission from the Cs-M SE to the tungsten electrode surface. By observing the neutral flux over long time, the neutral flux is decaying slowly with time. In the long run, the neutral flux goes to zero. The total amount of emitted neutrals is about equal to one monolayer of the M- matrix anions. This fact is not only proving the mechanism of the thermal leakage flux but also provides a method for exact control of the supply of cesium to the emitter surface. After depletion of the electrons from the emitter interface, there is no supply of cesium by the thermal leakage flux. Thus the supply of cesium to the emitter surface is then exactly controlled by the external

biasing current across the interface. Practically the electron charge to be depleted is of the order of 2 coulombs/cm<sup>2</sup>. This charge can be extracted in the reverse bias mode (i.e. positive potential on the emitting electrode and negative potential on the anode) in about 3 hours at total biasing current of 20  $\mu$ A prior to using the ion source.

The supply of cesium to the emitter surface is now exclusively controlled by the biasing current across the electrolyte. However, the biasing current is limited by the maximum electrode reaction current density across the interface. From both theoretical and experimental results, the limiting current density across the interface is of the order of 1 mA/cm<sup>2</sup> at 1000°C. In order to increase the emission current density to more than 10 mA/cm<sup>2</sup>, we have modified the emitter configuration. A thin diaphragm with an aperture of 0.08 cm in diameter is covering the emitter surface. Thus all cesium supplied to the emitting electrode is delivered to this emitting aperture by surface diffusion. The ratio of the tungsten electrode area to the area of emitting aperture is about 200. Thus the emission current density is 200 times larger than the supply current density. In this way, one can obtain a high emission current density while minimizing the supply current density across the electrolyte.

#### 4.4 High Cs<sup>+</sup> ion Emission Current Density

In order to have a steady state high emission current density, the following extraction arrangement has been used; an extraction electrode with a single aperture, 0.08 cm in diameter, is aligned with the emitting aperture. The distance between the two apertures is 0.05 cm. All the other experimental arrangements are the same as in Fig.9.

Since our source is a surface ionization source, the maximum ion emission current density depends on the critical temperature of the emitter. The critical cesium ion emission current density has been measured by R.G. Wilson [21,22] for several metal surfaces. His results are shown in Fig.13 as solid lines. The points show experimental results obtained with our source for porous platinum and tungsten emitter coating. The slightly smaller values compared to Wilson's data can be attributed to the porous surface of the emitter. In dc steady state operation, up to 20 mA/cm<sup>2</sup> current density at a temperature of 1100°C has been extracted for 30 hours at a total current of 100  $\mu$ A. The total amount of extracted cesium ions corresponds to 10 coulombs.

## V. SUMMARY

The new solid state Cs<sup>+</sup> source compares favorably with the metal ionizer type source with respect to the ion emission current density and life time. It has the simplicity in construction and operation comparable to the zeolite type source. Furthermore, it has the unique capability of exact control of cesium supply to the emitting electrode.

A solid state Cs<sup>+</sup> ion micro-probe (micron size beam and high current density >10 mA/cm<sup>2</sup>) has been developed by using this source. Design and operation of the micro-probe will be presented in a forthcoming paper.

## REFERENCES

1. H.A. Storms, K.F. Brown, and J.D. Stein, Anal. Chem., 49, 2023 (1977)
2. J.L. Lopes, J.A. Greer, and M. Seidl, J. Appl. Phys., 60, 17 (1986)
3. R.U. Martinelli, J. Appl. Phys., 45, 1183 (1974)
4. G.R. Brewer, Ion Propulsion (Gorden and Breach, New York, 1970)
5. D.G. Welkie, Secondary Ion Mass Spectroscopy SIMS V, A. Benninghoven et al. Editors (Springer 1986) p.146
6. O. Heinz and R.T. Reaves, Rev. Sci. Instrum. 39, 1230 (1968)
7. M. Seidl, A.E. Souzis, W.E. Carr, and G. Tompa, Pittsburgh Conference on Analytical Chemistry and Applied Spectroscopy, Absts. No.743 (Atlantic City, 1986)
8. M. Seidl, US Patent 4,783,595
9. S.I. Kim and M. Seidl, J. Electrochem. Soc., to be published
10. J. Ito, Am Mineralogist, 61, 170 (1976)
11. D.W. Breck, Zeolite Molecular Sieves (Academic Press, 1976)
12. Y. Haven and P. Hagenmuller, Solid Electrolytes, W. van Gool Editor (Academic Press, New York, 1978), chap.5
13. S.I. Kim and M. Seidl, *ibid*
14. D.Y. Wang and A.S. Nowick, J. Electrochem. Soc., 126, 1155 (1979)
15. S.I. Kim and M. Seidl, *ibid*
16. A.T. Forrester, J. Chem. Phys., 42, 972 (1965)



17. J.O'M. Bockris and A.K.N. Reddy, Modern Electrochemistry,  
Vol.2 (Plenum Press, New York, 1970), p.954
- 18 S.I. Kim and M. Seidl, *ibid*
19. R.G. Wilson, J. Appl. Phys., 37, 3161 (1966)
20. R.G. Wilson, J. Appl. Phys., 42, 972 (1965)

## FIGURE & TABLE CAPTIONS

Figure 1. Schematic diagram of various types of  $\text{Cs}^+$  source

- (a) metal ionizer type source
- (b) zeolite type source
- (c) our source, combination of (a) and (b)

Figure 2. Morphology of the porous tungsten thin film

- (a) top view
- (b) cross sectional view

Figure 3. Temperature dependence of the  $\text{Cs}^+$  ion conductivity

Figure 4. Electrified interface between metal electrode and solid electrolyte

- (a) space charge distribution in the interface double layer
- (b) potential distribution

Figure 5. Schematic diagram of the conductivity and interface potential measurements (cathode and reference electrodes are drawn in large scale on the upper-left side)

Figure 6. The current interruption method

- (a) constant current is applied, current interruption is made after the steady state is reached,
- (b) potential transient of the cathode with respect to the reference electrode.

Figure 7. Current-overpotential characteristics (lines are obtained numerically from the previous paper)

Figure 8. Critical charge of the anode depletion per an unit area

Figure 9. Schematic diagram of the measurement of cesium ion and neutral emission

Figure 10. Temperature dependence of cesium ion and neutral emission

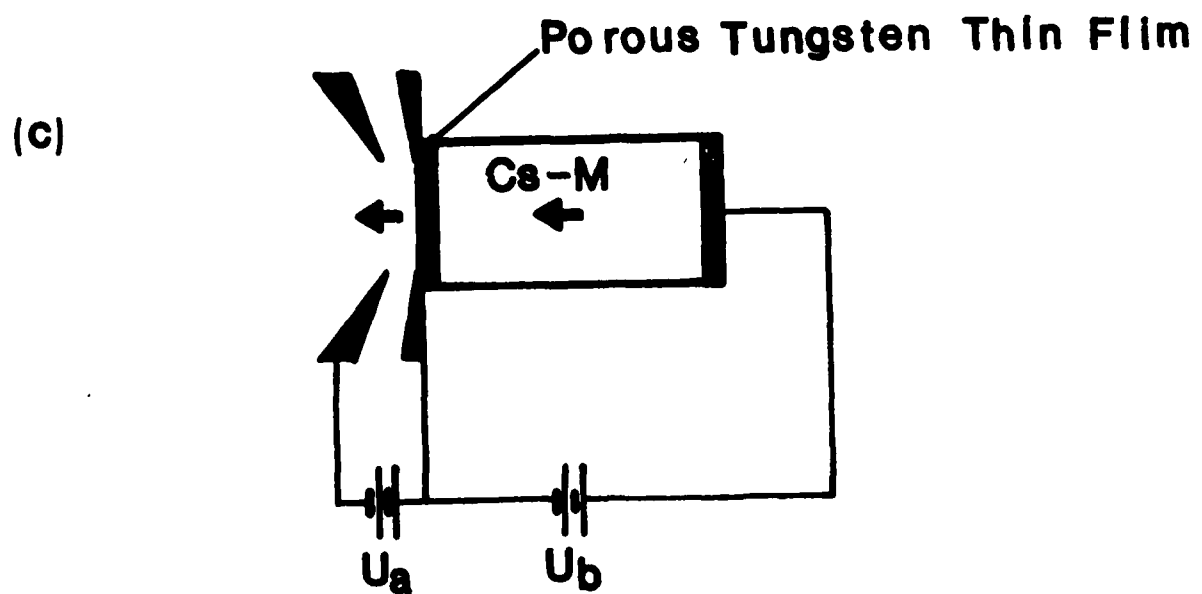
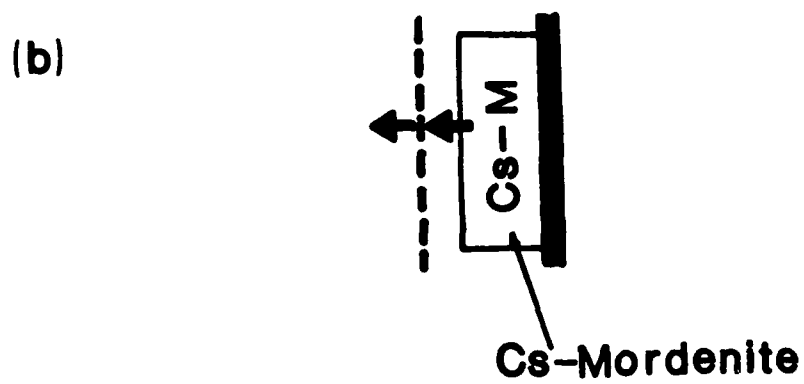
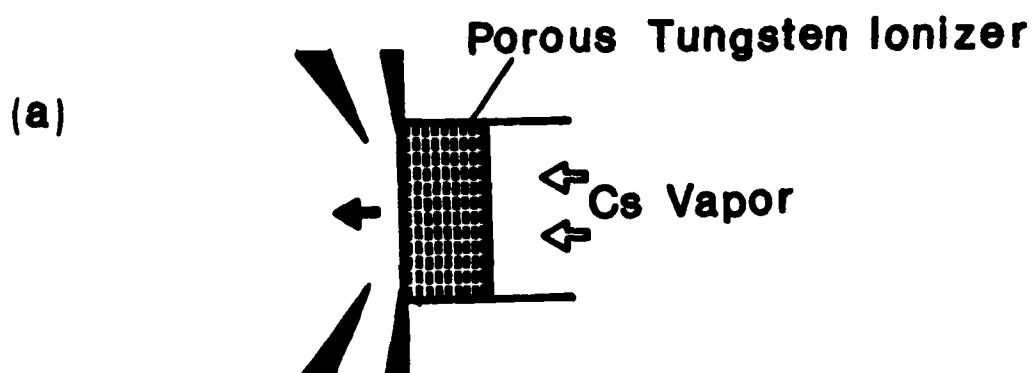
Figure 11. I-V characteristics of  $\text{Cs}^+$  ion emission (with and without biasing current)

Figure 12. Cesium neutral flux and the maximum space charge limited ion current density with a supply by the thermal leakage flux

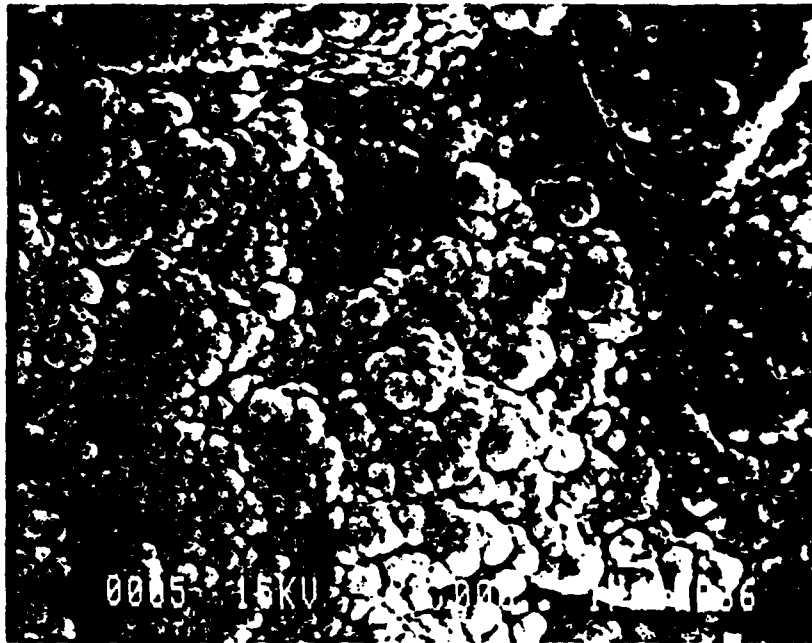
Figure 13. Critical  $\text{Cs}^+$  ion current density (solid lines are from R.G. Wilson, J. Appl. Phys., 42, 972, 1965)

Table 1. Chemical Analysis by EDX

Table 2. Calculation of Critical Charge for Anode Depletion

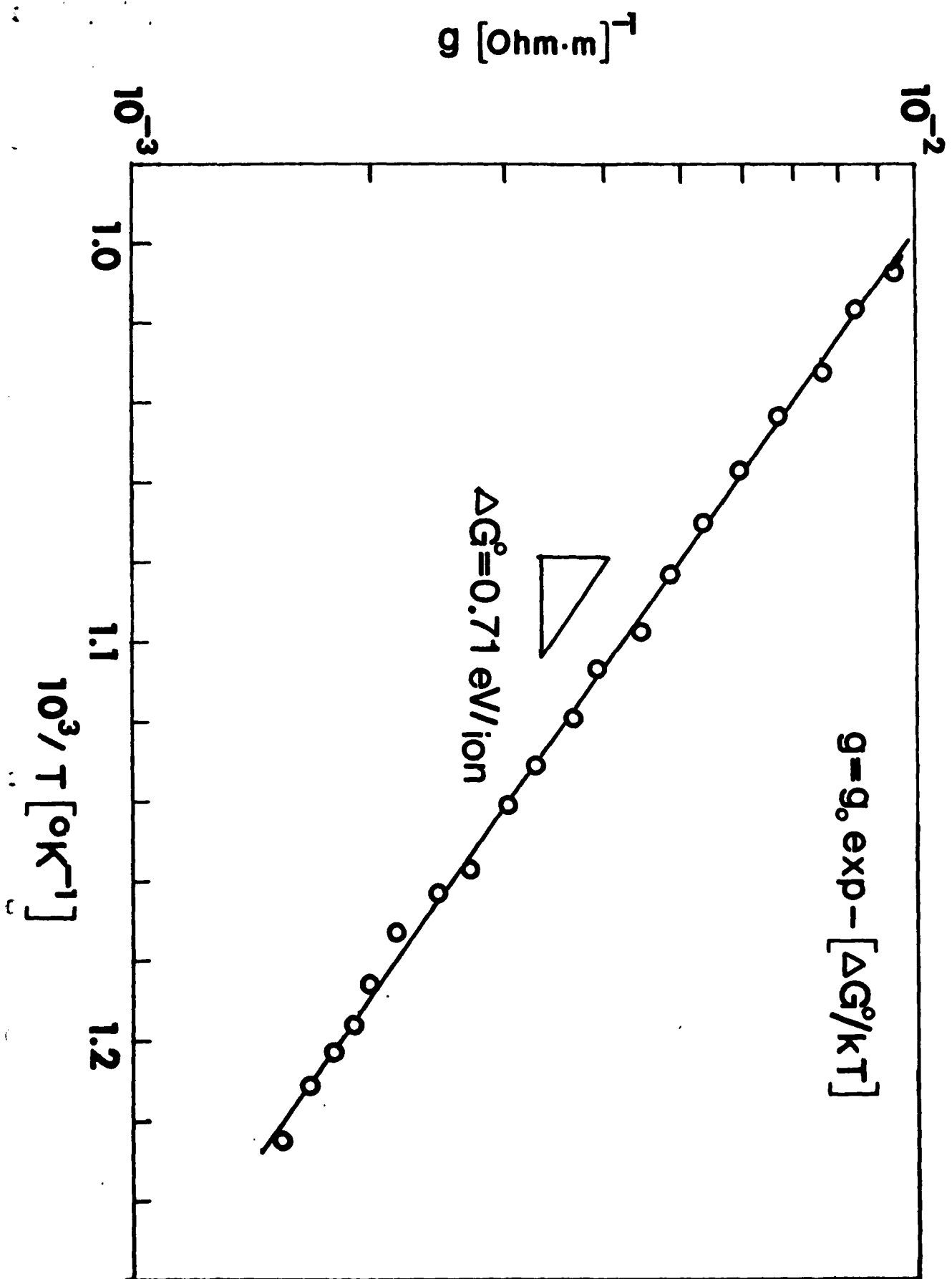


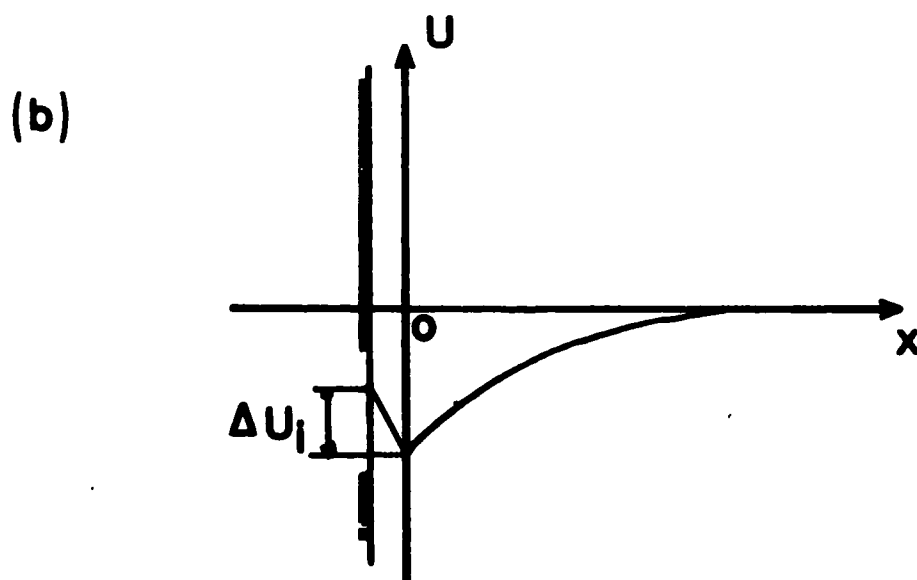
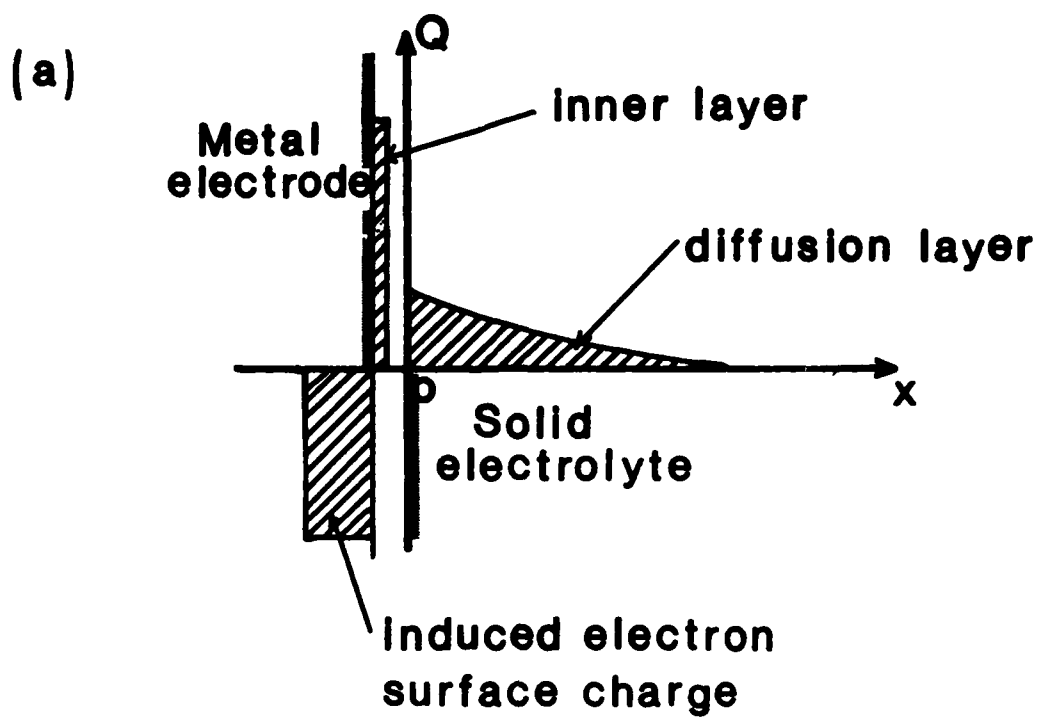
a

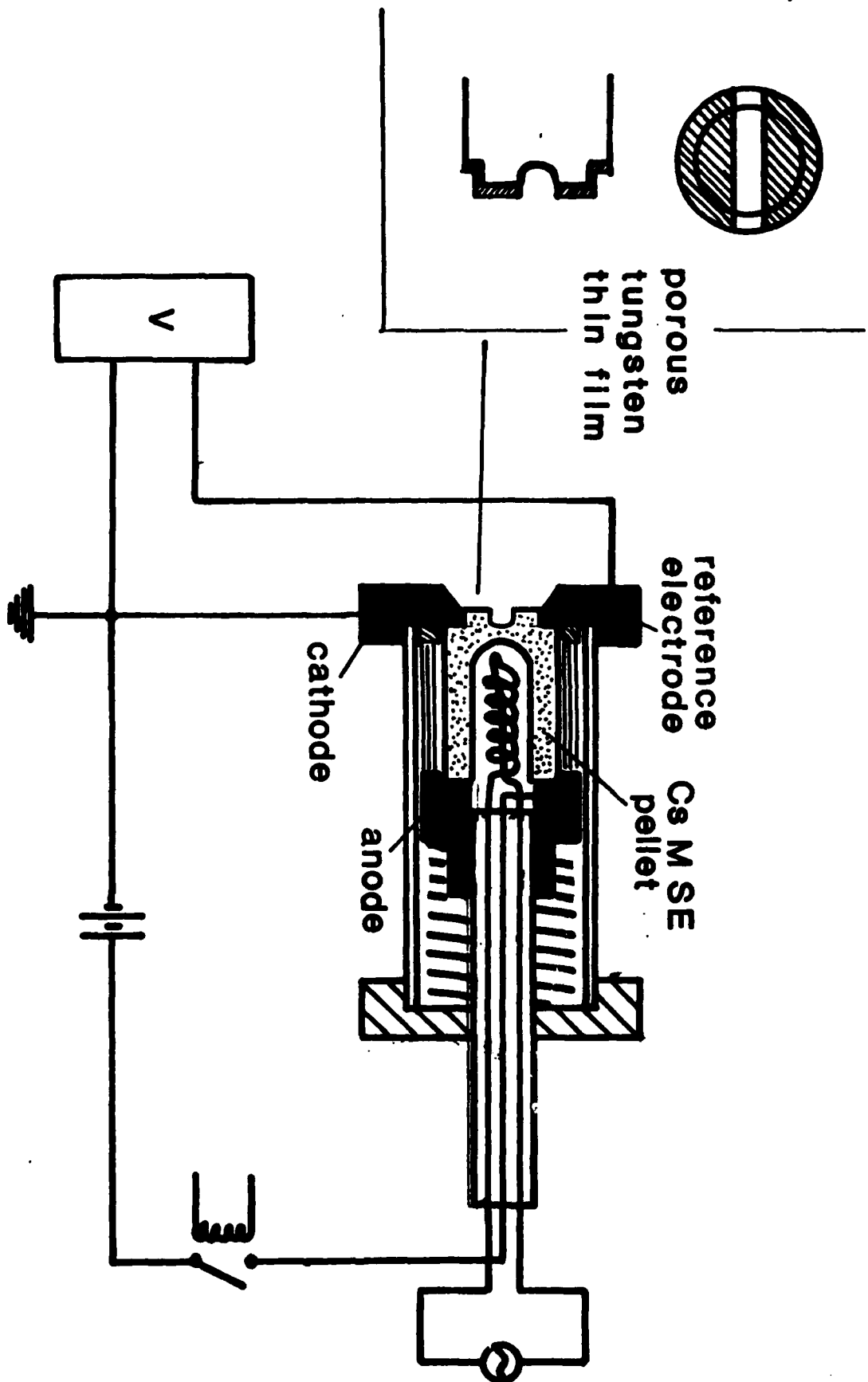


b



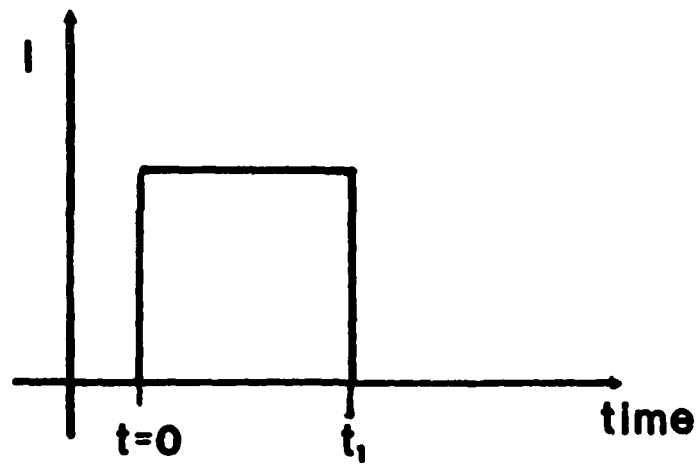




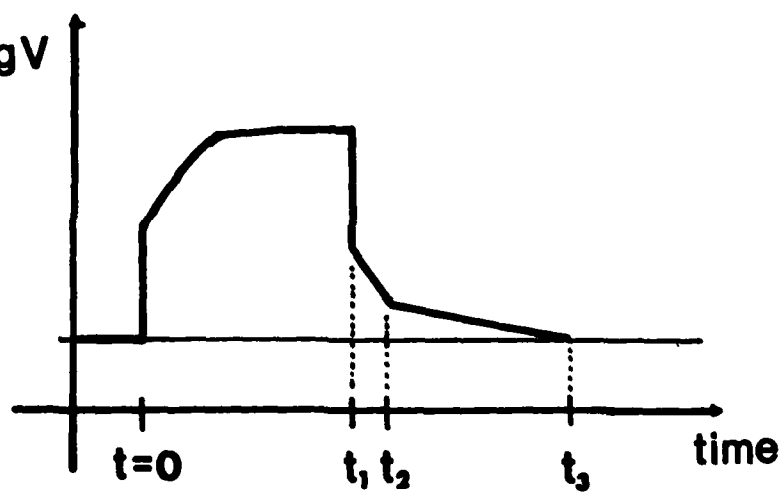


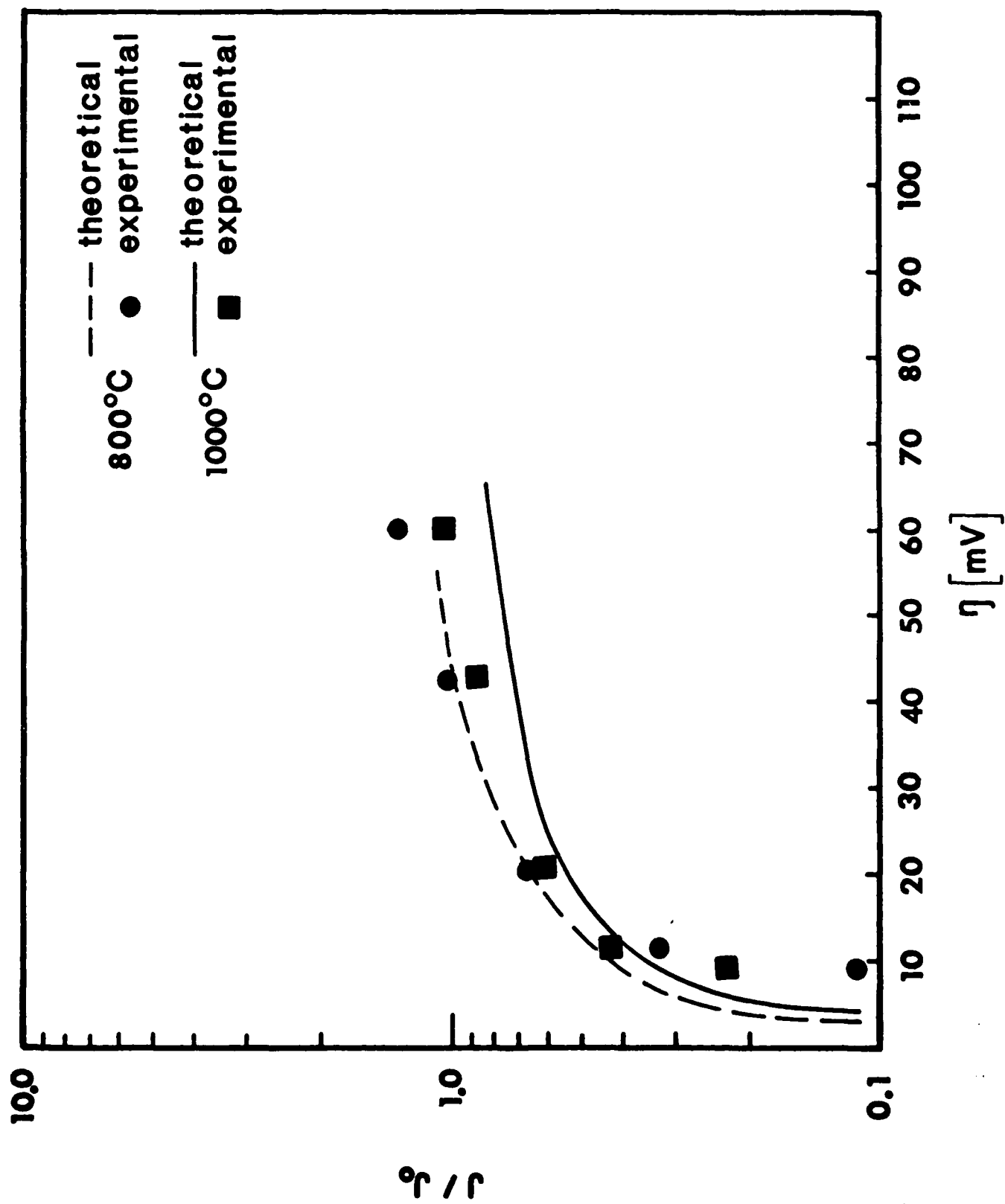


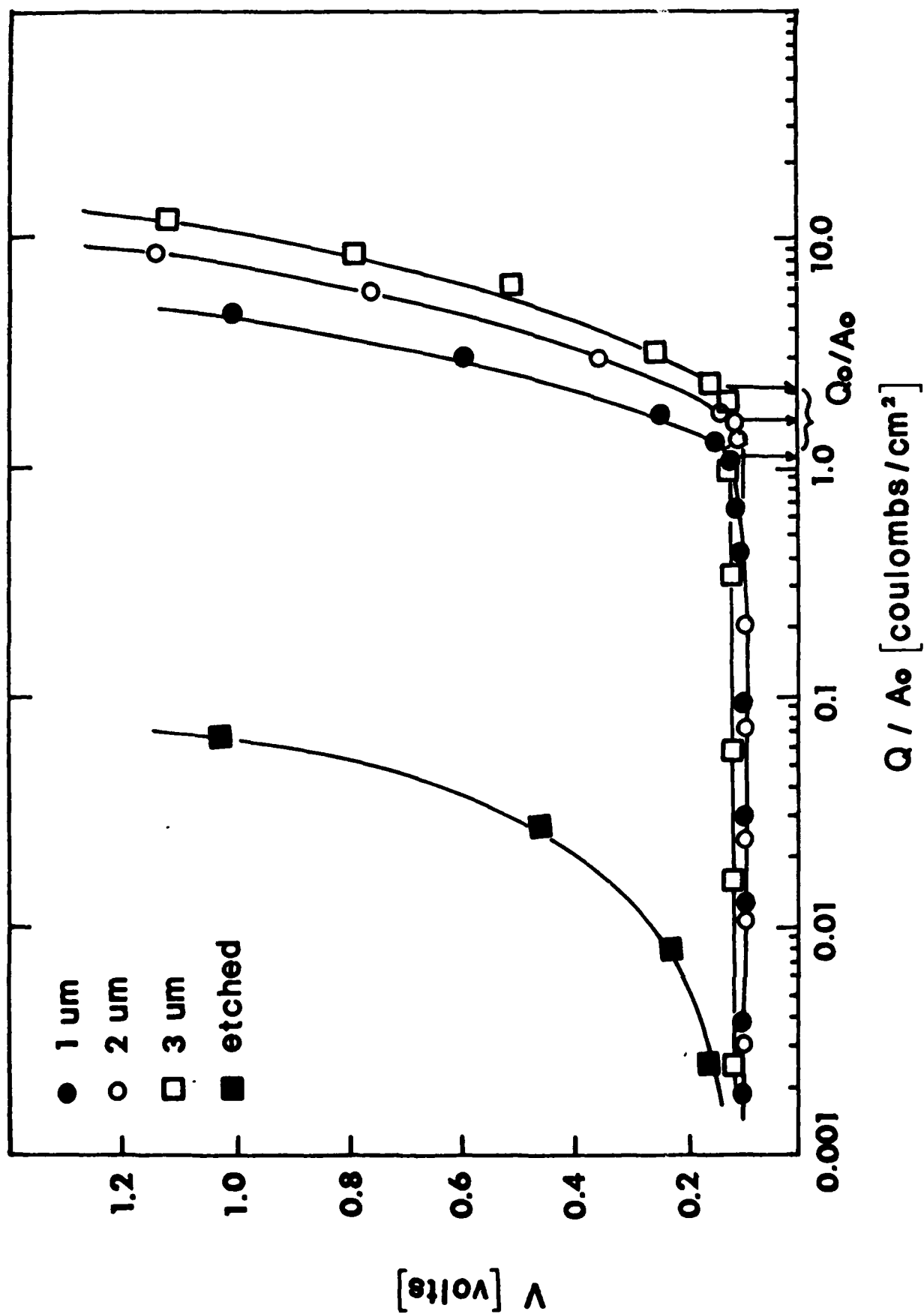
(a)

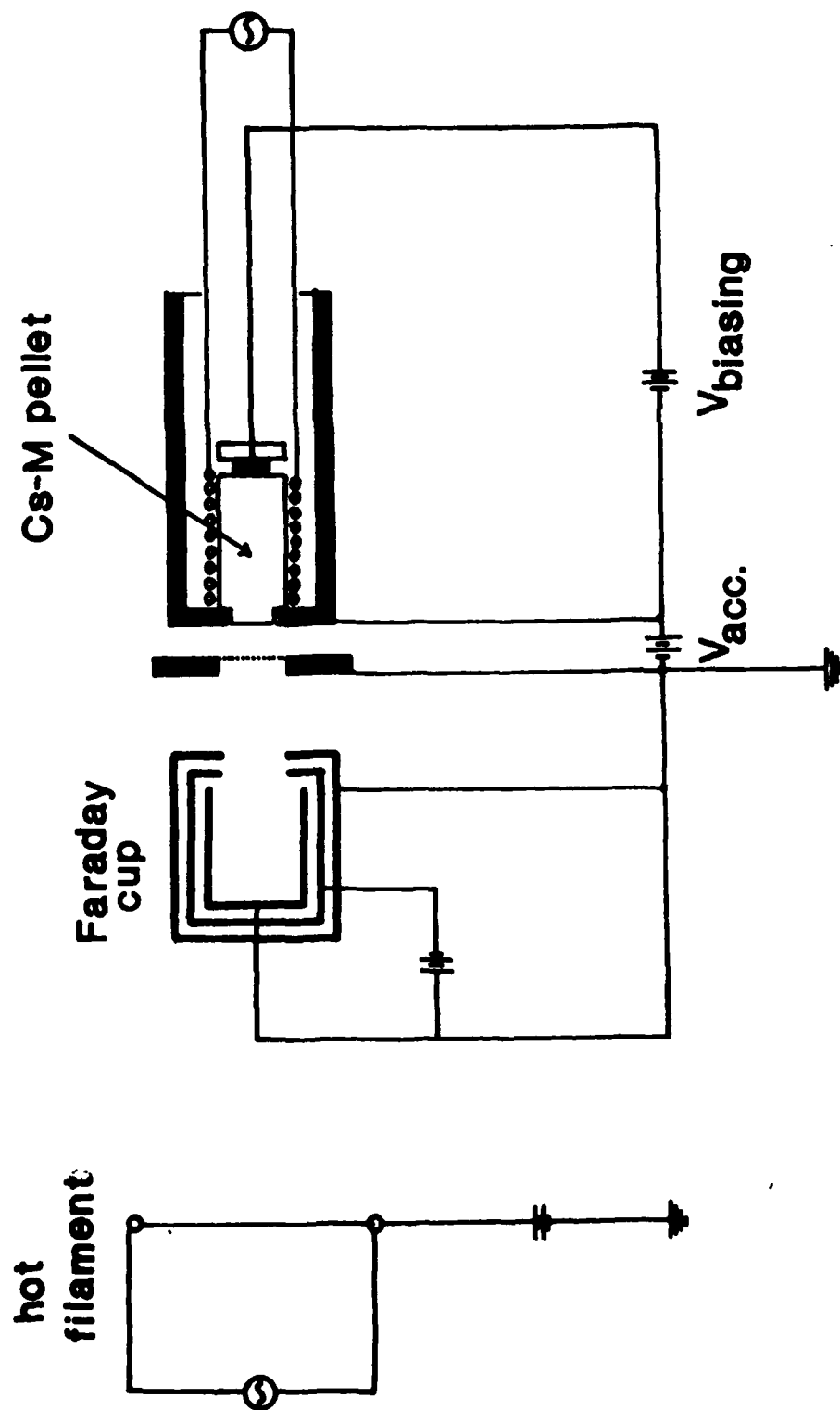


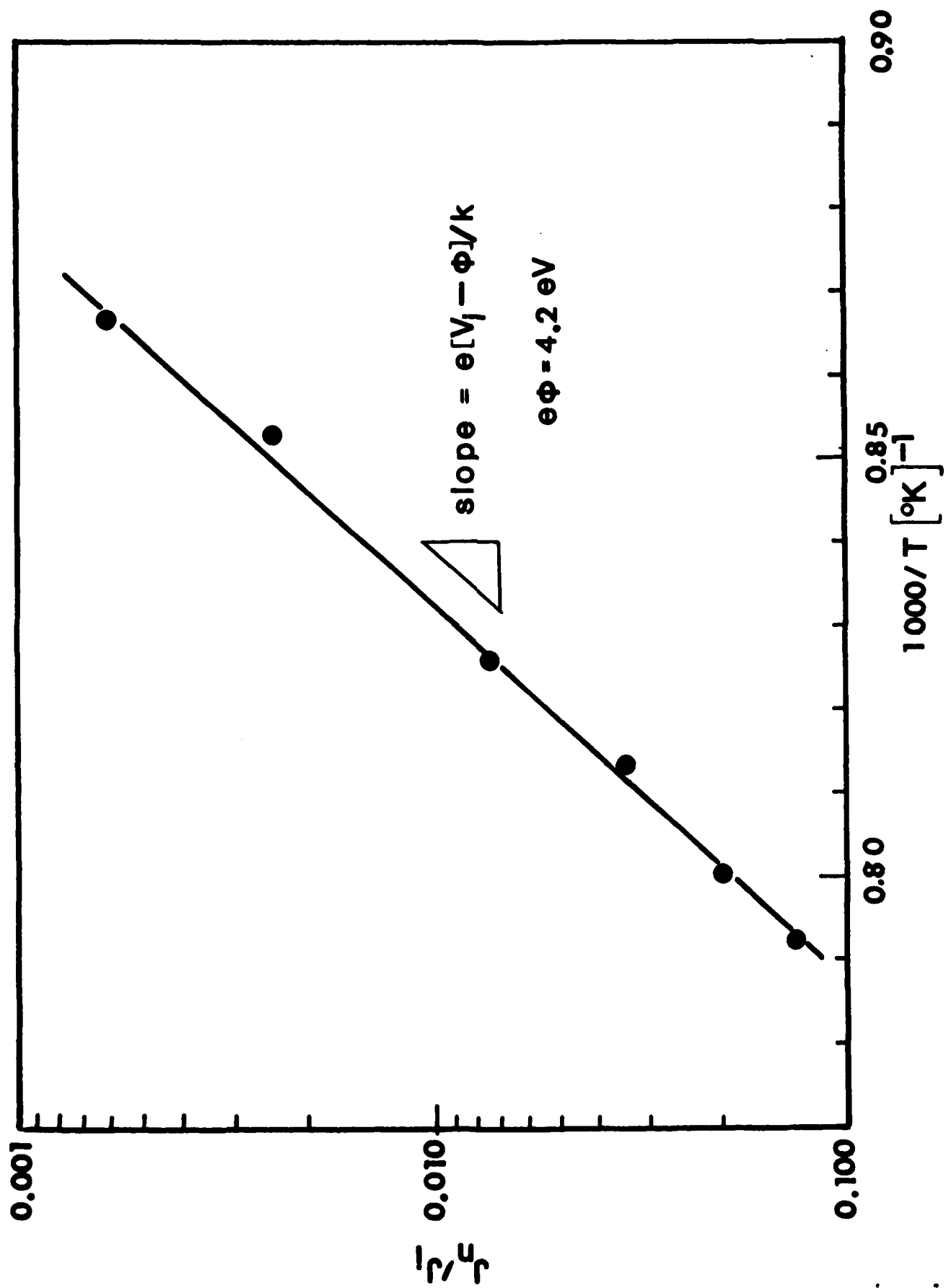
(b)  $\log V$

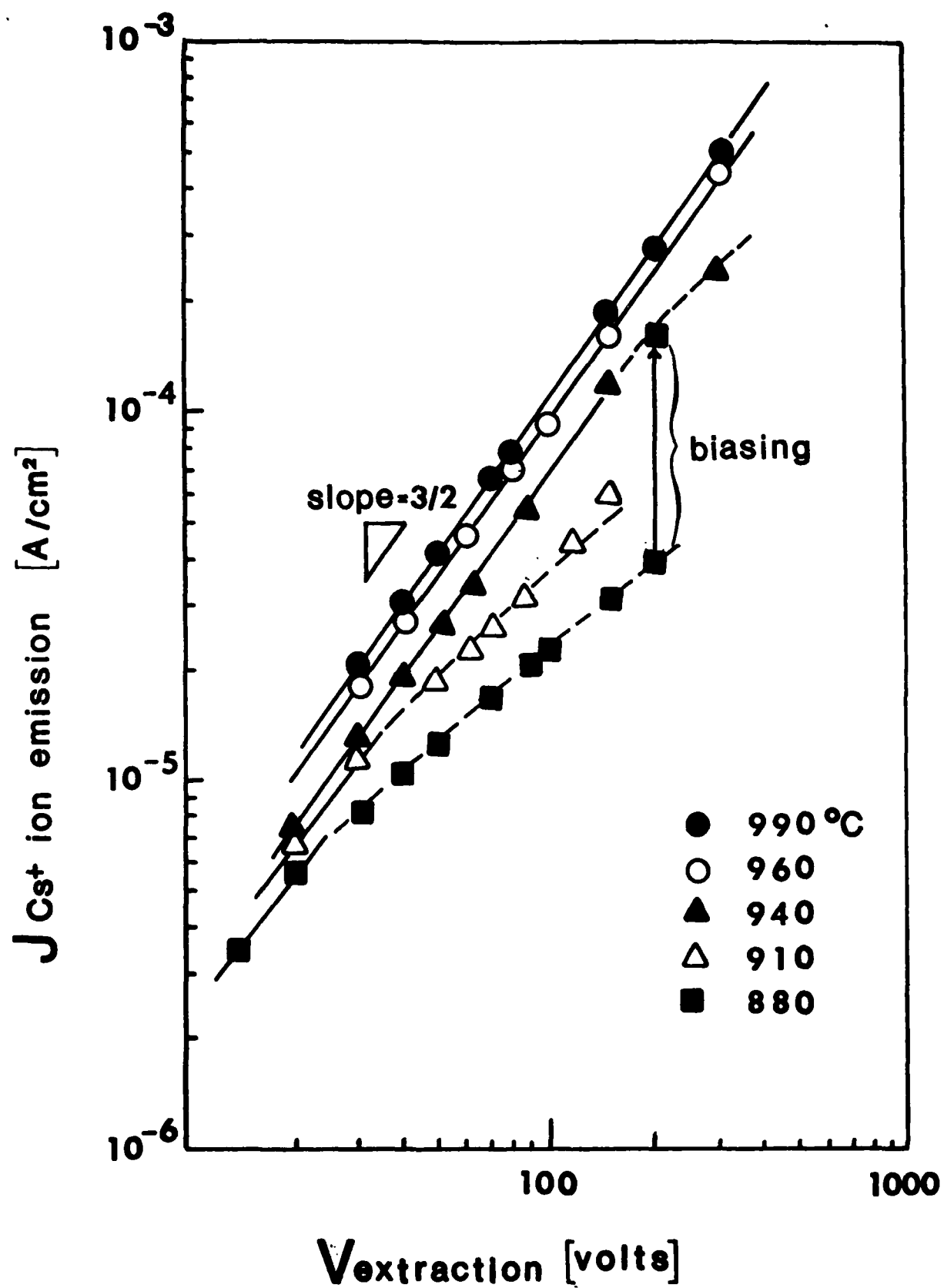


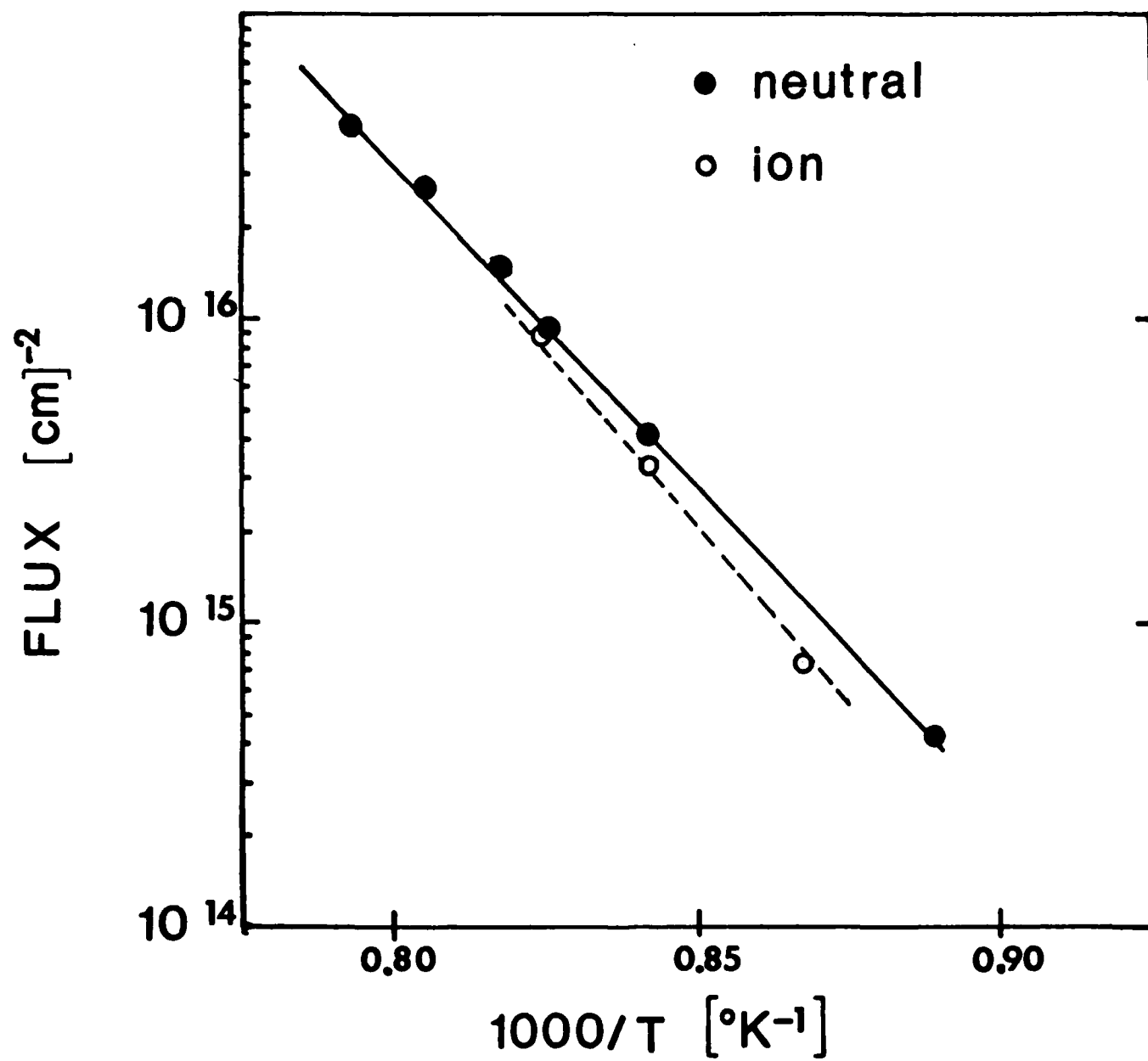


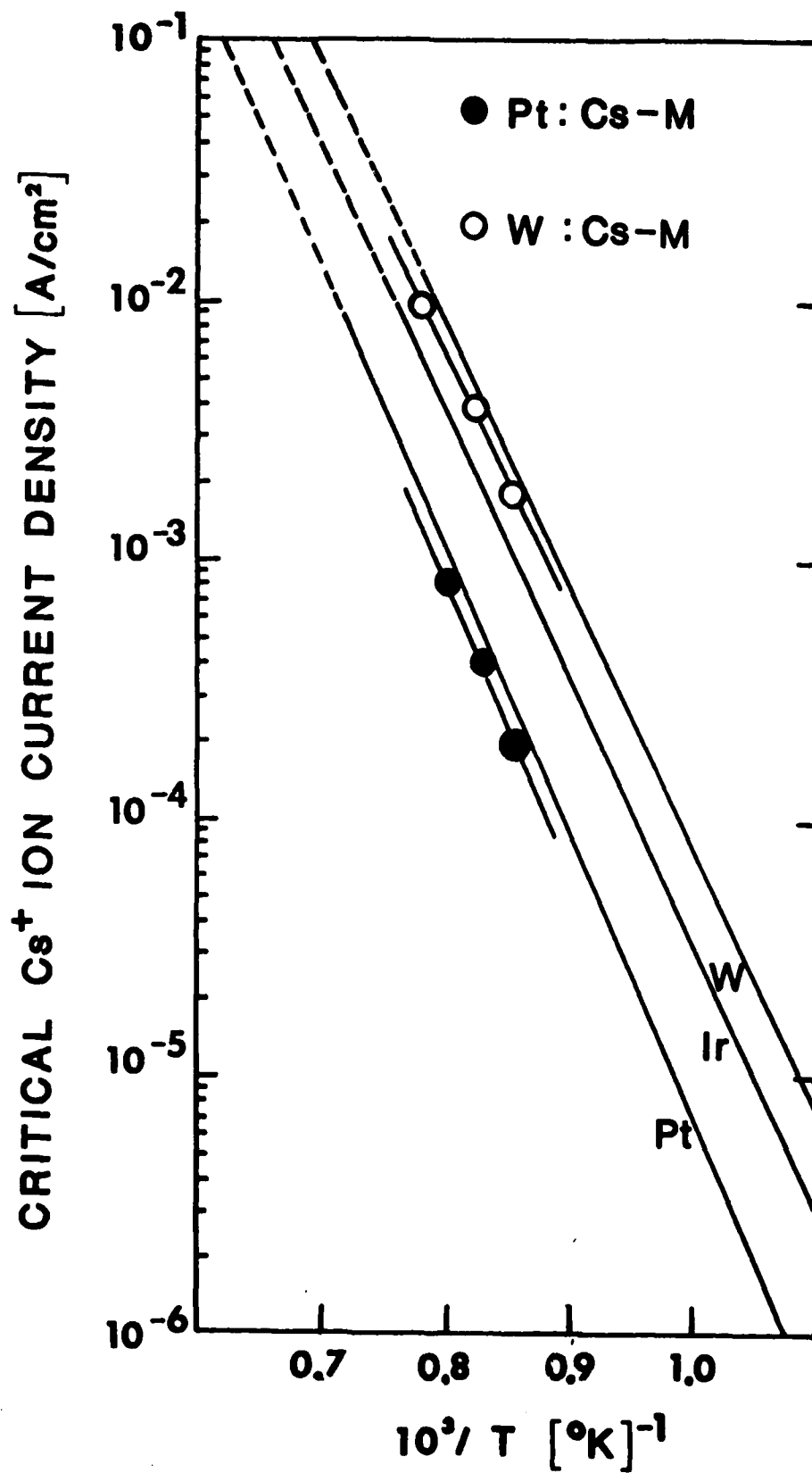














	Al	Si	Cs	Na	Cs/Si	Al/Si
ion exchanged	3.3	3 3.4	55.2	0.1	1.65	0.1
sintered	7.1	4 9.7	43.2		0.87	0.14
stoichiometry	8.8	4 9.3	41.9		0.85	0.18

$d_o[\mu\text{m}]$	$q[\text{coul./cm}^3]$	$k=A_o/A$	$Q_o[\text{coul.}]$	$Q_o/A_o[\text{coul./cm}^2]$
1	509	$5.6 \times 10^3$	0.20	1.18
2	437	$12.6 \times 10^3$	0.38	1.65
3	382	$23.6 \times 10^3$	0.64	2.06

## SOLID STATE CESIUM ION GUNS FOR SURFACE STUDIES

A.E. Souzis, W.E. Carr, S.I. Kim and M. Seidl

Physics and Engineering Physics Department

Stevens Institute of Technology, Hoboken, New Jersey 07030

### ABSTRACT

Three cesium ion guns covering the energy range of 5 to 5000 V are described. These guns use a novel source of cesium ions that combines the advantages of porous metal ionizers with those of aluminosilicate emitters. Cesium ions are chemically stored in a solid electrolyte pellet and are thermionically emitted from a porous thin film of tungsten at the surface. Cesium supply to the emitting surface is controlled by applying a bias across the pellet. A total charge of 10.0 coulombs can be extracted, corresponding to greater than 2000 hours of lifetime with an extraction current of 1.0  $\mu$ A. This source is compact, stable and easy to use, and produces a beam with  $> 99.5\%$  purity. It requires none of the differential pumping or associated hardware necessary in designs using cesium vapor and porous tungsten ionizers. It has been used in UHV experiments at pressures of  $< 10^{-10}$  torr with no significant gas load.

Three different types of extraction optics are used depending on the energy range desired. For low energy deposition, a simple space charge limited planar diode with a perveance of  $1 \times 10^{-7}$  A/V<sup>3/2</sup> is used. Current densities of 10.0  $\mu$ A/cm<sup>2</sup> at the exit aperture for energies  $< 20$  V are typical. This type of source provides an alternative to vapor deposition with the advantage of precise flux calibration by

integration of the ion current. For energies from 50 to 500 V and typical beam radii of 0.5 to 0.2 mm, a high perveance Pierce type ion gun is used. This gun was designed with a perveance of  $1 \times 10^{-9} \text{ A/V}^{3/2}$  and produces a beam with an effective temperature of 0.35 eV. For the energy range of 0.5 to 5 KeV, the Pierce gun is used in conjunction with two einzel lenses, enabling a large range of imaging ratios to be obtained. Beam radii of 60 to 300  $\mu\text{m}$  are typical for beam currents of 50 nA to 1.0  $\mu\text{A}$ . Results are presented and discussed for UHV studies of ion implantation, electronic surface changes induced by adsorbates and negative secondary ion mass spectrometry (SIMS).

## I. INTRODUCTION

It is well known that the work function of a metal or semiconductor surface is lowered when the surface is covered with a sub-monolayer deposit of cesium [1-5]. This effect has been used in cold cathode electron sources [6,7], negative ion sources [8], and for enhancing the secondary negative ion yield of atoms and molecules [9,10]. The presence of cesium greatly enhances the low temperature oxidation and nitridation kinetics on semiconductor surfaces [11,12].

Cesium may be deposited on surfaces either by vapor deposition, or an ion beam. Vapor deposition sources require shielding, differential pumping, and flux calibration. With an ion source, the incident flux is determined by direct measurement of the target current, and differential pumping may not be necessary. On the other hand, space charge effects put a lower limit on the incident ion energy.  $\text{Cs}^+$  ion sources are typically of the surface ionization type, since the ionization potential of cesium is smaller than the work function of most surfaces. Surface ionization sources also have an inherently low beam temperature.

There are two basic types of  $\text{Cs}^+$  surface ionization sources. One is a heated porous tungsten plug which is fed from behind with cesium vapor from a hot liquid metal oven [13,14]. It has a high current density, and low beam temperature, with the disadvantages of differential pumping and problematic routine venting due to pore clogging. A second type typically consists of a thin layer of aluminosilicate deposited on a heated tungsten base. Cesium ions are chemically stored in the aluminosilicate, and are emitted thermionically [15]. This arrangement is simpler, and

no differential pumping is required, but other disadvantages exist. The emitting surface is not unipotential, resulting in large energy spreads, and the amount of cesium stored in the thin layer is small.

We have developed a cesium ion source which combines the advantages of porous metal ionizers and aluminosilicate emitters [16]. Cesium ions are chemically stored in a solid electrolyte pellet whose emitting surface is coated with a porous thin film of tungsten. At an operating temperature of  $\approx 1000^\circ\text{C}$  the solid electrolyte is a good conductor of cesium ions. This makes it possible to control the cesium supply to the emitting surface by a voltage applied across the pellet. Cesium ion emission occurs on the surface of the porous tungsten cathode by surface ionization. This source is clean, compact, efficient, and is compatible with any vacuum system from  $10^{-6}$  to  $< 10^{-10}$  torr.

In this paper, we first describe the source in more detail. We then discuss three types of extraction geometries using this source. For energies from 5 to 50 eV a space charge limited planar diode geometry is used. In the energy range of 50 to 500 eV, we use a Pierce type [17] extraction geometry. For the energy range of 0.5 to 5 keV, this Pierce gun is followed by a two lens optical column. Applications of these guns are also discussed.

## II. $\text{Cs}^+$ SOURCE

The basic element of this source is a cylindrical pellet (0.5 cm in diameter and 1 cm long), sintered from cesium mordenite (Cs-M) powder. The pellet and its

emission characteristics are described in detail elsewhere [18], but the basics are as follows. Cs-M is a solid electrolyte which has an aluminosilicate matrix with an interchangeable cation. When heated,  $\text{Cs}^+$  ions are conducted through its channel structure. The structure has a two dimensional channel system and its pore size is about  $6 \text{ \AA}$  in diameter. This is known as large-port mordenite [19].

The Cs-M powder  $[\text{Cs}_2\text{OAl}_2\text{O}_3(\text{SiO}_2)_{10}]$  is obtained from Na-M  $[\text{Na}_2\text{OAl}_2\text{O}_3(\text{SiO}_2)_{10}]$  by ion exchange [20], and then heating to  $1050^\circ\text{C}$ , resulting in a phase transformation from Na-M to Cs-M structure. It is then crushed and ground to a particle size of  $\approx 1 \text{ }\mu\text{m}$ , pressed in a cylindrical die, and sintered at  $1350^\circ\text{C}$  for 3 hours. The resulting pellet can be machined with a small grinding wheel for use in special applications.

The pellet is heated by an alumina coated 0.25 mm tungsten filament coiled around the pellet. In order to reduce the power losses, coaxial Ta shields are mounted around the filament. The entire arrangement is placed inside a thin walled stainless steel tube with the emitting electrode at one end, and a spring loaded compression assembly at the other. Figure 1 shows this assembly as used with the Pierce electrodes to be discussed later. Around 15 to 18 watts of power are required to achieve an operating temperature of  $1000^\circ\text{C}$ . At this temperature, the Cs-M is an ionic conductor with a conductivity of  $\approx 10^{-6} (\text{ohm cm})^{-1}$ .

The emitting surface of the pellet is sputter coated with a thin porous tungsten layer. This layer improves the energy spread of the beam by providing a unipotential surface for emission, and provides a means to supply a flux of ions to the emitting surface. By coating the back of the pellet with a thick layer of

platinum, the flux of cesium ions can be controlled by a voltage placed across the pellet. Cesium diffuses through the porous tungsten film to the emitting surface, where it is surface ionized and extracted. A total charge of 10.0 Coulombs can be extracted from the source. This corresponds to greater than 2000 hours of lifetime at an extraction current of  $1 \mu\text{A}$ .

This source has the same high emission current density properties as the porous tungsten ionizers. In its present form, we have extracted up to  $30 \text{ ma/cm}^2$  in d-c steady state operation. However, it does not need to be differentially pumped, and the thin tungsten film can be vented repeatedly to atmosphere without any pore clogging problems, which can occur with thicker porous plugs. In addition, the cesium stored in the Cs-M is stable upon repeated exposure to atmosphere and can be handled without any special precautions or dangers, unlike the liquid metal based sources.

The time needed to degas the source is  $\approx 1$  day at a pellet temperature  $\approx 1100^\circ\text{C}$ . Once outgassed, there is no discernible gas load at a pressure of  $< 10^{-10}$  torr, and the source may be operated without changing the system pressure. After the initial break-in period, the source is normally kept hot ( $\approx 500^\circ\text{C}$ ), eliminating start up outgassing, and preventing adsorption of contaminants on the gun assembly. It has been reported that zeolite sources are gassy and easily contaminated by active gases [4], but we have not found this to be a problem with our arrangement.

The beam produced by an early version of this source contained  $< .40\% \text{ Rb}^+$ ,



$<.05\% \text{ K}^+$  and  $<.02\% \text{ Na}^+$ . The relatively high percentage of  $\text{Rb}^+$  was due to  $\text{Rb}$  impurity in the  $\text{CsCl}$  (99% pure) used in the ion exchange process. This form of contamination has been seen before [21] and is greatly reduced by using higher purity  $\text{CsCl}$  (99.9%).

### III. EXTRACTION GEOMETRIES AND RESULTS

#### A. PLANAR DIODE

For deposition energies from 5 to 50 eV, a planar diode extraction geometry is used. The source is assembled as shown in figure 1, with the substitution of planar electrodes for the Pierce electrodes. The emitting end of the pellet is machined with a small step, such that the emitting surface is flush with the exterior of the electrode surface. The extraction electrode is spaced 0.75 mm from the pellet surface, and has a tungsten mesh spot welded over the extraction aperture in order to provide a uniform field. The theoretical perveance of this planar diode arrangement is  $1 \times 10^{-7} \text{ A/V}^{3/2}$ . Target currents  $> 1 \mu\text{A}$  at energies  $< 20 \text{ V}$  are typical. This gun has been used in studies of electronic surface changes induced in silicon by cesium deposition [22], where it is seen to be fully equivalent to a vapor deposition source, with the advantage of precise calibration of the flux by integration of the ion current, and other advantages described previously. Results of this study include the attainment of a work function equal to 0.9 eV by  $\text{Cs}^+$  bombardment and oxygen co-adsorption and experimental support for an asymmetric dimer model for the sputter cleaned and annealed  $\text{Si}(100)$  target.

## B. PIERCE GUN

For energies from 50 to 500 V, a Pierce type [17,23] extraction system of our own design is used, as shown in figure 1. It consists essentially of three conical sections, two for the focus electrode and one for the extraction electrode. The analytic solution for the field in a spherically convergent ion gun has been worked out in detail [24]. It gives a complete representation of the potential distribution at the beam edge with the perveance, convergence angle and radius of curvature of the cathode as parameters. The perveance (P) is defined from the Child-Langmuir equation for space charge limited flow in a diode,

$$I = PV^{3/2} \quad \text{Eq. 1}$$

and is determined for a given set-up only by geometric factors. The design values were as follows: a perveance of  $1.0 \times 10^{-9} \text{ A/V}^{3/2}$ , a convergence angle of  $11.8^\circ$ , and a cathode radius of 9.76 mm.

A computer program written in house is used to determine the potential distribution at the beam boundary for a given electrode configuration. This calculation is subject to the boundary condition that the gradient of the potential at the beam edge be parallel to that edge, and to boundary conditions at the electrode surfaces. The program uses a triangular grid, which allows the density of grid points to be adjusted to give greater accuracy in the regions of higher field. This method gives good accuracy without requiring excessive computation time. The angles of the electrodes are varied until the error between the computed beam edge

potentials and the analytic values is less than 1%. These computer calculations indicate that a deviation in the angle of the electrode surface in contact with the emitter of as little as  $1^\circ$ , results in an average error close to the emitter of 4.5%.

The emitting surface of the pellet is placed in electrical contact with the beam forming electrode of the Pierce gun as shown in figure 1. The aperture in the extraction electrode is covered with an 84% transmitting W mesh to remove aberration and divergent lens effects [23]. The electrodes are assembled on a mounting jig and are then secured and insulated by glass rods. The rods are mounted by heating them until they are soft, and inserting the electrode supports into them. The machining accuracy of the focus electrode is critical to obtain an acceptable beam. We have seen experimentally that an electrode with a  $7^\circ$  error results in a source that is drastically different and in complete disagreement with the intended design. The electrodes used in this gun have an angular error of  $< 0.5^\circ$ .

In figure 2, the I-V characteristics are shown for several temperatures. A perveance of  $1.2 \times 10^{-9} \text{ A/V}^{3/2}$  is experimentally determined from the slope of these lines. The lowest temperature data illustrates the effect of sample bias. For zero bias, the current increases as  $V^{3/2}$ , as it should for space charge limited emission. However, at  $\approx 100 \text{ V}$  the rate of increase begins to drop, indicating that the current is becoming emission limited. With the proper bias voltage placed across the pellet, the emission increases to its space charge limited value.

The theoretical value for the position of minimum beam radius, taking only

space charge into account [23] is 10.9 mm from the cathode surface. The actual focal point varies slightly, from 10.5 mm at 100 V to 11.5 mm at 500 V. The beam radius at the focal point is measured by passing a Faraday cup with two slits a known distance apart, across the beam. The beam radius is then determined by measuring the peak half width at half maximum and calibrating using the known slit distance. In figure 3 are plotted experimental data, showing the beam radius at the focal point versus beam energy. The solid line represents the equation,

$$R = f \sqrt{\frac{T}{\pi U}} + \Delta \quad \text{Eq. 2}$$

where  $R$  is the beam radius at the focal point,  $f$  is the focal distance,  $T$  is the effective beam temperature in eV,  $U$  is the beam energy and  $\Delta$  is the spread due to space charge. The only variable parameter in this equation is the effective beam temperature. All the other values are known. This equation is arrived at by assuming that the beam starts off with a Maxwellian distribution of initial transverse velocities. The value for the spread due to space charge can be calculated [23], and is found to be  $D = 0.086$  mm. Using  $T$  as a fitting parameter we obtain the curve shown in figure 3 for an effective beam temperature of 0.35 eV. This is to be compared to the actual temperature of 0.11 eV. The fact that this effective spread is greater than the true thermal spread can be attributed to deviations from true Pierce geometry caused by a combination of design ( $< 1\%$ ), and machining ( $< 0.5^\circ$ ) errors.

This gun has been used in studies of composite thin film production by ion bombardment [25]. Results show the relationship between steady state surface

concentration of Cs, incident energy and substrate mass.

### C. HIGH ENERGY GUN

For energies from 0.5 to 5 keV, the Pierce gun described in the previous section is mated to an optical column consisting of two einzel lenses of the three tube type. This column is depicted schematically in figure 4. It consists of an initial aperture which is mounted at the Pierce gun focal point. This aperture is then imaged by a condenser lens to a point inside a drift tube, at the end of which is a beam limiting aperture. The ions that pass this aperture are then focused to the sample by an objective lens, and rastered by deflector plates mounted after the lens. Basic optics yields the imaging ratio [26] (see figure 4):

$$\frac{d_g}{d_0} = \frac{b_1}{a_1} \times \frac{b_2}{a_2} = \frac{b_2}{a_1} \left( \frac{c}{b_1} - 1 \right)^{-1} \quad \text{Eq. 3}$$

By changing the strength of the condenser lens, the focal point  $b_1$ , inside the drift tube is changed. If this focal point is close to the aperture at the end of the tube, a large beam diameter and high beam current result. If the focal point is close to the condenser lens, a small beam diameter with low beam current is obtained. By this method, a wide range of imaging ratios is covered.

An approximate relation for the beam radius as a function of beam current is derived [26],

$$R = \frac{1}{2} \sqrt{\left( \frac{4I}{\beta} (\pi\alpha)^{-2} + \frac{(C_s^2 \alpha^3)}{4} \right)} \quad \text{Eq. 4}$$

where  $\alpha$  is the convergence half angle and  $\beta$  is the beam brightness, defined as ( $\text{A cm}^{-2}\text{sr}^{-1}$ ).  $C_s$  is the spherical aberration coefficient. Because of the intrinsically low energy spread of the source, we can ignore chromatic aberrations. If we know the optical properties of the lens column, we can then determine the brightness. In figure 5, experimentally determined values for beam radius versus beam current are shown for a beam energy of 2.5 keV. The solid line is a plot of equation 3 using the estimated values [27],  $\alpha = 1.17 \times 10^{-2}$  rad,  $C_s = 100$  cm, and using  $\beta$  as a fit parameter. The brightness value for a best fit is found to be  $\beta = 1.0 \text{ A/cm}^2\text{sr}$ . We are presently developing a microprobe ion gun using a version of this same source, that will have an estimated brightness an order of magnitude larger.

This gun has been used for implantation studies, and for negative secondary ion mass spectrometry (SIMS). Implantation studies were undertaken to provide evidence for a simple model developed for formation of composite thin films by ion bombardment [25]. Calculated concentration profiles were found to match qualitatively the experimental SIMS depth profiles. Negative SIMS studies indicate that using cesium as a primary bombarding ion enhances the yield of atoms and molecules with high electron affinity [9,10]. In figure 6, the ratio of the  $\text{Si}^{-29}$  yield due to  $\text{Cs}^+$  ion bombardment to the yield due to xenon bombardment is shown as a function of  $\text{Cs}^+$  dosage. Xenon is used because its mass is essentially the same as that of cesium, thus only the electrochemical differences will affect the results. The data show a gradual increase as a function of dose, which is attributed to formation of a thin layer of cesium, as described in a previous paper [25]. At steady state, the yield levels off at a value 50 times greater than that due to xenon bombardment.

#### IV. SUMMARY

We have developed a solid state cesium ion source that can be used in a variety of extraction geometries. It is clean, compact, and is compatible with a wide range of system pressures.

Applications described in this paper are low energy bombardment as an alternative to vapor deposition, studies of low and high energy bombardment and implantation, and negative SIMS. Studies of low temperature oxidation and nitridation promoted by cesium deposition are in progress.

#### ACKNOWLEDGEMENTS

Special thanks goes to George Wohlrab whose machining capabilities and general assistance in keeping the experiment running are greatly appreciated and to Mr. Dorota at Apex Electronics.

This work has been supported by the Air Force Office of Scientific Research, the Department of Energy and the New Jersey Commission on Science and Technology.

## REFERENCES

- 1 D.L. Ferhs and R.E. Stickney, Surf. Sci. 8 (1967) p. 267
- 2 L.W. Swanson and R.W. Strayer, J. of Chem. Phys. 48(6) (1968) p. 2421
- 3 C.A. Papageorgopoulos and J.M. Chen, Surf. Sci. 39 (1973) p. 283
- 4 H. Yasunaga, Rev. Sci. Instrum. 47(6) (1976) p. 726
- 5 R.E. Weber and W.T. Peria, Surf. Sci. 14 (1969) p. 13
- 6 R.U. Martinelli, J. Appl. Phys. 45(3) (1974) p. 1183
- 7 A.H. Sommer, J. Appl. Phys. 51(2) (1980) p. 1254
- 8 J.L. Lopes, J.A. Greer and M. Seidl, J. Appl. Phys. 60(1) (1986) p. 17
- 9 M. Seidl, A.E. Souzis, W.E. Carr, and G.S. Tompa, 37th Pittsburg Conference  
and Exposition, Book of Abstracts, No. 743 (March 1986)
- 10 H.A. Storms, K.F. Brown and J.D. Stein, Anal. Chem. 49(13) (1977) p. 2023
- 11 A. Franciosi, et al., Phys. Rev. B 35(2) (1987) p. 910
- 12 P. Soukiassian, et al., J. Vac. Sci. Technol. A 6(3) (1988) p.1535
- 13 D.G. Welkie, *Secondary Ion Mass Spectrometry SIMS V*, A. Benninghoven  
et al. Editors, Springer-Verlag, New York, (1986) p. 146
- 14 G.R. Brewer, *Ion Propulsion*, Gordon and Breach, New York (1970) Chap. 4
- 15 O. Heinz and R.T. Reaves, Rev. Sci. Instrum. 39 (1968) p. 1230
- 16 M. Seidl, U.S. Patent # 4,783,595
- 17 J.R. Pierce, *Theory and Design of Electron Beams*, Van Nostrand Company,  
Inc., Princeton, New Jersey (1954), pp. 173-193 and chapter 10
- 18 S.I. Kim and M. Seidl, Submitted to Rev. Sci. Instrum.
- 19 J. Ito, Am. Mineralogist 61 (1976) p. 170



- 20 Donald W. Breck, *Zeolite Molecular Sieves*, John Wiley & Sons, NY-London-Sydney-Toronto (1974) Chapter 7
- 21 R.E. Weber and L.F. Cordes, *Rev. Sci. Instrum.* **37** (1965) p. 112
- 22 A.E. Souzis, M. Seidl, W.E. Carr and H. Huang, *J. Vac. Sci. Technol. A* **7**(3) (1989) p. 720
- 23 R.G. Wilson and G.R. Brewer, *Ion Beams With Applications to Ion Implantation*, John Wiley & Sons, New York, (1973) Chap. 3
- 24 I. Langmuir and D. Blodgett, *Phys. Rev.* **24** (1924) p. 49
- 25 W. Carr, M. Seidl, G.S. Tompa and A. Souzis, *J. Vac. Sci. Technol. A* **5**(4) (1987) p. 1250
- 26 H. Liebl, *Vacuum* **33**(9) (1983), p.525
- 27 A. Adams and F.H. Read, *J. Phys. E: Sci. Instrum.* **5** (1972), p.150

## FIGURE CAPTIONS

Figure 1. Cesium ion source assembly drawing, shown with the Pierce electrodes as an example.

Figure 2. Current versus voltage characteristics for the Pierce gun at several source temperatures. The 920 °C curve illustrates the effect of sample bias.

Figure 3. Pierce gun beam radius at the focal point versus beam energy. The squares are experimental data, and the curve represents eq. 2 in the text for an effective beam temperature of 0.35 eV.

Figure 4. Schematic drawing of the high energy cesium ion gun, showing the two lens arrangement used for acceleration and focusing.

Figure 5. Beam radius versus beam current for the high energy cesium ion gun at a beam energy of 2.5 keV. The squares are experimental data, and the line represents eq. 4 in the text.

Figure 6. Ratio of the SIMS yield of negative  $\text{Si}^{29}$  under cesium ion bombardment to the yield under xenon bombardment, as a function of cesium ion dose. Bombarding energies were both 4 keV.

